PSL UNIVERSITÉ PARIS

THÈSE DE DOCTORAT
DE L'UNIVERSITÉ PSL

Préparée à École Normale Supérieure de Paris

Rayonnement haute fréquence et précurseurs des séismes en laboratoire

High frequency radiation and foreshocks during laboratory earthquakes

Soutenue par
Samson Marty
Le 21 Janvier 2020

Ecole doctorale n° 560
Sciences de la Terre et de l'Environnement et Physique de l'Univers

Spécialité
Sciences de la Terre et de l'environnement

Composition du jury :

Elisa, Tinti Professeure, U-La Sapienza, Rome	*Rapporteur*
Michel, Bouchon Directeur de recherche, ISTerre, CNRS	*Rapporteur*
Kato, Aitaro Professeur, ERI, U-Tokyo	*Examinateur*
Clément, Narteau Professeur, IPGP	*Examinateur*
Eiichi, Fukuyama Professeur, U-Kyoto	*Invité*
Alexandre, Schubnel Directeur de recherche, CNRS	*Directeur de thèse*
Harsha, Bhat Suresh Chargé de recherche, CNRS	Co-*encadrant de thèse*

ENS | PSL

Avant-propos

A la surface du globe terrestre, les roches qui composent la lithosphère sont soumises à des forces tectoniques en raison du mouvement relatif des plaques qui la composent. Sous l'effet de ces forces tectoniques les roches se déforment et accumulent de l'énergie élastique. Dans les conditions relativements basses de température et de pression qui charactérisent la partie supérieure de la croûte terrestre, les roches finissent par libérer cette énergie élastique en se fracturant. Ce processus de fracturation se traduit par la production de failles qui permettent la localisation de la déformation. Sous l'effet du chargement tectonique, la déformation qui s'accumule sur les failles peut-être relâchée de façon lente et stable ou bien rapide et instable. Ce dernier cas correspond à une libération brutale de l'énergie élastique accumulée et constitue par définition ce qu'on appelle un séisme ou tremblement de terre. En comparaison de l'échelle de temps sur laquelle s'opère l'accumulation des contraintes tectoniques (de l'année au millier d'années), cette libération d'énergie s'opère sur une période extrêmement courte allant de la seconde à quelques minutes. Sur les plans de faille, un séisme peut donc être conceptualisé comme la frontière entre deux équilibres mécaniques :
- Etat pré-sismique: précédant la nucléation du séisme au cours duquel la faille est bloquée et l'énergie s'accumule dans les roches.
- Période co-sismique: qui commence par une période de nucléation après laquelle un front de rupture (détachement) se propage le long du plan de faille ce qui a pour conséquence de permettre le glissement et de libérer l'énergie élastique accumulée. Une fraction de cette énergie est libérée par la génération d'ondes sismiques.
Mise à part les marqueurs des failles en surface, nous n'avons pas accès à ces dernières et nous sommes donc dans l'impossibilité d'y installer des systèmes de mesure pour déterminer leur dynamique et leurs propriétés physiques. Les ondes sismiques générées pendant les phases de nucléation et de glissement sismique sont, en quasi-totalité, responsables des dégâts humains et matériels mais constituent également un des principaux vecteurs d'information de la dynamique des tremblements de terre. Dans la lithosphère terrestre, l'hétérogénéité des conditions de pression, de température, de lithologie, de présence de fluide, de chargement et de contexte tectonique est à l'origine de la complexité du comportement mécanique des roches. Au cours de cette thèse, nous avons reproduit des séismes en laboratoire, ce qui nous a permis d'explorer deux grandes thématiques : (i) la caractérisation des signaux précurseurs de la rupture sismique pendant la phase de nucléation et (ii) l'origine des ondes sismiques « hautes-fréquences » pendant le glissement sismique. Pour ce faire, nous avons utilisé deux types de roches constitutives de la croûte terrestre : le granite de Westerly et du Gabbro d'Inde.

Contents

1 Introduction **1**
1.1 Distribution de la sismicité mondiale et sismogénèse . . . 1
1.2 Cycle sismique et phases précurseurs. . . . 4
1.2.1 Cycle sismique et statistiques des séismes. . . . 4
1.2.2 Modèles conceptuels de l'origine des précurseurs. . . . 8
1.3 Source sismique et lois d'échelles des séismes. . . . 11
1.3.1 Déplacement en champ lointain : le cas d'un point source soumis à une force impulsionnelle. . . . 11
1.3.2 Déplacement en champ lointain : cas du double couple de forces et estimation du moment sismique. . . . 14
1.3.3 Modèles cinématiques d'une source de dimensions finies, origine des ondes hautes-fréquences et décroissance asymptotique. . . . 19
1.3.4 Mode de fracturation et vitesse de rupture . . . 25
1.4 Apport de la reproduction de séismes en laboratoire : de l'échelle des failles crustale à celle du laboratoire. . . . 27
1.4.1 Instabilité frictionelle . . . 27
1.4.2 Loi de friction. . . . 31
1.4.3 Etude de la microsismicité en laboratoire . . . 35
1.5 Plan du manuscript. . . . 38

2 Material and methods **39**
2.1 Experimental set-up . . . 39
2.1.1 Rock lithlogies & Sample preparation . . . 39
2.1.2 Producing experimental earthquakes using a triaxial cell . . . 41
2.1.3 Strain and acoustic emission high-frequency monitoring system 43
2.2 Acoustic sensors calibration . . . 49
2.2.1 Experimental procedure . . . 49
2.2.2 Estimation of Fourier spectra . . . 50
2.2.3 Calibration results . . . 53
2.3 Acoustic data treatment . . . 55
2.3.1 Acoustic emissions detection . . . 55
2.3.2 Auto-picking . . . 58
2.3.3 Localization . . . 58

2.4 Seismic source characterization . . . 60
2.4.1 Rupture velocity inversion . . . 60
2.4.2 The back-projection method . . . 61
2.4.3 Inversion of AE paramameters . . . 62

3 Foreshocks occurence and their link to nucleation: an experimental approach 65
3.1 Introduction . . . 65
3.2 Experimental set-up and methodology. . . . 67
3.3 Results . . . 68
3.3.1 Mechanical data . . . 68
3.3.2 AEs distribution . . . 69
3.3.3 AE and stick-slip nucleation locations . . . 73
Microstructural and fault surface roughness analysis . . . 75
3.4 Discussion . . . 80
3.4.1 Statistics of the nucleation phase . . . 80
Characterization of fault surfaces roughness . . . 80
Evolution of the precursory AEs activity towards nucleation . . . 82
Precursory AEs dynamics and fault maturation . . . 83
Spatial and temporal behavior of precursory AEs . . . 89
3.5 Scaling laws and implications for natural fault . . . 98
AE source parameters . . . 98
Pre-seismic moment and coupling . . . 99
Scaling of the AE moment release. . . . 104
3.6 Summary . . . 105

4 Origin of high-frequency radiation during laboratory earthquakes 109
4.1 Introduction . . . 109
4.2 Experimental set-up and methodology. . . . 111
4.3 Results . . . 111
4.3.1 Mechanical behavior of stick-slip instabilities . . . 111
4.3.2 Influence of rupture velocity and confining pressure on high-frequency radiation . . . 111
4.3.3 Back-projection analysis during rupture propagation. . . . 117
4.4 Discussion and conclusions . . . 119

5 Conclusions and perspectives 127
5.1 Summary of the results obtained during this thesis . . . 127
5.2 Perspectives: ongoing and future works . . . 129
5.2.1 Similar events, relative localization and completeness magnitude 129
5.2.2 Damage production during stick-slip instability . . . 131
5.2.3 Future works . . . 133
5.2.4 QTM catalog analysis . . . 136

References **143**

List of Figures

1.1 Sismicité mondiale de 1904 à 2014 pour les magnitudes $M_w > 5.5$. L'échelle de couleur renseigne sur la profondeur et la taille des symboles sur la magnitude. (`https://www.irsn.fr`). 2
1.2 Vision schématique de la transition déformation fragile - déformation ductile le long d'une interface de subduction. La limite basse de la zone sismogénique correspond environ à la limite de plasticité du Quartz (350-450 °C) 3
1.3 **A.**Vision schématique de la succession de plusieurs cycles sismiques dans le cas d'un système parfaitement périodique. **B.** Famille formée des précurseurs, du choc principal ainsi que des répliques. 6
1.4 **Corrélation entre glissement asismique et nucléation. a.** Migration de la sismicité dans le mois précédant la nucléation du séisme de Tohoku (03 mars 2011, M_w9.0). Les « repeaters » (séismes répétitifs) sont reportés en rouge et soulignent la propagation d'un glissement asismique. **b.** Surface de rupture du séisme de Tohoku, glissement cosismique et précurseurs sismiques. L'épicentre du séisme de tohoku est indiqué par l'étoile noire (extrait de Kato et al., 2012) 10
1.5 **A.** Répliques pendant les 2 années qui suivèrent le séismes de Homestead Valley en Californie (1979). Seules les répliques de $M_w > 1$ sont indiquées. **B.** Variation de la contrainte de coulomb résultante de la somme de la variation de contrainte cisaillante et de la variation de la contrainte effective (extrait de King et al., 1994) 12
1.6 Evolution spatio-temporelle de la variation de contrainte statique pendant la phase d'initiation du séisme d'Izmit de 1999 en Turquie. **a-d** Les positions indiquées par les carrés rouges correspondent aux centroïdes de quatre familles de précurseurs corrélés spatialement et temporellement (extrait de Ellsworth and Bulut, 2018) 13
1.7 Vision schématique du glissement sur une faille soumise à un double couple de forces. 15
1.8 Loi d'échelle entre surface de rupture, moment sismique (axe du bas), et magnitude (axe du haut) pour les séismes de $M_w > 6.0$ enregistrés entre 1991 et 2001 (extrait de Kanamori and Brodsky, 2004) 18

1.9 Relation entre la fréquence coin, le moment sismique (axe du bas) et la magnitude (axe du haut). Les lignes en rouge pointillées indiquent les valeurs théoriques pour une vitesse de rupture fixe et un saut de contrainte constant (extrait de Allmann and Shearer, 2009). 20
1.10 Comparaison de la loi d'échelle qui relie la durée d'un séisme à son moment sismique (axe du bas) et sa magnitude (axe du haut) entre les « séismes classiques » (**Regular earthquakes**) et les « séismes lents » qui regroupe les glissements asismiques, **SSE**, les séismes basse fréquence, **LFE**, les séismes très basse fréquence, **VLF**, les trémors non volcaniques, **ETS** et les séismes silencieux, **Silent EQ** (extrait de Ide et al., 2007). 21
1.11 **Modèle de propagation d'une dislocation sur une faille rectangulaire. a.** Glissement normalisé le long du plan de faille en fontion du temps de propagation. **b.** Glissement normalisé final le long du plan de faille. **c.** Illustration schématique de la géométrie du problème. . . . 23
1.12 **Modèle de propagation d'un crack circulaire. a.** Glissement normalisé final en fonction du temps et de la distance au point de nucléation. **b.** Glissement normalisé final en fonction de la distance au point de nucléation **c.** Illustration schématique de la géométrie du problème. . . 24
1.13 Les trois modes de fracturation. Les flèches indiquent le sens de la contrainte principale. 26
1.14 **Haut.**Vision schématique des vitesses de rupture possibles selon le mode de fracturation.**Bas.**Vision schématique de la formation d'un cone de Mach dans le cas d'une rupture Supershear. Le long du front de propagation de l'onde de Mach, les ondes S interfèrent constructivement et sont moins atténuées avec la distance (extrait de Das, 2010 28
1.15 Contrainte cisaillante maximale en fonction de la contrainte normale au moment de la rupture pour différentes lithologies. A relativement faible contrainte normale, le coefficient de friction statique égal 0.85 et chute à 0.6 à partir d'une contrainte normale d'environ 300 MPa (extrait de Byerlee, 1978). 29
1.16 **Modèle patin-ressort. A.**Schéma du modèle. La surface de contact entre le patin et l'interface simule une faille et le ressort simule le chargement tectonique lointain.**B.** L'instabilité se dévellope lorsque la résistance au frottement diminue plus rapidement avec le glissement que la décharge du ressort représentée par la pente $-k$. 31
1.17 Nucléation de la rupture selon le modèle de Ohnaka (Ohnaka, 2000). La nucléation débute par la propagation d'une zone de glissement quasi-statique jusqu'à une longueur L_t qui marque le début de l'instabilité. La zone de nucléation accélère jusqu'à atteindre la longueur critique L_c à partir de laquelle l'instabilité se propage dynamiquement. 32

1.18 **Modèles conceptuels de l'évolution du coefficient de friction f avec le glissement. a.** Linear slip weakening. **b.** Rate and State. 33
1.19 Corrélation entre la nucléation de la rupture par propagation d'une zone de glissement asismique (bleu clair) et précurseurs acoustiques (cercles noirs). La surface représente le plan de faille (extrait de McLaskey and Kilgore, 2013). 37

2.1 Sample preparation. Initially, rocks arrive in the form of rectangular blocks (1), inside which cylinders are drilled. Top and bottom parts of the cylinders are then made parallel (2). The samples are finally cut at 30°, with respect to their axis, to reproduce an experimental fault. (3). . 40
2.2 Triaxial apparatus and rock assemblage. **a.** Schematic of a triaxial oil-medium loading cell. Two external servo pumps control axial and radial stresses. The axial displacement is given by the displacement of the piston which, in this case, is measured by an LVDT at its top. **b.** Saw-cut rock specimen used to reproduce laboratory earthquakes. The fault plane is oriented at 30° with respect to the principal stress σ_1. Seismic waves generated during the experiments are recorded by acoustic sensors glued at the surface of the sample. 42
2.3 Typical evolution of shear stress and axial displacement during stick-slip cycles. The linear increase of the shear stress with the displacement corresponds to the inter-seismic loading. Once the shear-stress reaches the critical strength of the fault, a frictional instability develops and the stored elastic energy is suddenly released with seismic slip along the fault interface. 43
2.4 **a.** Schematic of an acoustic sensor. The piezoelectric ceramic allows to record surface vibrations in the form of a voltage. The signal is recorded by using an oscilloscope connected by a coaxial cable. **b.** Photograph of the type of acoustic sensor used in the experiments. **c.** Schematic view of the acoustic emissions monitoring system. Output signals are amplified to continuously record microseismicity during the experiments. 45
2.5 Strain measurements. **a.** Picture of the strain gauges glued on the surface of the sample. Strain gauges are positioned as close as possible to the simulated fault. **b.** Picture of the type of strain gauge used during the experiments. Strain gages are resistors whose resistance changes correspondingly to the strain. **c.** Picture of the amplifier used to set the recording gain of strain measurements. 46

2.6 **a.** Sensors map used in the experiments presented in chapter 3. Acoutic sensors were positioned homogeneously to better locate acoustic emissions and estimate their respective seismological parameters. **b.** Sensors map used in the experiments presented in chapter 3. The near-field acoustic sensors were used to invert rupture velocities and far-field acoustic sensors were used to perform back-projection analysis . 47

2.7 Triggered recording during stick-slip instabilities. Unamplified signals are digitized using a digital oscilloscope and can be recorded up to 50 MHz sampling rate. **a.** Strain gauge recording during stick-slip instability. The strong increase in voltage corresponds to the rapid unloading of the fault surface during stick-slip instability. The fault is able to slip only after the passage of the rupture front. **b.** Acoustic sensor recording during stick-slip instability. The first P-wave is emitted once the rupture becomes dynamic. 48

2.8 **Top**. Photograph of the experimental set-up used for acoustic sensors calibration. a. High Frequency Generator. b. Amplifier. c. Laser vibrometer acquisition system. d. Laser beam. e. Rock sample with the acoustic sensor and the source glued on. f. Digital oscilloscope. **Bottom**. Schematic view of the calibration procedure. The source is positioned at the center of the fault and subject to an input voltage. Surface vibrations of the opposing side are recorded by the acoustic sensor first and then by the LDV. 51

2.9 **a.** Fourier spectra of surface vibration measurements recorded by the LDV and the acoustic sensor. **b.** Sensitivity function obtained by the ratio of the two spectra. 52

2.10 **a.** Comparison between the sensitivity function estimated without windowing and the sensitivity function estimated from multitapered signals. **b.** First five Slepian sequences used for the multitapering. The total energy corresponding to the area under the curves equals 1. . 53

2.11 Example of voltage and velocity measurements for the two types of sources and the estimated spectra. The time window used to estimate the spectra is indicated by the black double arrow. This time window is 50 μs long and is centered pn the first P-wave arrival. 54

2.12 Calibration curves. **a.** Sensitivity functions corresponding to the source M110-sm. The dashed lines indicate the calibration curves obtained for an input voltage of 40 V and the solid lines for an input voltage of 200 V. **b.** Same as **a.** but for the source V109-rm. **c.** Comparison of the sensitivity function averaged over all input voltages and source durations. Acoustic sensors have a net non linear instrumental response showing a large resonance band between 1.2 MHz and 2.2 MHz (delimited by the two black arrows) 56

2.13 **Continuous recording.** On top is displayed an example of the total duration of one continuous acoustic recording. The large and regular spikes correspond to the stick-slip events. Close to failure (bottom right), microseismicity rate is increasing. Acoustic emissions (bottom left) are searched within the continuous waveform using a 406.9 μs long sliding time window. 57
2.14 **a.** Typical acoustic waveform. The estimated first P-wave arrival time is indicated by the black dashed line. **b.** Auto-picking function amplitude. In this example the amplitude threshold was set to 50, the length of the back-window and of the front-window were 10 μs and 3.5 μs respectively. The picked P-wave arrival time was set to the maximum peak amplitude. 59
2.15 Schematic view of the back-projection stacking procedure. The fault interface is divided into a grid of source points. Acoustic signals represent what would record 4 acoustic sensors. According to theoretical first wave arrivals, zones of energy release will result in coherent, large amplitude stacks which is shown by the intersection of the dashed red line and the schematic acoustic waveforms. 63
2.16 Fitted displacement spectra and acoustic waveforms. **a.** Displacement spectra and best fit for $Mw - 7.7$ and $Mw - 8.6$ events with their respective estimated corner frequencies indicated by the arrows (0.88 MHz and 1.5 MHz, respectively). **b.** Corresponding waveforms used to estimate the spectra, the color code is the same than in **a.**. Waveform amplitudes were multiplied by a factor two for visualization. The black dashed line indicates the von Hann window used to taper the waveforms. 64

3.1 Cumulative displacement, shear-stress and AE rate during the experiments. AEs were stacked into 1 second bins. The displacement was corrected from the elastic deformation of the sample and of the apparatus. 70
3.2 Distribution of the number of AEs (left) and the total AE moment release (right) per stick-slip cycle during the experiments. For particular SSEs, the total AE moment release is a lower bound due to the saturation of the acoustic sensors for $Mw > -7$. Star symbols indicate the AE sequences that contain at least more than 1 AE of $Mw > -7$. 72

3.3 Frequency-magnitude distribution of the generated AEs during the experiments. Colored circles correspond to the cumulative G-R distribution of the AEs moment magnitudes. Black arrows indicate the moment magnitude Mw that correspond to the beginning of the acoustic sensors saturation ($Mw = 7$). Black dashed lines show the b-values that we estimated according to the Aki-Utsu maximum likelyhood method. Bar plots are showing the distribution of the AEs moment magnitudes into 0.1 magnitude interval bins. 74
3.4 Fault surfaces conditions, AE and stick-slip nucleation locations. Circle size refers to the AE moment magnitude and was set according to the estimated source size. The colorscale refers to the SSE index. Only the AEs whose location errors are less than 2-3 mm are reported here. . 76
3.5 Microtexture of the fault surfaces after stick-slip experiments under Scanning Electron Microscopy at : **a.**, **b.** $Pc = 30\ MPa$, **c.**, **d.** $Pc = 45\ MPa$ and **e.**, **f.** $Pc = 60\ MPa$. The direction of sliding is indicated by the white arrow. **a.** Small scale view of gouge particles with various sizes ranging from few μm to 100 nm. **b.** Enlarged view of **a.** showing an highly damaged surface covered with patches of gouge particles heterogeneously distributed. We sense a small scale asperity at the center slightly deformed into the direction of sliding. **c.** Small scale view of amorphous fine gouge particles layer. **d.** Enlarged view of **c.** showing clusters of smashed gouge particles with sizes up to 10 μs. The fault surface presents striations along the sliding direction which suggest plastic deformation during stick-slip events. **e.** Small scale view of the fault surface showing evidence of partial melting during sliding. A fraction of the small gouge particles is trapped into the melt. **f.** Large scale view of **e.** showing stretched and elongated surfaces formed due to partial melting and covered with (more) homogeneously distributed gouge particles. 77
3.6 Microtopography of fault surfaces at: **a.** $Pc = 30\ MPa$, **b.** $Pc = 45\ MPa$ and **c.** $Pc = 60\ MPa$. The microtopography was measured using a laser profilometer presenting a resolution of 0.05 μm. The colorscale indicate the microtopography and is given in μm. Sampled surfaces are 15 mm wide and 30 mm long and correspond to the black rectangles shown on the right. 79
3.7 Power spectrum of the fault surfaces microtopography as a function of the wavenumber k and extracted from the stacking of the 1-D profiles along the perpendicular, **a.** and the parallel directions, **b.**, of the direction of sliding. Black dashed lines represent the power-law expected for a self-affine surface characterized by a Hurst exponent H of 0.4 82

3.8 Cumulative AE moment release and b-value evolution prior to failure at : **a.** $Pc = 30\ MPa$, **b.** $Pc = 45\ MPa$ and **c.** $Pc = 60\ MPa$. The cumulative AE moment release is relative to the normalized time to failure and results from the stacking of all the precursory AE sequences. Square and diamond symbols show the AEs b-values and their uncertainties that were estimated at various time intervals relative to the onset of stick-slip instability. Square symbols correspond to the b-values that were estimated after removing the saturated AEs ($Mw > 7$) and the diamond symbols show the b-values that were estimated using the full AEs catalogs. 84

3.9 **Comparison between the normalized along fault displacement, along fault velocity, cumulative number of AEs and cumulative AE moment release as a function of the normalized time to failure at: a.**, $Pc = 30\ MPa$, **b.**, $Pc = 45\ MPa$ and **c.**, $Pc = 60\ MPa$. All curves result from the stacking of all the SSEs. The grey shaded area around the AE moment release corresponds to the cumulative error of the magnitude estimates. **Evolution of of the normalized cumulative number of AEs as a function of the normalized time to failure at: d.**, $Pc = 30\ MPa$, **e.**, $Pc = 45\ MPa$ and **f.**, $Pc = 60\ MPa$. The colorscale indicates the SSE index and the black curves result from the stacking of all precursory AE sequences. 87

3.10 Distance to nucleation of the precursory AEs as a function of the normalized time to failure at : **a.** $Pc = 30\ MPa$, **b.** $Pc = 45\ MPa$, **c.** $Pc = 45\ MPa$. The cyan triangles indicate the average distance to nucleation and its standard deviation computed into 10 log-distributed time intervals. On the left is shown the pdf of the precursory AEs as a function of their distance to nucleation. 91

3.11 **a.** Cumulative AE moment release and along fault displacement in the last 10 seconds prior to SSE #6 during the experiment conducted at $Pc = 60\ MPa$. **b.** Distance to nucleation of the precursory AEs prior to failure. **c.** Locations, sizes and timing of the precursory AEs that occur prior to SSE #6 ($Pc = 60\ MPa$). The colorscale refers to the timing of the AEs relative to failure. Circle size indicates the moment magnitude and was set according to source size. The star symbol indicates the nucleation location. **d.** Schematic view of the shear-stress evolution on locked portions of the fault (i.e., in the interior of the nucleation zone) during nucleation. The black dashed lines indicate the shear-stress profile. The red line idealizes the critical strength of the locked fault patches in the case of an homogeneous medium. The star symbols depict a schematic view of the migration in time and space of precursory AEs towards nucleation initiation. The stress perturbations at the tips of the nucleation zone trigger the precursory AE activity far from nucleation. As the nucleation zone expands, stresses build-up in the interior of the nucleation. The shear-stress gradient leads to the migration of the precursory AEs towards the center of the nucleation zone. 94

3.12 Inverse power law of time of the average cumulative number of AEs towards failure at: **a.** $Pc = 30\ MPa$, **b.** $Pc = 45\ MPa$ and **c.** $Pc = 60\ MPa$. The red curves indicate the best fits obtained on parameters c and p. The inserted figures display the logarithm of the residuals normalized by the minimum (i.e., 0 indicates the minimum) as a function of c and p. 97

3.13 Relationship between M_0 and f_c at: **a.** $Pc = 30\ MPa$, **b.** $Pc = 45\ MPa$ and **c.** $Pc = 60\ MPa$. Dashed black lines represent stress drops of 0.01, 0.1, 1, 10, 100 MPa from Madariaga's source model (Madariaga, 1976). **d.** The AEs source paramters for all the experiments are plotted as gray circles. The other points represent a corpus of previous studies and were taken from Yoshimitsu et al., 2014. 99

3.14 **a.** Relationship between the pre-seismic moment release and the total AE moment release. Each diamond represents one SSE. Only the AE sequences that do not contain saturated AEs are shown here. The black-dashed lines indicate a power-law exponent of 4. **b.** Relationship between the pre-seismic moment release and the co-seismic moment release. The grey squares and circles correspond to the observations of two other experimental studies (Passelègue et al., 2017; Acosta et al., 2019). The black dashed line which indicates a slope of 0.56 corresponds to the scaling law between the pre-seismic moment release M_p and the co-seismic moment release M_c proposed by Acosta et al. (2019). A linear relation between both is given by the black dashed line whose slope = 1. The inserted figure displays the comparison between our observations and what was found for a set of large earthquakes ($Mw \geq 7.6$). 103

3.15 Scaling of the cumulative AE moment release with fault surface roughness and normal stress. On top is displayed the raw cumulative AE moment release in function of the normalized time to failure and below is displayed the same but scaled according to the fault surfaces roughness and to normal stress conditions. All curves result from the stacking of all the AE sequences excepted those which contained saturated AEs. 106

4.1 **a.** Evolution of shear stress and slip versus time at $Pc = 60MPa$. When the shear stress on the frictional interface exceeds the fault strength the stored elastic is suddenly released by seismic slip. The cumulative slip remains constant during loading because it is corrected from the elastic part of the deformation (sample + apparatus). **b.** Relationship between shear stress drop and slip for all experiments. The ratio between the stress drop and the slip is preserved (higher the stress drop, higher the amount of slip) and is equal to the stiffness of the whole system (sample + apparatus). 112

4.2 **a.** Travel time plot of near field acoustic recordings in function of their distance to the nucleation for one stick-slip event that ruptured at supershear speed. Blue, black and red dashed lines represent isochrones of rupture front arrivals and first P and S wave arrivals respectively. **b.** Same as (**a**) but for a sub-Rayleigh rupture. **c.** Time residual as a function of rupture velocity for the supershear event. **d.** Same as (c) but for the sub-Rayleigh event. 113

4.3 **a.** Schematic view of the arrival to a receiver S at distance Z_c to the fault of a Mach front emitted from a single point E. The position of the nucleation is indicated by N. **b.** Waveforms recorded by 4 far-field acoustic sensors positioned at different distances Z_s to the fault during a supershear event at $Pc = 45\ MPa$. Blued and red dashed lines represent the first P-wave and S Mach front arrivals respectively. The Mach wave corresponds to the light red area. 114
4.4 **a.** Rupture velocities obtained by inversion as a function of static shear stress drop. Rupture velocities are normalized by the shear wave velocity, values higher than 1 correspond to supershear velocity and lower than 0.92 to sub-Rayleigh velocities. Stars indicate stick-slip events whose Fourier spectra are displayed in Figure 4.4 b. **b.** Fourier spectra of the last stick-slip event during stick-slip experiments at varying confining pressures. Fourier spectra are averaged using both near-field and far-field acoustic sensors, and normalized by their respective stress-drop. The gray shaded areas indicate frequency bands used for the back-projection analysis. 115
4.5 Relationship between the static friction coefficient and the Seismic ratio according to eq. (4.3). 117
4.6 Acoustic waveforms used for the back-projection analysis displayed in Figure 4.7: raw acoustic waveforms (left) and band-pass (400-800 kHz) acoustic waveforms (right). Waveforms are aligned on the first P-wave arrivals and are normalized by their maximum amplitudes . . 118
4.7 Snapshots of back-projection results for one stick-slip event at Pc = 90 MPa from far-field waveforms bandpass filtered to 400-800 kHz (**top**) and highpass filtered above 800 kHz (**bottom**). The colorbar represents the value of the normalized coherency function on the fault plane. The time is relative to the onset of the nucleation. The red star indicates the nucleation location and the black dashed line indicates the rupture front theoretical position estimated from the average rupture velocity V_r obtained by inversion, here equal to 5.1 km/s. 119
4.8 Back-projection analysis applied on a noise window. **a.** Back-projection results in the 400-800 kHz frequency band. **b.** Same as (a) but above 800 kHz. **c.** Noise spectrum 122
4.9 Snapshots of back-projection results for the last stick-slip event at $Pc = 90\ MPa$ in the 400-800 kHz frequency band. The color scale represents the normalized coherency function and the time is relative to the onset of the nucleation. 123
4.10 Microtextures of the fault surface under Scanning Electron Microscope. **a.** Gouge particles and elongated residual material which supports that part of the surface melted due to frictional heating. **b.** Microcracks at the micrometer scale. 124

4.11 Synthetic tests. On the top is displayed the geometry of the far-field acoustic sensor array with respect to the fault (dark blue ellipse) used in the model. The sensor array geometry is similar than the one used for the back-projection analysis. On the top right is displayed the locations of the input point sources on the fault interface. An example of synthetic acoustic sensor recording is displayed in the middle. On the bottom are displayed synthetic tests for two scenarios, either for sources with a characteristic frequency equal to 400 kHz (left) or with a characteristic frequency equal to 800 kHz (right). The color-bar indicates the value of the normalized coherency function. The red color represents the maximum of energy and the blue color the minimum of energy. 126

5.1 **a.** Example of the coherency matrix for the experiment conducted at $Pc = 45\ MPa$. Here, only pairs of events whose coherence $C(\Delta\omega)$ was higher than 0.95 for at least 3 acoustic sensors are shown. **b.** Relationship between the average time delay and the average coherence. The time delay is the reciprocal in time domain of the phase delay in frequency domain. **c.** Extracted family of 10 similar AEs. Waveforms have been aligned to their first P-wave arrival but have been slightly shifted for visualization. 131

5.2 **a.**Example of the evolution of the time delays during one stick-slip experiment conducted at $Pc = 45\ MPa$. Time delays were measured following each stick-slip instability. Each vertical alignment of colored circles represents a source-receiver pair and is defined by the angle θ. The colorscale refers to the SSE index. **b.** Shear-stress and along fault displacement versus time. A sequence of 22 SSEs were reproduced. **c.** Schematic view of the acoustic sensors array geometry. One acoustic sensor is used as a source and is affixed on one edge of the sample. Seven acoustic sensors are used as receivers and are positioned on the other edge of the sample. Pairs of source-receiver are defined according to the angle θ between the ray source-receiver and the direction perpendicular to the fault plane. Damage will be concentrated in the tensional quadrant (T). 134

5.3 Summary of the QTM catalog. **a** Non cumulative frequency-magnitude distribution of earthquakes contained in the SCSN catalog, the full QTM catalog and the relocated QTM catalog. **b** Same as A but for the cumulative frequency-magnitude distribution of earthquakes. **c** Earthquake density in the QTM catalog computed into 2 km x 2 km bins. (Taken from Ross et al., 2019) 137

5.4 Nearest neighbor distance analysis. **a** Schematic view of the bimodal distribution of $log(\eta)$ in the case of the coexistence of weakly related and strongly related events. The threshold $log(\eta_0)$ is used to distinguish the clustered events from the background events and is given by the intersection of the two distributions. **b** Schematic view of the joint distribution of the rescaled time and space components T, R. The dashed line shows η_0. **c** Distribution of the nearest-neighbor distance η using the relocated QTM catalog. The blacked dashed line indicates the threshold η_0 used to cluster the event pairs. **d** Joint distribution of the rescaled time and space components T, R. The dashed lines show $log(\eta_0) = -4.2$ and $log(\eta_0) = -5$. Following Zaliapin and Ben-Zion, 2013, we used $log(\eta_0) = -5$. The figures **a** and **b** were extracted from Tamaribuchi et al., 2018 139

5.5 Cumulative number of foreshocks towards failure. **a.** Map of earthquake density in the QTM catalog (taken from Ross et al., 2019). The black dashed lines and the red dashed lines indicate the corresponding regions to figures **c.** and **d**. **b.** Normalized cumulative number of precursory AEs towards failure during the experiments conducted at $Pc = 30, 45$ and $60\ MPa$. **c.** Normalized cumulative number of foreshocks towards failure for various depth layers for the period 2008-2010. Only clusters whose mainshock magnitude Mw is comprised between 2 and 2.5 were used. All foreshocks were synchronized to the time of their respective mainshock and stacked. **d.** Same as **c.** but for the reduced region (red rectangle). In the former, all clusters whose mainshock magnitude was less or equal to 3 were used. 141

Chapter 1

Introduction

1.1 Distribution de la sismicité mondiale et sismogénèse

En janvier 1912, Alfred Wegener expose sa théorie de la dérive des continents. La surface du globe serait composée de plaques tectoniques dont les positions relatives varieraient au cours des temps géologiques. A cette date, nos observations étant restreintes aux continents, notre connaissance de la dynamique interne de la Terre, notamment des mouvements convectifs à large échelle qui existent dans le manteau supérieur, était encore embryonnaire et ardemment débattue. L'hypothèse proposée par Alfred Wegener fût donc rejetée, majoritairement en raison de l'absence d'explications convaincantes quant au moteur de la tectonique des plaques. Il fallût attendre les années 60 et la découverte des anomalies magnétiques du plancher océanique pour que la théorie de la tectonique des plaques commence à faire consensus. Alfred Wegener aurait obtenu un argument de taille si en 1912 la répartition de la sismicité mondiale avait été autant détaillée qu'actuellement.

La répartition des séismes (Figure 1.1) n'est en effet pas aléatoire à la surface du globe et se concentre aux frontières entre les plaques tectoniques. Plus précisément, la sismicité y est d'autant plus intense que les vitesses relatives à l'interface entre deux plaques est élevée (Ide and Aochi, 2013), si bien que c'est au niveau des zones de subduction, où les conditions de température et pression favorisent de plus un comportement de type « fragile » des roches et une déformation localisée à plus grande profondeur, que la majeure partie de la sismicité terrestre est dissipée.

En fonction des conditions P-T (pression et température) et de la vitesse de déformation, différents mécanismes de déformation peuvent coexister. On parlera de mécanismes de types « fragiles », ou bien de mécanismes de types « ductiles » ou « plastiques ». A relativement basses conditions P-T, les roches soumises à une déformation accumulent de l'énergie élastique (par analogie avec un ressort que l'on comprimerait ou que l'on étirerait) et libérent cette énergie de manière fragile. Le comportement « fragile » des roches se caractérise par une déformation accomodée

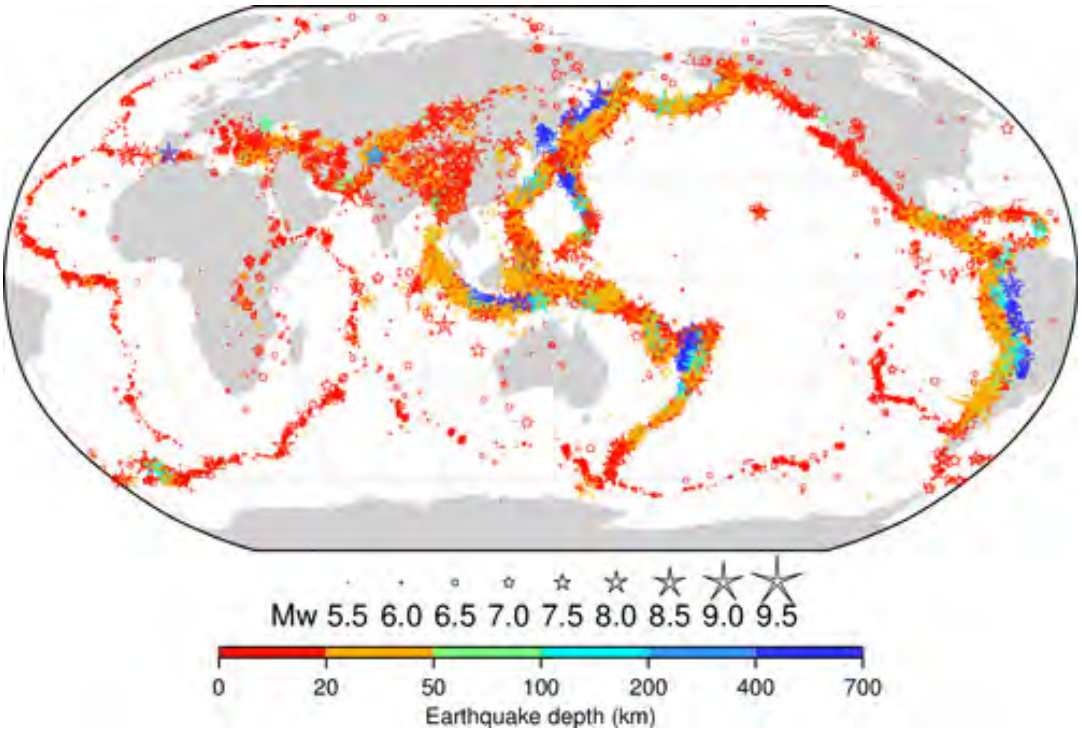

FIGURE 1.1: Sismicité mondiale de 1904 à 2014 pour les magnitudes $M_w > 5.5$. L'échelle de couleur renseigne sur la profondeur et la taille des symboles sur la magnitude. (https://www.irsn.fr).

localement par glissement sur un ou plusieurs plans de faiblesse macroscopiques qui résultent de la formation et de la coalescence de fissures. Les failles naturelles en sont l'illustration.

La localisation de la déformation sur les failles est précédée par un pic de résistance du matériau qui se traduit par un pic de contrainte cisaillante. Dans le cas présent, on parle d'approche type « Mohr-Coulomb », c'est-à-dire, où la résistance à la rupture d'un matériau est proportionnelle à la contrainte normale qui s'y applique. Ce rapport de contrainte au moment de la rupture définit le « coefficient de friction statique », nous reviendrons un peu plus tard sur cette notion. Avec l'augmentation de la profondeur dans la lithosphère terrestre, la température et la pression augmentent ce qui d'un point de vue mécanique se traduit par la transition d'un comportement fragile et d'une déformation localisée des roches à un comportement ductile et une déformation diffuse. Lorsque la pression augmente, les fissures n'ont plus la possibilité de coalescer pour former une fracture macroscopique et localiser la déformation. Interviennent alors d'autres processus de déformation à l'échelle intra-cristalline comme des mouvements de dislocations. Notons que ce type de ductilité résulte également en une déformation macroscopique. Ce dernier cas est couramment observé dans la plupart des roches (Tullis and Yund, 1992; Wong et al., 1997; Schubnel et al., 2006; Schubnel et al., 2007). L'augmentation de la température a également pour effet de

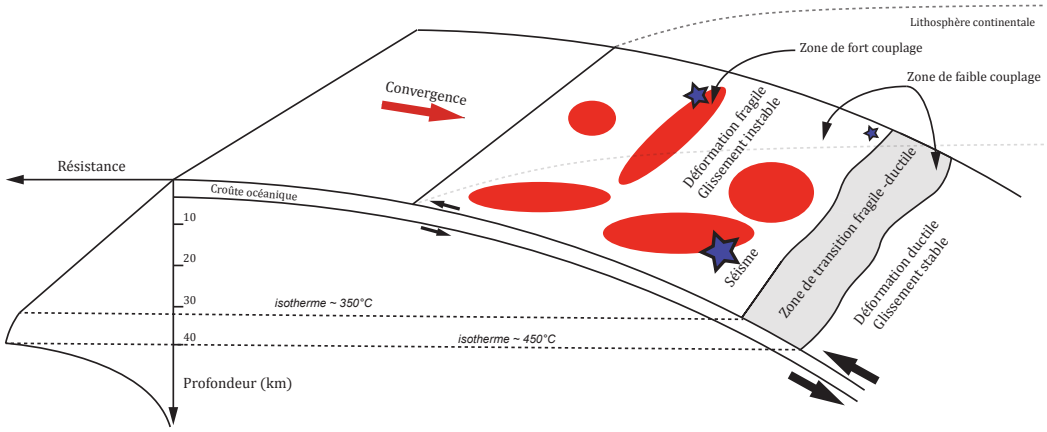

FIGURE 1.2: Vision schématique de la transition déformation fragile - déformation ductile le long d'une interface de subduction. La limite basse de la zone sismogénique correspond environ à la limite de plasticité du Quartz (350-450 °C)

permettre l'activation de processus de déformation de type ductile comme des mouvements de dislocations ou de défauts cristallins (Griggs, 1960). Le comportement rhéologique des roches est également fonction de la vitesse de déformation. Plus la température est élevée et la vitesse de déformation lente, plus la contrainte nécessaire pour induire une déformation est faible. De manière générale, la transition du domaine fragile au domaine ductile induit une diminution de la contrainte nécessaire pour déformer les roches (Brace and Kohlstedt, 1980).

Nous pouvons donc à présent mieux comprendre l'extension spatiale de la zone sismogénique (zone dans laquelle on enregistre des séismes) d'une zone de subduction (Figure 1.2) ou d'une faille en règle générale. A faible profondeur, les régions bloquées ou « couplées » des plans de faille libérent l'énergie élastique accumulée de manière brutale lors de glissements localisés, instables et sismiques. L'activation des mécanismes ductiles se fait ensuite en augmentant la pression et la température et permet une accommodation diffuse dans le temps et dans l'espace de la déformation. Shimamoto (1989) a montré que cette transition fragile-ductile n'est pas abrupte et se fait graduellement depuis un domaine fragile, fragile-ductile et puis enfin totalement ductile. Notons que la limite basse de la zone sismogénique se situe aux alentours des isothermes 350 et 450 °C qui correspondent aux températures de transition fragile-ductile de la majorité des minéraux de la croûte terrestre, notamment le Quartz.

1.2 Cycle sismique et phases précurseurs.

1.2.1 Cycle sismique et statistiques des séismes.

Sur de grandes échelles de temps et d'espaces, les séismes se regroupent pour former des cycles. La quantité d'énergie libérée par un séisme peut, d'un évènement à un autre, varier de plusieurs ordres de grandeur et est quantifiée par sa magnitude. L'échelle de magnitude la plus couramment utilisée est la magnitude de moment M_w introduite par Kanamori (1977). Cette échelle empirique utilise le moment scalaire sismique M_0 qui est une mesure exacte de l'énergie libérée par un séisme et qui a été proposé par Aki dans son article fondateur de 1967 (Aki, 1967). Dans le cas d'une faille dont la déformation est purement cisaillante (i.e. sans ouverture) le moment scalaire sismique M_0 s'exprime comme:

$$M_0 = \mu DS \tag{1.1}$$

avec μ, D et S le module de cisaillement du milieu, le glissement statique final, et la surface de faille. La magnitude de moment M_w est une fonction logarithmique de M_0 tel que:

$$M_w = (log_{10}(M_0) - 9.1)/1.5 \tag{1.2}$$

Charles Francis Richter et Beno Gutenberg (Gutenberg and Richter, 1956) proposèrent une loi statistique de la distribution des magnitudes des séismes au cours des cycles successifs. Cette loi appelée loi de Gutenberg-Richter est une loi purement empirique et fournit la relation suivante:

$$log_{10}(N(M)) = a - b(M) \tag{1.3}$$

avec $N(M)$ le nombre de séismes observés pour une magnitude supérieure à M. Les paramètres a et b ont des significations très différentes, a est une mesure du taux de sismicité alors que b quantifie le rapport entre petits et grands séismes. Sur de larges échelles de temps et d'espace, la valeur de b observée se situe autour de 1. Concrètement, cela signifie qu'à chaque incrément de magnitude, le nombre de séisme observé est diminué par 10. Les valeurs des coefficients a et b peuvent toutefois sensiblement varier d'une région à une autre et au cours du cycle sismique. Actuellement, la vision que l'on a du cycle sismique fait la distinction nette entre trois phases :

- Phase intersismique.
- Phase cosismique.
- Phase post-sismique.

Pendant la phase intersismique, les contraintes s'accumulent sous l'effet du chargement lent tectonique. Pendant la phase cosismique, l'énergie est brutalement relâchée lors du séisme, une partie est radiée sous forme d'ondes. Et enfin la phase post-sismique, durant laquelle les contraintes résiduelles au voisinnage et à l'intérieur du plan de rupture sont relaxées, ou ré-homogénéisées. C'est dans son papier fondateur de 1894 (Omori, 1894), que Fusakichi Omori mît en lumière l'existence de la phase post-sismique sur la base des observations sismologiques des séismes de Kumamoto (1889), de Mino-Owari (1891) et de Kagoshima (1893). Pendant la phase post-sismique, le taux de sismicité est initialement élevé et décroît comme l'inverse du temps (Omori, 1894):

$$N(t) = \frac{K}{c + \Delta t} \tag{1.4}$$

avec $N(t)$, le taux de sismicité à la suite d'un séisme, K la productivité, c une constante et Δt le temps de séparation du séisme (i.e., $\Delta t = t - t_{oc}$ avec t_{oc} le temps d'occurrence du séisme). L'accumulation des observations sismologiques a cependant permis de mettre en évidence la variabilité de cette loi selon les régions ou la magnitude des séismes, ce qui conduit Utsu (1961) à proposer une version généralisée de (1.4) :

$$N(t) = \frac{K}{(c + \Delta t)^p} \tag{1.5}$$

avec p un exposant qui en moyenne varie entre 0.7 et 1.5. Ce que traduit simplement la « loi d'Omori » c'est que chaque séisme donne naissance à une suite d'autres séismes. On définit le séisme principal comme le « choc principal » et les séismes qui le suivent comme des « répliques ». La loi d'Omori est initialement une loi purement observationnelle et non phénoménologique.

Les répliques, par définition, ont des magnitudes inférieures au choc principal. Mais que se passerait-il si une réplique devait avoir une magnitude supérieure au choc principal ? La réplique ne serait plus alors considérée comme telle mais comme le choc principal et le choc principal deviendrait ce qu'on appelle un précurseur ou « pré-choc ». Nous arrivons là à un sujet majeur en sismologie : celui des signaux précuseurs de l'occurrence du choc principal. Papazachos (1973) fût le premier à faire l'observation qu'à l'approche du choc principal, le taux de sismicité croît également comme une loi de puissance du temps. Cette loi empirique fût clairement établit quelques année plus tard par Kagan and Knopoff (1978) et Jones and Molnar (1979) et est par analogie avec (1.5) :

$$N^i(t) = \frac{K^i}{(c^i + \Delta t)^{p,i}} \tag{1.6}$$

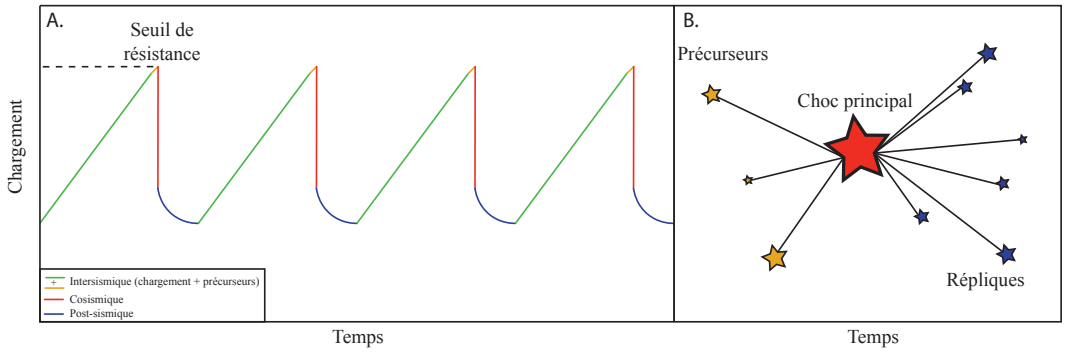

FIGURE 1.3: **A.**Vision schématique de la succession de plusieurs cycles sismiques dans le cas d'un système parfaitement périodique. **B.** Famille formée des précurseurs, du choc principal ainsi que des répliques.

avec $N^i(t)$ le taux de sismicité à l'approche du choc principal, K^i la productivité, c^i une constante temporelle et Δt le temps qui sépare du choc principal. Un choc principal ainsi que les précurseurs et les répliques associées forment alors une famille au sein du cycle sismique (Figure 1.3). Dans le cas des précurseurs on parlera de « loi d'Omori-inverse » (éq 1.6) et dans le cas de répliques on parlera de « loi d'Omori directe » (éq 1.5). La loi d'Omori directe et la loi d'Omori inverse montrent toutefois des différences significatives :

- Contrairement à la loi d'Omori direct, la loi d'Omori inverse émerge lorsque suffisamment de séquences de précurseurs sont synchronisées sur le temps d'origine du choc principal et additionnées.
- La loi d'Omori inverse est généralement observée sur des échelles de temps relativement courtes allant de quelques semaines à quelques mois en comparaison de la loi d'Omori direct qui peut s'observer à l'échelle de plusieurs années voire dizaines d'années pour les plus gros séismes (Lange et al., 2017).
- Pour un même séisme, l'exposant de la loi d'Omori inverse est toujours inférieur à l'exposant de la loi d'Omori directe (Kagan and Knopoff, 1978; Davis and Frohlich, 1991; Utsu and Ogata, 1995; Helmstetter and Sornette, 2003b).
- La distribution des magnitudes des précurseurs est différente de celle des répliques (Papazachos et al., 1967; Jin-Biao and Bai-Lin, 1978; Knopoff and Kagan, 1982), $b^p < b^r$ avec b^p et b^r la pente de Gutenberg-Richter des précurseurs et des répliques respectivement.

La loi d'Omori inverse ainsi que les spécificités des précurseurs peuvent simplement être expliquées par un modèle statistique, modèle uniquement basé sur les deux lois empiriques que sont la loi de Gutenberg-Richter et la loi d'Omori directe. Ce modèle appelé « modèle ETAS (Epidemic Type Aftershock Sequence)» fût pour la première fois introduit par Ogata (1988) et fût modifié et complété par la suite (Ogata et al., 1996; Helmstetter and Sornette, 2002b; Helmstetter and Sornette, 2002a; Helmstetter

et al., 2003a; Helmstetter and Sornette, 2003b; Helmstetter et al., 2004). Helmstetter and Sornette (2003b) utilise un modèle type ETAS qui pose les quatre conditions suivantes :

- Le taux de sismicité ou « sismicité de fond » suit une distribution de poisson homogène telle que décrite par la loi de Gutenberg-Richter (éq 1.3).
- Chaque séisme de magnitude M donne naissance à une famille de réplique selon la loi d'Omori directe (éq. 1.5) et dont les magnitudes sont distribuées selon la loi de Gutenberg-richter. Une réplique peut donc mener à une famille d'autres répliques et qui à leur tour donneront naissance à des familles de répliques et ainsi de suite.
- La productivité K de la loi d'Omori directe est une fonction de la magnitude du choc principal et est décrite par une loi de puissance tel que $K(M) \approx k(M^a)$ avec k et a des constantes qui dépendront principalement de la valeur b donnée par la pente de la loi de Gutenberg-Richter.
- Les magnitudes des répliques ne sont en aucun cas bornées par la magnitude du choc principal.

Cette dernière condition est un point essentiel du modèle car elle n'exclue pas la possibilité statistique que la magnitude d'une réplique puisse être supérieure à celle du choc principal. En conséquence, l'existence de la loi d'Omori inverse dérive statistiquement de la loi d'Omori directe : chaque séisme est précédé par une activité sismique, mais, en moyenne, cette activité sismique doit accélérer pour être statistiquement compatible avec l'occurrence du choc principal. En d'autres termes, la probabilité d'un évènement sismique augmente à l'approche du choc principal. Les modèles statistiques sont généralement critiqués car ils n'ont pas comme objectif de caractériser, de discriminer ou d'attester les potentiels mécanismes et processus physiques qui régissent l'objet d'étude. Ils fournissent cependant des arguments pour juger de la pertinence statistique de modèles phénoménologiques construits sur la base d'un nombre d'observations limitées. De plus, l'existence statistique de la loi d'Omori inverse n'exclut pas la possibilité que les précurseurs s'intègrent dans un processus de nucléation indicatif sur le temps d'occurrence, la localisation et la magnitude du choc principal (Helmstetter and Sornette, 2003b).

Du point de vue théorique, différents modèles phénoménologiques ont exploré l'origine des précurseurs, quelles en étaient les potentiels forçages extérieurs. Nous en donnons ici quelques exemples. Yamashita and Knopoff (1989) ont proposé que les précurseurs soient des marqueurs de la propagation de nouvelles fractures et de leur coalescence (cf. section 1.1) à l'approche de la rupture principale. Similairement, Sornette et al. (1992) ont proposé que les précurseurs soient la conséquence de la réactivation de fractures préexistantes à l'approche de la rupture principale. Dodge et al. (1996) proposèrent que les précurseurs reflétent les ruptures de petites aspérités

forcées par l'initiation du glissement qui s'opérerait lentement avant de se propager dynamiquement. D'autres études (Abercrombie and Mori, 1994; Mori, 1996; Kilb and Gomberg, 1999) ont également souligné la possibilité que les précurseurs soient dus à un processus de déclenchement en cascade par transfert de contrainte statique.

1.2.2 Modèles conceptuels de l'origine des précurseurs.

Encore aujourd'hui les processus physiques moteurs des précurseurs ne font pas consensus, bien que deux modèles semblent s'imposer : le modèle de glissement asismique et le modèle de déclenchement en cascade.

Déclenchement des précurseurs par glissement asismique :

Le modèle de glissement asismique prévoit que les précurseurs sont la conséquence de la rupture de zones bloquées et chargées par l'intermédiaire d'un glissement transitoire, lent et asismique dans la région avoisinante. Ce phénomène de glissement transitoire ou « glissement lent »a été observé dans différentes régions; le long des plans de subduction au Japon (Obara et al., 2004), aux Cascades (Rogers and Dragert, 2003), au Mexique (Payero et al., 2008), au Costa Rica (LaBonte et al., 2009), ou encore en Californie dans la partie profonde de la faille de San Andreas (Nadeau and Dolenc, 2005). Ces glissements lents peuvent s'étaler sur plusieurs semaines ou mois, se propager sur plusieurs dizaines de kilomètres et produire un glissement de l'ordre du centimètre. En raison de leur faible vitesse de propagation (i.e. vitesse de rupture), les glissements lents n'émettent pas d'ondes sismiques détectables.

Les mesures GPS (Global Postioning System) sont actuellement le moyen le plus fiable de détecter ces phénomènes transitoires. Le développement ces 15 dernières années de réseaux GPS en enregistrement continu a démontré que les glissements lents sont des phénomènes courants, particulièrement dans les zones de subduction, et qu'une fraction significative de la déformation accumulée pourraient être relaxée pendant ces glissements transitoires, lents et donc non dommageables (Peng and Gomberg, 2010). Les réseaux GPS ne sont cependant pas systématiquement en mesure de capturer les glissements lents du fait d'une mauvaise couverture spatiale ou bien d'une trop faible sensibilité instrumentale. Les observations sismologiques ont mis en évidence que les glissements lents étaient souvent couplés à d'autres processus comme les séismes « basse fréquence » (Shelly et al., 2006), les séismes « très basse fréquence » (Obara and Ito, 2005), les tremors non volcaniques (Rogers and Dragert, 2003), les essaims sismiques (Wicks et al., 2011) et les séismes répétitifs (Bouchon et al., 2011). Tous ces processus ont probablement en commun leur moteur qui est le glissement lent lui-même. Notons que le premier glissement lent détecté remonte à 1960, lorsque Steinbrugge et al. (1960) enregistrèrent la succession

de quatre phases de glissement asismique en Californie.

Pendant la phase d'initiation de plusieurs séismes de larges magnitudes, une corrélation spatiale et temporelle entre glissement lent et séquence de précurseurs a été établit. C'est le cas du séisme M_w 9.0 en 2011 de Tohoku au Japon (Kato et al., 2012, figure 1.4), du séisme M_w 7.6 en 1999 de Izmit en Turquie (Bouchon et al., 2002), du séisme M_w 7.3 en 1992 de Landers en Californie (Dodge et al., 1995) ou encore du séisme M_w 8.2 en 2014 de Iquique au Chili (Kato et al., 2016). Une étude menée par Bouchon et al. (2013) a permis de montrer sur la base d'une comparaison de 31 séismes localisés aux frontières de plaques et de 31 séismes intra-plaques que l'accélération de la sismicité dans les semaines/jours précédant l'occurrence des séismes était significativement plus prononcée dans le cas des séismes inter que intra-plaques. Les failles aux contacts de plaques distinctes sont sujettes à des taux de déformation significativement plus élevés que les failles contenues à l'intérieur d'une seule et même plaque. Cette dernière étude argumente donc en faveur de la propagation d'une zone de glissement asismique pendant la phase d'initiation de la nucléation comme moteur des précurseurs. De plus, le modèle de glissement asismique acte en faveur des observations expérimentales qui ont formellement établit que l'initiation de la rupture est toujours précédé par la propagation quasistatique d'un glissement asismique (Dieterich, 1992; Ohnaka, 2003; McLaskey and Kilgore, 2013; Latour et al., 2013). Notons que les séismes sont des processus physiques autosimilaires, ce qui traduit que le glissement final est directement proportionnel à la magnitude (nous le verrons plus en détail dans la section suivante).

D'un point de vue théorique (Perfettini et al., 2003; Fukuyama et al., 2003) et observationnel (Tinti et al., 2005; Cocco et al., 2009) , le glissement final est également positivement corrélé avec la taille de nucléation que l'on définit comme la taille critique au-delà de laquelle une zone de glissement asismique accélère et se propage dynamiquement (nous reviendrons sur cette notion dans la dernière partie de cette introduction). Par conséquent, plus la magnitude d'un séisme est élevée, plus l'étendue du glissement asismique le sera aussi, ce qui semble être confirmé par les observations de terrain (Dodge et al., 1995) et les observations faites en laboratoire (Acosta et al., 2019).

Déclenchement des précurseurs par transfert de contrainte statique :

Le modèle dit de « modèle en cascade » prévoit que les précurseurs se déclenchent les uns à la suite des autres par transfert de contrainte statique. Notons que c'est généralement ce modèle qui est privilégié dans les modèles statistiques types « ETAS » (Helmstetter and Sornette, 2003b). Le principe est très simple : suite à la rupture sur un plan de longueur arbitraire L les contraintes statiques sont modifiées au

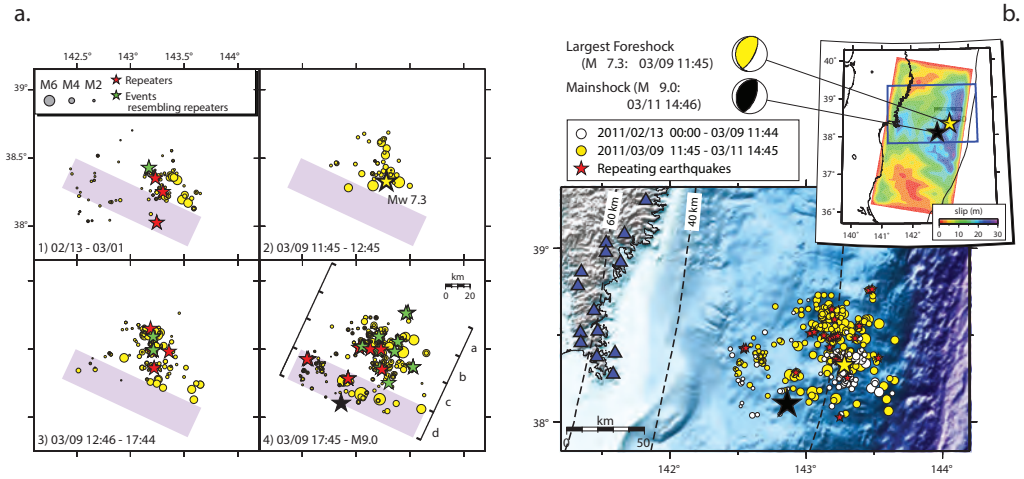

FIGURE 1.4: **Corrélation entre glissement asismique et nucléation.** **a.** Migration de la sismicité dans le mois précédant la nucléation du séisme de Tohoku (03 mars 2011, M_w9.0). Les « repeaters » (séismes répétitifs) sont reportés en rouge et soulignent la propagation d'un glissement asismique. **b.** Surface de rupture du séisme de Tohoku, glissement cosismique et précurseurs sismiques. L'épicentre du séisme de tohoku est indiqué par l'étoile noire (extrait de Kato et al., 2012)

voisinage du plan. Ce transfert de contrainte est couramment appelé « transfert de contrainte de Coulomb » et est exprimé au voisinage du plan de rupture par :

$$\Delta\sigma_c = \Delta\tau - \mu(\Delta\sigma_n - \Delta p) \tag{1.7}$$

Avec $\Delta\tau$, la variation de contrainte cisaillante statique, $\Delta\sigma_n$ la variation de contrainte normale (positive en compression), Δp la pression de pore et μ le coefficient de friction statique (voir Das and Scholz, 1983 pour une explication complète). La variation de la contrainte de Coulomb sera positive dans certaines régions et négatives dans d'autres selon la géométrie du plan de rupture et l'orientation du champ de contraintes (Figure 1.5 a). Les prochaines ruptures seront favorisées dans les zones où la variation de la contrainte de Coulomb sera positive et défavorisées dans le cas où elle sera négative.

A la suite d'un séisme les répliques se localisent préférentiellement sur le plan de rupture et dans les régions voisines où la variation de la contrainte de Coulomb est positive. La localisation des répliques suite au séisme de « Homestead Valley » (Figure 1.5 b) de magnitude M_w estimée entre 6.0 et 7.0 en fournit un excellent exemple. Dans le cas de failles suffisamment étendues, les observations sismologiques ont également montré une migration de la sismicité en réponse à la variation de la contrainte de Coulomb au cours des ruptures successives. L'évolution spatiale de la sismicité sur la faille Nord-Anatolienne l'illustre remarquablement (Roth, 1988;

Stein et al., 1997).

Un exemple de migration de la sismicité en direction de la nucléation du choc principal s'illustre par la séquence de précurseurs qui a précédé la nucléation du controversé séisme M_w 7.6 de 1999 d'Izmit en Turquie (Ellsworth and Bulut, 2018). Cette séquence comprend 29 précurseurs et s'est étalée sur 44 minutes, un temps relativement court. Les positions relatives des précurseurs (Figure 1.6) apparaissent consistantes avec un déclenchement en cascade par transfert de contrainte statique. A notre connaissance, il n'existe cependant que très peu d'exemples aussi marqués. Comme soulevé par les auteurs de l'étude, une potentielle explication réside dans le manque d'observations en champ proche de séquences de précurseurs, observations qui permettraient d'obtenir une vision détaillée de leur migration spatiale. La majorité des séquences de précurseurs observées le sont dans des contextes de séismes de subduction où les réseaux de sismomètres sont relativement éloignés du plan de faille. Les signaux sismiques émis par les précurseurs doivent alors traverser un milieu particulièrement diffusif et atténuant avant d'être enregistrés par les stations sismiques. Il n'est pas donc pas invraisemblable que les précurseurs de faibles magnitudes mais détenteurs néanmoins d'informations soient difficilement détectables. L'exemple du séisme d'Izmit est une très bonne illustration des incertitudes auxquelles nous faisons face aujourd'hui.

Les précurseurs sont potentiellement le moyen le plus prometteur pour anticiper la date, la localisation et la magnitude d'un séisme. Estimer leur valeur prédictive est donc crucial. Cependant, nous manquons d'observations suffisement denses pour comprendre les processus à leur origine et déterminer comment ces derniers s'intègrent au cours des cycles sismiques qui se succédent. Nous avons tenter d'y apporter quelques éléments de réponse.

1.3 Source sismique et lois d'échelles des séismes.

Abordons maintenant quelques notions et méthodes d'analyses en sismologie de la source. Celles-ci nous seront utiles dans la suite de ce manuscrit et permettront d'introduire la question de l'origine des ondes hautes-fréquences lors d'un séisme.

1.3.1 Déplacement en champ lointain : le cas d'un point source soumis à une force impulsionnelle.

Dans les paragraphes suivant nous considérerons uniquement le cas d'une source sismique confinée dans un milieu isotrope et homogène. Pour une extension des solutions à des milieux plus complexes (comme hétérogènes et anisotropes) nous conseillons au lecteur le livre «Quantitative seismology » de Aki and Richard, seconde édition (Aki and Richards, 2002). Cet ouvrage offre une description quasi exhaustive

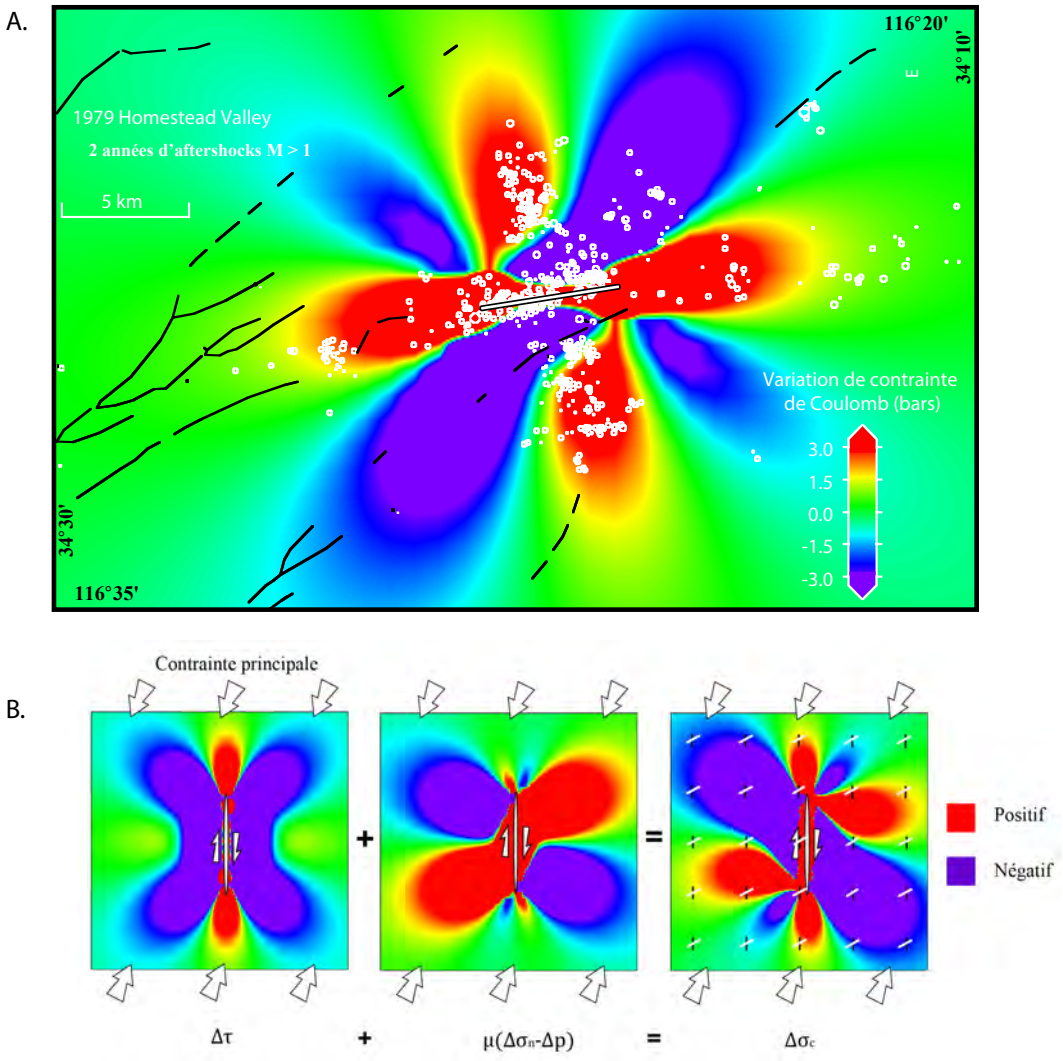

FIGURE 1.5: **A.** Répliques pendant les 2 années qui suivèrent le séismes de Homestead Valley en Californie (1979). Seules les répliques de $M_w > 1$ sont indiquées. **B.** Variation de la contrainte de coulomb résultante de la somme de la variation de contrainte cisaillante et de la variation de la contrainte effective (extrait de King et al., 1994)

des analyses et méthodes développées depuis le milieu du 20ème siècle nécessaires à une représentation fidèle de la dynamique de la source d'un tremblement de terre et des processus physiques sous-jacents.

Tout d'abord, qu'est-ce qu'une faille ? Une faille peut-être schématiquement représentée comme une surface contenue dans un volume au travers de laquelle s'opère une discontinuité du glissement au moment de sa rupture, c'est-à-dire au moment du séisme. Posons un problème simple : celui des ondes sismiques émises par un point source de position arbitraire x soumis à une force impulsionnelle f et contenu dans un milieu infini de densité ρ et de modules élastiques λ et μ. Le vecteur du champ

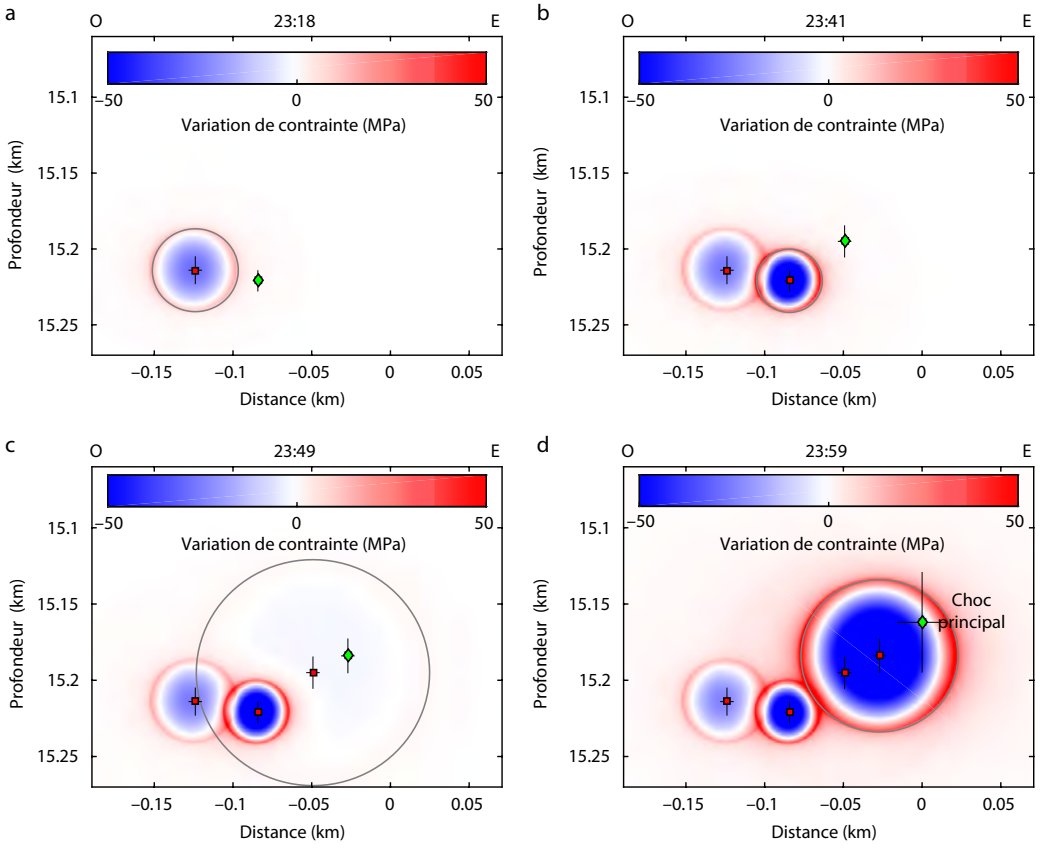

FIGURE 1.6: Evolution spatio-temporelle de la variation de contrainte statique pendant la phase d'initiation du séisme d'Izmit de 1999 en Turquie. **a-d** Les positions indiquées par les carrés rouges correspondent aux centroïdes de quatre familles de précurseurs corrélés spatialement et temporellement (extrait de Ellsworth and Bulut, 2018)

de déplacement $u(x,t)$ satisfait l'équation de l'elastodynamique :

$$\rho \frac{\partial^2}{\partial t^2} u(x,t) = (\lambda + \mu)\nabla(\nabla . u(x,t)) + \mu \nabla^2 u(x,t) + f(x,t) \tag{1.8}$$

Avec $f(x,t)$ une force de volume d'orientation arbitraire. Pour une source de position arbitraire $x0$ la distribution de $f(x,t)$ s'exprime comme :

$$f(x,t) = \delta(x - x0).f.s(t) \tag{1.9}$$

Avec $s(t)$ la fonction source. Pour un receveur à la position x on peut montrer que le champ de déplacement en $u(x,t)$ (Aki and Richards, 2002) s'écrit comme :

$$u(x,t) = G(x,t,x0,0).f * s(t) \tag{1.10}$$

Ou en notation indicielle :

$$u_i(x,t) = \sum_{ij} G_{ij}(x,t,x0,0).f_i(t) * s(t) \tag{1.11}$$

Avec $*$ qui désigne la convolution. Nous avons introduit ici le tenseur de Green, G. Ce tenseur décrit la réponse impulsionnelle du milieu à n'importe quelle position x pour une force impulsionnelle et unitaire appliquée en $x0$ qui dans le cas d'un milieu isotrope et homogène peut-être facilement obtenu (Achenbach, 1975). Pour une force orientée selon la direction 1, la solution de (1.11) est (Aki and Richards, 2002):

$$\begin{aligned} u_i(x,t) = \frac{1}{4\pi\rho}\left(\frac{\partial^2}{\partial x_i \partial x_1}.\frac{f_i}{r}\right) \int_{\frac{r}{\alpha}}^{\frac{r}{\beta}} \tau.s(t-\tau)d\tau + \\ \frac{f_i}{4\pi.\rho.\alpha^2.r}\left(\frac{\partial r}{\partial x_i}\frac{\partial r}{\partial x1}\right).s(t-\frac{r}{\alpha}) + \\ \frac{f_i}{4\pi.\rho.\beta^2.r}\left(\delta_{ij} - \frac{\partial r}{\partial x_i}\frac{\partial r}{\partial x1}\right).s(t-\frac{r}{\beta}) \end{aligned} \tag{1.12}$$

Avec α et β la vitesse des ondes P et S respectivement et r la distance à la source. Cette solution peut bien sûr être généralisée à une force de direction arbitraire. Il paraît ici important d'expliciter les termes dans (1.12). Le premier terme est appelé champ proche et décroit en $1/r^2$ et $1/r^4$. Le second terme correspond au terme en champ lointain et décroit en $1/r$. Celui-ci traduit le champ de déplacement au point x au passage des ondes P et S. Pour des distances suffisamment éloignées de la source, le terme en champ proche peut-être ignoré. Nous verrons par la suite que le terme en champ lointain peut être utilisé pour déterminer la taille d'un séisme et en mesurer l'énergie.

Nous avons évoqué ici le problème simple du champ de déplacement induit par un point source soumis à une force ponctuelle et unidirectionnelle. Ce dernier cas n'est évidemment pas représentatif de la réalité de la source d'un séisme qui traduit une déformation dans un volume fini et dans différentes directions. Dans le paragraphe suivant nous abordons la description actuelle que l'on fait des forces en action lors d'un séisme.

1.3.2 Déplacement en champ lointain : cas du double couple de forces et estimation du moment sismique.

Pour la majorité des séismes, la déformation élastique du milieu est équivalente à l'action d'un double couple de forces. Originellement, les travaux de Honda (1962) ont permis de montrer qu'un modèle de source basé sur un couple unique de forces échouait à expliquer les radiations en champ lointain des ondes S. Très rapidement

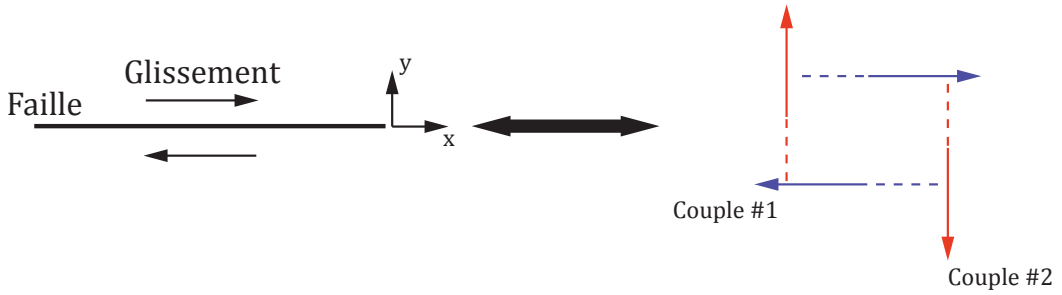

FIGURE 1.7: Vision schématique du glissement sur une faille soumise à un double couple de forces.

après, les travaux théoriques de Maruyama (1963) et Burridge and Knopoff (1964) ont démontré qu'une faille contenue dans un milieu élastique pouvait être fidèlement représentée par un double couple de forces (Figure 1.7). En dépit du fait qu'un simple couple de forces ne saurait expliquer les observations des ondes S émises par un tremblement de terre, ce modèle ne permet pas de conserver le moment angulaire sur la faille et induirait une rotation du milieu. Plutôt qu'en terme de forces, on préférera représenter la source en terme d'énergie ce qui nous permet d'introduire le tenseur du moment sismique M.

Pour le cas d'un dipôle linéaire construit par l'action de deux forces f égales et opposées et distantes de h, le moment sismique $M = fh$. N'importe quelle source sismique, peu importe sa géométrie, peut-être représentée comme la combinaison de trois dipôles linéaires et orthogonaux entre eux. Dans un repère cartésien, le tenseur du moment sismique prend la forme générale :

$$M = \begin{bmatrix} M_{xx} & M_{xy} & M_{xz} \\ M_{yx} & M_{yy} & M_{yz} \\ M_{zx} & M_{zy} & M_{zz} \end{bmatrix} \tag{1.13}$$

Les composantes orthogonales du tenseur M_{kk} représentent une déformation compressive ou extensive selon le signe, les autres composantes M_{ij} représentent une déformation cisaillante. Le cas indiqué en figure 1.7 représenterait donc le cas où seules les composantes M_{xy} et M_{yx} seraient différentes de zéro en plus d'être égales. Le champ de déplacement dû à la composante M_{ij} pour une force positionnée en $x0$ s'écrit:

$$u_k(x,t) = \sum_{ij} G_{ki,j}(x,t,x0,0) * M_{ij}(t) \tag{1.14}$$

De (1.14) on obtient le champ de déplacement lointain dû aux ondes P et S à une distance r :

$$u_i^p(r,t) = \frac{1}{4\pi.\rho.\alpha^3}\frac{1}{r}\sum_{jk}\Re_{ijk}^{\alpha}.\dot{M}_{jk}(t-\frac{r}{\alpha}) \tag{1.15}$$

$$u_i^s(r,t) = \frac{1}{4\pi.\rho.\beta^3}\frac{1}{r}\sum_{jk}\Re_{ijk}^{\beta}.\dot{M}_{jk}(t-\frac{r}{\beta}) \tag{1.16}$$

avec $\Re_{ijk}^{\alpha}$ et $\Re_{ijk}^{\beta}$ les diagrammes de radiation des ondes S et P qui décrivent la variation d'amplitude des ondes selon la direction du rai par rapport à la source. Leurs expressions générales sont données par Aki and Richards (2002) dans un système de coordonnées sphériques (r,θ,ϕ) avec comme point d'origine la position de la source. On observe que le déplacement en champ lointain est proportionnel au taux de moment, et non au moment lui-même, c'est-à-dire à la vitesse à laquelle est libérée l'énergie. Le champ en déplacement lointain peut s'écrire de façon plus générale :

$$u_i^c(r,t) = \frac{1}{4\pi.\rho.c^3}\frac{R^c(\theta,\phi)}{r}.\Omega(t-\frac{r}{c}) \tag{1.17}$$

avec c pouvant correspondre aux ondes P ou S. Nous avons introduit dans (1.17) la fonction source $\Omega = M_0.\dot{s(t)}$ avec M_0 le moment sismique scalaire et $s(t)$ sa variation temporelle. Le moment du tenseur $M_0(t)$ est équivalent à $I_0.M_0.s(t)$, avec I_0 un tenseur qui contient les informations de la géométrie de la source. A $t \to \infty$ on a $M_0(t) = M_0$, ce qui implique :

$$\int_0^{\infty} s(t)dt = 1 \tag{1.18}$$

La transformée de Fourier directe de (1.17) donne :

$$u_i^c(r,\omega) = \frac{1}{4\pi.\rho.c^3}\frac{R^c(\theta,\phi)}{r}.\Omega(\omega)\exp\frac{-i\omega r}{c} \tag{1.19}$$

$$\lim_{t\to\infty}\Omega(\omega) = M_0 * \int_0^{\infty}\dot{s(t)}dt = M_0 \tag{1.20}$$

Nous arrivons ici à un résultat majeur en sismologie, à basse fréquence le spectre du champ de déplacement lointain tend vers un plateau dont la hauteur est directement proportionnelle au moment sismique de la source. En pratique, c'est sur ce principe là que les sismologues déterminent la magnitude des séismes et leurs caractéristiques sur la base des observations en champ lointain. En reprenant l'expression du moment sismique $M_0 = \mu.D.S$, et en exprimant la chute de contrainte d'un séisme $\Delta\sigma$ comme :

$$\Delta\sigma = \frac{\mu.D}{L} \tag{1.21}$$

avec $L = C.\sqrt{S}$ (où C est une constante géométrique), Aki (1967) proposa la loi d'échelle suivante :

$$M_0 \propto \Delta\sigma.L^3 \tag{1.22}$$

ou de manière équivalente:

$$M_0 \propto \Delta\sigma.S^{3/2} \tag{1.23}$$

L'énergie libérée par un séisme est proportionnelle au cube de la racine carré de sa surface, ou similairement au cube de sa longueur caractéristique, multiplié par la chute de contrainte. En addition d'être d'une remarquable simplicité, cette loi d'échelle donne une estimation directe de la taille de la source sur la base des observations en champ lointain. Kanamori and Brodsky (2004) ont comparé l'aire de rupture S à la magnitude M_w de tous les séismes de magnitudes supérieurs à $M_w = 6.0$ survenus de 1991 à 2001 (Figure 1.8). Leurs résultats ont suggéré:

$$M_0 \propto S^{3/2} \tag{1.24}$$

La loi d'échelle (1.24) implique que la chute de contrainte $\Delta\sigma$ est approximativement constante et indépendante de la magnitude pour $6.0 \leq M_w \leq 9.0$ (condition d'auto-similarité). Les chutes de contraintes pour ces séismes ont été estimées entre 1 et 10 MPa avec une moyenne de 3 MPa.

Brune (1970) proposa un modèle universel de fonction source en champ lointain. Ce modèle appelé « omega-squared model » dans la terminologie anglo-saxonne propose la forme suivante du spectre de la fonction source en champ lointain $\Omega(\omega)$:

$$\Omega(\omega) = \frac{\Omega(0)}{1 + (\frac{\omega}{\omega_0})^2} \tag{1.25}$$

Ce modèle extrêmement simple possède seulement deux paramètres : le plateau spectral à basse fréquence égal au moment sismique M_0 et une fréquence ω_0 qualifiée de « fréquence coin » au-delà de laquelle le spectre décroît asymptotiquement en ω^{-2} . Pour arriver à ce résultat, Brune (1970) détermina la solution du déplacement en champ lointain dû à la propagation d'un pulse de glissement et en considérant simplement que l'énergie transportée par les ondes se répartissait sur une sphère. Brune (1970) apporta une explication physique de ω_0:

$$\omega 0 \approx \frac{V_r}{L} \tag{1.26}$$

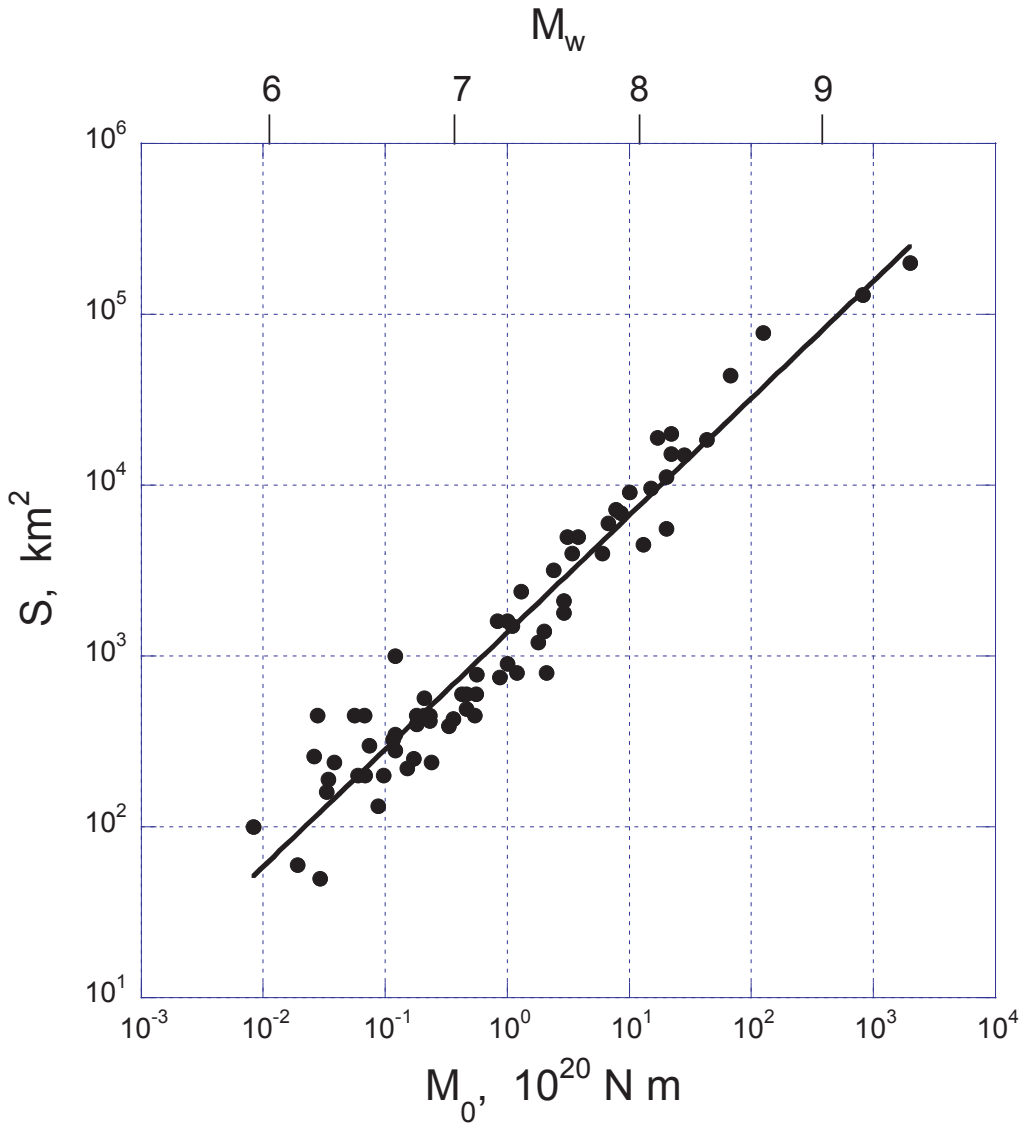

FIGURE 1.8: Loi d'échelle entre surface de rupture, moment sismique (axe du bas), et magnitude (axe du haut) pour les séismes de $M_w > 6.0$ enregistrés entre 1991 et 2001 (extrait de Kanamori and Brodsky, 2004)

avec V_r, et L la vitesse de rupture et sa taille respectivement. La fréquence coin est donc inversement proportionnelle à la taille de rupture. En combinant (1.22) et (1.26) et en considérant que la vitesse de rupture V_r et la chute de contrainte $\Delta\sigma$ sont constantes on obtient :

$$M_0 \propto \omega_0^{-3} \tag{1.27}$$

Cette loi d'échelle a été observée pour des magnitudes couvrant plusieurs ordres de grandeur et démontre l'auto-similarité du processus de rupture (Figure 1.9). On peut retrouver la même loi d'échelle dans le cas de la durée charactéristique d'un séisme τ_0 qui est égale à l'inverse de la fréquence coin. Par analogie avec (1.27):

$$M_0 \propto \tau_0^3 \tag{1.28}$$

Une étude relativement récente (Ide et al., 2007) a cependant montré que (1.28) n'était pas valide dans le cas des séismes lents (Figure 1.10). Dans le cas des séismes lents, le moment sismique M_0 est simplement proportionel à la durée charactéristique τ_0 et donc à l'inverse de la fréquence coin, ω_0^{-1}. Cette différence a été attribué aux vitesse de propagation ($\approx 1\ m/s$) des séismes lents qui sont de trois ordres de grandeur inférieures à celles des séismes classiques.

La fréquence coin est un paramètre essentiel car il décrit à partir de quelle fréquence l'énergie sismique libérée décroît, ou plus simplement la quantité d'énergie émise à haute-fréquence. Les ondes hautes-fréquences se situent entre 1 et 10 Hz et sont les plus destructrices. Comprendre les processus physiques à leur origine est donc crucial.

1.3.3 Modèles cinématiques d'une source de dimensions finies, origine des ondes hautes-fréquences et décroissance asymptotique.

Le cas du point source évoqué précédemment est une approximation justifiée dans le cas d'observations suffisamment éloignées de la source ou dans le cas de séismes suffisamment petits pour pouvoir s'affranchir de leur géométrie et de la dynamique de propagation de la rupture. Cependant, pour les séismes à plus larges échelles ou dans le cas d'observations en champ proche, détailler la cinématique de la source sera indispensable afin d'en obtenir soit le déplacement statique en champ proche ou bien le champ lointain du déplacement.

C'est principalement entre les années 1960 et 1990 que la majorité des modèles cinématiques ont été développés. Un premier type de modèle conceptualise la source d'un séisme comme la propagation d'une dislocation le long d'un plan, c'est le cas

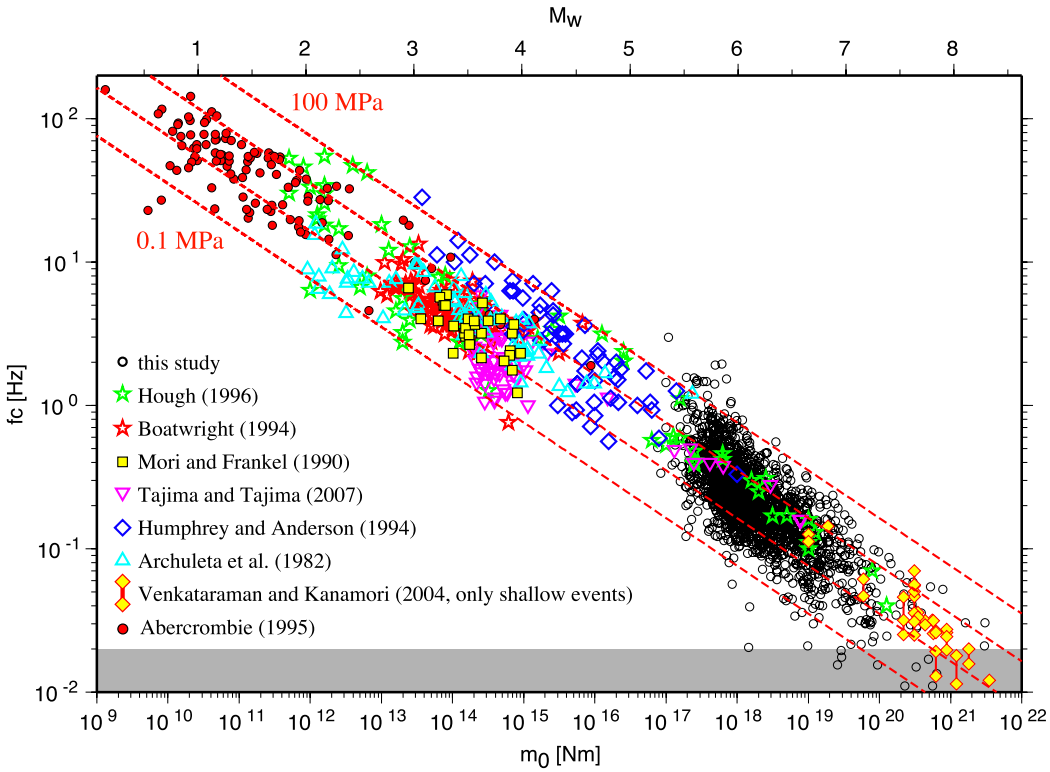

FIGURE 1.9: Relation entre la fréquence coin, le moment sismique (axe du bas) et la magnitude (axe du haut). Les lignes en rouge pointillées indiquent les valeurs théoriques pour une vitesse de rupture fixe et un saut de contrainte constant (extrait de Allmann and Shearer, 2009).

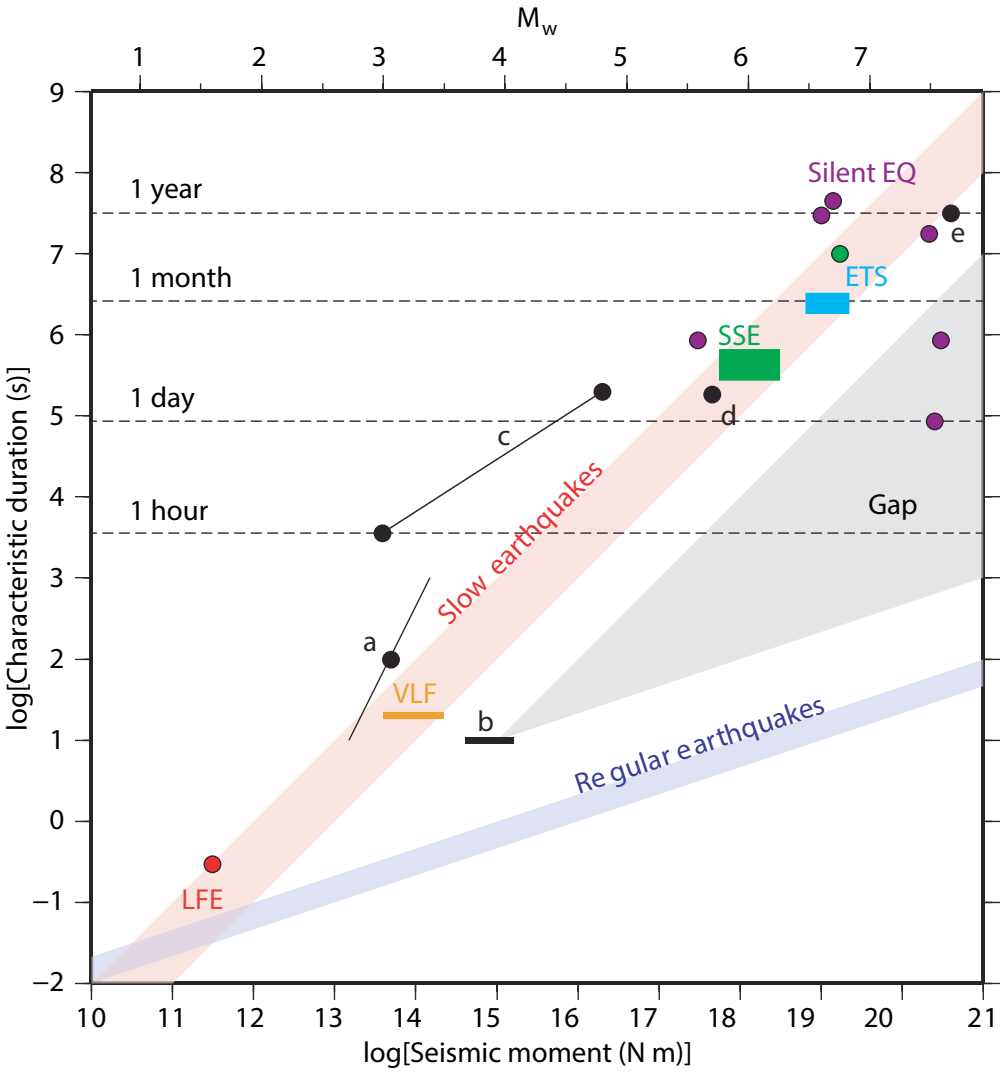

FIGURE 1.10: Comparaison de la loi d'échelle qui relie la durée d'un séisme à son moment sismique (axe du bas) et sa magnitude (axe du haut) entre les « séismes classiques » (**Regular earthquakes**) et les « séismes lents » qui regroupe les glissements asismiques, **SSE**, les séismes basse fréquence, **LFE**, les séismes très basse fréquence, **VLF**, les trémors non volcaniques, **ETS** et les séismes silencieux, **Silent EQ** (extrait de Ide et al., 2007).

des modèles développés par Haskell (1964) and Haskell (1966), Burridge et al. (1964), Savage (1972), Madariaga (1978) et Bernard and Madariaga (1984) pour ne citer que ces derniers. Ici, la terminologie « dislocation » désigne une discontinuité de glissement et non des processus de plasticité comme évoqués précédemment. Un autre type de modèle couramment utilisé est celui du crack circulaire.

Ce modèle a été étudié et développé sous différentes formes, soit de façon analytique (Kostrov, 1964; Savage, 1966; Brune, 1970; Sato and Hirasawa, 1973) ou soit de façon numérique (Madariaga, 1976). Ces différentes études mettent précisément en lumière la variabilité des résultats selon la géométrie de la source, sa durée ou encore les conditions de glissement imposées sur la faille. Une seule caractéristique du spectre en champ lointain de la fonction source semble s'imposer : la décroissance asymptotique en ω^{-2}, bien que dans certains cas particuliers cette décroissance soit en ω^{-3} (Haskell, 1964; Haskell, 1966). Les expressions théoriques de la fréquence coin ou encore les phases cinématiques à l'origine des ondes hautes-fréquences montrent cependant des différences significatives. Notons un inconvénient de taille dans les modèles cinématiques type « dislocation » (bien que ceux-ci soient les plus couramment utilisés pour inverser le glissement statique sur la base d'observations en champ lointain) : le glissement sur la faille est toujours imposé de façon arbitraire, c'est-à-dire par la propagation d'une dislocation type pulse, fonction rampe ou bien fonction porte. Dans le cas des modèles types « crack-circulaire », la solution analytique quasi-statique du glissement à l'intérieur du crack est connue (Kostrov, 1964). Pour illustrer les points de divergence des différents modèles cinématiques nous présenterons deux types de modèles diamétralement opposés: (i) le modèle proposé par Savage (1972), celui de la propagation bilatérale d'une dislocation le long d'une faille rectangulaire et (ii) le modèle de Sato and Hirasawa (1973) de propagation d'un crack circulaire s'arrêtant soudainement à une distance arbitraire.

Modèle de rupture bilatérale (Savage) :

Le modèle de Savage (1972) établit le problème suivant: une dislocation de type pulse apparaît soudainement sur une faille de longueur W et se propage bilatéralement jusqu'à une longueur L. Les figures 1.11 a, b et c illustrent respectivement l'histoire du glissement, le glissement final sur le plan de faille ainsi que la géométrie du problème. Par effet de directivité, les fréquences coins sont fonctions de la direction de propagation de la rupture par rapport à la position du point d'observation. Moyennées sur l'ensemble de l'espace, Savage obtient les fréquences coins pour les ondes P et S suivantes :

$$\omega_0^p = \sqrt{2.9}.\frac{\alpha}{2\pi}.\frac{1}{\sqrt{LW}} \tag{1.29}$$

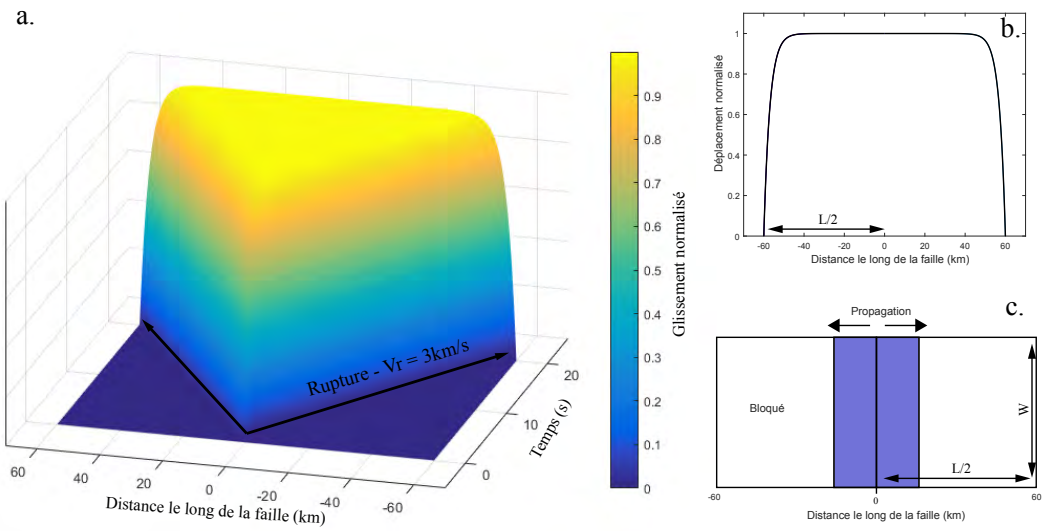

FIGURE 1.11: **Modèle de propagation d'une dislocation sur une faille rectangulaire. a.** Glissement normalisé le long du plan de faille en fontion du temps de propagation. **b.** Glissement normalisé final le long du plan de faille. **c.** Illustration schématique de la géométrie du problème.

$$\omega_0^s = \sqrt{14.8}.\frac{\beta}{2\pi}.\frac{1}{\sqrt{LW}} \tag{1.30}$$

Ces résultats sont obtenus pour une vitesse de rupture $V_r = 0.9\beta$. Les constantes numériques sont fonctions de la vitesse de rupture et augmentent avec celle-ci. On observe que le modèle de Savage prédit $\omega_0^p < \omega_0^s$ avec $\omega_0^s \approx 1.25\omega_0^p$.

Modèle du crack circulaire (Sato & Hirawasa) :

Le modèle de Sato and Hirasawa (1973) établit le problème suivant: celui de la propagation circulaire d'un crack jusqu'à s'arrêter soudainement à une distance a. Les figures 1.12 a, b et c illustrent respectivement l'histoire du glissement, le glissement final sur le plan de faille ainsi que la géométrie du problème. Par effet de directivité, les fréquences coins sont également moyennées sur l'ensemble de l'espace. Ce faisant, Sato & Hirasawa obtiennent les relations suivantes :

$$\omega_0^p = C_p.\frac{\alpha}{2\pi}.\frac{1}{a} \tag{1.31}$$

$$\omega_0^s = C_s.\frac{\beta}{2\pi}.\frac{1}{a} \tag{1.32}$$

Avec C_p et C_s des fonctions de la vitesse de rupture. On observe que le modèles de

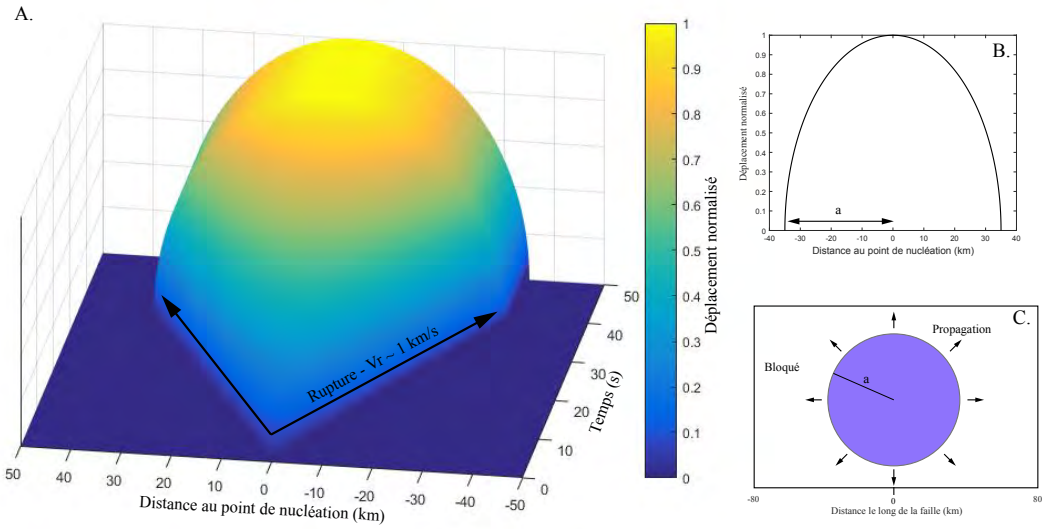

FIGURE 1.12: **Modèle de propagation d'un crack circulaire. a.** Glissement normalisé final en fonction du temps et de la distance au point de nucléation. **b.** Glissement normalisé final en fonction de la distance au point de nucléation **c.** Illustration schématique de la géométrie du problème.

Sato & Hirasawa prédit $\omega_0^p > \omega_0^s$ avec $\omega_0^p \approx 1.25\omega_0^s$. Notons que Madariaga (1976) en résolvant ce même problème mais de façon numérique arriva à des résultats similaires.

La première différence notable entre ces deux modèles est que l'un prédit une fréquence coin des ondes S supérieure à celle des ondes P (Savage) et l'autre l'inverse (Sato & Hirasawa). De plus, pour le cas des ondes S, le modèle de dislocation de Savage prédit une fréquence coin deux fois supérieure à celle prédit par le modèle du crack de circulaire de Sato & Hirasawa. Ceci implique tout simplement plus d'énergie à haute-fréquence transportée en champ lointain pour une taille caractéristique de source équivalente. De plus, le modèle de Savage ne donne pas d'indication de l'origine des radiations hautes-fréquences. Ces dernières ont été généralement attribuées à la phase d'initiation de la rupture (Savage, 1966). L'étude de Sato & Hirawasa a permis d'aboutir à un résultat majeur, diamétralement opposé, au sens littéral du terme : les ondes hautes-fréquences sont produites pendant la phase d'arrêt de la rupture et non de départ.

C'est quelques années plus tard que Madariaga (1978) apporta une explication plus complète. Les émissions hautes-fréquences peuvent avoir deux origines toutes deux liées à la vitesse de rupture. Soit le front de rupture rencontre une barrière, par exemple une zone où le coefficient de friction serait relativement élevé, et décélère au passage de cette barrière ou s'arrête partiellement voir complétement : ce dernier cas extrême est celui du modèle de Sato & Hirasawa. Soit le front de rupture rencontre une zone d'hétérogénéité des contraintes, de concentration de celles-ci, dans ce cas la vitesse de glissement augmente brutalement au passage de la zone ce qui

génèrera localement des ondes hautes-fréquences. Que ces deux cas puissent arriver simultanément pendant un séisme ne paraît pas aberrant.

En effet, une faille naturelle a souvent connu une histoire complexe et plusieurs ruptures qui ont pu mener à l'accumulation de contraintes résiduelles. Ceci, en addition des hétérogénéités intrinsèques reliées par exemple à des surpressions de fluide ou des contrastes de lithologie qui pourraient elles aussi jouer un rôle important.

Sur la base des modèles de rupture cinématiques, trois paramètres essentiels dans la production des radiations hautes-fréquences émergent:

- La géométrie du front de rupture.
- La dynamique du front de rupture.
- L'état de contrainte sur le plan de rupture.

Leurs études devraient donc reccueillir toute notre attention.

1.3.4 Mode de fracturation et vitesse de rupture

Les concepts physiques sur lesquelles a été développée l'intégralité de la mécanique de la fracture sont probablement attribuables à Alan Arnold Griffith (Griffith, 1920). Partant du principe de conservation de l'énergie dans un systême fermé, Griffith posa deux conditions à la propagation d'une fracture (i.e., un crack) contenue dans un milieu isotrope et homogène : (1) que la fracture relâche de la contrainte au fur et à mesure de sa propagation et (2) que l'énergie disponible en tête de fracture sur un incrément de longueur dl excède l'énergie requise pour la création d'un nouvel incrément de surface dS, communément appelée énergie de surface. On distingue généralement trois « modes » de fracturation (Figure 1.13) qui dépendent de l'orientation de la contrainte principale appliquée et de la direction de celle-ci relativement au plan et au front de rupture :

- Mode I : Une contrainte de traction normale au plan de rupture (mode d'ouverture).
- Mode II : Une contrainte de cisaillement parallèle au plan de rupture et perpendiculaire au front de rupture (cisaillement plan).
- Mode III : Une contrainte de cisaillement parallèle au plan et au front de rupture (cisaillement anti-plan).

De façon générale, les fractures peuvent se propager en faisant intervenir les trois modes de fracturation. Dans le cas des séismes, seuls les modes II et III sont généralement considérés et le mode I ignoré en raison des fortes contraintes normales le long des failles qui limitent l'ouverture de ces dernières. Les vitesses de propagation limites dépendent du mode de fracturation et découlent directement

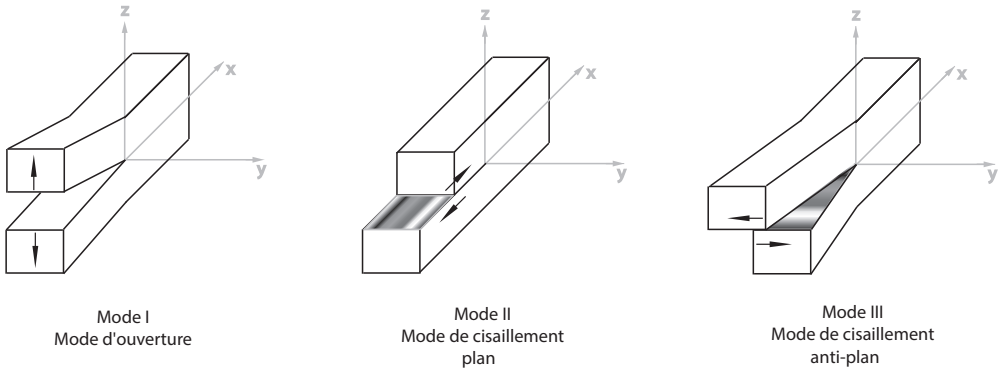

FIGURE 1.13: Les trois modes de fracturation. Les flèches indiquent le sens de la contrainte principale.

de l'expression du flux d'énergie par unité de surface G en tête de fissure pendant la propagation. Pour un crack circulaire de rayon a, Kostrov (1966), Eshelby (1969) et Freund (1972) ont montré que G s'exprime comme :

$$G = G^*.g(V_r) \tag{1.33}$$

avec G^* le flux d'énergie statique et $g(V_r)$ une fonction de la vitesse de rupture et donc du mode de fracture. G^* est indépendant du mode de fracture et s'exprime comme :

$$G^* = \frac{K^2}{2\mu} \tag{1.34}$$

où K est le facteur d'intensité des contraintes en tête de fissure et s'exprime pour un crack de rayon a comme suit:

$$K = \sqrt{\pi.a}\Delta\sigma \tag{1.35}$$

avec $\Delta\sigma$ la chute de contrainte statique au passage de la rupture. En mode II, $g^{II}(V_r)$ prend la forme :

$$g^{II}(V_r) = \frac{1 - V_r/C_r}{\sqrt{1 - V_r/\beta}} \tag{1.36}$$

Avec C_r, la vitesse des ondes de Rayleigh. En mode III, $g^{III}(V_r)$ prend la forme :

$$g^{III}(V_r) = \sqrt{\frac{1 - V_r/\beta}{1 + V_r/\beta}} \tag{1.37}$$

Les équations (1.36) et (1.37) indiquent simplement que lorsque la vitesse de rupture tend vers sa borne supérieure (la vitesse des ondes de Rayleigh C_r, en mode II et la vitesse des ondes S, β, en mode III) l'énergie mécanique dissipée sous forme d'énergie de surface tend vers 0. Toute l'énergie disponible est alors dissipée sous forme d'ondes sismiques.

Cependant, Andrews (1976) mis en évidence numériquement que dans certains cas, les ruptures en mode II, pouvaient se propager à des vitesses supérieures à celle des ondes S et atteindre celle des ondes P. Notons, que pour une rupture purement en mode II, la vitesse de propagation ne peut théoriquement pas prendre des valeurs contenues entre la vitesse des ondes de Rayleigh, C_r et la vitesse des ondes S, β. Dans cette gamme de vitesse le flux d'énergie en tête de fissure devient négatif (Figure 1.14). En pratique les ruptures se propagent en mode mixte (i.e. mode II et III), dans ce cas le flux d'énergie n'est plus négatif pour $C_r < V_r < \beta$ et la vitesse de rupture devient un continuum.

La possibilité de ruptures se propageant à des vitesses supérieures à la vitesse des ondes S fût expérimentalement prouvé sur des matériaux synthétiques (Rosakis et al., 1999; Xia et al., 2004; Schubnel et al., 2011; Kammer et al., 2018) et par une étude récente sur des roches (Passelègue et al., 2013). Ce phénomène appelé « rupture supershear » dans la terminologie anglo-saxonne a également été observé dans le cas de failles naturelles (Archuleta, 1984; Bouchon et al., 2001; Bouchon and Vallée, 2003; Bhat et al., 2007). On emploie le terme de « rupture sub-Rayleigh » lorsque la vitesse de propagation est inférieure à la vitesse des ondes de Rayleigh.

Les ruptures supershear possèdent une singularité : elles se propagent en produisant une onde de Mach au front de rupture (Figure 1.13), exactement de la même façon qu'un avion émet une onde de Mach lorsqu'il dépasse la vitesse du son. Cette onde conique s'atténue moins vite avec la distance qu'une onde sphérique et est donc susceptible de propager les radiations hautes-fréquences sur de plus grandes distances. Il n'existe cependant que peu d'observations en champ proche de ruptures supershear, leur potentiel haute-fréquence reste donc à éclaircir.

1.4 Apport de la reproduction de séismes en laboratoire : de l'échelle des failles crustale à celle du laboratoire.

1.4.1 Instabilité frictionelle

Nous avons vu en section 1.1 comment les réponses mécaniques des roches soumises à un chargement tectonique pouvaient varier en fonction, au premier ordre, de la température, de pression et de la vitesse de chargement ou taux de déformation.

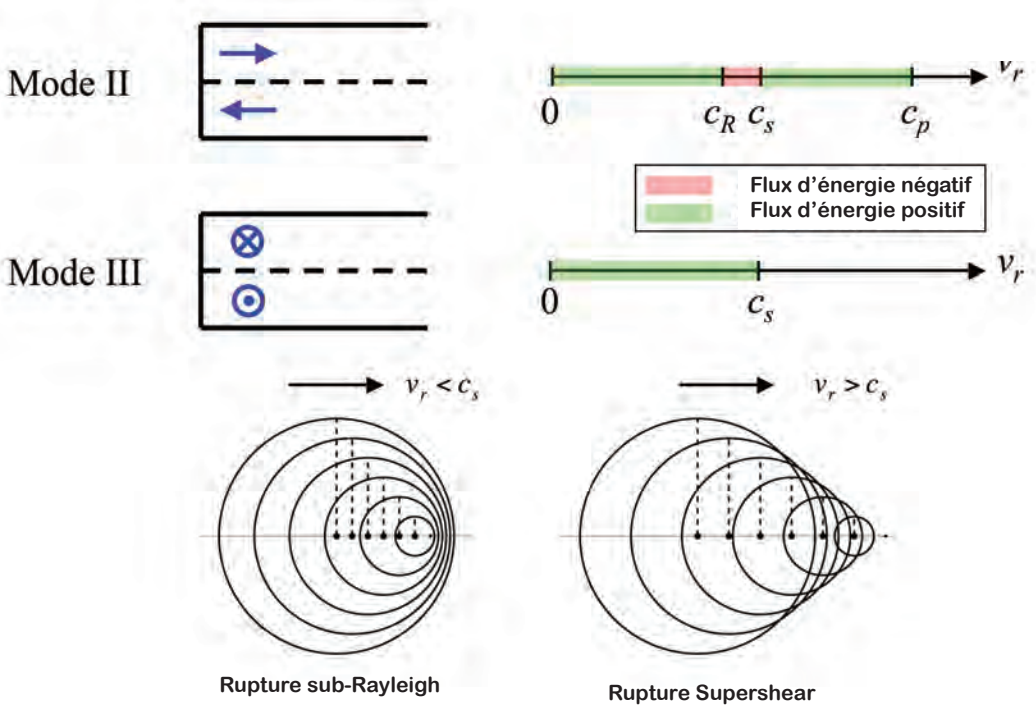

FIGURE 1.14: **Haut.**Vision schématique des vitesses de rupture possibles selon le mode de fracturation.**Bas.**Vision schématique de la formation d'un cone de Mach dans le cas d'une rupture Supershear. Le long du front de propagation de l'onde de Mach, les ondes S interfèrent constructivement et sont moins atténuées avec la distance (extrait de Das, 2010

La reproduction de séismes en laboratoire s'est révélé un outil extrêmement efficace pour expliciter et modéliser le comportement mécanique des roches ainsi que les processus physiques mis en jeu lors des tremblements de terre.

Brace and Byerlee (1966) sont les premiers à avoir proposé que les expériences de «glissements saccadés» (ou «stick-slip» en anglais) en laboratoire soient un analogue des tremblements de terre. A cette date, le laboratoire offrait donc un environnement inédit dans lequel il serait possible de reproduire des tremblements de terre dans des conditions contrôlées: Byerlee (1978) fît la remarquable observation que dans le cas d'une interface frictionelle déjà existante (par analogie avec une faille), le coefficient de friction statique était constant au moment de la rupture, et ceci indépendament du type de roche (excepté certains argiles). De cette observation (Figure 1.15) découla la loi de Byerlee qui prévoit qu'en moyenne le coefficient de friction statique se situe autour de 0.85 pour une contrainte normale relativement faible (environ 300 MPa) et chute ensuite à 0.6. Celle-ci indique simplement que dans le domaine fragile, la contrainte cisaillante requise pour rompre n'importe quelle interface frictionelle croît linéairement avec la profondeur.

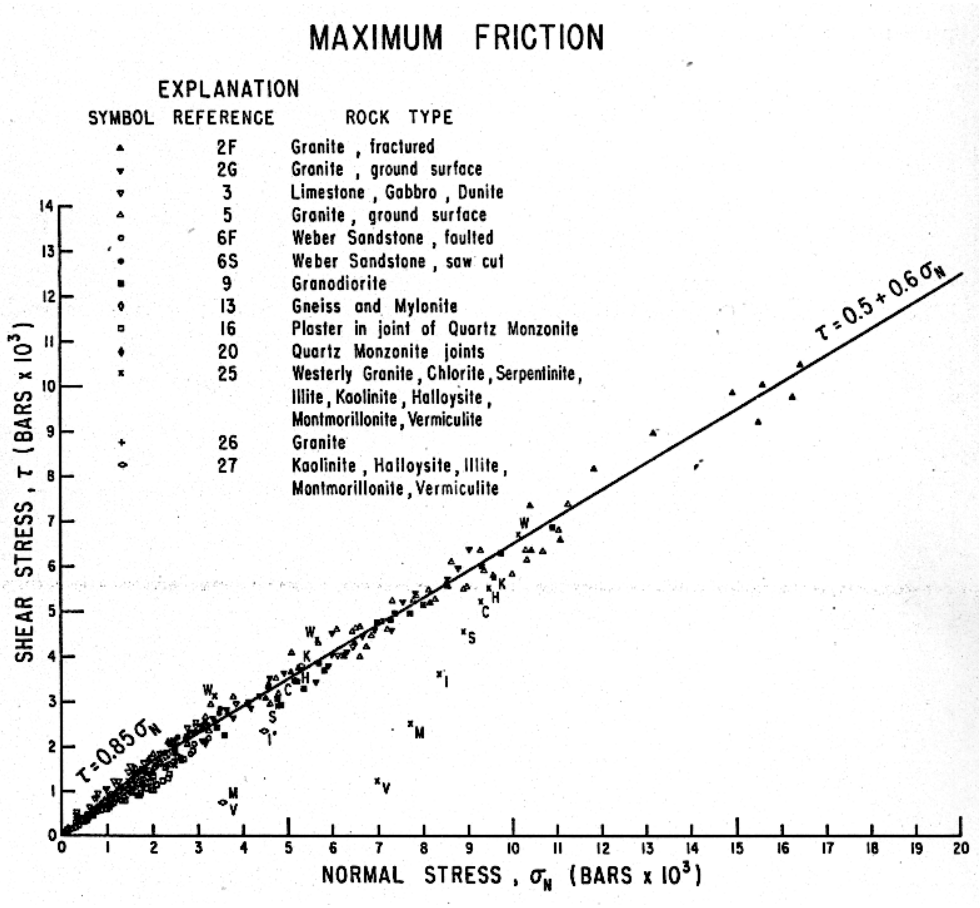

FIGURE 1.15: Contrainte cisaillante maximale en fonction de la contrainte normale au moment de la rupture pour différentes lithologies. A relativement faible contrainte normale, le coefficient de friction statique égal 0.85 et chute à 0.6 à partir d'une contrainte normale d'environ 300 MPa (extrait de Byerlee, 1978).

La rupture d'une interface frictionelle, ou simplement une faille, est un glissement instable et dynamique. D'un point de vue macroscopique, le glissement s'initiera lorsque la contrainte cisaillante excédera le seuil de résistance de la faille. La stabilité du glissement a été largement débattue dans le passé (voir Scholz, 2019 pour un résumé) et peut-être aisément compris dans le cas d'un modèle simple, celui du patin-ressort (Figure 1.16). L'interface du patin avec le socle représente une faille. Le chargement s'effectue au travers du ressort de raideur k (en N/m), celui-ci représente l'élasticité du milieu dans lequel la faille est contenue. La vitesse de chargement tectonique est simulée par le déplacement imposé du ressort à son extrémité, donc à une certaine distance. Au moment où le glissement s'initie les forces sont à l'équilibre:

$$F_s = k(l_0 - l) \tag{1.38}$$

avec F_s la résistance au cisaillement, k la raideur du ressort, l_0 la position du point de chargement et l la position du patin. Si F_s augmente avec le déplacement dl , le glissement est stable, le système se charge et accumule de l'énergie élastique. Si F_s diminue avec dl, deux cas peuvent se présenter. Soit :

$$|\frac{\partial F_s}{\partial l}| \leq k \tag{1.39}$$

où F_s diminue moins vite avec le déplacement dl que se décharge le ressort et le glissement est lent et stable ou bien:

$$|\frac{\partial F_s}{\partial l}| > k \tag{1.40}$$

où F_s diminue plus vite avec le déplacement dl que se décharge le ressort, ce qui se traduit par une pente résistance/glissement plus forte que k, le glissement devient instable et rapide. Le glissement ralentira au moment de l'intersection de la pente $-k$ avec la courbe de résistance au cisaillement de la faille. La stabilité du systême est donc en partie controlée par la raideur critique k_c du ressort qui s'exprime directement comme:

$$k_c = |\frac{\Delta F_s}{\Delta l}| \tag{1.41}$$

La stabilité du glissement peut également être établit en termes d'équilibre de contraintes. La variation de résistance au cisaillement F_s est équivalente à la variation de la contrainte de cisaillement τ et la stabilité du système est contrôlée par la rigidité critique du ressort k_c^r qui par analogie prend la forme:

$$k_c^r = |\frac{\Delta \tau}{\Delta l}| \tag{1.42}$$

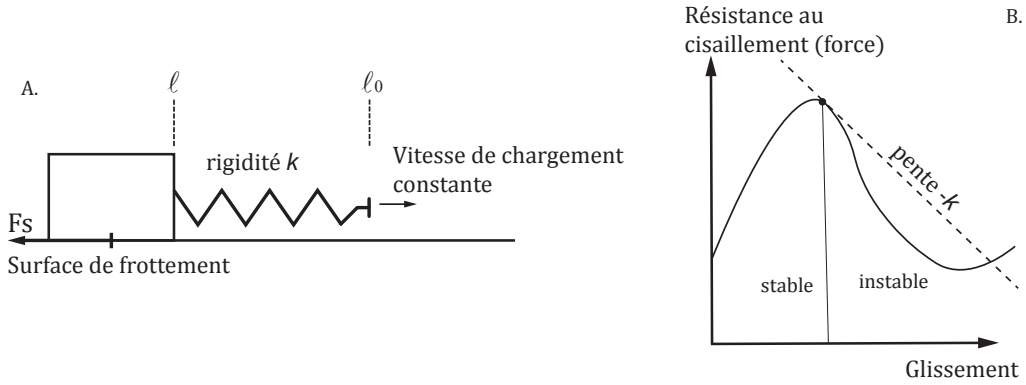

FIGURE 1.16: **Modèle patin-ressort. A.**Schéma du modèle. La surface de contact entre le patin et l'interface simule une faille et le ressort simule le chargement tectonique lointain.**B.** L'instabilité se dévellope lorsque la résistance au frottement diminue plus rapidement avec le glissement que la décharge du ressort représentée par la pente $-k$.

où k_c^r est exprimée en Pa/m.

La phase de nucléation d'une instabilité frictionelle (i.e. d'un séisme) est un sujet majeur en sismologie car elle offre une fenêtre de temps potentiellement utilisable pour en prévoir l'occurence. Ohnaka (2000) a conceptualisé la nucléation d'un séisme par trois phases successives (Figure 1.17) : (i) une première phase de glissement quasi-statique dans une zone localisée sur le plan de faille, que l'on définit comme la zone de nucléation (ii) une deuxième phase d'accélération du glissement et d'expansion de la zone de nucléation jusqu'à une taille critique et (iii) la propagation de la zone de nucléation sur l'intégralité du plan de faille permettant le glissement dynamique. La propagation dynamique de la rupture sera donc toujours précédée par la propagation lente d'un glissement asismique.

De nombreuses observations expérimentales ont permis de le valider: que ce soit dans le cas d'expérences réalisées sur des plastiques (Latour et al., 2013), ou sur des roches à l'échelle centimétrique (Passelègue et al., 2017) et à l'échelle métrique (McLaskey and Kilgore, 2013; Fukuyama et al., 2018). La taille au delà de laquelle la zone de nucléation se propagera dynamiquement est une échelle de longueur primordiale et dépendra de l'évolution de la résistance de la faille avec le glissement, en d'autres termes, de l'évolution du coefficient de friction statique avec ce dernier.

1.4.2 Loi de friction.

De manière générale, une instabilité frictionelle se développera seulement dans le cas où le coefficient de friction f diminue avec le glissement. Deux grandes lois ont été développées en laboratoire et sont généralement utilisées pour comprendre l'affaiblissement du coefficent de friction: la loi de «linear slip-weakening» et la loi

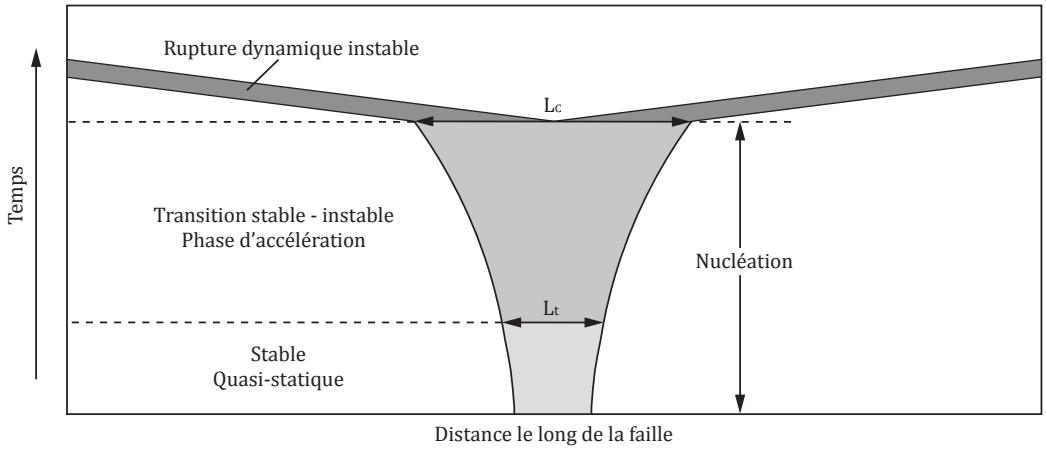

FIGURE 1.17: Nucléation de la rupture selon le modèle de Ohnaka (Ohnaka, 2000). La nucléation débute par la propagation d'une zone de glissement quasi-statique jusqu'à une longueur L_t qui marque le début de l'instabilité. La zone de nucléation accélère jusqu'à atteindre la longueur critique L_c à partir de laquelle l'instabilité se propage dynamiquement.

«rate and state».

Modèle «slip-weakening» :

Dans le modèle de slip-weakening, l'évolution du coefficent de friction dépendra uniquement de la quantité de glissement (Ida, 1972; Campillo and Ionescu, 1997; Uenishi and Rice, 2003). Si le glissement est égal à zéro, le coefficent de friction égale le coefficient de friction statique f_s (Byerlee, 1978). Avec le glissement D, le coefficient de friction f décroît linéairement jusqu'à atteindre une valeur résiduelle f_d appelée coefficient de friction dynamique soit:

$$f = f_s - (f_s - f_d).\frac{D}{D_c} \tag{1.43}$$

La quantité de glissement nécessaire D_c pour atteindre cette valeur résiduelle est appelée «slip-weakening distance» (Figure 1.18 a.) et intervient dans l'expression de la taille critique de nucléation L_c. Pour obtenir L_c, considérons un crack de longueur L, et de module de cisaillement μ. La quantité de contrainte cisaillante $\Delta\tau$ nécessaire pour glisser d'une quantité D à l'intérieur du crack est égale à:

$$\Delta\tau = \frac{\mu.D}{L} \tag{1.44}$$

En reprenant (1.42) et en exprimant τ comme $f.\sigma_n$, on obtient l'égalité suivante au démarrage de l'instabilité dynamique:

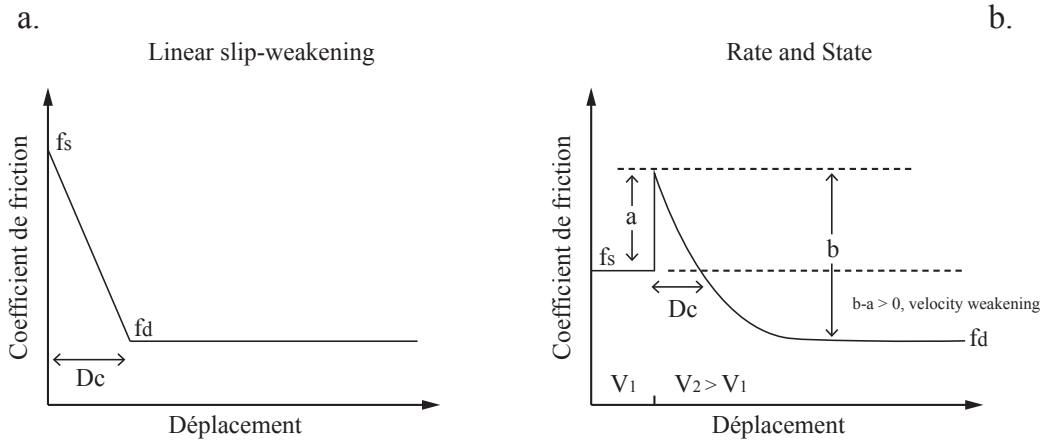

FIGURE 1.18: **Modèles conceptuels de l'évolution du coefficient de friction f avec le glissement. a.** Linear slip weakening. **b.** Rate and State.

$$k_c^r.D_c = \sigma_n.(f_s - f_d) \tag{1.45}$$

Selon (1.44), on peut exprimer k_c^r comme:

$$k_c^r \approx \frac{\mu}{L_c} \tag{1.46}$$

En combinant (1.45) et (1.46) on obtient l'expression théorique de la taille de nucléation L_c (Campillo & Ionescu,1997):

$$L_c = \beta.\frac{\mu D_c}{\sigma_n.(f_s - f_d)} \tag{1.47}$$

avec β une constante qui dépendra du mode de fracturation ($\beta = 1.158$ pour une rupture en mode III). Pour une longueur $L < L_c$, le glissement est lent et asismique, au delà de L_c la zone de nucléation accélère et le glissement devient dynamique et sismique. L_c fournit donc une taille critique en dessous de laquelle aucune rupture ne peut se propager dynamiquement. L_c est linéairement proportionelle à D_c, ce qui signifie que plus la distance nécessaire pour affaiblir la résistance au glissement est grande, plus l'extension de la zone de nucléation le sera également. Comment D_c évolue avec la taille d'un séisme est une question donc cruciale.

Les données de laboratoire montrent généralement que $D_c \approx 10^{-6}$ m (Passelègue et al., 2016), alors que les observations sismologiques prédisent $D_c \approx 10^{-1} - 1$ m. Ce désaccord a généralement été attribué aux différences de rugosité entre les failles

naturelles et les surfaces sur lesquelles le glissement s'effectue en laboratoire (Dieterich, 1979; Scholz, 1988; Ohnaka, 2003).

Modèle «rate and state» :

A la fin des années 70, Dieterich (1979) introduit un autre paramètre cinématique nécessaire à l'étude de la résistance frictionnelle, la vitesse. Sur la base des travaux de Diectrich, Ruina (1983) proposa le modèle de rate-and-state qui exprime l'évolution du coefficient de friction f comme une fonction de la vitesse de glissement V et d'une variable d'état représentative de l'état de l'interface θ selon :

$$f = f_0 + a.ln(\frac{V}{V_0}) + b.ln(\frac{V_0\theta}{D_c}) \tag{1.48}$$

avec f_0, le coefficient de friction de statique, a et b deux paramètres adimensionnels et V_0 une vitesse de glissement de référence. La variable d'état θ a la dimension d'un temps et peut-être interprétée comme le temps de contact moyen des aspérités ou en d'autres termes le temps necéssaire pour reformer une nouvelle population d'aspérités. L'évolution temporelle de θ est formulée par deux lois distinctes:

$$\dot{\theta} = 1 - \frac{\theta V}{D_c} \tag{1.49}$$

ou

$$\dot{\theta} = -\frac{\theta V}{D_c}.ln(\frac{\theta V}{D_c}) \tag{1.50}$$

La première (éq. 1.49) correspond à la «Aging law» et la seconde (éq. 1.50) à la «Slip law». La différence significative entre ces deux lois est que l'une considère que l'évolution de la variable d'état θ est uniquement fonction de la vitesse de glissement (« Slip law ») alors que dans le cas contraire (« Aging law ») θ évolue également avec l'âge de contact des aspérités (voir Rubin and Ampuero, 2005, Ampuero and Rubin, 2008 pour une discussion détaillée).
Le modèle «rate and state» est une réelle avancée car il permet une vision détaillée de la friction d'un plus large ensemble de matériaux que seulement les roches (par exemple les plastiques, verres etc...). Ce type de modèle est particulièrement adapté dans les cas où l'interface frictionnelle est décrite comme une surface discontinue en contact à travers une population d'aspérités et donc caractérisée par une rugosité. Le succès du modèle «rate and state» pour décrire la dynamique des tremblements de terre a été largement exploré, à la fois expérimentalement (voir Marone, 1998, pour une revue complète) que théoriquement (Rice and Ruina, 1983; Blanpied and Tullis, 1986; Dieterich, 1992; Rice et al., 2001). Ces travaux ont permis, en partie, de montrer que suite à un changement abrupt de la vitesse de glissement, le coefficient de friction statique f_s augmente brusquement. Une instabilité n'est alors possible

que si le coefficient de friction dynamique f_d diminue avec la vitesse de glissement et atteint une valeur inférieure à f_s (Figure 1.18 b.). Ce scénario n'est possible que si (a-b) < 0, dans le cas contraire, (a-b) > 0, le coefficient de friction augmentera avec la vitesse de glissement. Dans le modèle rate-and-state, la longueur critique de nucléation L_c est reliée à a et b selon (Rubin and Ampuero, 2005):

$$L_c = \frac{\mu D_c}{\sigma_n.(b-a)} \tag{1.51}$$

Les paramètres constitutifs a et b reflétent des propriétés intrinsèques au matériau et pourront fortement varier selon la température, la vitesse de chargement, la taille des grains ou encore l'épaisseur de gouge (Marone, 1998; Mitchell et al., 2015; Yamashita et al., 2014; Urata et al., 2018). En pratique, les observations expérimentales montrent que le modèle rate-and-state est quasiment toujours valide car l'interface frictionnelle peut être approximée par un plan d'épaisseur infinitésimal. Dans le cas de failles naturelles, cette approximation peut avoir certaines limites, majoritairement du fait que les zones de faille ont une épaisseur finie par accumulation de gouge avec les glissements successifs.

Le modèle rate-and-state permet donc d'établir une description phénoménologique des processus à l'interface frictionnelle en lien direct avec l'évolution de la friction avec la quantité et la vitesse de glissement. Ces processus s'opèrent à l'échelle des aspérités et peuvent être décrits comme des phénomènes de plasticité ou de changements de phase des minéraux, activés thermiquement par échauffement frictionnel (Baumberger et al., 1999; Nakatani, 2001). Terminons par le fait que la dynamique d'une faille avec le glissement et donc sa stabilité pourra également montrer une forte variabilité dûe aux interactions fluide-roche, les fluides pouvant par effet physique (surpression de pore) ou par effet chimique modifier les propriétés mécaniques du matériau.

1.4.3 Etude de la microsismicité en laboratoire

Dans la section précédente, nous nous sommes focalisés sur l'aspect mécanique des expériences réalisées en laboratoire. L'enregistrement de la microsismicité (i.e. des émissions acoustiques) au cours de celles-ci a été une source d'information majeure en mécanique des matériaux et dans le cas de problématiques en lien direct avec la physique des tremblements de terre. Dans le cadre de son doctorat, Joseph Kaiser (1950) mis en place un des premiers dispositifs d'enregistrements acoustiques pour étudier si la qualité de différents métaux pouvait être évaluée au « son » qu'ils émettaient lors de leur déformation. Du début des années 60 au début des années 90, la majorité des études expérimentales ont cherché à établir un lien entre la production d'émissions acoustiques et les processus de fracturation (Mogi, 1962; Mogi, 1968; Scholz, 1968a; Scholz, 1968b; Tapponnier and Brace, 1976; Lockner and Byerlee, 1977;

Lockner, 1980; Sondergeld and Estey, 1981; Sondergeld and Estey, 1982; Lockner, 1993). Scholz (1968b) a observé le comportement spatio-temporelle des émissions acoustiques produites lors d'expériences en déformation uni-axiale sur des roches intactes. Cette étude a démontré que les émissions acoustiques étaient corrélées à un phénomène de « dilatance» à l'approche de la rupture qui traduit une augmentation de volume du matériau. Cette augmentation de volume est la conséquence de la production et de l'interaction de fissures qui se connecteront au moment de la rupture. La même année, Mogi (1968) établit un catalogue des émissions acoustiques produites lors d'expériences en déformation tri-axiale, avant, pendant et après la fracturation. Les caractéristiques émissions acoustiques montrèrent de grandes similarités avec les tremblements de terre, notamment dans la distribution de leurs magnitudes et dans leur comportement temporelle. Cette observation a une implication majeure: les processus et mécanismes en lien avec la fracturation des matériaux en laboratoire sont invariables selon l'échelle et peuvent donc être directement étendus aux tremblements de terre.

La question de savoir si oui ou non les observations faites en laboratoire à petites échelles sont transposables aux grandes échelles qui s'appliquent dans le cas des tremblements de terre est fondamentale et est toujours sujette à débat. Un argument de taille pour répondre à cette question réside dans les lois d'échelles des séismes. A cet égard, différentes études ont soutenu les observations de Mogi (1962) and Mogi (1968) et permis de valider que les magnitudes des émissions acoustiques en laboratoire se distribuaient selon la loi de Gutenberg-Richter (Scholz, 1968b; Weeks et al., 1978; Cai et al., 1988; Lockner, 1993). La loi d'Omori qui prédit l'augmentation et la décroissance temporelle de la sismicité suite à un choc principal a elle aussi été observée en laboratoire, dans sa forme la plus exacte (Lord Jr and Koerner, 1983) ou bien dans une forme dérivée (Lockner and Byerlee, 1977; Hirata, 1987). Dans une étude récente, Yoshimitsu et al. (2014) ont utilisé des capteurs acoustiques calibrés (i.e. grâce auxquels on peut obtenir une mesure absolue de vitesse) pour faire l'analyse des spectres des émissions acoustiques générées lors d'une expérience en déformation tri-axiale. Les magnitudes M_w des émissions acoustiques ont été estimées entre ~ -7.0 et -8.0. L'estimation des fréquences coins (entre $\sim 200\ kHz$ et $1\ MHz$) des émissions acoustiques a permis de confirmer que la loi d'échelle entre la magnitude d'un séisme et sa fréquence coin était également conservée à l'échelle de la micro-sismicité. De plus, les chutes de contraintes associées aux émissions acoustiques étaient de l'ordre de 1 à 10 MPa ce qui est typiquement de l'ordre de celles des séismes naturels. Ces résultats confortent donc dans l'idée que la micro-sismicité générée en laboratoire est la manifestation de micro-séismes. Une étude ultérieure (Sellers et al., 2003) avait également utilisé des capteurs acoustiques calibrés pour faire l'analyse des spectres de la micro-sismicité générée pendant une expérience en déformation unixiale (i.e., sans confinement). Au contraire des résultats obtenus par Yoshimitsu et al. (2014) , les fréquences coins estimées des émissions acoustiques ne

satisfaisaient par la relation en w_0^{-3}. Ceci principalement en raison du dispositif expérimental de calibration qui ne permettait de calibrer les capteurs acoustiques dans une bande de fréquences suffisamment large.

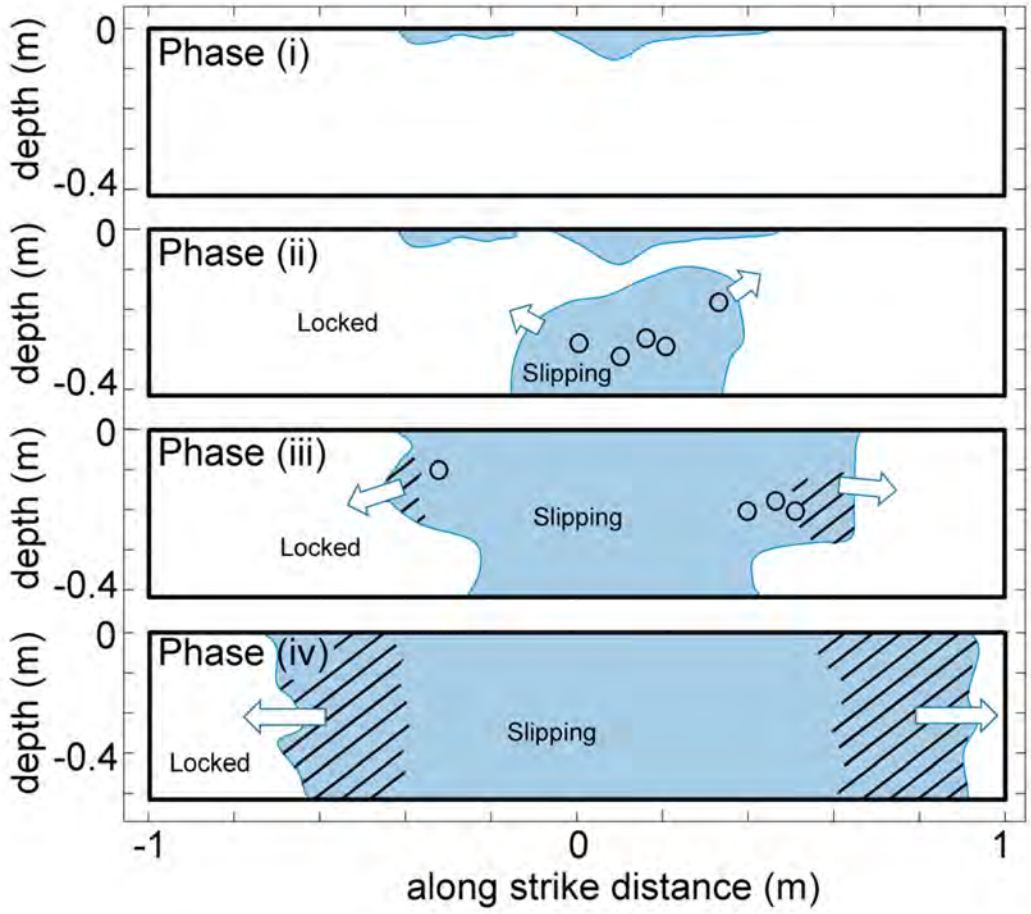

FIGURE 1.19: Corrélation entre la nucléation de la rupture par propagation d'une zone de glissement asismique (bleu clair) et précurseurs acoustiques (cercles noirs). La surface représente le plan de faille (extrait de McLaskey and Kilgore, 2013).

L'analyse de la microsismicité en laboratoire a également été bénéfique pour mieux contraindre comment nuclée une rupture et déceler des potentiels signaux précurseurs. Weeks et al. (1978) ont enregistré plus de 8000 emissions acoustiques pour un total de 14 stick-slip successifs et ont mesuré la valeur b de la pente de Gutenberg-Richter au cours des cycles. Les résultats obtenus ont indéniablement prouvé que la valeur de b chutait à l'approche de la rupture. En d'autres termes, les magnitudes des précurseurs acoustiques augmentent à l'approche du choc principal. Ce comportement observé au cours d'autres expériences (Ohnaka and Mogi, 1982; Main et al., 1989; Lei et al., 2000) est consistent avec les résultats obtenus par Scholz (1968b) qui ont établi une corrélation positive entre la valeur de b et la valeur de la contrainte différentielle (différence entre contrainte minimum et contrainte maximum).

Cependant, excepté dans le cas de larges séismes de subduction (Nuannin et al., 2005) , il existe peu d'observations qui l'atteste à l'échelle des failles crustales. Dans une récente étude, Passelègue et al. (2017) ont analysé la dynamique temporelle des émissions acoustiques pour un grand nombre de stick-slip et ont montré que la nucléation de la rupture s'accompagnait d'une accélération exponentielle du nombre d'émissions acoustiques. Ce type de comportement est cohérent avec une vision conceptuelle de la nucléation comme la propagation lente d'une zone de glissement quasi-statique (Dieterich, 1978; Okubo and Dieterich, 1984; Ohnaka et al., 1987; Ohnaka and Shen, 1999; Nielsen et al., 2010). Au cours d'une expérience sur un échantillon de granite de dimension métrique, McLaskey and Kilgore (2013) ont capturé la propagation d'un front de glissement lent au moment de la nucléation et ont observé une nette corrélation entre sa position et celles des émissions acoustiques (Figure 1.19). Cependant, les expériences sur des échantillons de grandes tailles en laboratoire nécessitent pour des raisons techniques d'être réalisées dans des conditions de pressions faibles et peu représentatives de celles des failles naturelles.

Une partie des efforts au cours de cette thèse s'est donc portée sur l'analyse des signaux acoustiques précuseurs pendant la nuléation de séismes expérimentaux dans des conditions proches de celles des failles naturelles.

1.5 Plan du manuscript.

Dans le chapitre 2 nous présentons les deux types de roches que nous avons utilisé dans nos expériences, du Granite de Westerly et du Gabbro d'Inde, ainsi que les dispositifs expérimentaux. Nous décrivons également les méthodes d'analyses utilisées et/ou dévellopées au cours de cette thèse. Le chapitre 3 est une étude expérimentale des processus et variables physiques qui determinent l'occurence des précurseurs au cours des cycles sismiques et qui en contrôlent la dynamique spatiale et temporelle. Cette étude a été menée sur le Gabbro d'Inde. Le chapitre 4 est une étude expérimentale de l'influence de l'état de contrainte et de la vitesse de rupture sur les radiations hautes-fréquences ainsi que de leur origine pendant la propagation de la rupture. Cette étude a été menée sur le Granite de Westerly. Dans le chapitre 5 nous mettons en perspective et discutons les résultats obtenus. En particulier, nous présentons l'analyse préliminaire d'un catalogue de sismicité de Californie du Sud dans le but de connecter les résutats obtenus sur les précurseurs à l'échelle du laboratoire, centimétrique, à l'échelle des observations de terrain, kilométrique.

Chapter 2

Material and methods

In this section we first describe the two types of rocks used in the experiments and the experimental set-up. We then explain the methods used and developed to analyse and process the data.

2.1 Experimental set-up

2.1.1 Rock lithlogies & Sample preparation

The experiments conducted during this thesis were performed on samples of Westerly Granite and Indian-Gabbro. Both types of rocks have the common advantage of being lithologies constitutive of the Earth's continental and oceanic crust respectively. Also, their acceptable level of isotropy simplifies data processing and interpretation.

Westerly Granite :

Westerly granite comes from the state of Rhode Island in the U.S. and is probably one of most commonly used rock type in experimental mechanics. Its physical properties are well known and have been extensively described (Dieterich, 1979; Wong, 1982; Lockner and Okubo, 1983; Scholz, 1986; Lockner, 1993). Major minerals of the Westerly Granite are quartz ($\sim$ 28 %), plagioclase ($\sim$ 33 %), K-feldspar ($\sim$ 33 %), muscovite and biotite ($\sim$ 5 %). Grain sizes range from 0.05-2 mm with an average of about 0.75 mm. Young's modulus, density, P-wave velocity and S-wave velocity are 64 GPa, 2650 $kg.m^{-3}$, 5800 $m.s^{-1}$ and 3500 $m.s^{-1}$ respectively (Passelègue et al., 2016).

Indian Gabbro :

Indian Gabbro is a metagabbro coming from Tamil Nadu in India. This rock was notably used for meter-scale rock friction experiments (Togo et al., 2015; Xu et al., 2018; Yamashita et al., 2018; Fukuyama et al., 2018). Major minerals are clinopyroxene ($\sim$

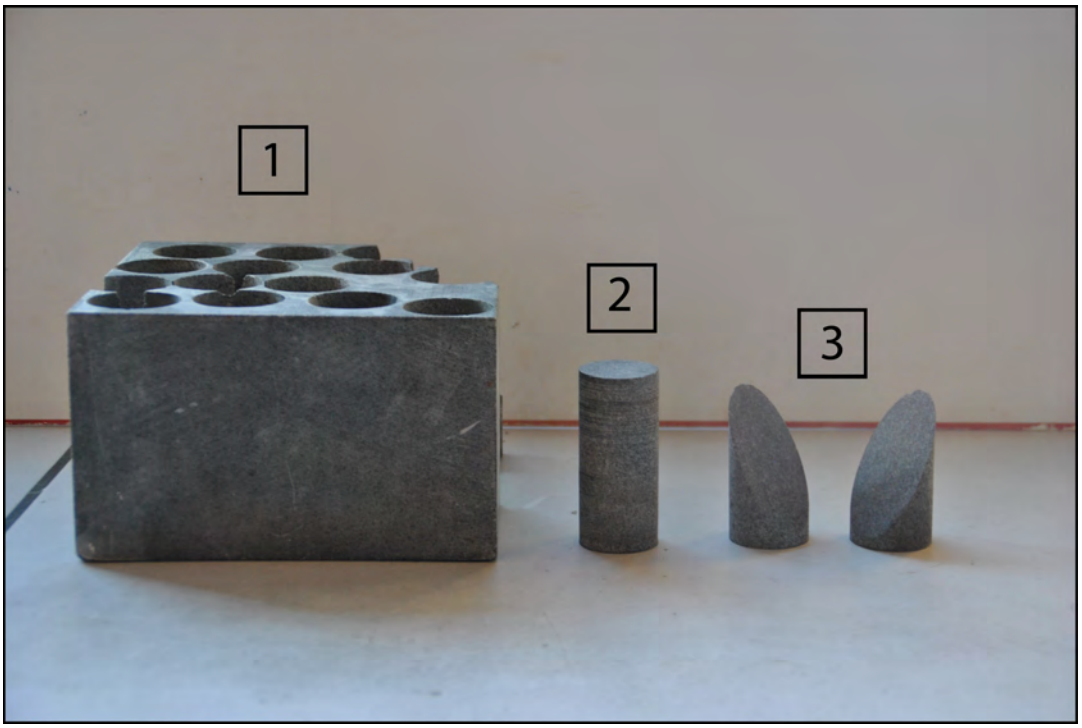

FIGURE 2.1: Sample preparation. Initially, rocks arrive in the form of rectangular blocks (1), inside which cylinders are drilled. Top and bottom parts of the cylinders are then made parallel (2). The samples are finally cut at 30°, with respect to their axis, to reproduce an experimental fault. (3).

37 %) , plagioclase ($\sim$ 33 %), hornblende ($\sim$ 11 %), hilmenite and hematite ($\sim$ 5 %), and biotite ($\sim$ 4 %) .Grain sizes range from 0.5-3 mm. Young's modulus, density, P-wave velocity and S-wave velocity are 103 GPa, 2980 $kg.m^{-3}$, 6400 $m.s^{-1}$ and 3600 $m.s^{-1}$ respectively.

Initially, rocks arrive as rectangular blocks. The first stage consists of drilling a cylinder into the block. The top and bottom part of the cylinder are then rectified and polished with a surface grinder to make them parallel. The final shape is a cylinder 40 mm wide and approximately 88 mm long. To accurately represent the behavior of a natural fault, a weak fault interface is obtained by cutting the cylinders at an angle of 30° with respect to the vertical axis. The sample's geometry is referred to as a saw-cut. The upper and lower part of the fault interface are rectified and then polished to maximise contact area. Finally, to preserve a minimum cohesion we use sandpaper to roughen both sides of the fault interface. Fault surfaces were roughen with #240 grit (average particle diameter 59 μm, smoother) and with #120 grit (average particle diameter 125 μm, rougher) sandpaper for the experiments conducted on samples of Westerly Granite and Indian-Gabbro respectively. Figure 2.1 is showing a photograph of the three main stages of sample preparation.

2.1.2 Producing experimental earthquakes using a triaxial cell

The type of apparatus used in the experiments is a triaxial oil-medium loading cell ($\sigma_1 > \sigma_2 = \sigma_3$). A triaxial apparatus is basically composed of (i) a confining chamber and (ii) an axial piston (Figure 2.2 a.). The rock sample is positioned at the center of the confining chamber and is isolated from the confining oil into a 125 mm long and 5 mm thick viton jacket. The axial piston comes into contact with the top part of the sample. The pressures applied into the confining chamber and at the top of the piston chamber are independently controlled by two servopumps. The confining pressure ($\sigma_2 = \sigma_3$) plays the role of the minimum stress while the axial stress of the maximum stress. The confining pressure and the pressure into the piston chamber are measured by pressure transducers with $10^{-3} MPa$ resolution. The axial stress applied to the sample is given by the pressure at the surface of the piston chamber and by surface area ratio between both side of the piston. The axial displacement of the rock sample during the experiments is obtained by measuring the displacement of the axial piston with 0.1 μm resolution. The confining pressure, the axial stress and the axial displacement can be recorded up to 1 kHz sampling rate. One should note that the axial displacement includes the displacement of the whole system: the rock sample and the axial column. Both the rock sample and the axial column will deform elastically during loading. Thus, the displacement along the fault surface D^{FS} is obtained by first correcting the axial deformation of the elastic deformation of the sample and the axial piston such as :

$$\epsilon_{ax}^{FS} = \epsilon_{ax}^{WS} - \frac{\Delta\sigma}{E_{ap}} - \frac{\Delta\sigma}{E_s} \tag{2.1}$$

where ϵ_{ax}^{FS} is the axial deformation of the fault surface, ϵ_{ax}^{WS} is the axial deformation of the whole system measured at the top of the axial piston, $\Delta\sigma$ is the differential stress, and E_{ap} and E_{ap} are the rigidity of the apparatus and the sample respectively. And second, by multiplying ϵ_{ax}^{FS} by the length of the sample l_s after being projected on the fault plane such as:

$$D^{FS} = \epsilon_{ax}^{FS}.l_s.\cos\theta \tag{2.2}$$

where θ is the angle between the direction of σ_1 and the fault plane ($\theta = 30°$).
Two different triaxial apparatus were used during this thesis but both are almost identical. The differences are as follows:

- One of the triaxial apparatus has an additional auto-compensated chamber. This auto-compensated chamber is positioned at the center of the axial piston and is connected to the confining chamber. Therefore the confining pressure is also applied on the surface of the auto-compensated chamber: whatever the

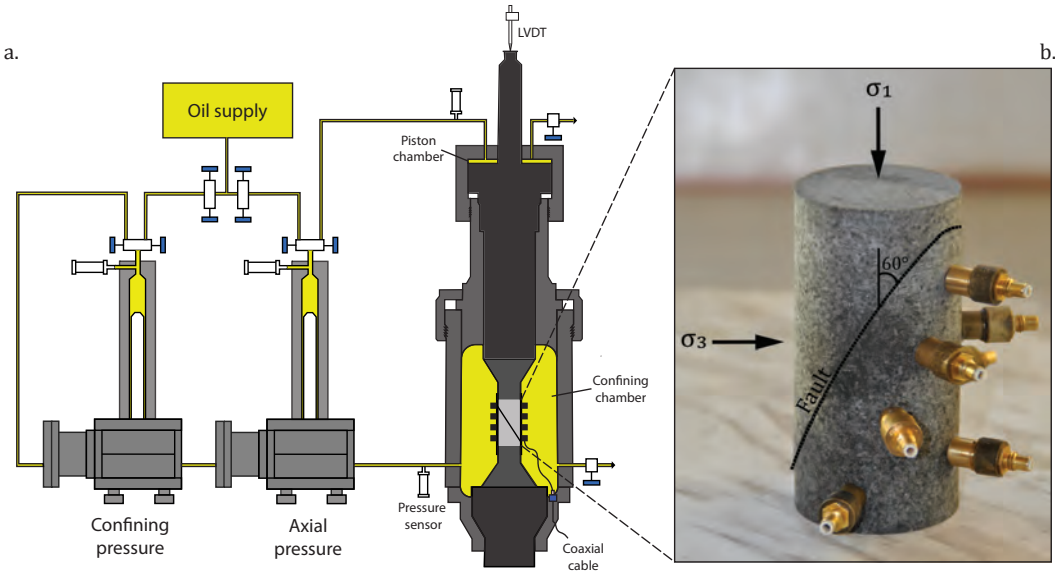

FIGURE 2.2: Triaxial apparatus and rock assemblage. **a.** Schematic of a triaxial oil-medium loading cell. Two external servo pumps control axial and radial stresses. The axial displacement is given by the displacement of the piston which, in this case, is measured by an LVDT at its top. **b.** Saw-cut rock specimen used to reproduce laboratory earthquakes. The fault plane is oriented at 30° with respect to the principal stress σ_1. Seismic waves generated during the experiments are recorded by acoustic sensors glued at the surface of the sample.

pressure into the confining chamber, the axial piston will « float ». Hereafter, we call this apparatus apparatus #1.

- For apparatus #1 the confining pressure can go up to 300 MPa while for apparatus #2 the confining pressure is limited to 100 MPa.
- For apparatus #1 the axial displacement is measured by an LVDT (Linear Variable Differential Transducer) at the top of the axial piston while the axial displacement is measured by three gap sensors (outside of the cell as well) for apparatus #2. The axial displacement is then averaged over the three measurements.

To produce stick-slip instabilities, the procedure is the following: (i) once the sample positioned into the confining chamber the cell is closed (ii) the confining chamber is filled with oil (iii) the confining pressure is increased up to the desired stress conditions (iv) the axial piston is put into contact with the sample and (v) oil is injected at a constant rate in the piston chamber to increase the axial stress. This corresponds to a constant axial shortening rate and during our experiments, this shortening rate was imposed at about 0.36 $\mu m/s$ (i.e., strain rate of about 4.10^{-6}). The shear stress τ and the normal stress σ_n acting onto the fault can be expressed as:

$$\tau = \frac{\sigma_1 - \sigma_3}{2}.sin(2\theta) \tag{2.3}$$

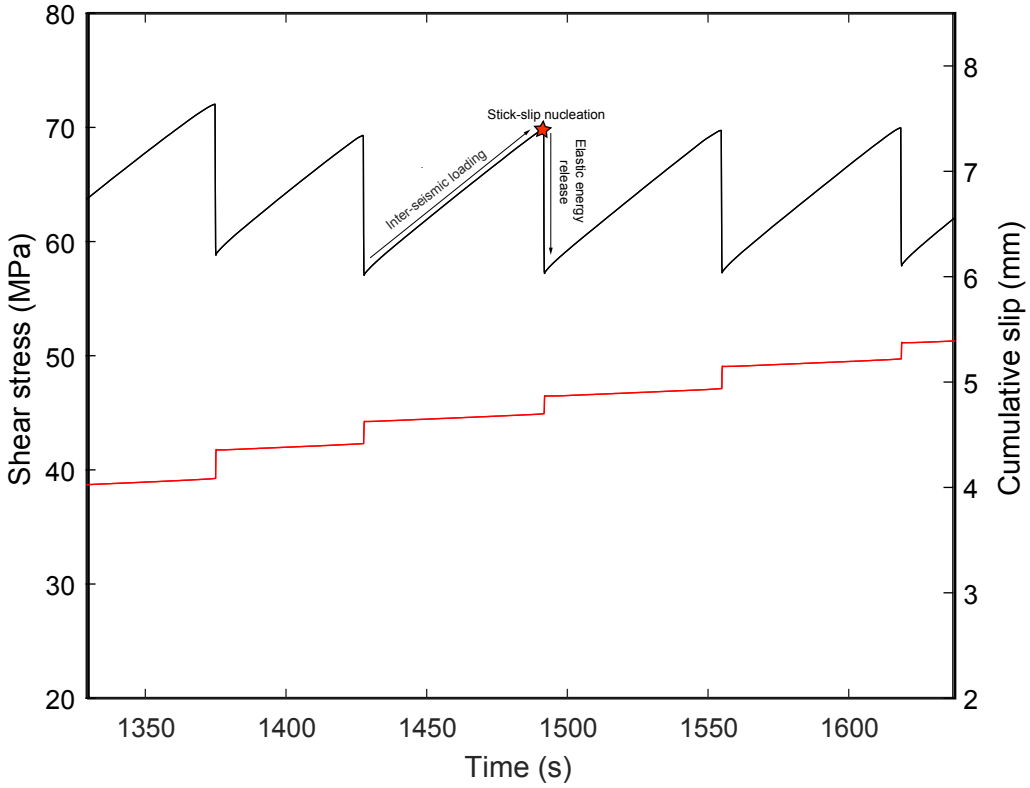

FIGURE 2.3: Typical evolution of shear stress and axial displacement during stick-slip cycles. The linear increase of the shear stress with the displacement corresponds to the inter-seismic loading. Once the shear-stress reaches the critical strength of the fault, a frictional instability develops and the stored elastic energy is suddenly released with seismic slip along the fault interface.

and

$$\sigma_n = \frac{\sigma_1 + \sigma_3}{2} + \frac{\sigma_1 - \sigma_3}{2}.cos(2\theta) \tag{2.4}$$

where σ_1 and σ_3 are simply the axial stress and the confining pressure respectively and θ is defined in the same way as for (2.2). Figure 2.3 shows a typical shear stress/displacement curves versus time during an experiment. With increasing the axial stress the shear stress τ increases, the sample deforms and stores elastic energy. Once the critical strength of the fault is reached, the elastic energy is suddenly released which corresponds to an abrupt shear stress drop, accompanied by rapid frictional slip along the experimental fault interface.

2.1.3 Strain and acoustic emission high-frequency monitoring system

Sixteen coaxial cables allow for local measurements during stick-slip experiments. Two types of sensors are usually used: strain gauges to record local strain or/and acoustic sensors to record the acoustic wavefield.
An acoustic sensor is simply a ceramic encased within a brass casing (Figures 2.4

a, b) and is called a piezoelectric transducer. In response to a mechanical stress, an electrical potential difference develops between the two faces of the ceramic. The electrical potential difference is recorded as a voltage. This voltage is proportional to the mechanical stress. The sensitivity of a ceramic will depend on its width and thickness and on the type of material. For a given width, the thicker the ceramic, the less sensitive is its response. Acoustic sensors are glued to the rock sample with cyanocrylate adhesive through holes already perforated into the jacket. To avoid any, sealing is performed using a flexible and non-brittle adhesive (Loctite 9455 Hysol).
The type of strain gauge used during this thesis is the electrical resistance strain gauge which is of the commonest type. Strain gauges are simply resistors whose resistance is a function of their cross-section area. When deforming, the cross-section area of a strain gauge changes which in turn causes the resistance to change correspondingly to the strain. Strain gauges can measure either single or multiple components of strain. The strain gauges used in this study were manufactured by the company Kyowa (type KFG-2-350-C1-11) and presented a length and a resistance of 2 mm and 350 Ω respectively (Figures 2.5 a,b).

During the experiments conducted on the Indian Gabbro (chapter 3), 8 P acoustic sensors polarized in the direction perpendicular to the sample surface and 8 single component 350 Ω strain gauges were used. Ceramics were 5 mm wide and 0.5 mm thick and made of an assemblage of lead oxides, titanium and zircon (Pb, Zr and Ti). This type of ceramic is commonly used and is called PZT ceramic. Ceramics presented a resonant frequency of 1 MHz for compressional waves. In the experiments conducted on the Westerly granite (chapter 4), 16 P/S acoustic sensors polarized at 10° with respect to the perpendicular direction to the sample surface were used. Ceramics were 5 mm wide and 4 mm thick and made of an assemblage of Lithium-Niobate (an oxide of lithium, Li, and niobium, Nb). Ceramics presented a resonant frequency of 1 MHz for compressional waves and of 0.6 MHz for shear waves. Positions of the sensors for both experiments are shown in Figure 2.6.

Internal measurements were recorded at 10 to 50 MHz sampling rate using a 16 channel digital oscilloscope and the software Insite (Itasca Image). Depending on the objectives, signals were either amplified or unamplified. In order to avoid saturation, recorded signals during stick-slip instabilities were kept unamplified. To record the unamplified signals only during the time of stick-slip instabilities we set an amplitude trigger threshold to all acoustic sensors. The recording of unamplified signals was triggered (Figure 2.7) if more than 1 acoustic sensor were recording a signal with higher amplitude than the threshold in a same time window. Before being recorded, strain gauge signals were first delayed to an amplifier (manufactured by Kyowa company, figure 2.5 c) which allowed us to set the output voltage as a function of the expected strain (for instance, 10 V = 4000 $\mu\epsilon$)

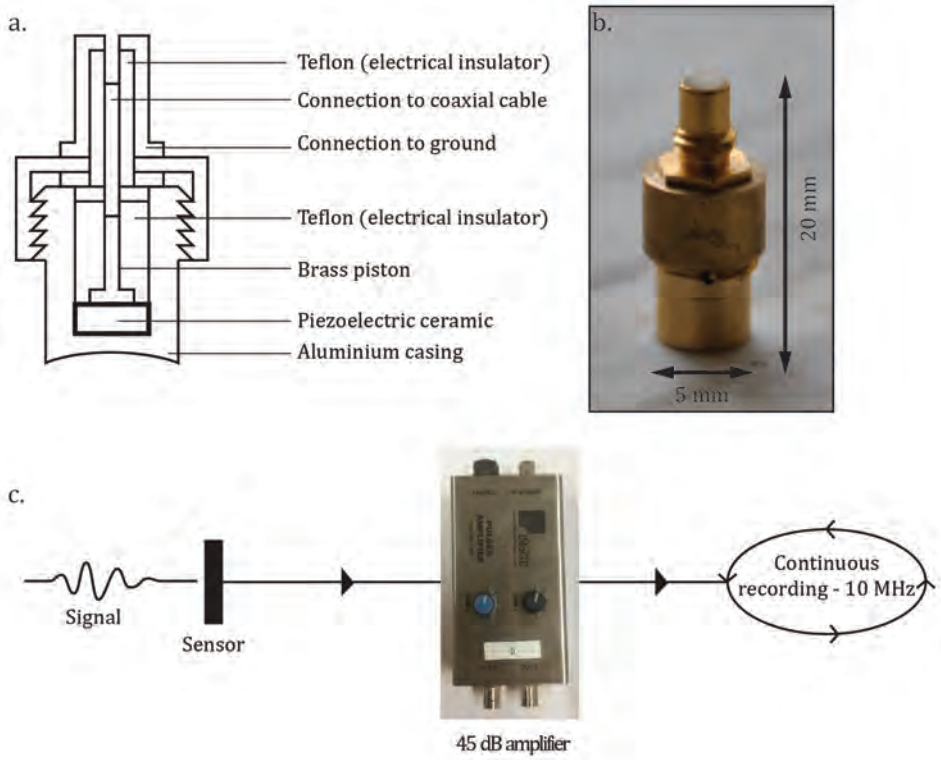

FIGURE 2.4: **a.** Schematic of an acoustic sensor. The piezoelectric ceramic allows to record surface vibrations in the form of a voltage. The signal is recorded by using an oscilloscope connected by a coaxial cable. **b.** Photograph of the type of acoustic sensor used in the experiments. **c.** Schematic view of the acoustic emissions monitoring system. Output signals are amplified to continuously record microseismicity during the experiments.

In the experiments conducted on the Indian Gabbro, strain gauges and acoustic sensors signals were continuously recorded at 10 MHz sampling rate. Strain gauges signals were kept unamplified while acoustic sensors signals were amplified. To amplify the acoustic signals, sixteen 45dB amplifiers were used (Figure 2.5 c). Continuous recordings were triggered after the first stick-slip occurrence in order to reduce data overhead (only 1 minute of continuous recording by 1 channel represents 6.10^8 sampling points). As explained hereafter, the continuous recordings allows us to record the microseismicity during the experiments.

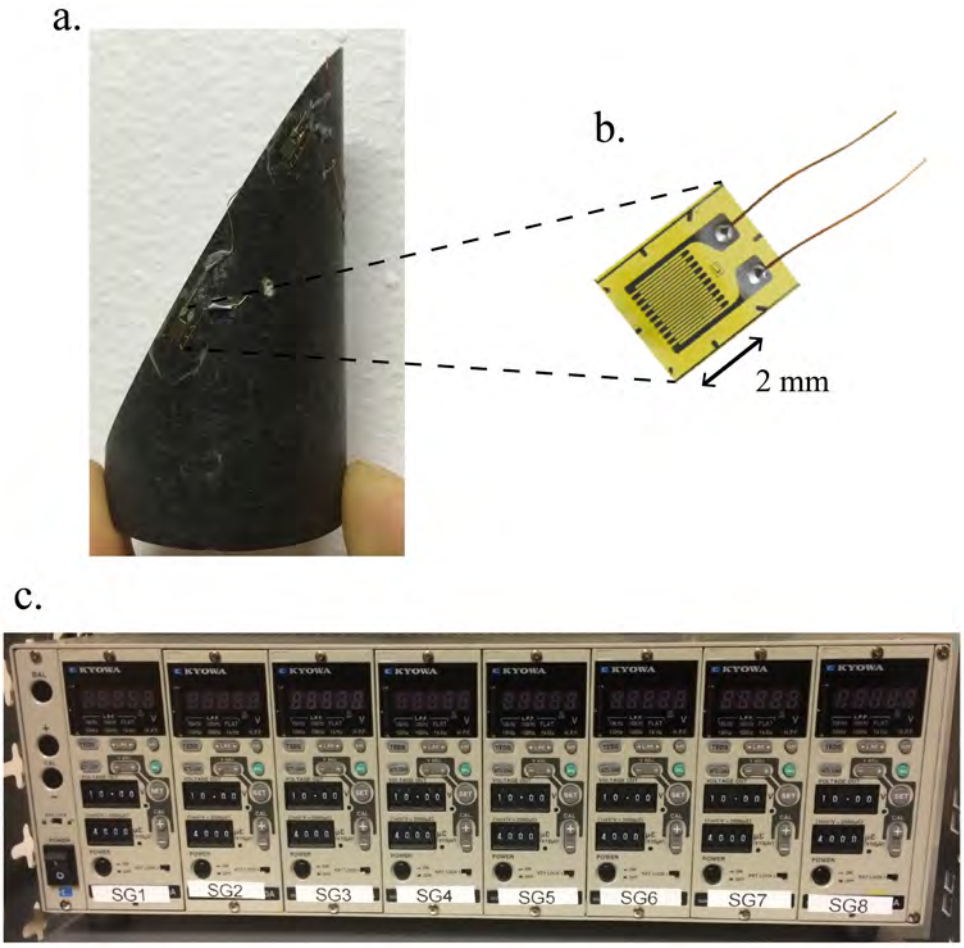

FIGURE 2.5: Strain measurements. **a.** Picture of the strain gauges glued on the surface of the sample. Strain gauges are positioned as close as possible to the simulated fault. **b.** Picture of the type of strain gauge used during the experiments. Strain gages are resistors whose resistance changes correspondingly to the strain. **c.** Picture of the amplifier used to set the recording gain of strain measurements.

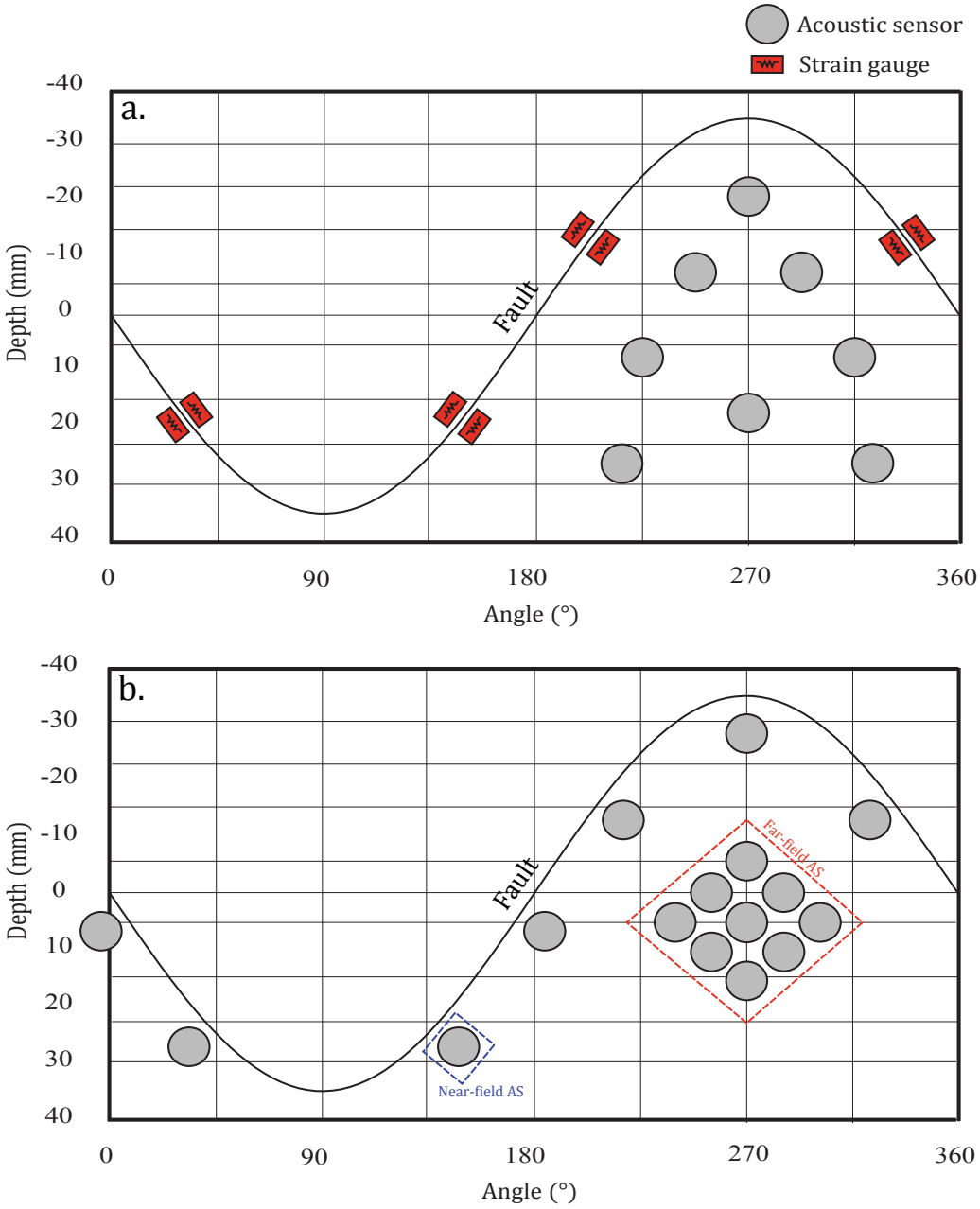

FIGURE 2.6: **a.** Sensors map used in the experiments presented in chapter 3. Acoutic sensors were positioned homogeneously to better locate acoustic emissions and estimate their respective seismological parameters. **b.** Sensors map used in the experiments presented in chapter 3. The near-field acoustic sensors were used to invert rupture velocities and far-field acoustic sensors were used to perform back-projection analysis

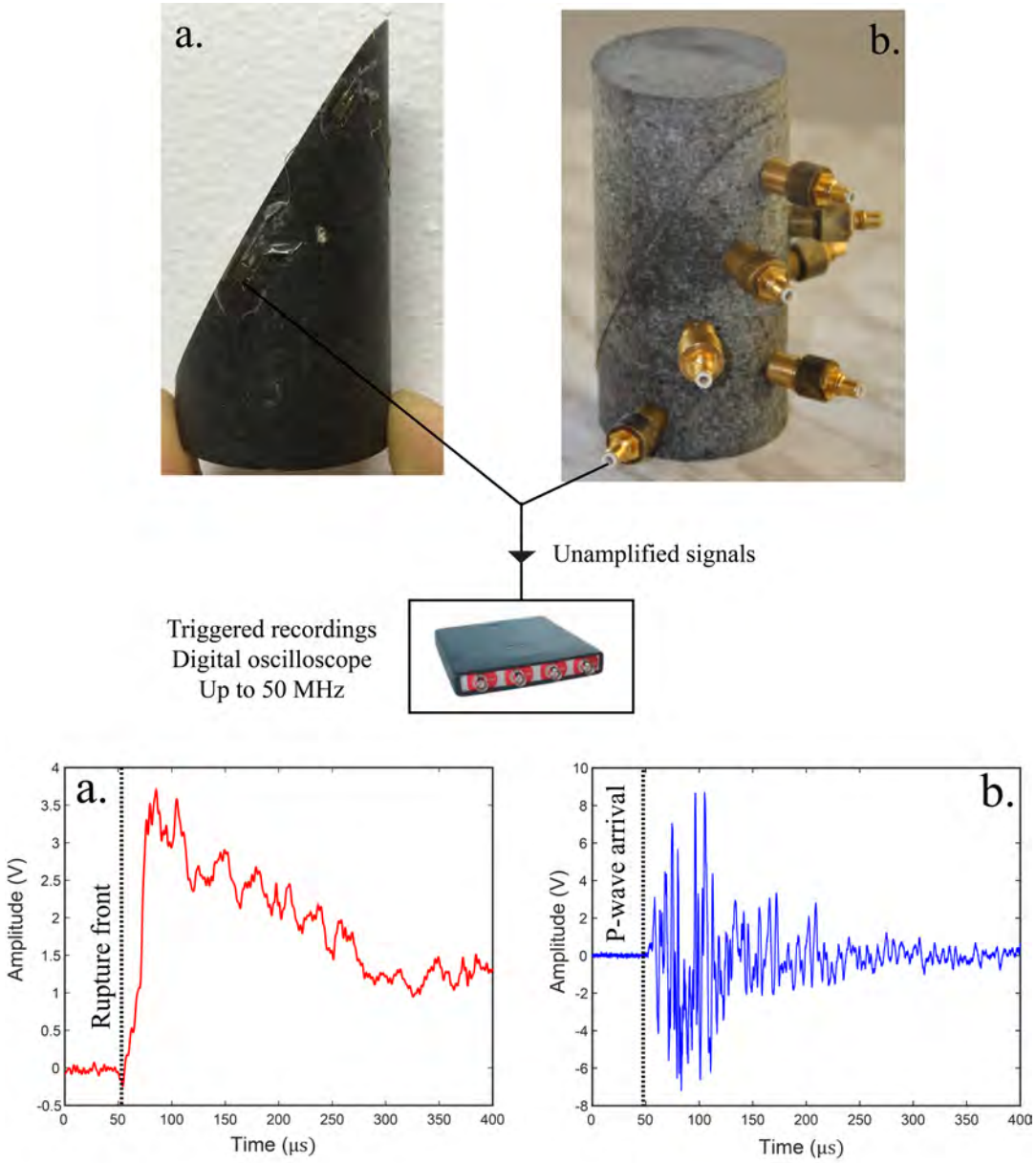

FIGURE 2.7: Triggered recording during stick-slip instabilities. Unamplified signals are digitized using a digital oscilloscope and can be recorded up to 50 MHz sampling rate. **a.** Strain gauge recording during stick-slip instability. The strong increase in voltage corresponds to the rapid unloading of the fault surface during stick-slip instability. The fault is able to slip only after the passage of the rupture front. **b.** Acoustic sensor recording during stick-slip instability. The first P-wave is emitted once the rupture becomes dynamic.

2.2 Acoustic sensors calibration

2.2.1 Experimental procedure

Without additional steps, waveforms recorded by an acoustic sensor have a unit of voltage which limits the information that can be extracted from them. Part of the information is related to the sensor's sensitivity and what a sensor is recording (i.e., a displacement, a velocity or an acceleration) might change depending on the frequency band. During this thesis, we used a lased Doppler vibrometer as a calibration device to convert voltage measurements into velocity measurements. The principle is straightforward. Any signal $S_a(t)$ recorded by an acoustic sensor can be expressed as the convolution of the shape of the source, the response of the medium (i.e. the Green's function or called sometimes the path effect) and the instrumental response. In frequency domain thus,

$$S_a(f) = \Omega(f).G(f).I_a(f) \tag{2.5}$$

Where $\Omega(f)$, $G(f)$ and $I_a(f)$ are respectively the shape of the source, the response of the medium and the instrumental response. In eq. (2.5), the instrumental response is precisely what we are looking for. A laser Doppler vibrometer (called LDV hereafter) measures surface vibration with Doppler effect and its instrumental response is flat (in a certain bandwidth) which means $I_v(f) = 1$. Thus, any signal $S_v(f)$ recorded by a LDV $S_v(f)$ becomes simply:

$$S_v(f) = \Omega(f).G(f) \tag{2.6}$$

It is therefore theoretically easy to obtain $I_a(f)$: one just has to record at the same location a signal emitted by a single source with an LDV and with the acoustic sensor sensor that we want to calibrate and deconvolve one signal from the other:

$$I_a(f) = \frac{S_a(f}{S_v(f)} \tag{2.7}$$

After several trials, the calibrations were performed on one of the half cylinders of a saw-cut sample of Indian Gabbro used during the experiments to be as consistent as possible to experimental conditions. The sample was first fixed to an optical table to filter parasite signals. A broadband transducer was affixed to the center of the fault interface which had been preliminarily rectified to ensure good contact. Using a high frequency generator, an amplified step voltage was applied to the transducer. The vibration of the opposing sample surface was measured at 10 MHz sampling rate by the acoustic sensor in the form of a voltage and relayed to a digital oscilloscope. To make sure that the LDV and the acoustic sensor would sample surface vibrations at the exact same location, the position of the acoustic sensor was pointed by the laser beam. Then the acoustic sensor was removed and the same procedure was

repeated with the LDV which was set to measure particle velocity. Figure 2.8 shows a photograph and a schematic view of the experimental set-up. The acoustic sensor's instrumental response (also called the sensitivity function) was obtained from the ratio between the spectrum of the waveform recorded by the acoustic sensor and the spectrum of the velocity waveform recorded by the LDV. The unity of the sensitivity function is $V/m.s^{-1}$.

2.2.2 Estimation of Fourier spectra

Estimation of Fourier spectra requires some careful precautions. The most common technique to obtain an estimated Fourier spectrum of a time series $x(t)$ is to compute the Fourier transform $X(\omega)$, to multiply it by its complex conjugate and to take the square root of the product. This usually results in noisy spectra and causes spectral leakage. This is due to the fact that the length of a signal is finite which equates to multiplying the signal by a boxcar function (i.e. a rectangular window). The Fourier transform of a boxcar function has multiple side lobes which inherently introduces artificial features. As illustration, figure 2.9 displays spectra estimated from 50 μs long LDV and acoustic sensor waveforms and their ratio which gives the sensitivity function. The variance of the sensitivity function is large which would make its use difficult. One solution to smooth the results is to first multiply the portion of signal that is analysed by a tapering window in the time-domain. There are many possibilities but the idea is to use a tapering window characterized by a Fourier transform with less energy in its side lobes. However, this will reduce spectral leakage but won't affect the variance of the spectrum at each frequency. In order to avoid spectral leakage and to reduce the variance of the results we applied a multitaper approach which was initially proposed by Thomson (1982). Multitapering consists of using a set of different tapering windows which, when combined, minimize the variance and avoid spectral leakage. We describe now the general idea, and refer the reader to Prieto et al. (2007) for a more detailed description.

The estimated spectrum $S(\omega)$ of a signal $x(t)$ which has been multiplied by a window $a(t)$ takes the form :

$$S(\omega) = \int_{-Nyq}^{Nyq} A(\omega').X(\omega - \omega')d\omega' \tag{2.8}$$

The limits of integration correspond to the Nyquist frequency and $A(\omega)$ and $X(\omega)$ are respectively the Fourier transform of the tapering window and the signal (we recall here that a multiplication in time domain is a convolution in frequency domain). We would like to find a set of K tapering windows to create a set of K spectral

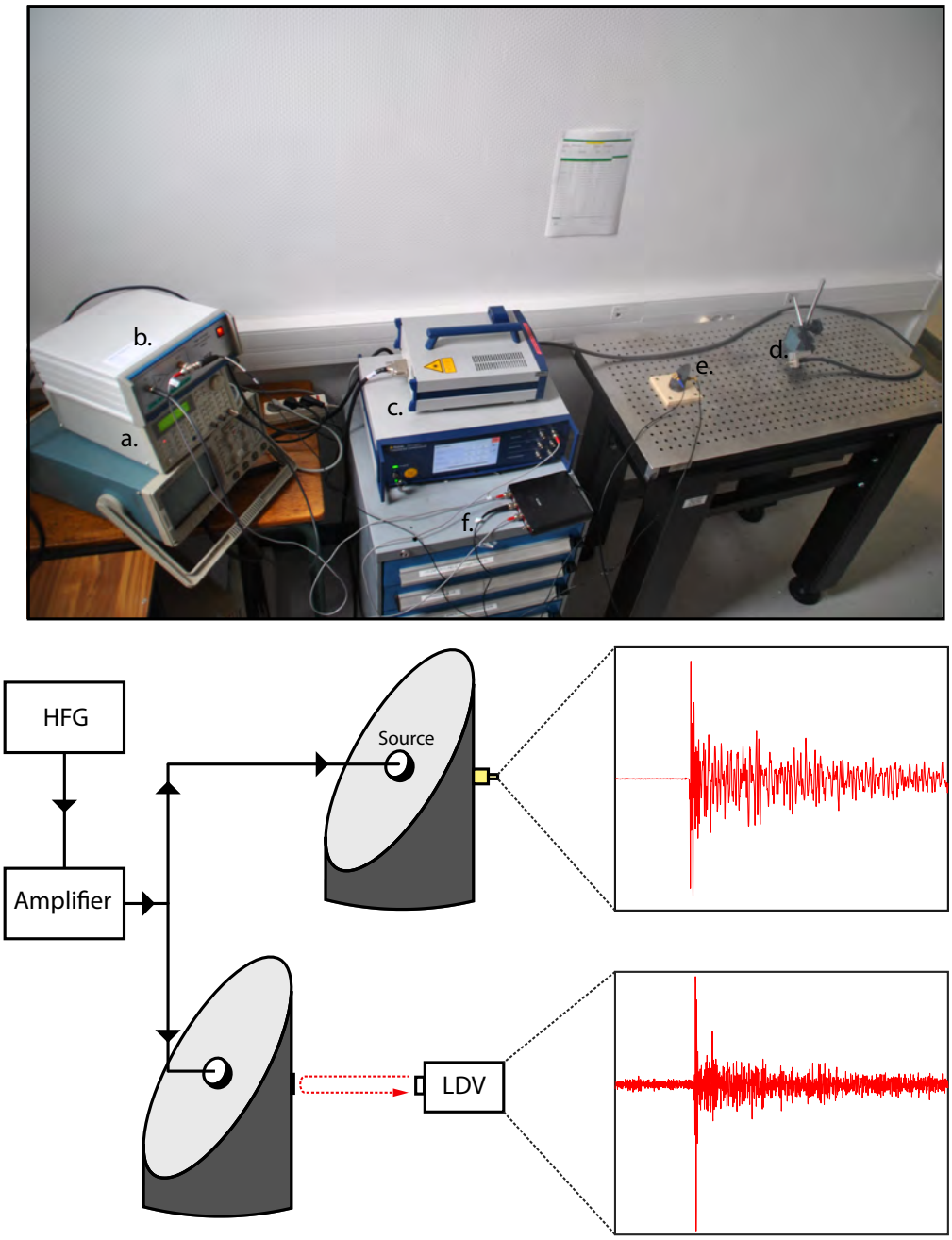

FIGURE 2.8: **Top**. Photograph of the experimental set-up used for acoustic sensors calibration. a. High Frequency Generator. b. Amplifier. c. Laser vibrometer acquisition system. d. Laser beam. e. Rock sample with the acoustic sensor and the source glued on. f. Digital oscilloscope. **Bottom**. Schematic view of the calibration procedure. The source is positioned at the center of the fault and subject to an input voltage. Surface vibrations of the opposing side are recorded by the acoustic sensor first and then by the LDV.

estimates $S_k(\omega)$ that can be used to compute the average spectra $S(\omega)$ as:

$$S(\omega) = \frac{1}{K} \sum_{k=1}^{K} S_k(\omega) \tag{2.9}$$

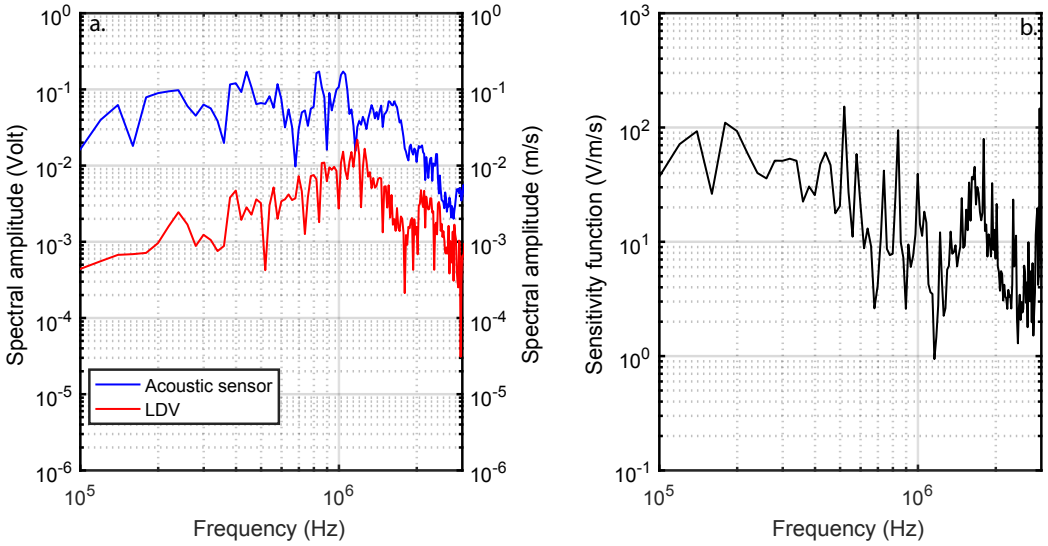

FIGURE 2.9: **a.** Fourier spectra of surface vibration measurements recorded by the LDV and the acoustic sensor. **b.** Sensitivity function obtained by the ratio of the two spectra.

According to eq (2.8), we aim to obtain a tapering window which would have low energy for all frequencies larger than $|\omega - \omega'|$. Such a tapering window will then reduce spectral leakage by having low energy in the side lobes. We would also like to reduce the variance of the spectrum which aims to average the spectrum in a certain bandwidth $(-W, W)$ at each frequency. For a signal of length N, W will necessarily lie between $1/N$ and the Nyquist frequency. The fraction of energy $\lambda(N, W)$ of a tapering window within the bandwidth $(-W, W)$ can be expressed as:

$$\lambda(N, W) = \frac{\int_{-W}^{W} A(\omega) d\omega}{\int_{-Nyq}^{Nyq} A(\omega) d\omega} \tag{2.10}$$

Targeted tapering windows will maximize $\lambda(N, W)$, in other terms solutions are given by:

$$\frac{\partial \lambda(N, W)}{\partial a(t)} = 0 \tag{2.11}$$

Eq. (2.11) corresponds to finding the eigenvalues and the corresponding eigenvectors of (Prieto et al., 2007):

$$[D].a = \lambda a \tag{2.12}$$

Here, D is a NxN symmetric matrix expressed as:

$$D(t, t') = \frac{sin(2\pi W(t - t'))}{\pi(t - t')} \tag{2.13}$$

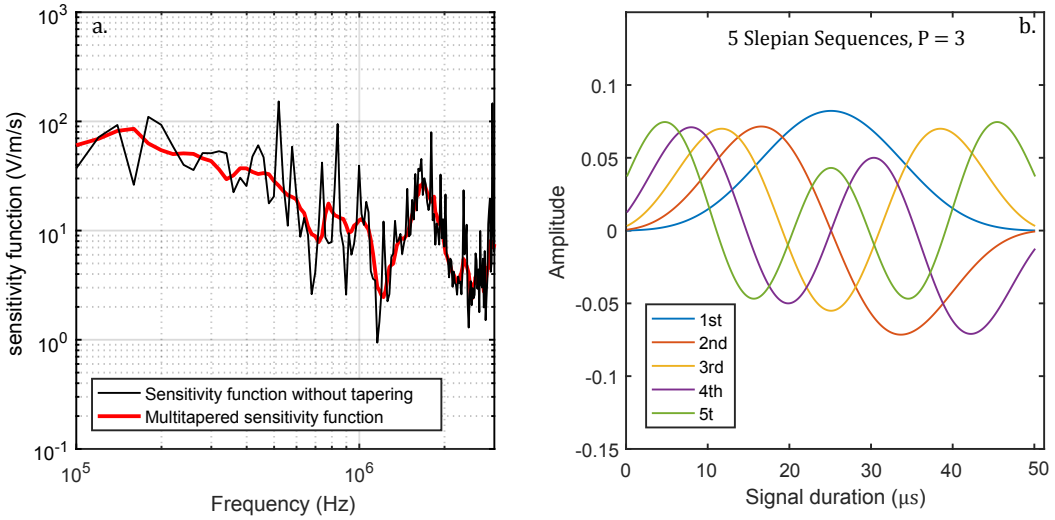

FIGURE 2.10: **a.** Comparison between the sensitivity function estimated without windowing and the sensitivity function estimated from multitapered signals. **b.** First five Slepian sequences used for the multitapering. The total energy corresponding to the area under the curves equals 1.

Solutions are given by N eigenvalues $(\lambda_0, ..., \lambda_{N-1})$ and eigenvectors $(v_0, ..., v_{N-1})$. The eigenvectors v_k are called Slepian sequences (Slepian, 1978) and simply represent N tapering windows. The eigenvalues indicate the energy captured by the eigenvectors (i.e., tapering windows). Minimizing spectral leakage lies in choosing tapering windows that correspond to high eigenvalues while smoothing is controlled by the selected bandwidth W (i.e. the resolution). However, a good balance must be found between the number of tapers and the resolution. Increasing the number of tapers will reduce the variance but will also reduce the resolution. W can be expressed as :

$$W = P/T \tag{2.14}$$

with P the number of points contained in bandwidth W and T the total duration of the signal. All waveforms were analyzed within 50 μs long time window corresponding to 501 data samples. P was set to 3 which yields a reasonable resolution of 60 kHz. For P=3, the 5 first eigenvalues are really close to unity (Park et al., 1987). We therefore used 5 tapers (i.e. Slepian sequences). The tapers are displayed in Figure 2.10 b. Figure 2.10 a shows the comparison between the estimated sensitivity function shown in Figure 2.7 b without and with windowing.

2.2.3 Calibration results

Acoustic emissions will likely result from sources with variable amplitudes and source duration which questions whether the calibration curves can be used for any type of source. We addressed this issue by performing the calibration using two different types of broadband transducers together with changing the amplitude of the step voltage applied to the transducers and its duration. Both transducers, V109-rm

and M110-sm, are broadband panametrics ultrasonic transducers from the Olympus company with a central frequency of 5 MHz. Because the acoustic sensors and the LDV are polarized perpendicular to the sample surface, we have selected ultrasonic transducers that produce compressional waves. The transducer V109-RM has a nominal element size of 13 mm while M110-RM has a nominal element size of 6 mm. The LDV had a flat frequency response up to 2.5 MHz, which therefore gives an upper limit to the calibration range.

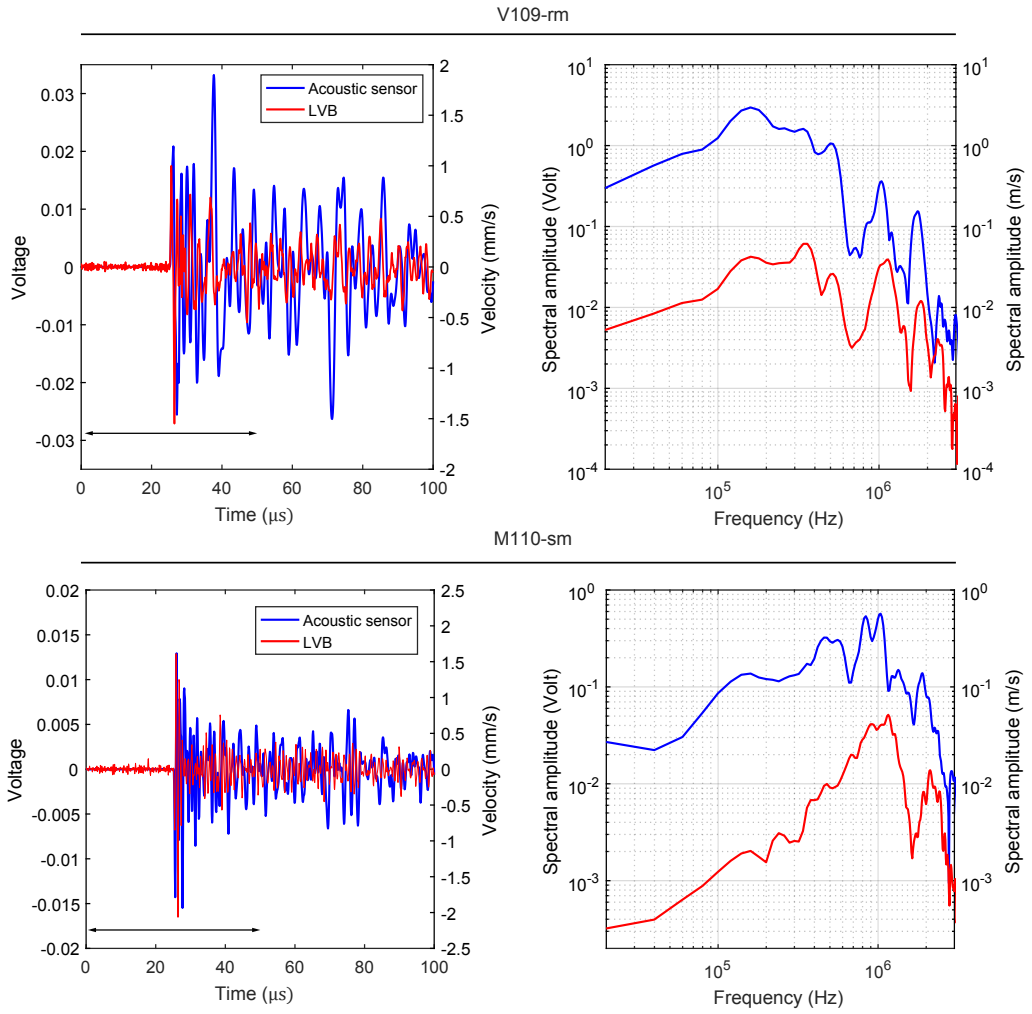

FIGURE 2.11: Example of voltage and velocity measurements for the two types of sources and the estimated spectra. The time window used to estimate the spectra is indicated by the black double arrow. This time window is 50 μs long and is centered pn the first P-wave arrival.

Figure 2.11 shows an example of the waveforms recorded by the LDV and the acoustic sensor with their respective spectra for the two types of sources. The black double arrow indicates the 50 μs long time window used to estimate the spectra. The length

of the time window was chosen according to the one used to estimate acoustic emissions seismological parameters. This is required if we don't want to introduce artificial features when deconvolving acoustic emission spectra of the acoustic sensor's intrumental response. It is interesting to note that the spectra are really different with respect to the source. The source M110-sm shows a spike of energy centered around 1 MHz while the source V109-rm generated more energy at lower frequencies. This is convenient because it offers a path to judge of the robustness of the calibration results relative to the frequency content of the source. Moreover, both types of sources have produced sufficiently high-frequency energy to confirm that the acoustic sensors are sensitive to frequencies up to at least 2.5 MHz.

Figure 2.12 summarizes the calibration results that we obtained. The calibration curves were reproduced for two input voltages, 40 V and 200 V and with three source durations, 2 μs, 1 μs and 0.5 μs (i.e. 0.5 MHz, 1 MHz and 2 MHz). For the same type of source we observed no significant differences with respect to the input voltage and its duration. All calibration curves almost collapse (Figures 2.12 a, b). The figure 2.12 c, displays the sensitivity function averaged over all input voltages and source durations for both transducers. In both case, it is clear that the sensitivity of the acoustic sensors shows non linearity, with a large band of resonance between about 1.2 and 2.2 MHz. This might be related to the specific properties of the PZT ceramics. Above 1 MHz, wavelengths are of the order of few millimeters which lies in the range of the length scales that characterize the acoustic sensor casing. This could also induce strong sensitivity variations at high-frequency. Although the sensitivity functions are quite similar up to 1 MHz, some differences emerge when increasing the frequency. In the case of the larger source, V109-rm, the resonance band is narrower and the sensitivity function decreases to a lower value after the maximum peak. A larger source size is equivalent to the multiple point source scenario that would generate waves at the same time. This might reduce the curvature of the wavefronts and induce negative interferences with increasing frequency. Although the sources of acoustic emissions may cover different sizes, we assume the synchronized multiple point source scenario to be unlikely. For this reason we chose to use the sensitivity function obtained in the case of the smaller source, M110-sm.

2.3 Acoustic data treatment

2.3.1 Acoustic emissions detection

Acoustic emissions generated during the experiments were obtained from the continuous acoustic waveforms (Figure 13). The first step was to set an amplitude threshold for each channel (i.e. for each acoustic sensor) according to the signal to noise ratio of the latter. Then, acoustic emissions were searched within the continuous waveforms by using a 406.9 μs sliding time window with 102.4 μs overlap. Time

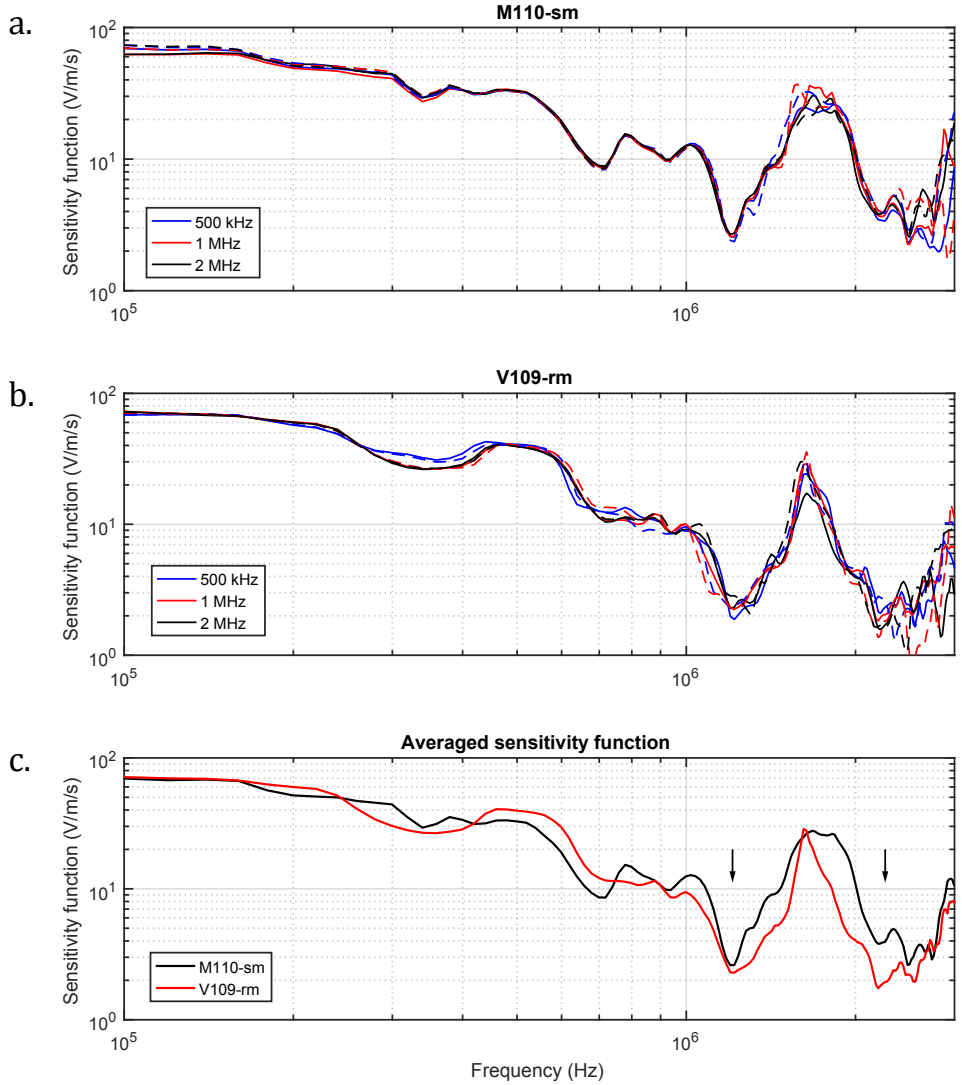

FIGURE 2.12: Calibration curves. **a.** Sensitivity functions corresponding to the source M110-sm. The dashed lines indicate the calibration curves obtained for an input voltage of 40 V and the solid lines for an input voltage of 200 V. **b.** Same as **a.** but for the source V109-rm. **c.** Comparison of the sensitivity function averaged over all input voltages and source durations. Acoustic sensors have a net non linear instrumental response showing a large resonance band between 1.2 *MHz* and 2.2 *MHz* (delimited by the two black arrows)

window overlap guarantees in part the separated detection of events that would happen close in time. If in a same time window 3 or more channels had recorded an amplitude higher than their respective threshold, the corresponding portion of the continuous waveforms were saved for all channels. As we wanted to record as much acoustic emissions as possible, the amplitude thresholds used were close to the noise level. Therefore, we visually checked all the saved waveforms to sort between acoustic emissions and noise.

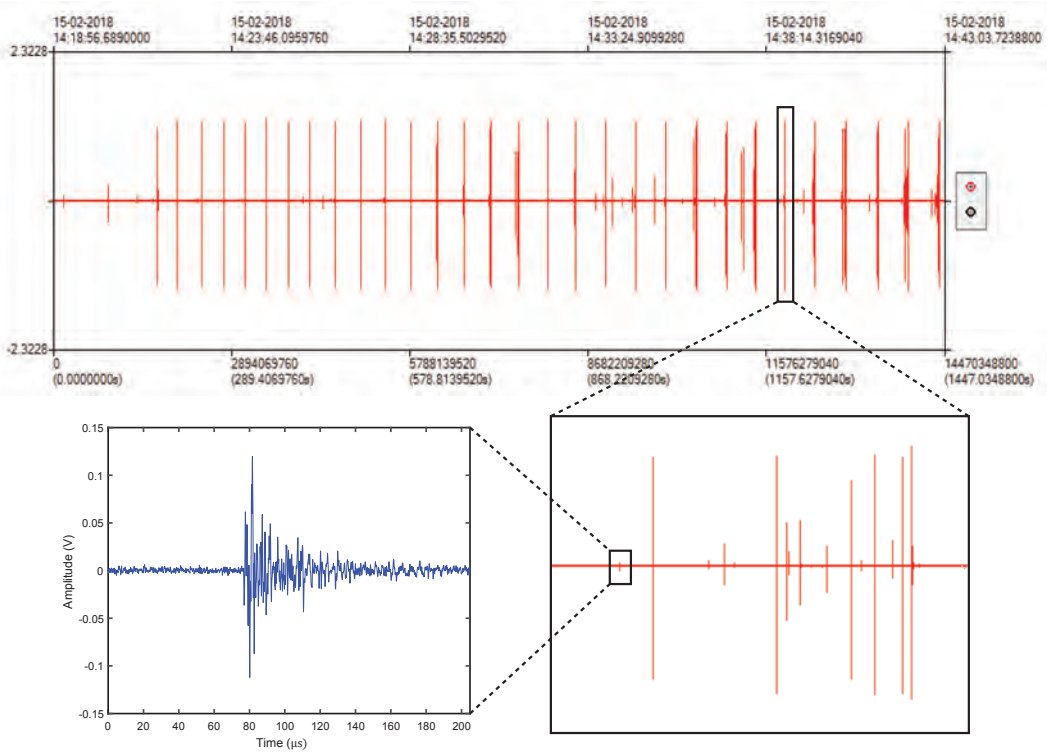

FIGURE 2.13: **Continuous recording.** On top is displayed an example of the total duration of one continuous acoustic recording. The large and regular spikes correspond to the stick-slip events. Close to failure (bottom right), microseismicity rate is increasing. Acoustic emissions (bottom left) are searched within the continuous waveform using a 406.9 μs long sliding time window.

2.3.2 Auto-picking

Acoustic emissions and stick-slip nucleation were located according to first P-wave arrival times. First P-wave arrival times were automatically picked using the software Insitelab. This software allows us to use different methods. The auto-picking was achieved using the RMS amplitude method. The RMS auto-picking algorithm operates by first calculating an auto-picking function using a moving time window approach. At each waveform data point i, two windows are generated: a front window and a back window. The auto-picking function F_i is calculated by:

$$F_i = \frac{\sum_{j=i+1}^{i+FW} A_j^2}{\sum_{j=i-1}^{i-BW} A_j^2} \tag{2.15}$$

where FW is the length of the front window, BW the length of the back window and A_j the amplitude of the signal. The auto-picking function thus computes the ratio of the energy contained in the front window to the energy contained in the back window. Peaks occur in the function when waveform amplitude suddenly increases. P-wave arrival times can be estimated by setting a threshold amplitude to the auto-picking function (Figure 2.14). The RMS algorithm works quite well for impulsive signals with high signal to noise ratios. However, for low amplitude signals significant errors were often observed. We tried other techniques such as the STA/LTA, analytic envelop and kurtosis methods. All these methods require specific parameters which might be right for one event or one channel but not for another. Therefore, all picking results were visually inspected and modified if necessary.

2.3.3 Localization

Acoustic emissions and stick-slip nucleation were localized according to first P-wave arrival with $0.1\mu s$ resolution. Possible positions were restricted to the fault plane which is a reasonable assumption. Let (X_i, Y_i, Z_i) indicate the spatial coordinates of a position onto the fault plane and (X_s, Y_s, Z_s) the spatial coordinates of the acoustic sensors. Over many stick-slip cycles waves velocity might vary slightly. For this reason we used a "double difference" algorithm to locate acoustic emissions or stick-slip nucleation. Acoustic emissions and nucleation positions were obtained by minimizing the L2 norm (least-square) of the sum of the differences between observed and theoretical arrival time differences of all possible pairs of acoustic sensors. This is mathematically expressed as :

$$\Delta t(C_p, i) = \sum_{cref=1}^{n} \sum_{c \neq cref}^{n-1} \frac{\sqrt{(\Delta t^{obs}_{cref,c,i} - \Delta t^{t}_{cref,c,i})^2}}{n(n-1)} \tag{2.16}$$

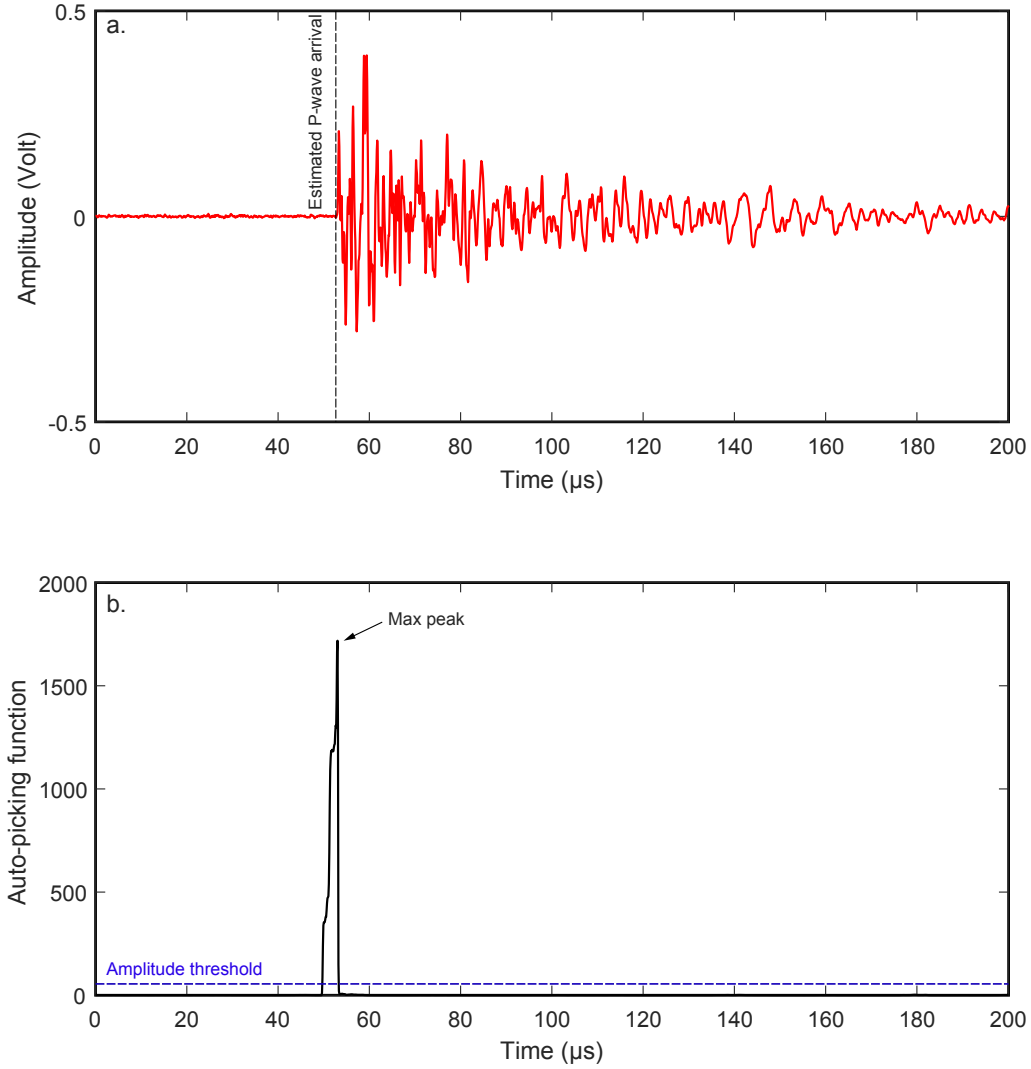

FIGURE 2.14: **a.** Typical acoustic waveform. The estimated first P-wave arrival time is indicated by the black dashed line. **b.** Auto-picking function amplitude. In this example the amplitude threshold was set to 50, the length of the back-window and of the front-window were 10 μs and 3.5 μs respectively. The picked P-wave arrival time was set to the maximum peak amplitude.

where C_p is the P-wave velocity and with:

$$\Delta t^t_{cref,c,i} = (t_{i,cref} - t_{i,c}) \tag{2.17}$$

Theoretical travel times $t_{i,c}$ are calculated by the expression :

$$t_{i,c} = \frac{\sqrt{(X_i - X_c)^2 + (Y_i - Y_c)^2 + (Z_i - Z_c)^2}}{C_p} \tag{2.18}$$

2.4 Seismic source characterization

2.4.1 Rupture velocity inversion

In this section, we explain the method that we used to estimate rupture velocities during laboratory earthquake. This method is related to chapter 4.
Cracks produce a strain concentration at their edges. If positioned close enough to the fault, acoustic sensors are able to record the passage of the rupture front (Schubnel et al., 2011; Passelègue et al., 2013). For convenience, let us call the acoustic sensors positioned close to the fault, near-field acoustic sensors (Figure 2.7 b.). Rupture velocities during stick-slip instabilities are then simply obtained by searching the rupture velocity V_r that best explains observed arrival times of the rupture front by near-field acoustic sensors.
As mentioned in the introduction, ruptures can propagate according to three different modes. Due to the relatively high normal stress conditions, mode I is disregarded. During stick-slip instabilities, the displacement can be considered to be parallel to the shear traction direction. Therefore, the rupture propagates in mode II (in-plane) along the slip direction and in mode III (anti-plane) in the direction perpendicular to it. This implies that the rupture velocity will be limited to the P-wave velocity C_p along fault length and by the S-wave velocity C_s along the fault width. For sub-Rayleigh ruptures, $V_r \leq C_s$ we assume a circular self-similar rupture (i.e. V_r is the same in all directions). For supershear ruptures, $C_s \leq V_r \leq C_p$ along the fault length and $V_r = C_s$ along the fault width, therefore we assume an elliptical self-similar rupture.
The first step is to localize the initiation of the nucleation according to observed P-wave arrival times. Let's $(X_{nuc}, Y_{nuc}, Z_{nuc})$ be the spatial coordinates of the nucleation and (X_{nf}, Y_{nf}, Z_{nf}) the spatial coordinates of the near-field acoustic sensors. Theoretical rupture front arrivals $t^t(nuc, nf)$ are calculated as follow:

$$t^t(nuc, nf, V_r) = \frac{\sqrt{(X_{nuc} - X_{nf})^2 + (Y_{nuc} - Y_{nf})^2 + (Z_{nuc} - Z_{nf})^2}}{\sqrt{C^2_{III} cos(\theta) + C^2_{II} sin(\theta)}} \tag{2.19}$$

For sub-Rayleigh ruptures, $C_{III} = C_{II} = V_r$ with $V_r \leq C_s$ and for supershear ruptures, $C_{II} = V_r$ with $C_s \leq C_{II} \leq C_p$ and $C_{III} = C_s$. θ defines the angle between the

rupture front propagation direction and the in-plane direction. The rupture velocity is obtained by minimizing the residual time $\Delta t(nuc, V_r)$ between observed rupture front arrival times and theoretical ones such as:

$$\Delta t(nuc, V_r) = \frac{\sum_{k=1}^{n} \sqrt{(t^{obs}(nuc, nf, V_r) - t^{t}(nuc, nf, V_r))^2}}{n} \tag{2.20}$$

with n the total number of near-field acoustic sensors.

2.4.2 The back-projection method

Here, we describe the method used to image high-frequency sources during rupture propagation. This method is related to chapter 4.
After its most succsessful application to the Mw 9.3 Sumatra Andaman earthquake in 2004 (Ishii et al., 2005) back-projection became a technique commonly used to study earthquake dynamics. This technique takes advantage of large and dense seismic arrays to spatially and temporally track the seismic source(s) during an earthquake. The back-projection method takes recorded seismograms and propagate their waveforms backward in time so they constructively interfere at the source origin time and at the source location (Ishii, 2011). Back-projection does not require any knowledge of the Green's function of the medium because it does not seek to compute synthetic seismograms. Only the time and location of the hypocenter, a velocity structure model and a grid of potential sources are required. Applying the back-projection at the laboratory scale has two key advantages : the fault plane and the velocity structure are well constrained.
The first step is to divide the fault plane into a grid of potential source points and to compute the theoretical P-wave travel times from each potential source to each acoustic sensor used for the analysis. We assume the medium as isotropic and homogeneous so that the P-wave velocity is the same in all directions. According to P-wave travel times, waveforms are then synchronized and stacked at each grid point. At a position i, at a time t with respect to nucleation initiation, the stacked waveform $s(t)$ takes the form:

$$s_i(t) = \frac{1}{k} \sum_{n=1}^{k} w_n u_n(t + t_{i,n} + \Delta t_n) \tag{2.21}$$

where k is the total number of acoustic sensors, $u_n(t)$ the recorded acoustic waveforms by the $n'th$ acoustic sensor, $t_{i,n}$ the predicted P-wave travel time between the $i'th$ grid location and the acoustic sensor n and Δt_n the time correction of the $n'th$ acoustic sensor that we obtain by cross-correlating the initial few μs of each acoustic waveform with a reference waveform. Δt_n ensures that all waveforms align well at the nucleation location. The stacked waveform $s(t)$ has the weighting factor $w_n = p_n / A_n$ with p_n that corrects for first P-wave polarity (either equals to -1 or 1) and A_n a normalization factor equals to the ratio between the maximum absolute

amplitude of the reference acoustic sensor and the maximum amplitude of the $n'th$ acoustic sensor so that no single waveform dominates the stack. For a given time, acoustic waveforms should coherently stack at the true location of the source and the stack amplitude should be high (Figure 2.15).
This approach has however the disadvantage that it relies on the amplitude of waveforms to retrieve energy source locations, hence strong energy sources can significantly obscure weak energy sources. Rather than relying on stacks we prefer to use the coherency function introduced by Ishii (2011). At a time t, the coherency function $x_i(t)$ at the position i is expressed as:

$$x_i(t) = \frac{1}{k}\sum_{n=1}^{k} \frac{p_n \sum_{t+T}^{\tau} u_n(\tau + t_{i,n} + \Delta t_n).s_i(\tau)}{\sqrt{\sum_{t+T}^{\tau} u_n^2(\tau + t_{i,n} + \Delta t_n)}\sqrt{\sum_{t+T}^{\tau} s_i^2(\tau)}} \tag{2.22}$$

The coherency function quantifies the average cross correlation over a time window T of the stacked waveform and each individual acoustic waveform. It reflects the energy radiated over the time window T as a function of space and time and has the advantage to rely on waveform similarity and not on waveform amplitudes.
The back-projection technique was applied using the set of sensor defined as « far-field sensors » (Figure 2.7 b.).

2.4.3 Inversion of AE paramameters

Seismic parameters estimation relies on the analysis of displacement spectra to estimate the absolute magnitude of the source, its size and stress-drop. Because we expected that most of the energy would come from S-waves, the seismological parameters were obtained based on S-wave displacement spectra.
Acoustic waveforms were analysed within a 27.5 μs time window occuring 2.5 μs before the theoretical S-wave arrival times. The energy contained between the beginning of the selected time-window and the S-wave arrival was damped with a ramp function to reduce energy related to P-waves. The selected time window was then rescaled to a 50 μs time window centered to the theoretical S-wave arrival and multiplied by a von Hann window (Figure 2.13 b). This allows us to lower energy contributions coming from reflections and surface waves. We obtained S-wave displacement spectra $\Omega_s(\omega)$ by first averaging over all acoustic sensors the spectra corrected by deconvolution with the estimated sensitivity function $S_f(\omega)$. The final displacement spectra were then obtained by integration in frequency domain (a simple factorisation). This takes the form:

$$\Omega_s(\omega) = \frac{\sum_{k=1}^{K} S_k^{as}(\omega)}{K.S_f(\omega)}.\frac{1}{2\pi\omega} \tag{2.23}$$

where K corresponds to the total number of acoustic sensors and $S_k^{as}(\omega)$ to the spectrum of the $k'th$ acoustic waveform. The next step was to fit the S-wave displacement

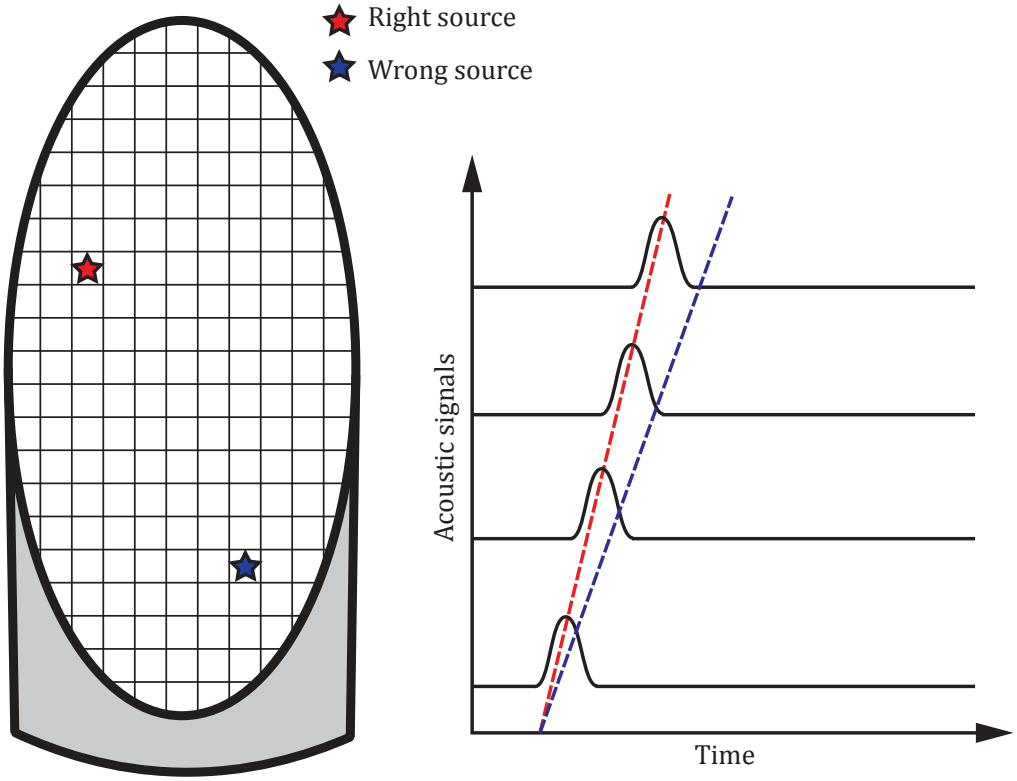

FIGURE 2.15: Schematic view of the back-projection stacking procedure. The fault interface is divided into a grid of source points. Acoustic signals represent what would record 4 acoustic sensors. According to theoretical first wave arrivals, zones of energy release will result in coherent, large amplitude stacks which is shown by the intersection of the dashed red line and the schematic acoustic waveforms.

spectra with a Brune model (Brune, 1970) corrected for attenuation. The S-wave displacement specta $\Omega_s(\omega)$ were modelled as:

$$\Omega_s(\omega) = \Omega_0 \exp^{(-\pi\omega t/Q)} . \frac{1}{1 + (\omega/\omega_c^2)} \tag{2.24}$$

where Ω_0 is the long period spectral plateau, t is the averaged S-wave travel time, Q the attenuation factor and ω_c the corner frequency. Ω_0, ω_c and Q were estimated by performing a grid search over the three parameters. Here, Q is an important parameter because it controls the high-frequency decay together with the corner frequency ω_c. Therefore, to avoid significant trade-offs between Q and f_c we limited Q search from 30 to 50 based on values found in the literature (Goldberg et al., 1992; Liu and Ahrens, 1997; Yoshimitsu et al., 2014). Search ranges were from 10^{-18} to 10^{-15} $m.s$ for Ω_0 and 100 kHz to 2.5 MHz for ω_c. The seismic moment was computed from Ω_0 according to:

$$M_0 = \frac{4.\pi.\rho.C_s.R.\Omega_0}{\Lambda_{\theta,\phi}} \tag{2.25}$$

where ρ is the density, C_s the shear wave velocity, R the averaged distance and $\Lambda_{\theta,\phi}$

the averaged S wave radiation pattern (0.63, Richards and Aki, 1980). From M_0 we obtained the absolute moment magnitude as:

$$M_w = (log10(M_0) - 9.1)/1.5 \tag{2.26}$$

Assuming the circular crack model of Madariaga (1976), the estimated corner frequency provided the radius of the source according to:

$$r = \frac{0.21.C_s}{\omega_c} \tag{2.27}$$

Finally, the stress drop $\Delta\sigma$ was computed as a function of the seismic moment and the radius of the source such as (Eshelby, 1957):

$$\Delta\sigma = \frac{7M_0}{16r^3} \tag{2.28}$$

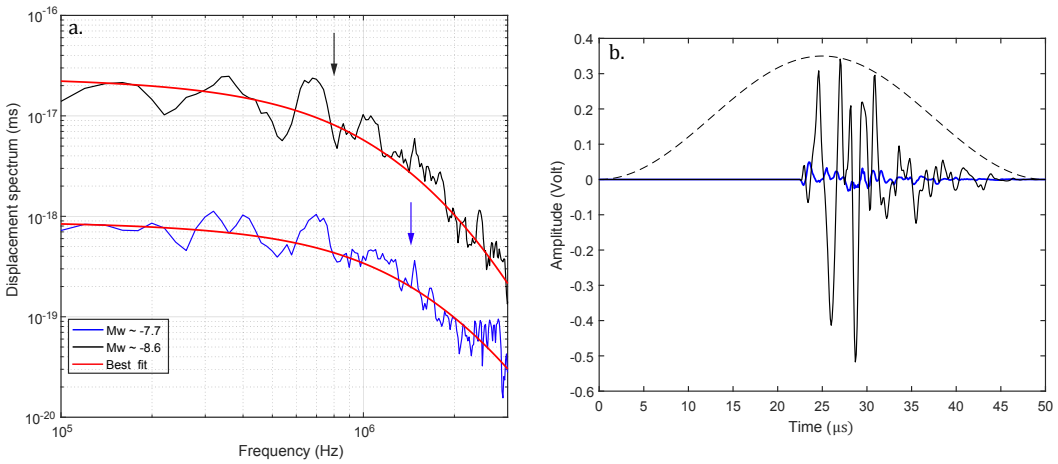

FIGURE 2.16: Fitted displacement spectra and acoustic waveforms. **a.** Displacement spectra and best fit for $Mw - 7.7$ and $Mw - 8.6$ events with their respective estimated corner frequencies indicated by the arrows (0.88 MHz and 1.5 MHz, respectively). **b.** Corresponding waveforms used to estimate the spectra, the color code is the same than in **a.**. Waveform amplitudes were multiplied by a factor two for visualization. The black dashed line indicates the von Hann window used to taper the waveforms.

The Figure 2.16 a displays an example of fitted displacement spectra for two events of magnitudes $Mw - 7.7$ and $Mw - 8.6$ and the associated waveforms. Corner frequencies were found to be 0.88 MHz and 1.5 MHz, respectively, which yield source radius of the order of 0.8 mm and 0.45 mm respectively. Estimated stress drops are approximately 0.75 MPa for the Mw -8.6 event and 3.35 MPa for the Mw -7.7 which is in the range of those observed for natural earthquakes. The absence of the resonance band in the displacement spectra confirms in part that the sensitivity function was well estimated.

Chapter 3

Foreshocks occurence and their link to nucleation: an experimental approach

3.1 Introduction

The term "foreshocks" refers to small earthquakes that would occur nearby in the time and space of a larger earthquake to come. In 1973, Papazachos (1973) made the observation that when a sufficient number of foreshock sequences were synchronized to the time of their respective mainshock and then stacked, the seismicity rate increases as an inverse power law of the time to the mainshock. This law called "the inverse Omori law" had then provided a potential path to earthquake prediction. Since that time, most efforts have been made to understand the driving forces of foreshocks occurence.

Upper crustal earthquakes are dynamic instabilities which result from the weakening of frictional properties of a seismogenic fault that has started to slip. Earthquake nucleation processes are characterized by constitutive laws that describe the evolution of friction with slip. Based on either slip weakening or rate and state friction laws, theoretical (Ida, 1972; Campillo and Ionescu, 1997; Uenishi and Rice, 2003) and numerical models (Rubin and Ampuero, 2005; Ampuero and Rubin, 2008) have demonstrated that before propagating dynamically, slip initially develops on a localized, slowly growing zone, which is defined as the nucleation zone. A large number of stick-slip experiments have supported this conceptual view of earthquake nucleation, whether it is for experiments conducted at low normal stress conditions on synthetic materials (Latour et al., 2013; Nielsen et al., 2010) and on crustal rocks (Okubo and Dieterich, 1984; Ohnaka and Kuwahara, 1990; Ohnaka, 2003; McLaskey and Kilgore, 2013; Fukuyama et al., 2018).

Although rupture nucleation is a process thought to be aseismic, laboratory friction experiments (Thompson et al., 2009; McLaskey and Lockner, 2014; Kwiatek et al., 2014; Passelègue et al., 2017) have found the acoustic emission (AE) rate to be correlated to aseismic slip propagation and have reinforced the possibility of earthquake forecasting. Experimental works have also investigated changes in the frequency-magnitude distribution (i.e. the b-value of the Gutenberg-Richter slope) of AEs during stick-slip cycles. When the shear stress increases and the rupture is developing, a significant drop of the b-value has been reported, i.e. the ratio between large and small AEs increases (W. Goebel et al., 2013; Rivière et al., 2018; Lei et al., 2018). This was thought to be driven by accelerating slip before dynamic rupture propagation. Consequently, this indicates that b-value changes could be used as a tool for seismic hazard assessment. However, under the assumption that foreshocks only reflect nucleation processes, it is necessary to constrain the length and time scales over which earthquakess nucleate.

Rate and state models that use friction parameters of laboratory experiments predict the nucleation zone to be of the order of meters and to expand over the last millisecond prior to dynamic rupture propagation (Lapusta and Rice, 2003; Kaneko and Lapusta, 2008; Fang et al., 2010). This is a consequence of the characteristic slip distance D_c (i.e. the length required for the friction to reach its residual value inferred from rock friction experiments being of the order of 1-100 μm. In the former case, it would be almost impossible to detect earthquakes nucleation from geodetic of seismological measurements. On the other hand, seismological observations have suggested that D_c should be scale dependent (Ide and Takeo, 1997; Olsen et al., 1997), of the order of the centimeter at the scale of crustal earthquakes. The scaling of D_c has been attributed to length scales inherent to the size of earthquakes such as long wavelength roughness of fault zones (Ohnaka, 2003) or gouge thickness (Marone, 1998). If we consider that the critical slip distance involved during coseismic slip is the same that governs earthquake nucleation (see Cocco et al., 2009 for discussion), this would imply nucleation processes to happen at much larger length and time scales.

At the scale of crustal earthquakes, numerous seismological observations have reported on increasing foreshock activity preceding the occurrence of large earthquakes (Jones and Molnar, 1976; Abercrombie and Mori, 1996; Bouchon et al., 2011; Kato and Nakagawa, 2014). Foreshock activity preceding large subduction earthquakes has been found to correlate with the occurrence of slow slip transients in the region close to the hypocenter (Kato et al., 2012; Ruiz et al., 2014). When examining the occurrence of foreshock sequences with respect to the geodynamic context, it has been demonstrated that faults subject to high-slip rates produce more foreshock sequences (McGuire et al., 2005; Bouchon et al., 2013). Moreover, compared

with the ordinary seismicity, foreshocks present singular characteristics such as migration and acceleration prior to the mainshock (Marsan et al., 2014; Kato et al., 2016). Therefore, it has been argued that foreshocks are a by-product of the larger nucleation of the upcoming mainshock. However, because of the sparsity of the observations, the physical processes that govern the occurrence of foreshocks are still controversial. For instance, statistical ETAS models (Ogata, 1988; Helmstetter and Sornette, 2003b) are able to reproduce most of the features attributed to foreshock sequences which was used as an argument to suggest that foreshocks reflect stochastic rather than physical processes. One of the underlying questions is whether or not the earthquakes dynamically propagate following the slow propagation phase of the nucleation zone or start as small dynamic instabilities that rapidly grow into a larger one. These two opposite views are termed the "preslip" and the "cascade" models respectively (Ellsworth and Beroza, 1995; Beroza and Ellsworth, 1996). In the latter scenario, the use of foreshocks as a predictive tool for the occurrence of a larger earthquake would be compromised.

Here we report on precursory AE sequences prior to stick-slip instabilities. The purpose of this study is to use generated precursory AEs as a proxy to investigate the mechanisms that control foreshocks dynamics.

3.2 Experimental set-up and methodology.

Here, we briefly describe the experimental set-up that we used to produce stick-slip events (SSEs) and the methods used to analyse and process the data.

Stick-slip experiments were conducted on saw-cut samples of Indian Gabbro under tri-axial conditions. The tri-axial apparatus used is described in details in section 2.1.2. Saw cut samples were axially loaded by injecting oil at a constant rate in the piston chamber. Strain rate was imposed at about 4.10^{-6} (about 0.02 MPa/s). Pressure sensors positioned outside of the cell allowed us to measure the axial stress and the confining pressure from which we calculated the average macroscopic shear stress, the macroscopic normal stress and the friction coefficient acting onto the fault plane (section 2.1.2). Displacement was measured by an LVDT at the top of the axial piston and thus includes the elastic shortening of the whole system (i.e. apparatus + sample). Along fault displacement was calculated by correcting the overall displacement from the elastic shortening of the axial piston and the sample (section 2.1.2). Stresses and displacement were measured at 10 Hz sampling rate with respectively $\pm$ 0.001 MPa resolution and $\pm$ 0.1 μm of resolution.

The acoustic wave-field was continuously recorded at 10 MHz sampling rate by 8 acoustic sensors whose positions are given in figure 2.7. AEs were detected within

the continuous acoustic waveforms (see section 2.3.1). Note that we opted to position all the acoustic sensors on the same half of the sample so their relative positions do not change with cumulative displacement. Acoustic signals were amplified at 45 dB, i.e. by a factor of about 177. This allowed us for recording the microseismicity close to the noise level. Local strain measurements were also continuously measured at 10 MHz sampling rate by 8 single component strain gauges located on both sides of the fault (section 2.1.3). It should be noted that here we only focus on acoustic measurements, strain gauges data will be further analyzed in a future study.

AEs locations were inverted according to first P-wave arrival (section 2.3.3). We made the assumption that AEs all came from the fault (i.e. 2-D grid search) which seems a reasonable assumption given that (i) by localizing AEs with a 3-D grid search we found that AE locations align with the fault plane and (ii) we often observed positive and negative first P-wave polarities (expected for AEs located at one edge of the fault plane) which indicates double-couple seismic sources. The smallest AEs could not be located due to their first P-wave arrivals really close to the noise level and not easily distinguishable. The location procedure was thus restricted to AEs with sufficiently high-amplitude and impulsive first P-wave arrivals.

Finally, we converted voltage waveforms into an absolute velocity measurements using the calibration curves (see section 2.2.3), which allowed us for computing the displacement spectra of the AEs. The seismic moment and the corner frequency of the AEs were estimated by fitting their displacement spectra with a Brune model (see section 2.4.3). From the seismic moment and the corner frequency, we obtained the source dimension and the stress drop.

For the sake of clarity we explain here the next term that will come up frequently in this chapter: "Normalized time to failure". The normalized to failure refers to the time prior to failure divided by the total duration of loading.

3.3 Results

3.3.1 Mechanical data

Three experiments were performed at varying confining pressures, P_c: 30, 45 and 60 MPa. The figures 3.1 a, b and c display the evolution of shear-stress, along fault cumulative displacement and AE rate at P_c = 30, 45, 60 MPa respectively.

At $P_c = 30$ MPa (Figure 3.1 a) we have reproduced a sequence of 55 stick-slips. The first one occurred when the macroscopic shear-stress was about 22 MPa, this equates to a static friction coefficient of 0.5. 'The associated coseismic displacement was 31

μm. From the beginning to the end of the experiment, the maximum shear-stress (i.e. the shear stress at the time of the rupture) has increased from 22 to 36 MPa which corresponds to an increase of the static friction coefficient from 0.5 to 0.7. Although the static friction coefficient continuously increased with successive stick-slips, it started to stabilize after approximately 5 mm of cumulative displacement. At the beginning of the experiment we recorded only few AEs in the last second prior to dynamic rupture propagation. This can be observed by the relatively low acoustic activity that only arises close to stick-slip instabilities. Then, up the to the end of the experiment, the acoustic activity intensified. One interesting feature is that the acoustic activity started to occur earlier but at a lower rate when the static friction coefficient started to stabilize.

At $P_c = 45$ MPa (Figure 3.1 b) we have reproduced a sequence of 29 stick-slips. The mechanical behavior of the rock specimen has shown some similarities with the one at $P_c = 30$ MPa. The first stick-slip occurred at relatively low stress conditions, when the shear stress was about 32 MPa which corresponds to a static friction coefficient of 0.5. The corresponding coseismic displacement was 58 μm. Then the maximum shear stress has increased from 32 to 51 MPa which equates to an increase of the static friction coefficient from 0.5 to 0.68. Quite remarkably, similarly to the experiment at $P_c = 30$ MPa the static coefficient of friction has approximately stabilized after 5 mm of cumulative displacement. Regarding the acoustic activity, the AE rate has rapidly increased with the successive stick-slip cycles. However a noticeable difference with the experiment conducted at $Pc = 30$ MPa is that the AEs remained concentrated in the last 2-3 seconds prior to stick-slip instabilities.

At $P_c = 60$ MPa (Figure 3.1 c) we have reproduced a sequence of 13 stick-slips. The mechanical behavior of the sample has shown significant differences with the experiments at $P_c = 30$ MPa and $P_c = 45$ MPa. The first stick-slip happened when the shear stress reached 64 MPa and the static friction coefficient 0.65. The corresponding coseismic slip was 184 μm. After the first stick-slip, the static friction coefficient oscillated between 0.65 and 0.72 and was almost constant for the last 5 SSEs. The AE rate has largely fluctuated from the beginning to the end of the experiment. Prior to particular SSE (SSEs 9 and 13 for instance) we recorded intense bursts of AEs while for other SSEs the AE rate preceding failure was really low (SSEs 11, 12 and 13). AEs mostly happened during the last 1-2 seconds prior to failure.

3.3.2 AEs distribution

The figure 3.2 displays the number of precursory AEs recorded (left) and the total AE moment release (right) per SSE. The total AE moment that we show here is likely to be underestimated for particular SSE because acoustic sensor recordings started to saturate for moment magnitudes M_w higher than -7, although for such a magnitude

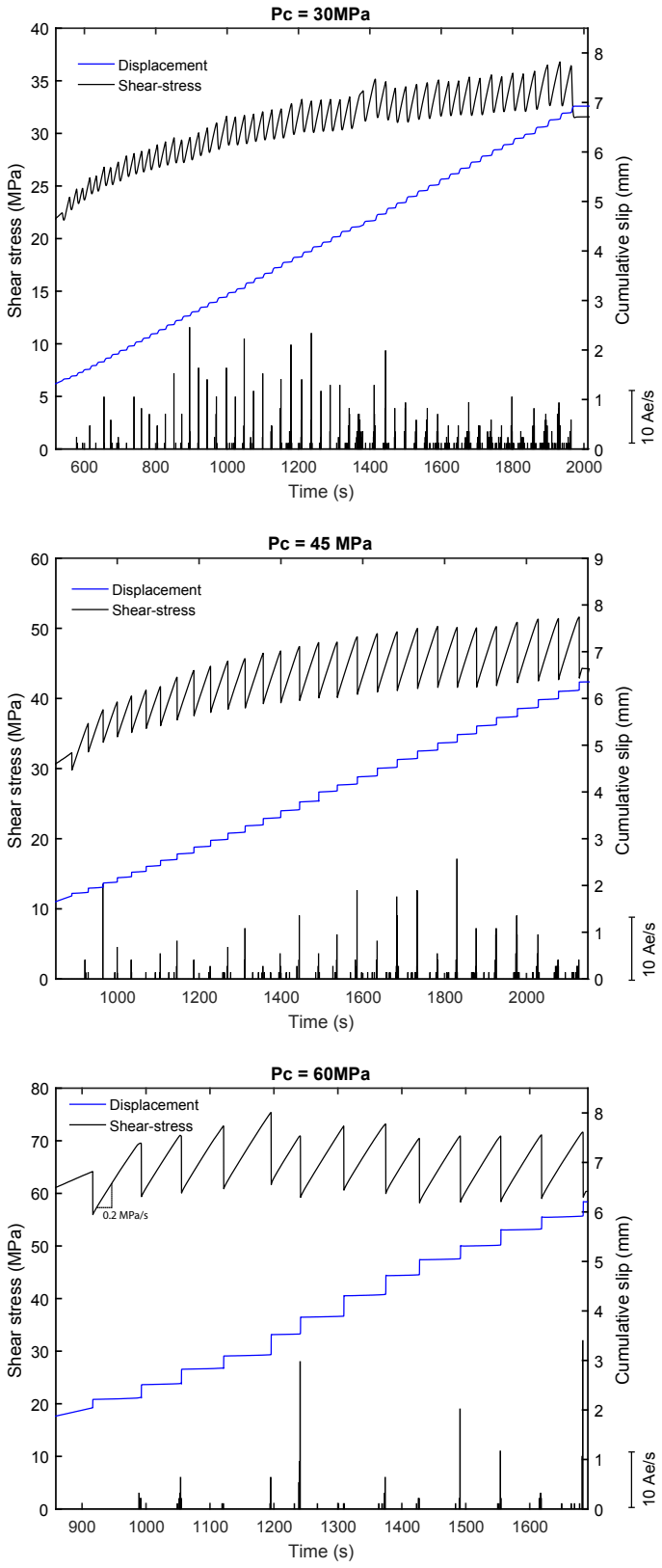

FIGURE 3.1: Cumulative displacement, shear-stress and AE rate during the experiments. AEs were stacked into 1 second bins. The displacement was corrected from the elastic deformation of the sample and of the apparatus.

we usually observed that only few acoustic sensors were saturating. Star symbols mark the SSEs prior to which we recorded at least one AE with moment magnitude Mw higher than -7 (in total, 23 at $Pc = 30\ MPa$, 5 at $Pc = 45\ MPa$ and 2 at $Pc = 60\ MPa$).
The total number of AEs recorded during the experiments was 905, 380 and 185 for respectively $Pc = 30$, 45 and 60 MPa. This equates to an average number of AEs per SSE of about 17, 13 and 14 respectively. As we could have expected according to the AE rate presented in figure 3.2, the number of AEs per stick-slip cycle fluctuates somewhat but tends to increase with the successive SSEs although it is less significant at $Pc = 60\ MPa$. The maximum number of precursory AEs within one sequence (i.e. for one SSE) that we recorded was 48, 31 and 46 at $Pc = 30, 45$ and 60 MPa respectively
The total AE moment per SSE depicts a different picture. A common feature to all the experiments is that the seismic energy released can largely vary from one precursory AEs sequence to another. At the early stage of the experiments conducted at $Pc = 30$ and 45 MPa we only recorded small AEs, which corresponds to the periods during which the static friction coefficient on the fault increased relatively fast. Then, we recorded oscillations between low and high energy AE sequences. During the experiment conducted at $Pc = 60\ MPa$ the seismic energy released onto the fault prior to stick-slip instabilities was slightly more stable (for instance from SSE 8 to SSE 12) but has shown significant variations as well.
A notable feature is that we recorded more large AEs during the experiment conducted at $Pc = 30\ MPa$ compared to $Pc = 45$ and 60 MPa (note that for visualization, the axis of the total AE moment release is different at $Pc = 30\ MPa$). The maximum precursory AE moment release that we estimated for a single sequence was 0.8 at $Pc = 30\ MPa$ and 0.18 at both $Pc = 45$ and 60 MPa. We recall that these values are lower bounds due to the saturation of acoustic sensors.

The figure 3.3 shows the frequency-magnitude distributions of the AEs that we detected during the experiments conducted at varying confining pressures (blue, red and black circles correspond to $Pc = 30$, 45 and 60 MPa respectively). The colored circles indicate the cumulative Gutenberg-Richter (G-R) distribution of the estimated AEs magnitudes and the bar plots display their distribution into 0.1 magnitude interval bins. We estimated that the magnitude of completeness M_c was close to $Mw = -8.7$. M_c might vary a little depending on the confining pressure (for instance between $P_c = 30$ and $Pc = 45\ MPa$) but it is not significant given that the typical error in magnitude estimation was 0.1. The black arrows indicate the upper limit magnitude ($Mw = -7$) beyond which acoustic sensors started to saturate. The estimated moment magnitudes M_w went beyond $M_w = -7$ for 71 AEs during the experiment conducted at $Pc = 30\ MPa$, for 6 AEs at $Pc = 45\ MPa$ and for 5 AEs at $Pc = 60\ MPa$. As mentioned earlier, we found from visual inspection that only few acoustic sensors would saturate close to $Mw = -7$ and, this, over a short portion of

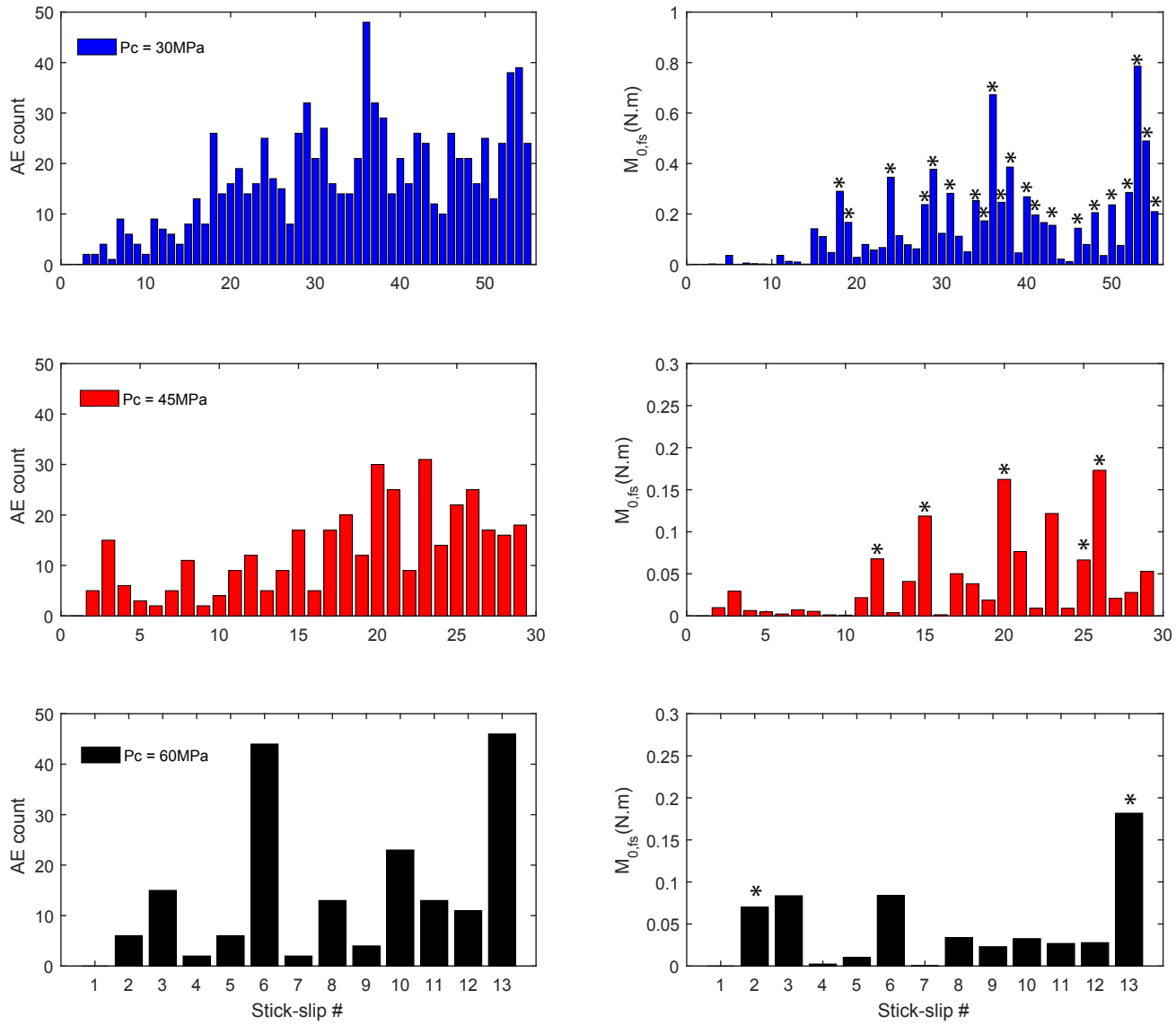

FIGURE 3.2: Distribution of the number of AEs (left) and the total AE moment release (right) per stick-slip cycle during the experiments. For particular SSEs, the total AE moment release is a lower bound due to the saturation of the acoustic sensors for $Mw > -7$. Star symbols indicate the AE sequences that contain at least more than 1 AE of $Mw > -7$.

the signal. Therefore we believe that close to this upper limit magnitude, our estimations are not significantly biased. However, beyond $Mw = -6.8$ almost all acoustic sensors were saturating over a large portion of the signal, which in the former case unambiguously indicates a significantly larger moment magnitude. Such a case only happened during the experiments conducted at $Pc = 30\ MPa$, for 21 AEs.
Using $M_c = -8.7$ we estimated the G-R b-value based on the Aki-Utsu maximum likelihood method (Aki, 1965; Utsu 1965). The best fits we obtained are given by the black dashed lines and are $b = 0.57 \pm 0.02$, $b = 0.65 \pm 0.03$ and $b = 0.66 \pm 0.04$ at $P_c = 30MPa$, 45 and 60 MPa respectively. The experiments conducted at $P_c = 45$ MPa and $P_c = 60$ MPa show a similar G-R distribution of the AEs with a net decrease of the number of AEs beyond $M_w\ -7.6$. This is in sharp contrast with the experiment conducted $P_c = 30$ MPa which is characterized by a significant larger number of AEs beyond $M_w\ -7.6$. Quite remarkably, at $P_c = 30$ MPa the G-R distribution of the AEs tends to follow a double distribution.

3.3.3 AE and stick-slip nucleation locations

The figure 3.4 displays on the left the photographs of the simulated faults after the experiments. AE (circles) and stick-slip nucleation (stars) locations onto the fault planes are shown at the center and on the right respectively. The colorscale refers to the SSE index. The size of the circles was set according to the estimated moment magnitudes. Assuming a circular source shape, the typical source sizes for an AE with $M_w = 7$ and for an AE with $M_w = 8$ are about 3 mm and 1 mm respectively. Only the AEs for which the residual times were less than 0.3 μs (which equates to 2-3 mm of location accuracy depending on the location of the AE with respect to the acoustic sensors array) are shown. Therefore large AEs are over represented on the figure.
The fault surface at $Pc = 30\ MPa$ is the one that presents the largest amount of gouge particles. Gouge particles tend to concentrate in the middle of the fault and to cluster into patches that are elongated in the direction of sliding. The typical size of these patches is of the order of few millimeters. It should be noted that we looked at the other surface condition and both surfaces were symmetrical. Therefore, zones without gouge particles are not due to gouge removal when the two pieces of the rock specimen were separated after the experiments. AEs correlate well with areas where gouge particles are concentrated. However, there are zones covered with gouge particles where no AEs where detected (for instance on the area on the top part of the fault). Although it is hard to get a precise view of the evolution of AE locations with the successive ruptures, it seems that most of the AE activity at the last stage of the experiment is concentrated in the middle of the fault plane. Quite remarkably, we can observe that SSEs nucleation tend to locate in the same area at the early stage of the experiment and then migrate to another region. Another characteristic that is easily observable at the last stage of the experiment is that SSEs tend to nucleate at the edges of the areas where most of the precursory AE moment was released.

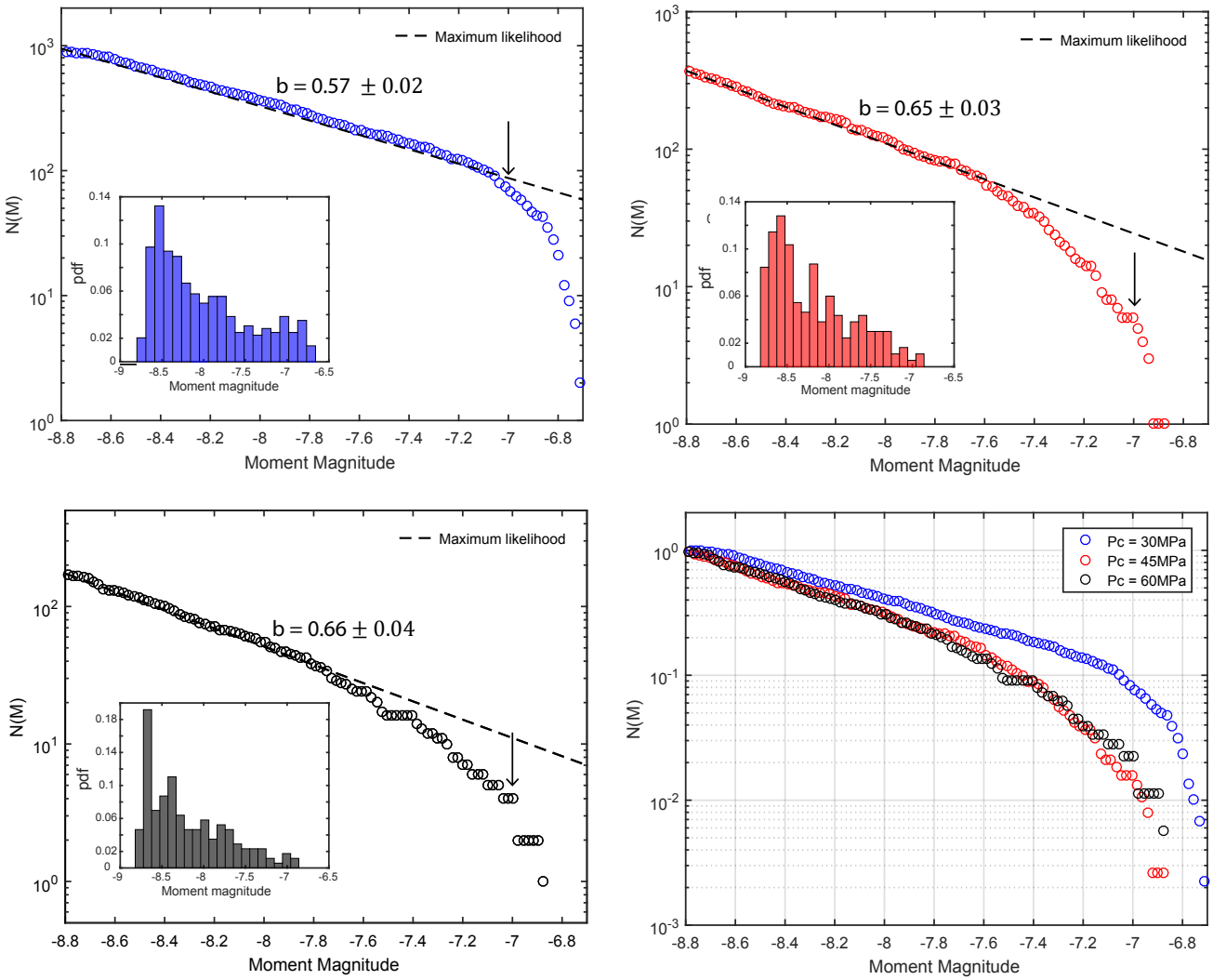

FIGURE 3.3: Frequency-magnitude distribution of the generated AEs during the experiments. Colored circles correspond to the cumulative G-R distribution of the AEs moment magnitudes. Black arrows indicate the moment magnitude Mw that correspond to the beginning of the acoustic sensors saturation ($Mw = 7$). Black dashed lines show the b-values that we estimated according to the Aki-Utsu maximum likelyhood method. Bar plots are showing the distribution of the AEs moment magnitudes into 0.1 magnitude interval bins.

The simulated fault at $Pc = 45\ MPa$ presents less gouge particles compared to the experiment conducted at $Pc = 30\ MPa$. We still observe patches where gouge particles concentrate but these are more heterogeneously distributed on the fault. Similarly to the experiment conducted at $Pc = 30\ MPa$ there are areas covered by gouge particles where few or no AEs were detected (for instance, on the lower edge of the fault on the left). Because there are less AEs here, it is easier to observe that their locations mirror fairly well the geometry of the areas covered by gouge particles. In the same way than the experiment conducted at $Pc = 30\ MPa$, SSEs nucleation migrated over time (from the left edge of the fault plane to the right edge). We can observe as well that SSEs do not necessarily nucleate where most of the AE is concentrated.
At $Pc = 60\ MPa$, gouge particles are homogeneously distributed over the fault surface. Unlike the other two experiments, we no longer observe patches of gouge particles. AEs tend to locate in a reduced region of the fault surface with respect to the other two experiments. In that case, we can observe migration of the AE activity with the successive ruptures, which seems roughly correlated with SSEs nucleation locations.

Microstructural and fault surface roughness analysis

The figure 3.5 displays the post-mortem fault surfaces observed using scanning electron microscopy (SEM). The large scale view of the fault surfaces at $Pc = 30\ MPa$ and $Pc = 45\ MPa$ (Figures 3.5 . and d respectively) reveals highly damages zones with a large quantity of generated gouge particles that cluster into patches. Gouge particles present a size ranging from 10 μm to 100 nm (Figure 3.5 a) and cover topographic highs with size of the order of few tens of μm (Figure 3.5 b) that we might interpret as small scales asperities. The enlarged view of the fault surface at $Pc = 60$ MPa (Figure 3.5 d) also reveals fine gouge particles production but the latter are not aggregated but rather homogeneously distributed on top of stretched and elongated surfaces in the direction of sliding. Zooming on the fault surface at $Pc = 60\ MPa$ allows us to observe stringy microstructures that contain gas bubbles. This suggest partial metling of the fault surface during slip. The micro-crack that crosses the residual melt results likely to the rapid cooling following melting. We can observe that a fraction of the small gouge particles are trapped into the melt. We can guess that the temperature reached a level close to the melting point at $Pc = 45\ MPa$. The fault surface displays elongated patterns as well (Figure 3.5 d). On a smaller scale (Figure 3.5 c), the fault surface has compacted and flatten microstructures that follow the direction of slip which could result from plastic processes.

Fault surfaces roughness were accurately measured over 15 mm x 30 mm surfaces using a laser profilometer with 0.05 μm of resolution (figures 3.6 a, b and c at $Pc = 30$, 45 and 60 MPa respectively). Sampling points are separated by $\approx 20\ \mu m$ which

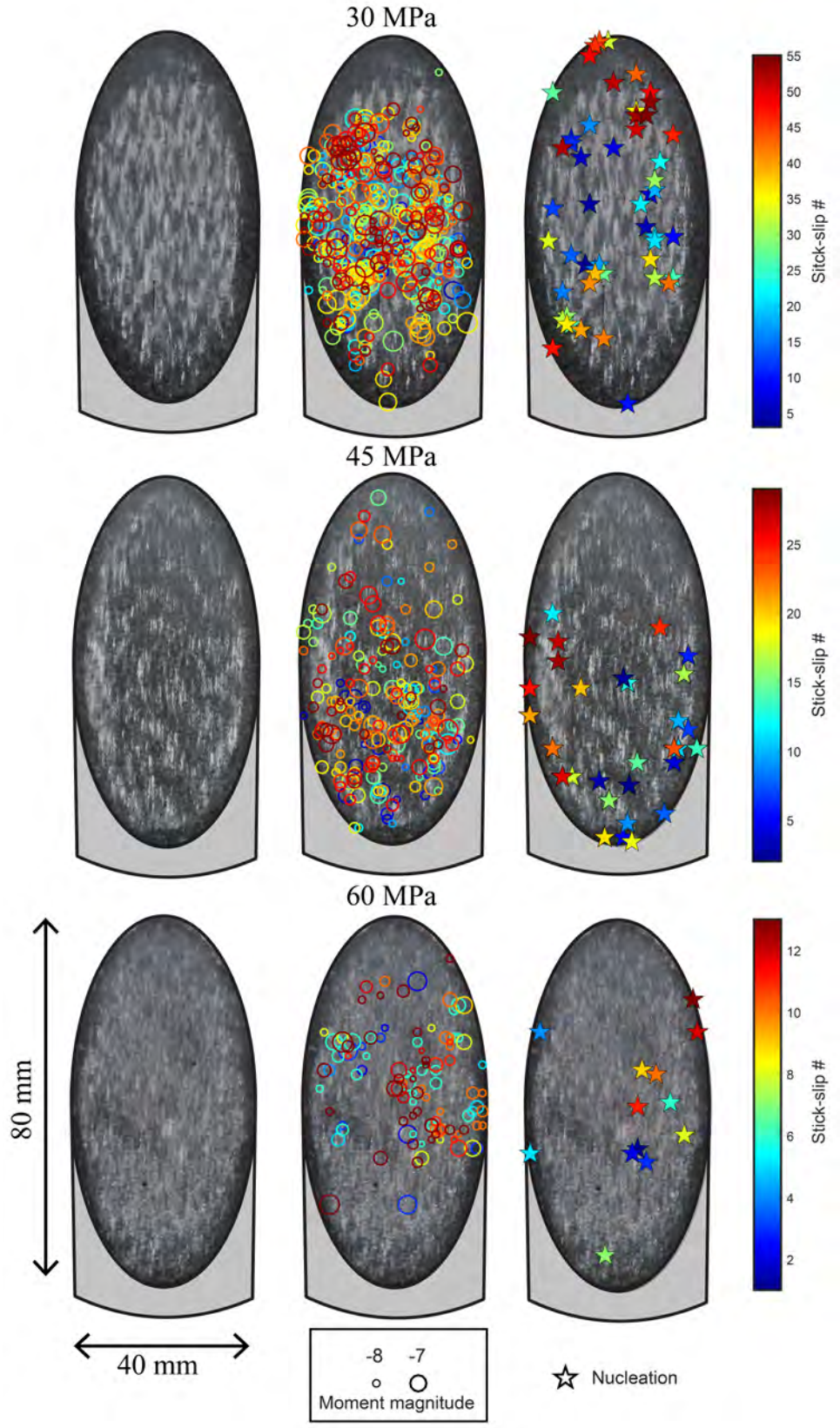

FIGURE 3.4: Fault surfaces conditions, AE and stick-slip nucleation locations. Circle size refers to the AE moment magnitude and was set according to the estimated source size. The colorscale refers to the SSE index. Only the AEs whose location errors are less than 2-3 *mm* are reported here.

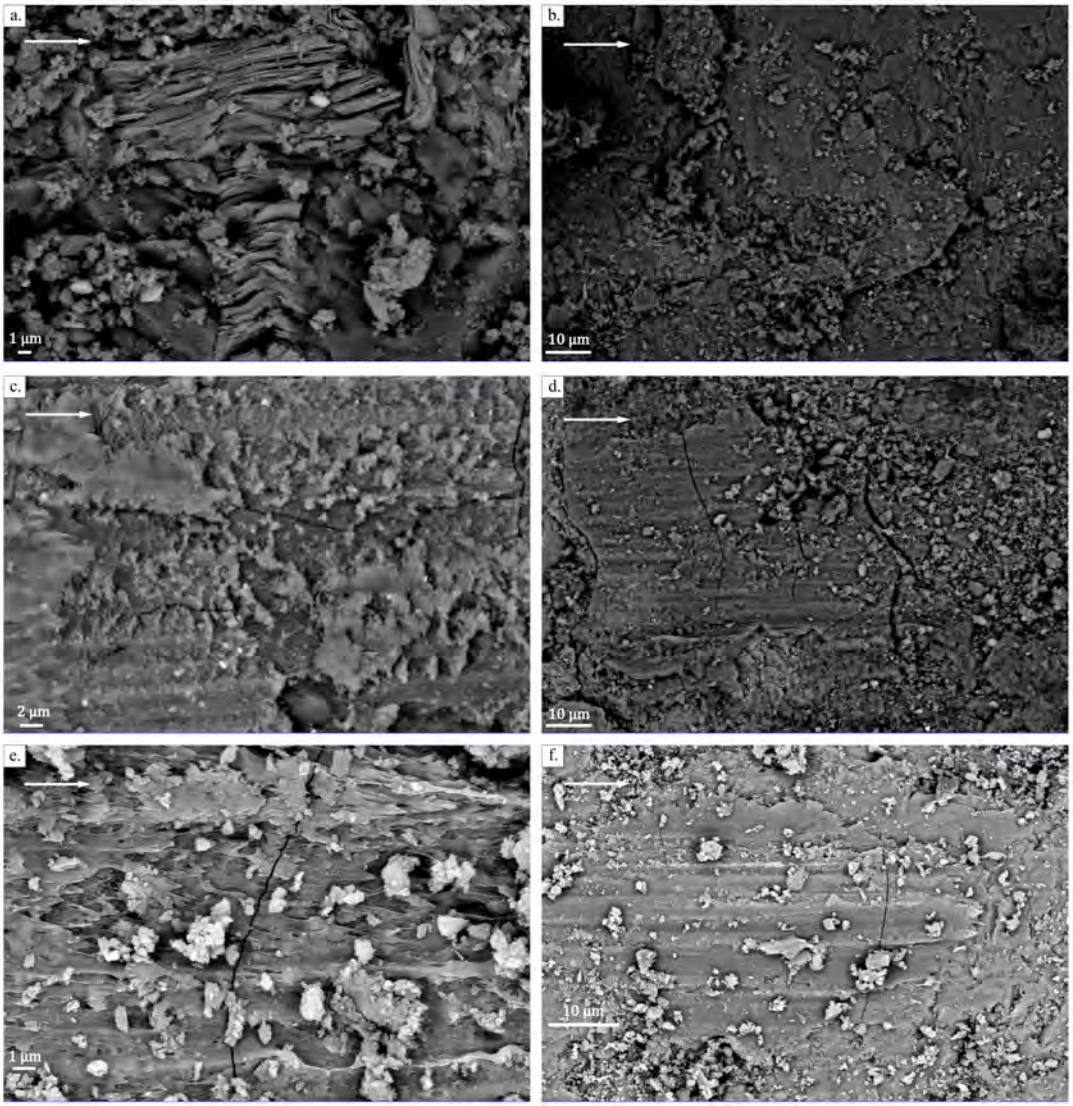

FIGURE 3.5: Microtexture of the fault surfaces after stick-slip experiments under Scanning Electron Microscopy at : **a.**, **b.** $Pc = 30\ MPa$, **c.**, **d.** $Pc = 45\ MPa$ and **e.**, **f.** $Pc = 60\ MPa$. The direction of sliding is indicated by the white arrow. **a.** Small scale view of gouge particles with various sizes ranging from few μm to 100 nm. **b.** Enlarged view of **a.** showing an highly damaged surface covered with patches of gouge particles heterogeneously distributed. We sense a small scale asperity at the center slightly deformed into the direction of sliding. **c.** Small scale view of amorphous fine gouge particles layer. **d.** Enlarged view of **c.** showing clusters of smashed gouge particles with sizes up to 10 μs. The fault surface presents striations along the sliding direction which suggest plastic deformation during stick-slip events. **e.** Small scale view of the fault surface showing evidence of partial melting during sliding. A fraction of the small gouge particles is trapped into the melt. **f.** Large scale view of **e.** showing stretched and elongated surfaces formed due to partial melting and covered with (more) homogeneously distributed gouge particles.

equates a total number of sampling points of 1538x769 for each surface. Note that due to a light contrast issue, the measure of the topography at $Pc = 30\ MPa$ failed over a fraction of the sampled surface (indicated in light grey). Elevations range from about -25 to 25 μm. At the lowest confining pressure we can observe coarse topographic highs (red colors) elongated in the direction of slip. These large and rough asperities likely correspond to the accumulation of gouge material with slip. The bigger one that we can see (at the bottom left) is about 2 mm thick, 5 mm long and 25 μm high. Compared to the other two experiments, there are no patterns that mark the coseismic displacement accumulated with the successive ruptures at $Pc = 60\ MPa$. which is likely due to partial melting of the fault during stick-slip instabilities. At the intermediate confining pressure $Pc = 45\ MPa$, striations of the fault surface likely formed by mechanical abrasion have been preserved and reveal a flattened surface. At that scale it can clearly be seen that the roughness of the fault surfaces at $Pc = 45\ MPa$ and $Pc = 60\ MPa$ are similar and less rough compared to the experiment conducted at $Pc = 30\ MPa$.

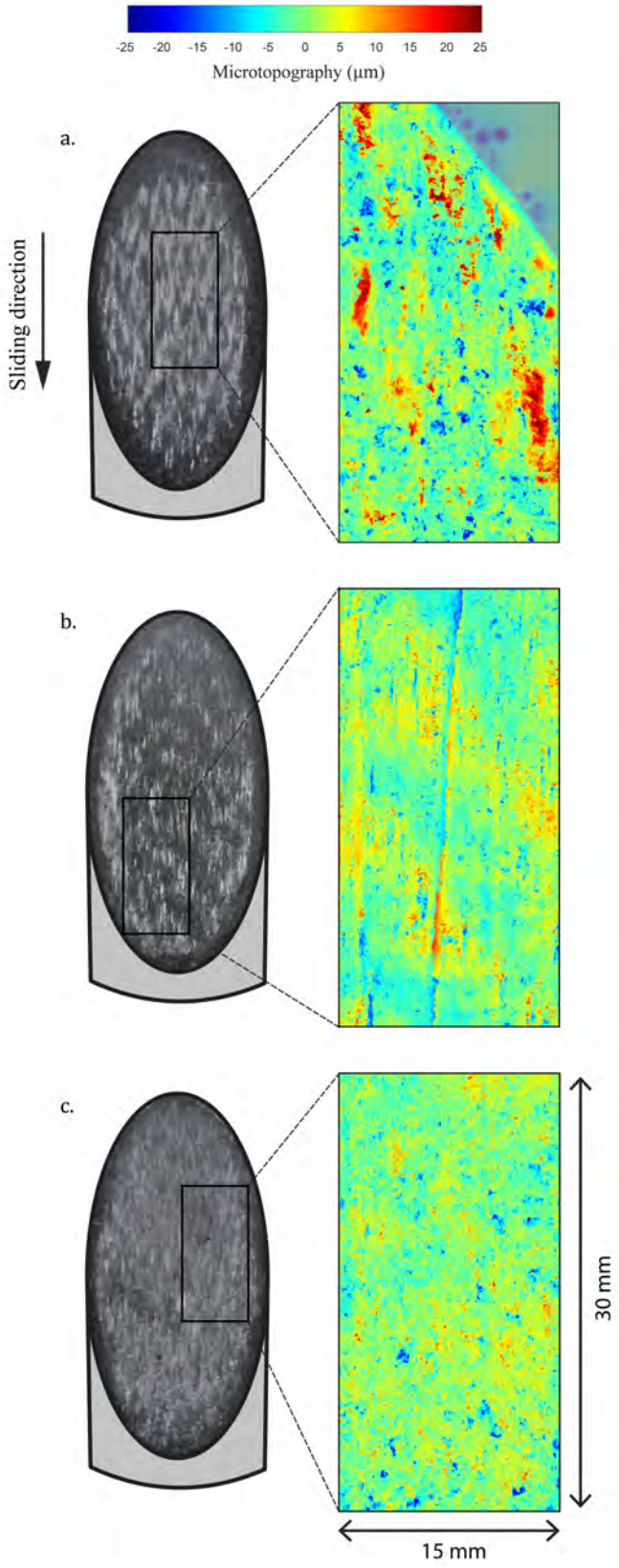

FIGURE 3.6: Microtopography of fault surfaces at: **a.** $Pc = 30\ MPa$, **b.** $Pc = 45\ MPa$ and **c.** $Pc = 60\ MPa$. The microtopography was measured using a laser profilometer presenting a resolution of 0.05 μm. The colorscale indicate the microtopography and is given in μm. Sampled surfaces are 15 mm wide and 30 mm long and correspond to the black rectangles shown on the right.

3.4 Discussion

3.4.1 Statistics of the nucleation phase

Characterization of fault surfaces roughness

We estimated the Hurst exponent H which is a scaling exponent that characterizes the fault surfaces roughness or more precisely the energy ratio between long and short wavelengths. To estimate H, we compute the Fourier power spectrum for each individual parallel profiles $I(k)$ perpendicularly and parallel to the slip direction as a function of the wavenumber k. Then we compute the average spectrum $P(k)$ (Figures 3.7 a and b) of the whole surface in both directions (i.e., perpendicular and parallel to the slip direction) by stacking the individual Fourier transforms such as:

$$P(k) = \sum_{n=1}^{n=N} I_n(k) \tag{3.1}$$

where N is the total number of 1-D profiles. This ensures to lower the noise contained in 1-D individual profiles. For a self-affine 1-D profile, the Hurst exponent ranges between $0 \leq H \leq 1$ and $P(k)$ satisfies a power law of the form $P(k) \propto 1^{-1-2H}$. The physical meaning of a self-affine (i.e. fractal) 1-D profil of length n is that its roughness r will increase as Δn^H after the linear transformation $n \longrightarrow n\Delta n$.
A common feature to all the experiments is that fault surfaces roughness are similar both in terms of shape and amplitudes along the perpendicular and the parallel directions of sliding. This implies quasi-isotropic fault surfaces roughness and contrasts with what is observed in the case of natural faults. A large majority of natural faults are characterized by anisotropic self-affine surfaces (Candela et al., 2009). Although the Hurst exponents vary in the range [0.4 - 0.9], H is found to be around 0.6 along the direction of sliding, and around 0.8 in the direction perpendicular to the sliding direction. We may assume that the initially smooth fault surfaces in our experiments prevent the production of roughness anisotropy. Another possibility is that additional rapid slip episodes are required for the production of roughness anisotropy. It is noteworthy that isotropic roughness also implies that gouge particles produced during slip are not only transported along the direction of slip but also perpendicular to it.
We found that for wavenumbers k less than 4.10^3 ($\approx 0.25\ mm$), fault surfaces roughness are characterized by a similar Hurst exponent H close to 0.4 which is rather low compared to what is typically found for natural fault but is a lower bound. A low Hurst exponent as opposed to a high Hurst exponent has the primary physical meaning that the long wavelength amplitudes are smaller relative to the short wavelength amplitudes which in the case of our experiments may be intrinsically related to fault surface preparation. The topography at long wavelength is necessarily damped to ensure an homogeneous contact between the two parts of the sample. However, to ensure a minimum of cohesion, the fault surfaces are lapped with a

fine-grained abrasive paper (#120 grit paper in this case, average particle diameter of about 125 μm), which, in turns, produces small wavelength topography.
It can be clearly observed that fault surfaces roughness are nearly identical at $Pc = 45$ and $Pc = 60\ MPa$. At $Pc = 30\ MPa$ the long wavelength roughness that has been increased due to gouge particles accumulation emerges for wavenumbers k less than about 4.10^3 ($\approx 0.25\ mm$) in comparison with the other two experiments. It can be clearly observed that Fourier power spectra of fault surfaces topography share significant similarities with the G-R frequency magnitude distributions of the precursory AEs. For moment magnitude M_w larger than about -7.6, the G-R slope rapidly drops at $Pc = 45\ MPa$ and $Pc = 60\ MPa$ but is unchanged at $Pc = 30\ MPa$. This could be the reciprocal of the decrease in roughness amplitudes for the wavelengths higher than about 0.25 mm ($k \approx 4.10^3$) observed at $Pc = 45\ MPa$ and $Pc = 60\ MPa$. We can speculate onto the fact that the G-R distribution of the AEs moment magnitudes mirrors the fault surfaces roughness. This is intriguing but would require quantitative analysis to be validated.

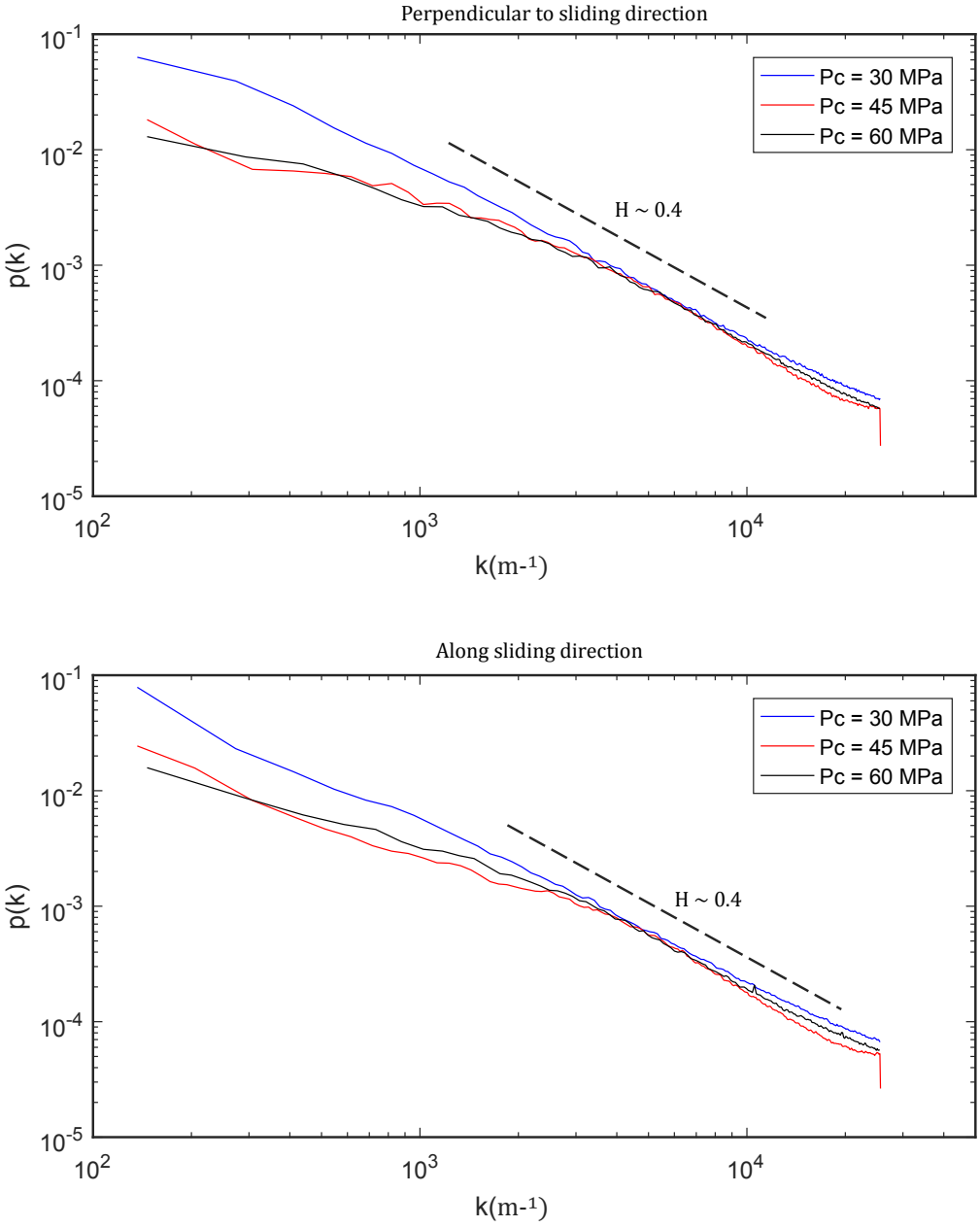

FIGURE 3.7: Power spectrum of the fault surfaces microtopography as a function of the wavenumber k and extracted from the stacking of the 1-D profiles along the perpendicular, **a.** and the parallel directions, **b.**, of the direction of sliding. Black dashed lines represent the power-law expected for a self-affine surface characterized by a Hurst exponent H of 0.4

Evolution of the precursory AEs activity towards nucleation

The figures 3.8 a,b and c display the evolution of the AEs b-values with respect to the time to failure at different time intervals at $Pc = 30MPa$, $Pc = 45MPa$ and $Pc = 60$ MPa. Here, all AE sequences were aligned with respect to the normalized time to failure and stacked. For each experiment, the time intervals were selected in order

to contain a similar number of AEs. To ensure that no bias would be introduced due to AEs saturation we computed the b-value either by tacking into account all AEs magnitudes (diamond symbols) or by removing AEs with $M_w > -7$ (square symbols). Taking into account or not the AEs that saturated impacts only the absolute b-values but not the general trend.
Hereafter, we discuss on the fluctuations of the b-values for the complete AEs catalogs (i.e. that includes all magnitudes). At $Pc = 30$ MPa we estimate that the b-value is about 0.68 ± 0.02 up to (on average) ≈ 3 seconds prior to failure. Then, the b-value drops rapidly to an almost constant level: 0.49 ± 0.02 and 0.52 ± 0.02. At $Pc = 45$ MPa the b-value is close to 0.7 ± 0.04 up to ≈ 2.5 s prior to failure and then drops to 0.54 ± 0.04 and 0.59 ± 0.04. For both experiments, the b-value seems to increase slightly in the last tenths of a second but this lies into the range of uncertainties. Variations of the AEs b-value prior to failure are more complicated to analyse for the experiment conducted at $Pc = 60$ MPa for two reasons (i) the large uncertainties and (ii) about 90 % of the AEs were recorded in the last 3 seconds prior to failure which lowers considerably the temporal resolution of b-value variations during stick-slip cycles. In comparison about 30 % and 25% of the total number of AEs were generated before entering the last 3 seconds before failure. However, unlike the other two experiments the b-value is initially low, close to 0.61 ± 0.06. In the last second prior to failure the b-value returns to a fairly high value, about 0.76 ± 0.08 and then decreases again to 0.67 ± 0.05.
Temporal variation in b-value prior to failure has been well documented during fracture experiments conducted on intact rock samples (Scholz, 1968b) and during rock friction experiments (Goebel et al., 2012; Kwiatek et al., 2014; Rivière et al., 2018). Fracture experiments on intact samples lead to a decrease of the b-value with increasing the differential stress which takes its origin in the formation and the coalescence of microfractures. Such a process causes a large number of AEs to be generated and a smooth and accelerating drop of the b-value up to the time of failure. In the case of foreshock sequences preceding large subduction earthquakes (Suyehiro, 1966; Enescu and Ito, 2001; Nanjo et al., 2012; Tormann et al., 2015), decreased in b-value has also been observed. However, foreshocks that precede large earthquakes can happen over different time scales, ranging from hours to years. Long term variations of the b-value are usually attributed to stress accumulation or partial stress release while short term variations are related to the mainshock nucleation. Based on the two experiments conducted at $Pc = 30$ MPa and $Pc = 45$ MPa we can at least say that large AEs rapidly grow in the last seconds preceding failure. The rapid drop of the b-value prior to stick-slip instabilities better suggests rapid weakening of the fault interface in a short interval of time close to rupture propagation.

Precursory AEs dynamics and fault maturation

The figures 3.9 a,b and c compares the along fault displacement, the along fault velocity, the cumulative number of AEs and the cumulative AE moment release with

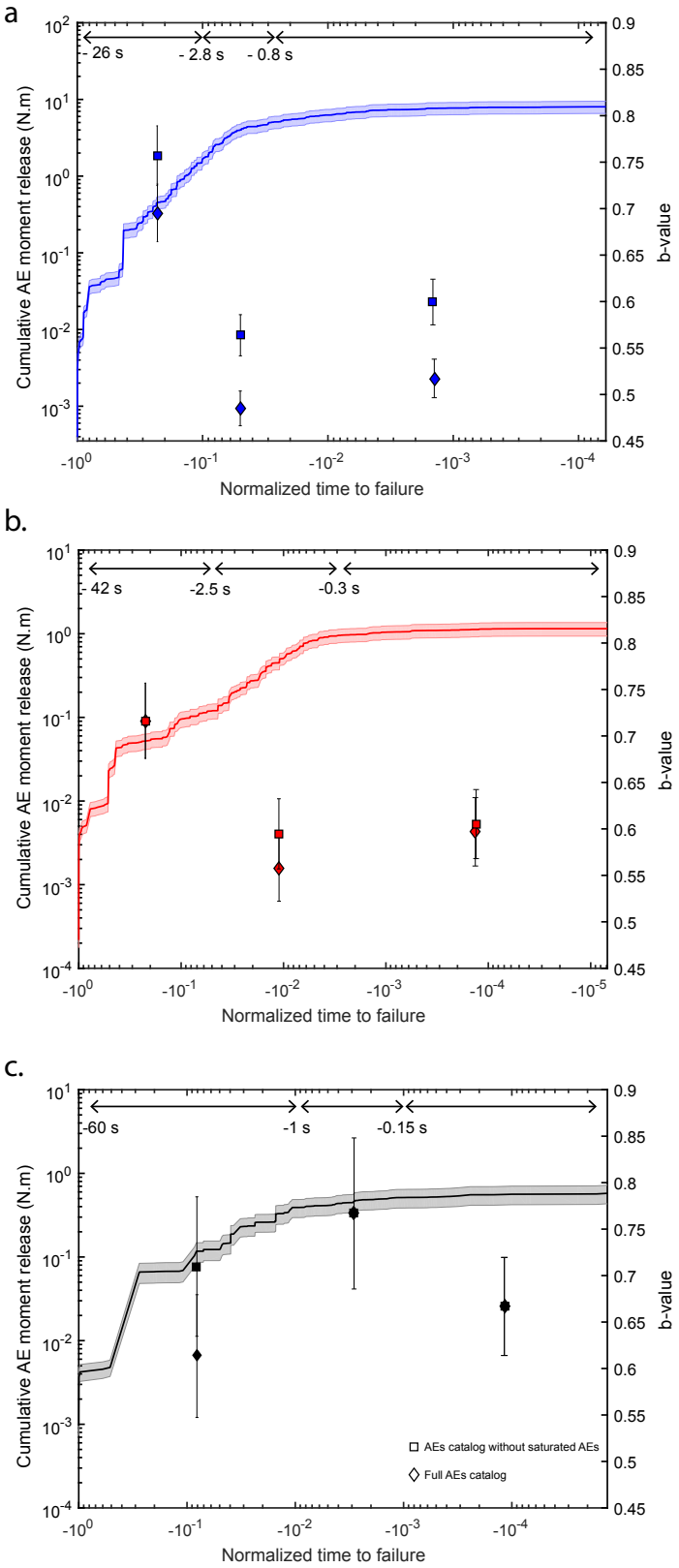

FIGURE 3.8: Cumulative AE moment release and b-value evolution prior to failure at : **a.** $Pc = 30\ MPa$, **b.** $Pc = 45\ MPa$ and **c.** $Pc = 60\ MPa$. The cumulative AE moment release is relative to the normalized time to failure and results from the stacking of all the precursory AE sequences. Square and diamond symbols show the AEs b-values and their uncertainties that were estimated at various time intervals relative to the onset of stick-slip instability. Square symbols correspond to the b-values that were estimated after removing the saturated AEs ($Mw > 7$) and the diamond symbols show the b-values that were estimated using the full AEs catalogs.

respect to the time to failure at $Pc = 30\ MPa$, $Pc = 45\ MPa$ and $Pc = 60\ MPa$ respectively. Each quantity is normalized by its maximum value at the time of the failure. Here again, all AE sequences are stacked to bring out a general trend. The grey shaded area around the AE moment release corresponds to the cumulative error of the magnitude estimates. The figures 3.9 d, e and f show the cumulative precursory AE activity per SSE during the experiments at $Pc = 30\ MPa$, $Pc = 45\ MPa$ and $Pc = 60\ MPa$ respectively . The cumulative precursory AE activity is normalized by its final value (i.e. at the time of failure) and is shown with respect to the normalized time to failure. The colorscale refers to the SSE index and the black curves result from the stacking of all sequences. Note that for visual inspection, not all AE sequences are shown at $Pc = 30\ MPa$ (Figure 3.9 d) and at $Pc = 45\ MPa$ (Figure 3.9 e).

Consistently with previous experimental studies (McLaskey and Lockner, 2014; Passelègue et al., 2017), we have always observed that the displacement onto the fault accelerates preceding failure. However, fault slip appears to be necessary, but not sufficient, for the production of AEs. Both the number of AEs and the AE moment appear to correlate with the slip rate onto the fault. This is particularly well illustrated in the last seconds prior to failure during which the AE moment release almost collapses with the slip rate onto the fault. However, there are notable differences in term of both the AE moment release and the mechanical behavior of the fault surfaces between the experiments. Regarding the AE moment release, the experiment conducted at the $Pc = 30\ MPa$ exhibits the smoothest behavior. Seismic energy is continuously radiated from the fault but in a delayed fashion with respect to the slip rate. For instance, between about -15 s and -5 s, the slip rate linearly increases with time while the AE moment release remains low. These features can be retrieved for the experiments conducted at $Pc = 45\ MPa$. The AE moment release follows the fault slip rate but is delayed and starts to intensify only once the fault accelerates. In the same way than the experiment conducted at $Pc = 30\ MPa$, the slip rate increases linearly before accelerating (between about -5 and -2 s prior to failure). However, compared to the experiment conducted at $Pc = 30\ MPa$, the slip rate onto the fault and the AE moment release increase later prior to stick-slip instabilities and at higher rate. The picture depicted by the experiment conducted at $Pc = 60\ MPa$ is somewhat different. Here, we can get a better picture of the cause of the low b-value far from nucleation. Although we observe a clear correlation between the fault slip velocity , the seismic energy is not released continuously, but rather in bursts. For instance, the two largest AEs that we recorded ($Mw > -6.9$) happen about -17 s and -5 s prior to failure, while the fault had not accelerated yet. This case is not limited to the experiment conducted at $Pc = 60\ MPa$ and also occurred during both the experiments conducted at $Pc = 30\ MPa$ and $Pc = 45\ MPa$. Even at the small scale of the experiments presented here, stress and thus strain are not homogeneously released

during coseismic displacement. These variations are extremely small given the orders of magnitude of difference between the SSEs and the precursory AEs here (SSEs have Mw of the order of $\approx$ -3.5 typically) but are sufficient to trigger the rupture of small patches without external forcing such as slip acceleration. Also, the stacking procedure inherently smooths the variability of precursory AEs occurrence prior to failure. Precursory AE sequences can be very variable from one to another. It is likely that if a larger number of AE sequences would had been stacked together, as it is the case for the other two experiments, the general trend described above would have emerged better.
Increasing the slip rate will cause local stressing rate and will lower the frictional resistance of locked portions of the fault as could be expected from rate and state models (Dieterich, 1978; Ruina, 1983) or from pure mixed velocity-dependent and slip-dependent weakening law (Rabinowicz, 1958). AEs may occur when stress applied onto the fault exceeds the strength of local brittle fault patches or may reflect the brittle destruction of fault surface topography. Most of the time for the sufficiently large AEs ($Mw > 8.6$) we could observe positive and negative first P-wave arrivals which implies that most of the moment release is deviatoric. According to the observation that the acceleration of pre-slip precedes and drives the AE moment release, this better suggests that precursory AEs highlight the rupture of locked portion of the fault within a larger portion that is slipping aseismically. Similar behavior was observed by the experimental studies of McLaskey and Kilgore (2013) conducted on a large scale bi-axial apparatus. This is also consistent with the observations at the scale of crustal faults. Bouchon et al. (2013) showed that foreshock sequences were more common for interplate than for intraplate earthquakes due to facilitating slow slip phase at plate boundaries. Similarly, McGuire et al. (2005) have observed that oceanic tranform faults with relatively high-slip rates were producing more foreshock sequences. However, how much and how long a loaded fault subject to slow slip can radiate seismic energy will depend at first order on its degree of heterogeneity.

The experiment conducted at $Pc = 30\ MPa$ gives the clearest example of what we would call "fault maturation" (Figure 3.9 d). The number of precursory AEs occurs earlier during loading when increasing fault slip history. At the last stage of the experiment, AE sequences (dark red colors) exhibit a high level of similarity. Summing all AE sequences results in a smooth increase of the cumulative number of AEs. These characteristics can be approximately retrieved at the intermediate confining pressure, $Pc = 45\ MPa$ (Figure 3.9 e) but not at $Pc = 60\ MPa$ (Figure 3.9 f). During this experiment, AEs occur later which results in a sharper acceleration of the cumulative number of AEs towards the nucleation. A noticeable difference at $Pc = 60\ MPa$ lies in the absence of AEs early during loading. In the other hand, the experiment conducted at $Pc = 60\ MPa$ is the only one during which the first sequence of AEs has released a comparable amount of seismic energy with respect to

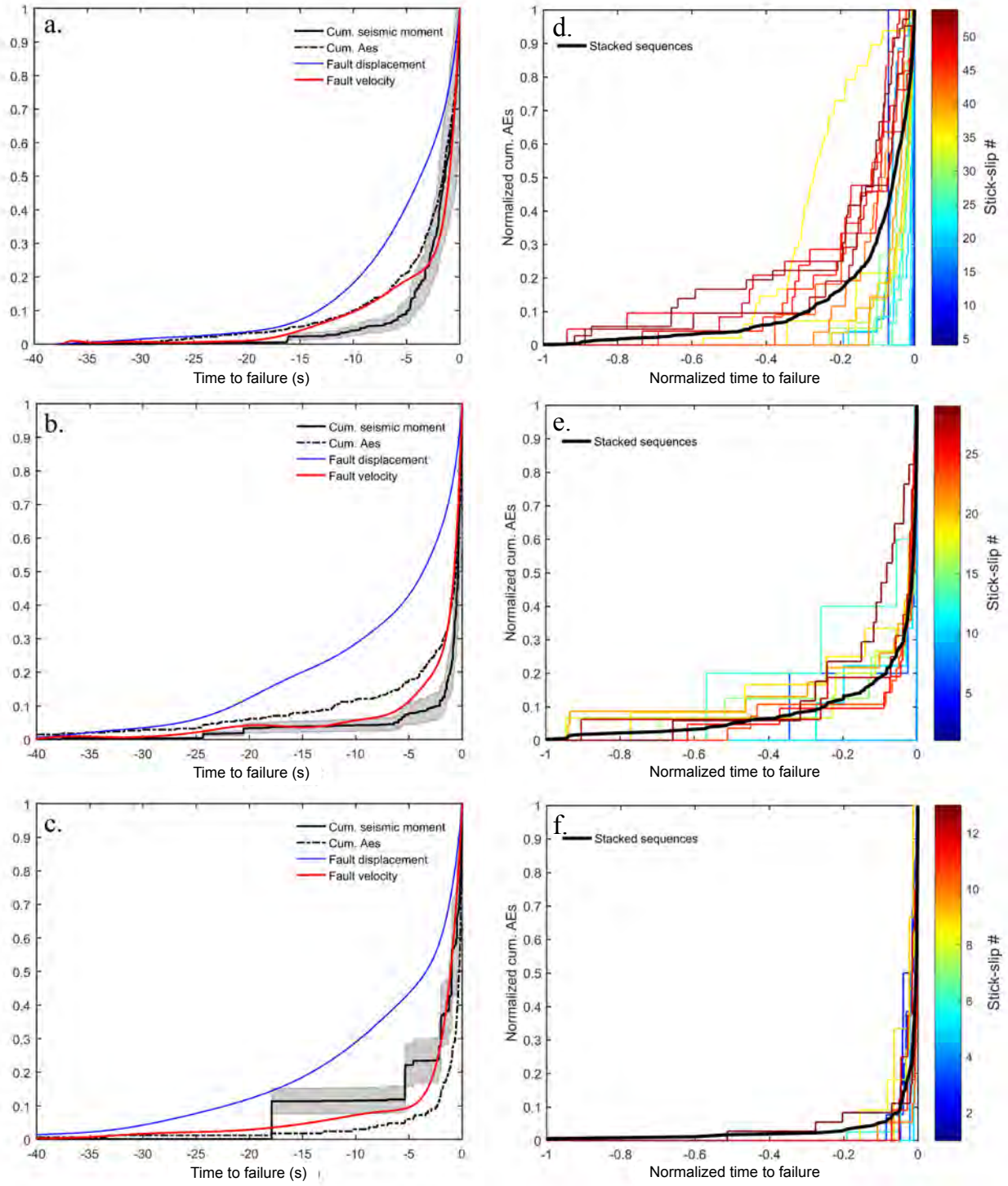

FIGURE 3.9: **Comparison between the normalized along fault displacement, along fault velocity, cumulative number of AEs and cumulative AE moment release as a function of the normalized time to failure at: a.**, $Pc = 30\ MPa$, **b.**, $Pc = 45\ MPa$ and **c.**, $Pc = 60\ MPa$. All curves result from the stacking of all the SSEs. The grey shaded area around the AE moment release corresponds to the cumulative error of the magnitude estimates. **Evolution of of the normalized cumulative number of AEs as a function of the normalized time to failure at: d.**, $Pc = 30\ MPa$, **e.**, $Pc = 45\ MPa$ and **f.**, $Pc = 60\ MPa$. The colorscale indicates the SSE index and the black curves result from the stacking of all precursory AE sequences.

the ones that followed. At $Pc = 30\ MPa$ and $Pc = 45\ MPa$, the AE moment release prior to failure started to significantly increase after 10 stick-slip cycles. However, when averaging over all the AE sequences, the experiments conducted at $Pc = 45\ MPa$ and $Pc = 60\ MPa$ are characterized by a similar frequency-magnitude distribution of the AEs. Conversely, significantly more large AEs were generated during the experiment conducted at $Pc = 30\ MPa$. We can attempt to interpret these differences of time of occurrence of AEs prior to failure and of AE moment release relying on microstructural and fault surface roughness analysis.

Multiscale roughness may provides the heterogeneity of fault strength necessary to produce small ruptures. Large asperities that have been formed at $Pc = 30\ MPa$ have increased the level of heterogeneity in terms of stress concentration and thus in term of fault strength compared to the other two experiments. This has lead to larger AEs prior to failure at $Pc = 30\ MPa$ compared with the other two experiments. At $Pc = 45\ MPa$ and $Pc = 60\ MPa$, same roughness produce similar AEs. We can argue that fault surfaces were more scrubbed at $Pc = 45\ MPa$ and $Pc = 60\ MPa$ because of the thermal activation of either plastic deformation processes or partial melting. It is noteworthy that during the experiment conducted at $Pc = 45\ MPa$ and $Pc = 60\ MPa$ the amount of pre-slip was quite similar (about 9 μm on average) compared to the experiment conducted at $Pc = 30\ MPa$ (about 6 μm) on average. This is probably caused by the organized large scale roughness resisting slip (Schaff et al., 2002) that has developed at $Pc = 30\ MPa$.

However, almost no large AEs were produced at the early stage of the experiments conducted at $Pc = 30\ MPa$ and $Pc = 45\ MPa$. Let us take a step back to the mechanical data. At $Pc = 30\ MPa$ and $Pc = 45\ MPa$, the first SSE happened at particularly low stress conditions, when the average normal stress σ_n onto the fault was about 43 MPa and 65 MPa respectively. The associated coseismic displacements were about 31 μm and 59 μm. In comparison, at $Pc = 60\ MPa$ the first SSE occurred when the normal stress acting onto the fault was about 98 MPa and lead to a coseismic displacement of 184 μm. Slip during the first SSE at $Pc = 60\ MPa$ probably produced fine gouge or accentuated topographic heterogeneities that effectively increased the roughness and promoted the generation of relatively large AEs prior to the subsequent SSE. Therefore, the fault was already "mature". At the other two confining pressure conditions, more SSEs were required to increase the roughness due to lower coseismic displacements and lower normal stress conditions. Once a sufficient amount of gouge particles or topographic heterogeneities were produced, both the number of AEs and the AE moment release started to intensify.

Finally, the absence of AEs far from nucleation at $Pc = 60MPa$ may be related to the distribution of the gouge particles and theit interactions with the underlying surface. AEs that happen early during loading are considerably small, which cause the high b-values far from nucleation at $Pc = 30\ MPa$ and $Pc = 45\ MPa$. We interpret these small AEs as either micro-shear events or sudden buckling in a force chain that would happen in a compacted granular gouge layer (Mair et al., 2002; Hartley and

Behringer, 2003). Thus, these small AEs cannot be generated at $Pc = 60\ MPa$ because of either the homogeneous distribution of the gouge particles onto the fault or due to the fact that a significant fraction of the gouge particles are trapped into the melt. However another possibility if that small AEs that happen early during loading at $Pc = 30\ MPa$ and $Pc = 45\ MPa$ reflect microfracturing processes promoted by the accumulation of damaged with the successive ruptures.

Spatial and temporal behavior of precursory AEs

Here we look at the evolution of the precursory AEs spatial distribution towards failure. The figures 3.10 a, b and c display the distance to nucleation of the precursory AEs with respect to the normalized time to failure at $Pc = 30\ MPa$, $Pc = 45\ MPa$ and $Pc = 60\ MPa$ respectively. The distance to nucleation was binned into 10 log-distributed time intervals (horizontal axis). The average distance and its standard deviation into each bin is indicated by the cyan triangles. To the left is shown the pdf of the precursory AEs as a function of their distance to nucleation. Note that, AEs located with more than 0.3 μs travel time residuals (about 2-3 mm of location accuracy) were removed. At the lowest confining pressure, $Pc = 30\ MPa$, nothing indicates on spatial migration of the precursory AEs towards the nucleation. Precursory AEs remain randomly distributed over the fault surface, up to the time of failure. Most of the precursory AEs occur at larger distances than 20 mm. Although we cannot talk appropriately speaking of a well defined migration, migration patterns only emerge, on average, when increasing the confining pressure. At the highest confining pressure, $Pc = 60\ MPa$, AEs occur on a more localized portion of the fault surface and get closer to the nucleation as the rupture is approaching. On average, most of the precursory AEs are located within 10 to 15 mm to the nucleation.
The first information that is given by the distance to nucleation of the precursory AEs is related to the way SSEs initiate. In all experiments, we have always observed that SSEs only initiate when preslip is already accelerating. This preslip corresponds to the large nucleation of the SSE and drives the smaller scale seismicity (i.e. AEs). However, one may ask if the SSEs correspond to the growth of a small AE in a cascade-up process or to the dynamic propagation of the nucleation zone that has reached the critical nucleation length L_c. For instance, we could imagine that SSEs initiate with preslip, that this preslip triggers the AEs but also weakens sufficiently the strength of the fault to allow a small instability to grow large. In such a scenario we would expect to consistently observe that precursory AEs that occur in the last milliseconds are co-localized with the nucleation. This would result in a clear migration of the precursory microseismicity towards the nucleation which is not what we observe. In our experiments, we found that SSEs do not nucleate where the precursory AE activity concentrates. Instead, SSEs tend to nucleate at the edges of the areas where most of the precursory AE moment was released. This is well illustrated for the last SSEs at $Pc = 30\ MPa$ and $Pc = 45\ MPa$ (Figure 3.4). Moreover, we would expect that cascade process would be promoted by the occurrence of large

AEs. The largest AEs were generated during the experiment conducted at the lowest confining pressure pressure $Pc = 30\ MPa$. In this experiment, there is no indication of migration over time. Therefore, we can argue that, in most cases, the dynamic propagation of the rupture results from the large nucleation process of the SSE but not from a small AE that dynamically triggers the SSE in a cascade-up process. The latter case may have happened but that would be more the exception than the rule. We attempt here to give a qualitative explanation to the migration patterns that are promoted by increasing the confining pressure. We may assume that if the nucleation zone is smaller, there is more chance that the precursory AEs occur at shorter distances to the nucleation which would favor migration. According the slip weakening linear (Ida, 1972; Campillo and Ionescu, 1997; Uenishi and Rice, 2003) or rate and state friction (RAS) laws (Rubin and Ampuero, 2005; Ampuero and Rubin, 2008) we expect the critical nucleation length L_c to decrease with increasing the normal stress acting onto the fault such as:

$$L_c = 2.\beta.\frac{\mu D_c}{\sigma_n(f_s - f_d)} \tag{3.2}$$

for the linear slip weakening law where μ is the shear modulus of the rock sample, D_c is the critical slip distance, σ_n is the normal stress acting onto the fault, f_s and f_d are the static and the dynamic friction coefficient respectively and β is a non-dimensional shape factor coefficient (≈ 1.158). For RAS friction laws:

$$L_c = \frac{\mu D_c}{\sigma_n(b - a)} \tag{3.3}$$

whereh b and a are the constitutive parameters of RAS friction laws. According to (3.2) and (3.3), L_c will decrease with increasing the normal stress acting onto the fault and the friction drop. However, D_c is expected to increase with increasing the normal stress acting onto the fault. For instance, assuming a purely slip weakening behavior, D_c is expressed as (Ida, 1972; Palmer and Rice, 1973; Rice, 1979):

$$D_c = \frac{16(1-\nu)}{9\pi}\frac{V_r t_w \sigma_n(f_s - f_d)}{\mu} \tag{3.4}$$

where V_r is the local rupture velocity, t_w is the weakening time and ν is the poisson's ratio of the rock specimen. Therefore, D_c is also expected to increase with the normal stress acting onto the fault and the friction drop. Moreover, while the weakening time t_w does not vary with stress conditions (Passelègue et al., 2016), we expect that the rupture velocity will, on average, increase with increasing the normal stress acting onto the fault. Therefore, we do not necessarily expect that the nucleation length L_c decreases with increasing σ_n.

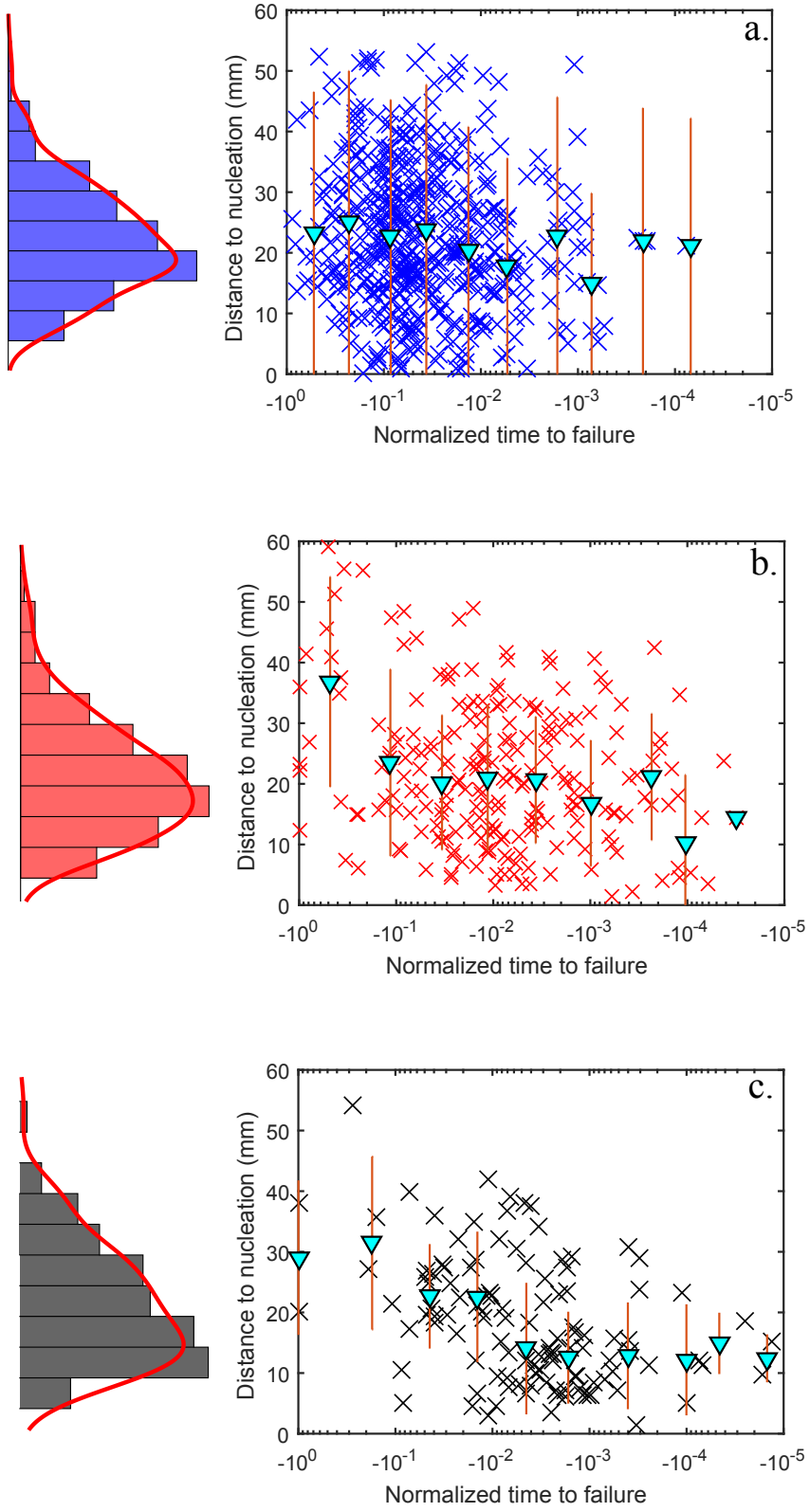

FIGURE 3.10: Distance to nucleation of the precursory AEs as a function of the normalized time to failure at : **a.** $Pc = 30\ MPa$, **b.** $Pc = 45\ MPa$, **c.** $Pc = 45\ MPa$. The cyan triangles indicate the average distance to nucleation and its standard deviation computed into 10 log-distributed time intervals. On the left is shown the pdf of the precursory AEs as a function of their distance to nucleation.

One possibility may lie into stresses heterogeneity. Let us assume that the nucleation expands in a crack-like fashion. Inside the crack, the shear-stress drop $\Delta\tau$ can be approximated as the shear modulus μ inside the crack times the ratio between the slip velocity V_s and the shear-wave velocity C_s such as:

$$\Delta\tau = -\mu\frac{V_s}{C_s} \tag{3.5}$$

In the case of an expanding crack, the slip velocity is maximum at the tips and nearly uniform inside the crack. As the nucleation zone expands, the unlocked portion of the fault in the interior of the nucleation zone releases stresses. Due to stress perturbations close to the tips of the nucleation zone, the stress-drop $\Delta\tau$ is positive near the tips and decreases and becomes negative in direction of the center of the nucleation zone. However, this is only valid for the unlocked portions of the fault inside the nucleation zone. Stresses on locked portions of the fault in the interior of the nucleation zone continuously increase during nucleation. In that case, the stress-drop $\Delta\tau$ is positive near the tips and decreases but remains positive in direction of the center of the nucleation zone. Let us propose the following mechanism for migration. AEs may occur if the applied stress to a locally brittle patch exceed its strength. The precursory AEs at relatively large distances from the center of the nucleation zone are triggered first due to stress perturbations at the tips of the nucleation zone, which are sufficient to overcome the critical strength of the locked portions of the fault interface. As the nucleation zone expands, the stresses increase in the interior of the nucleation zone. Because of the negative gradient of the stress profile that goes from the edges of the nucleation zone to its center, the precursory AEs will tend to migrate towards the center of the nucleation zone. This mechanism is schematically presented in figure 3.11 d. As an illustration, the figures 3.11 a, b and c display a summary of the precursory AEs sequence prior to SSE #6 during the experiment conducted at $Pc = 60\ MPa$. The cumulative AE moment release and along fault displacement in the last 10 seconds prior to failure are shown in figure 3.11 a. The figure 3.11 b displays the distance to nucleation of the precursory AEs prior to failure and the figure 3.11 c shows the locations on the fault plane of the precursory AEs. The colorscale refers to the occurrence time of the precursory AEs relative to failure and the star symbol indicates where the nucleation initiated. This sequence is characterized by three bursts of microseismicity which occurred about -2.2, -0.5 and -0.1 s prior to failure (Figure 3.11 a). The AE moment release rapidly increased in the same way that the displacement onto the fault which is consistent with the interpretations made so far (i.e., AEs highlight the rupture of brittle fault patches within the interior of the nucleation zone). In that case, the migration of the precursory AE activity towards the nucleation can clearly be seen. Initially, the precursory AEs occurred at distances of about 20-25 mm from the nucleation and then rapidly migrated towards the nucleation (Figure 3.11 b). To be fully consistent with the interpretation proposed above, the edges of the nucleation zone were close to

the locations of the first burst of microseismicity that occurred about -2.2 s prior to failure (Figure 3.11 c). In the case of a self-similar crack, we expect that the displacement in the interior of the nucleation zone grows as the nucleation zone expands. According to the displacement along the fault, we can assume that the nucleation zone has then rapidly expanded after -2.2 s prior to failure. This has resulted into the fast loading of the locked portions of the fault and the subsequent bursts of microseismicity. The spatial migration of the precursory AEs was then controlled by the shear-stress gradient in the interior of the nucleation zone. In such a scenario, migration will be promoted if the brittle patches that rupture are characterized by an homogeneous critical strength, otherwise, the precursory AEs will tend to randomly distribute relative to the center of the nucleation zone. Assuming that fault strength heterogeneity is provided by multiscale roughness of the fault plane, this may explain why migration is not observed at the lowest confining pressure $Pc = 30$ MPa but only emerges when increasing the normal stress applied onto the fault. It should also be noted that AEs may also be able to trigger each other due to dynamic or static stress transfer. In that case, we would expect them to draw a well defined path, both in time and space, which is not what we observe. Therefore, this may happen but is likely of second order for the occurrence of precursory AEs.
Foreshock migration prior to large earthquakes is often attributed to slow-slip propagation towards the hypocenter of the mainshock (Kato et al., 2012; Ruiz et al., 2014; Kato and Nakagawa, 2014). It has also been suggested that fluids diffusion towards the hypocenter of the mainshock may trigger foreshock swarms by reducing the effective normal stress (Moreno et al., 2015; Socquet et al., 2017). The experiment were conducted under dry conditions which makes the latter case unlikely. Slow slip transients usually involve slip rates that range from 10 to 100 $\mu m/s$. This is more that what we observe during our experiments, fault slip rates are typically of the order of few $\mu m/s$ in the last tenth of a second prior to failure. The question whether slow slip transients prior to large earthquakes are part of the nucleation process or not is still debated. Prior to the 2014 Mw 8.2 Iquique earthquake and to the 2011 Mw 9.0 Tohoku-oki earthquake it has been observed that slow slip transients were not associated with the acceleration of slip and thus the acceleration of foreshock rate characteristics of the nucleation process. Therefore, slow-slip transients were not interpreted as part of the nucleation process. This contrasts with the case of the 1999 Mw 7.6 Izmith earthquake prior to which foreshock migration and acceleration close to the mainshock hypocenter was reported (Bouchon et al., 2011). We have attempted to give a qualitative interpretation of the migration of the microseismicy towards the nucleation during our experiments. This may also be a plausible explanation of foreshock migration and acceleration prior to natural earthquakes. In such a case, there is no need to involve fluids diffusion of slow-slip propagation.

Here we look at the temporal evolution of the cumulative number of precursory AEs prior to failure. When averaged over numerous foreshock sequences, it is known that the foreshock rate $N(t)$ increases as an inverse power law of the time to the

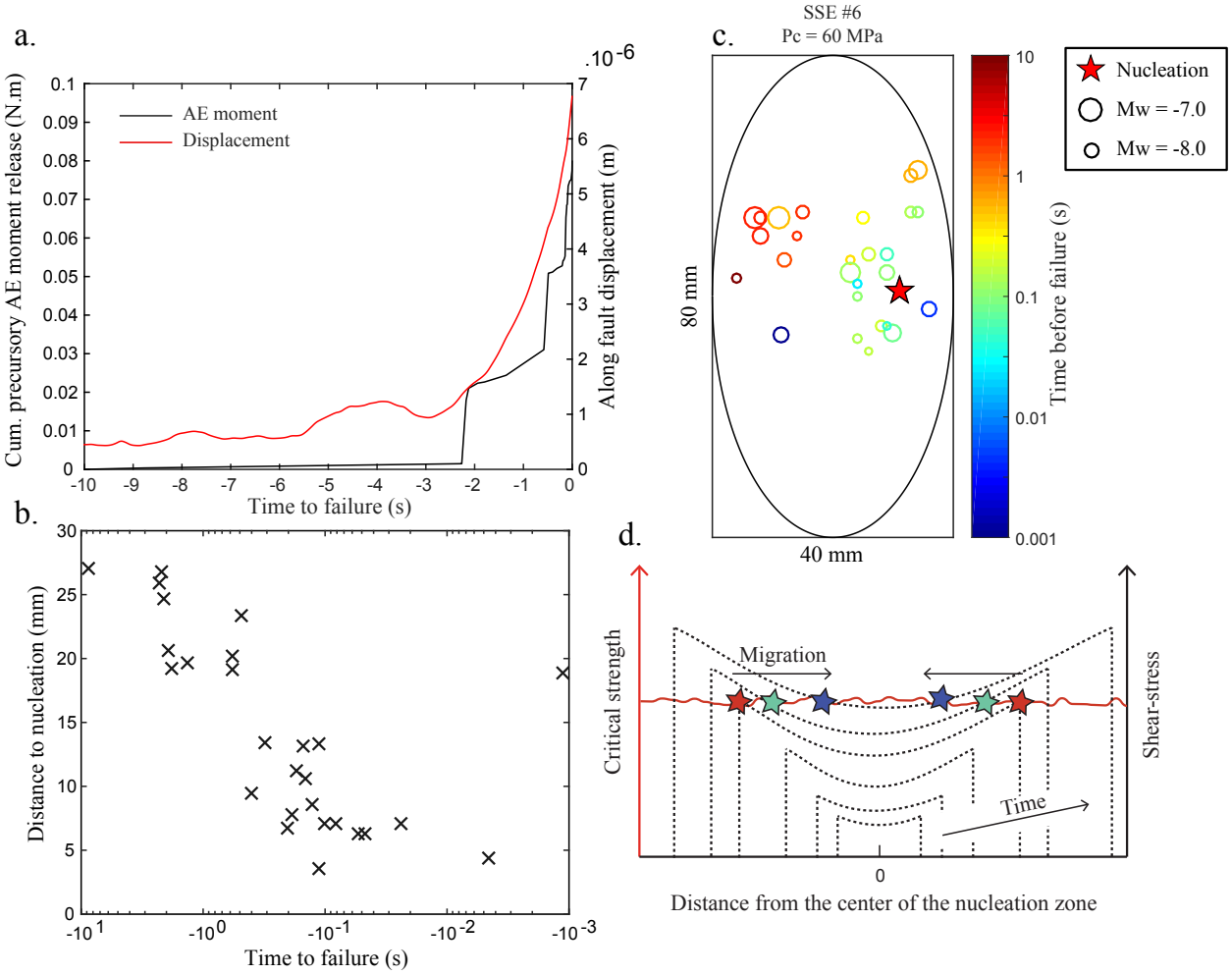

FIGURE 3.11: **a.** Cumulative AE moment release and along fault displacement in the last 10 seconds prior to SSE #6 during the experiment conducted at $Pc = 60\ MPa$. **b.** Distance to nucleation of the precursory AEs prior to failure. **c.** Locations, sizes and timing of the precursory AEs that occur prior to SSE #6 ($Pc = 60\ MPa$). The colorscale refers to the timing of the AEs relative to failure. Circle size indicates the moment magnitude and was set according to source size. The star symbol indicates the nucleation location. **d.** Schematic view of the shear-stress evolution on locked portions of the fault (i.e., in the interior of the nucleation zone) during nucleation. The black dashed lines indicate the shear-stress profile. The red line idealizes the critical strength of the locked fault patches in the case of an homogeneous medium. The star symbols depict a schematic view of the migration in time and space of precursory AEs towards nucleation initiation. The stress perturbations at the tips of the nucleation zone trigger the precursory AE activity far from nucleation. As the nucleation zone expands, stresses build-up in the interior of the nucleation. The shear-stress gradient leads to the migration of the precursory AEs towards the center of the nucleation zone.

mainshock (Jones and Molnar, 1979) such as:

$$N(t) = \frac{K}{(c + \Delta t)^p} \tag{3.6}$$

where K is the foreshock productivity, c and p are empirical constants and Δt is the time that separates from the mainshock. A previous experimental study (Passelègue et al., 2017) showed that the number of precursory AEs was increasing exponentially towards failure. It has been argued that the exponential increase in precursory AE activity is a consequence of the preslip that evolves exponentially up to the time of the rupture. In our experiments, we found that precursory AE activity better follows an inverse power law of time of the form of (3.6). The figures 3.12 a, b and c show the cumulative number of AEs $N_a(t)$ in the last 35 seconds prior to failure at $Pc = 30$ MPa, $Pc = 45$ MPa and $Pc = 60$ MPa respectively. The cumulative number of AEs results from the stacking of all AE sequences and is averaged over all sequences. This allows us to conserve the smooth shape of the cumulative total number of AEs and to compare between the experiments the average number of precursory AEs during individual sequence. Thus we can express $N_a(t)$ as:

$$N_a(t) = \frac{K}{(c + \Delta t)^p} \tag{3.7}$$

where Δt is the time to failure which is positive in that case. The red curves display the best fits that we obtained over the parameters c and p. The parameters p and c were searched in the range [0.1-3] with a step of 0.01. We made the choice to link K to c and p such as $K = N_f.(c^p)$ where N_f is the average cumulative number of AEs at the time of failure. This ensures that the average cumulative number of AEs at the time of failure equals N_f. The logarithm of the residuals is given by the inserted panels as a function of p and c. Residuals are normalized by the minimum (i.e., the value 0 indicates minimum). The best fits were obtained for $c = 2.39 \pm 0.3$ s and $p = 1.31 \pm 0.08$, $c = 0.6 \pm 0.25$ s and $p = 0.79 \pm 0.1$ and $c = 0.24 \pm 0.09$ s and $p = 0.82 \pm 0.05$ at $Pc = 30$ MPa, $Pc = 45$ MPa and $Pc = 60$ MPa respectively. Uncertainties correspond to the 90 % confidence level. The average AE rate is given by the time derivative of (3.7) such as:

$$\dot{N_a}(t) = -K\frac{p(c + \Delta t)^{p-1}}{(c + \Delta t)^{2p}} \tag{3.8}$$

which gives:

$$\dot{N_a}(t) = -K\frac{p}{(c + \Delta t)^{p+1}} \tag{3.9}$$

As we could have expected, the power exponent p is higher for the average AE rate. If we use the best values of p that we estimated, we obtained $p = 2.31$, $p = 1.79$ and $p = 1.82$ at $Pc = 30\ MPa$, $Pc = 45\ MPa$ and $Pc = 60\ MPa$ respectively. This values are larger that the typical values found for tectonic seismicity which are less or close to unity (Helmstetter and Sornette, 2003b). It should be noted that we have linked K to c and p which may affect the results. Indeed, the three parameters K, c and p are linked to each other. The commonest way to estimate them if to use the maximum likelihood method (Ogata, 1983). However, since we have linked K to c and p in the same way for each experiment and that N_f do not differ much (N_f equals 17, 13 and 14 at $Pc = 30\ MPa$, $Pc = 45\ MPa$ and $Pc = 60\ MPa$ respectively) we believe that the results obtained can be compared relative to each other. Most of the time, the seismicity rate, either it is for foreshocks or aftershocks, is only related to the parameter p. The physical meaning of c received far less attention while both will impact the seismicity rate. A decrease of c or an increase of p will result in a higher seismicity rate. At the laboratory scale, it has been demonstrated that p was increasing with increasing the strain rate (Ojala et al., 2004). A positive correlation between p and stress heterogeneity has also been proposed in the context of rate and state friction law (Dieterich, 1994). This would be consistent with the high value of p that we found at $Pc = 30\ MPa$ compared with the other two experiments since the fault surface presented higher roughness for this experiment (i.e. higher stress heterogeneity). The parameter c may control in a sense when the microseismicity starts. We can assume that precursory seismicity (precursory AE activity in the present case) may occur at earlier time in the case of an heterogeneous medium. This will have a counter effect on the seismicity rate since the rupture of the locked brittle patches of the fault plane will be more diffuse in time. In that case the parameter c will increase and the seismicity rate will decrease. This may explain why we found an higher value of c for the experiment conducted at $Pc = 30\ MPa$. However, this is only speculation and would require further analysis and additional data to be validated.

According to (3.9) and using the best parameters for c and p that we obtained, we find that the average AE rate is about 5 times larger at $Pc = 60\ MPa$ compared with $Pc = 30\ MPa$ and about two times larger $Pc = 45\ MPa$ compared with $Pc = 30\ MPa$ at the time of failure. This correlates well with the fault velocity. If we compare with the average fault slip velocity in the last tenth of a second we find that the fault slip rate is about four times larger at $Pc = 60\ MPa$ (about 4 $\mu m/s$) compared with $Pc = 30\ MPa$ and about three times larger at $Pc = 45\ MPa$ compared with $Pc = 30\ MPa$. Given the good correlation that we found between the shape of the cumulative number of AEs prior to failure and the fault velocity along the fault (Figure 3.9), we suggest that the AE rate close to rupture initiation is primarily controlled by slip acceleration. However, it should be noted that this is only valid on average since precursory AE sequences exhibit variable behaviors with respect to each other.

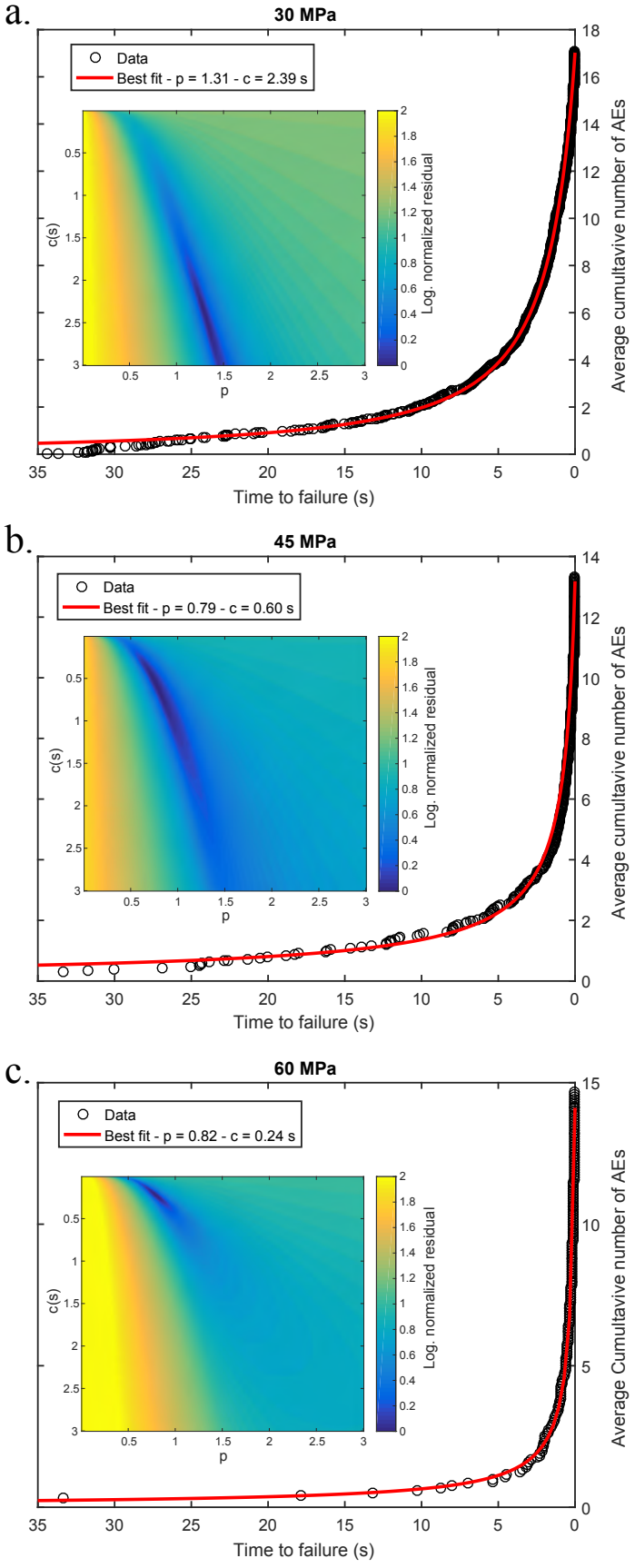

FIGURE 3.12: Inverse power law of time of the average cumulative number of AEs towards failure at: **a.** $Pc = 30\ MPa$, **b.** $Pc = 45\ MPa$ and **c.** $Pc = 60\ MPa$. The red curves indicate the best fits obtained on parameters c and p. The inserted figures display the logarithm of the residuals normalized by the minimum (i.e., 0 indicates the minimum) as a function of c and p.

3.5 Scaling laws and implications for natural fault

AE source parameters

Earthquakes having a moment magnitude M_w of -4 to 8 satisfy the scaling relationship $M_0 \propto f_c^3$ (Aki, 1967; Abercrombie, 1995; Hiramatsu et al., 2002; Prieto et al., 2004; Yamada et al., 2007; Kwiatek et al., 2011). The question whether the AEs generated during laboratory experiments are similar to earthquakes will determine if knowledge obtained in the laboratory can be extrapolated to the natural field. The figures 3.13 a, b and c display the estimated corner frequencies f_c of AEs versus their seismic moment M_0 and their moment magnitude M_w at $Pc = 30\ MPa$, $Pc = 45\ MPa$ and $Pc = 60\ MPa$ respectively. Errorbars for the estimated corner frequencies and moment magnitudes are indicated in light gray. We recall that we could not estimate f_c for the AEs with moment magnitudes less than $M_w - 8.6$ due to too low signal to noise ratio neither for the AEs with $M_w > -7$ due to the saturation of the acoustic sensors. The figure 3.13 d shows the comparison between the AEs source parameters and a corpus of other studies which gathers natural earthquakes and laboratory generated AEs having moment magnitudes of -4 to 4. The figure 3.13 d was re-adapted from the study of Yoshimitsu et al. (2014).
According to the expected scaling relationship between M_0 and f_c we find no differences between the AEs and the natural earthquakes. AEs have corner frequencies that mostly range from 300 kHz (source size $\approx 3\ mm$) to 1.5 MHz (source size $\approx 0.5\ mm$). The average stress-drops we obtained are 1 MPa, 0.88 MPa and 0.68 MPa at respectively $Pc = 30\ MPa$, $Pc = 45\ MPa$ and $Pc = 60\ MPa$. Quite surprisingly, we find that larger AEs have larger stress-drops. This might be directly related to insufficiently well calibrated acoustic sensors. Using momentum transfer from a ball drop for acoustic sensors calibration McLaskey et al. (2015) showed that the peaks of resonance that characterize the instrumental response of an acoustic sensor were diminished under confinement. Because the acoustic sensors were calibrated under atmospheric pressure, it is possible that particular frequency bands were artificially over damped. Thus, corner frequencies lower than these frequency bands would not be well estimated. Another possibility is that the length of the time window that we used (50 μs centered on the theoretical first S-wave arrival) to compute the spectra was too long to sufficiently reduce the energy coming from surface waves. Surface waves carry high-frequency energy which, thus, will be contained into the spectra. As we expect surface waves to be less attenuated for larger AEs this would be consistent with overestimated corner frequencies for the largest AEs. However, this feature might also be related to true characteristics of the AEs. Large AEs tend to occur closer to stick-slip instability when the stressing rate is higher due to accelerating aseismic slip which will thus result in larger stress-drops for larger AEs.
Source parameters of the generated AEs during our experiments suggest that the latter can be considered as microearthquakes. In a sense, AEs might be closer to natural earthquakes than SSEs since they involve the rupture of portions of the simulated

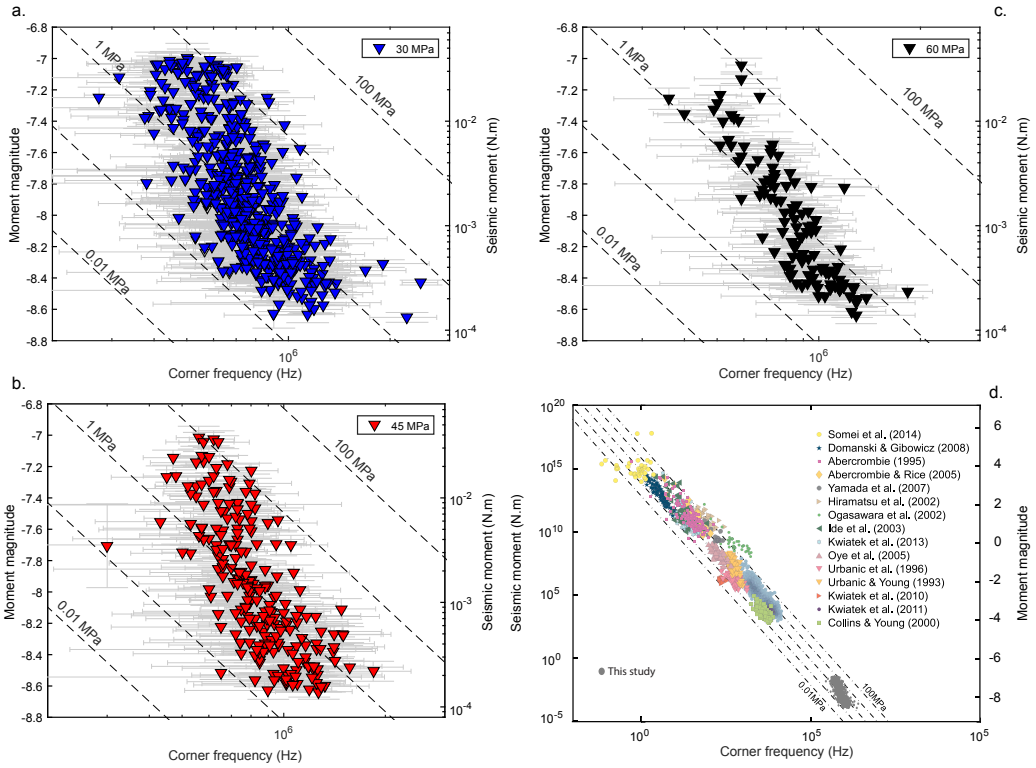

FIGURE 3.13: Relationship between M_0 and f_c at: **a.** $Pc = 30\ MPa$, **b.** $Pc = 45\ MPa$ and **c.** $Pc = 60\ MPa$. Dashed black lines represent stress drops of 0.01, 0.1, 1, 10, 100 MPa from Madariaga's source model (Madariaga, 1976). **d.** The AEs source paramters for all the experiments are plotted as gray circles. The other points represent a corpus of previous studies and were taken from Yoshimitsu et al., 2014.

fault that are contained in an elastic material with the same mechanical properties.

Pre-seismic moment and coupling

We inferred that in our experiments, SSEs initiated as slow but accelerating aseismic fault slip that was driving the occurrence of the precursory AEs. The figure 3.14 a compares the total AE moment release per SSE M_a with the pre-seismic moment release M_p. Note that we report here only the precursory AE sequences that do not include saturated AEs which equates to 67 SSEs out of 97. The figure 3.14 b shows the pre-seismic moment release as a function of the co-seismic moment release. Our data (diamond symbols) are plotted together with the observations made by two previous experimental studies (Passelègue et al., 2017; Acosta et al., 2019, grey symbols). The inserted figure displays the comparison between our observations made on M_p and M_c and what was found for a set of large earthquakes. These earthquakes are the 1999 Mw 7.6 Izmit earthquake (Bouchon et al., 2011), the 2011 Mw 9.0 tohoku-Oki earthquake (Kato et al., 2012), the 2012 Mw 7.6 Nicoya earthquake (Voss et al., 2018), the 2014 Mw 8.2 Iquique earthquake (Socquet et al., 2017) and the 2015 Mw 8.4 Illapel earthquake (Huang and Meng, 2018). The pre-seismic moment release

and the co-seismic moment release were estimated according to $M_{p,c} = \mu D_{p,c} S$ with μ being the gabbro shear modulus ($\mu = 40\ GPa$), S the surface of the fault and D_p and D_s the pre-seismic slip and the co-seismic slip respectively. It should be noted that M_p is an upper bound since the nucleation zone might be smaller than the total surface of the fault.

The total AE moment release prior to nucleation represents only a very small percentage of the pre-seismic slip (Figure 3.14 a). The ratio between both ranges from about 5.10^{-7} (5.10^{-5}%) to 4.10^{-4} (0.04 %). Such a low coupling is consistent with the fact that the SSEs principally nucleate after slow but accelerating aseismic fault slip that reaches the critical length of nucleation L_c. It is likely that cascading failure processes would require the rupture of sufficiently large locked portion of the fault to propagate over the entire fault which might explain why SSEs do not begin as small dynamic instabilities that rapidly grow into larger ruptures. However and without a doubt, the precursory AE sequences that include saturated AEs imply higher coupling. The largest number of oversaturated ($M_w > 6.8$) AEs was generated prior to SSE #53 at $Pc = 30\ MPa$. Let us assume a drastic scenario in which all of them would have been $M_w \approx 6.0$ AEs. But, even in that hypothetical case, we estimate that the coupling would be still low, of the order of 0.2%.

We find a relationship between the total AE moment release M_a and the pre-seismic moment M_p which indicates that M_a goes as M_p^4. In the case of an isotropic expansion of a circular crack with length L the moment release inside the crack would scale as $\Delta\tau L^3$ Madariaga, 1976. For a self-similar crack, the amount slip D inside the crack scales with its length L. Therefore, by making the approximation that the nucleation zone expands in the same way that a self-similar circular crack, we could have expected that M_a goes as M_p^3. The fact that M_a scales as M_p^4 can only be explained if the AEs have their stress-drops that scale with their sizes which would be consistent with the AEs source parameters that we obtained (Figure 3.13). Extending this scaling relationship to larger pre-seismic moments would rapidly lead to 100 % of coupling. Taking the experiment conducted at $Pc = 45\ MPa$, as an example, M_a would equal M_p for $M_p \approx 10^{4.5}\ N.m$. $M_p \approx 10^{4.5}\ N.m$ equates an amount of pre-slip of about 300 μm. If we consider a ratio of M_p/M_c of about 5% this implies a co-seismic slip displacement of about 6 mm. Assuming a linear scaling between the co-seismic displacement and the rupture length, 6 mm of coseismic slip is expected for an earthquake of magnitude Mw about 3.5-4. A recent study (Tamaribuchi et al., 2018) investigated the foreshock activity characteristics using the JMA catalog over the last 20 years. Despite the fact that the magnitude of the largest foreshock within a sequence scales with the magnitude of the mainshock, it has been observed that many mainshocks are not preceded by foreshock activity, at least not by foreshocks of $Mw > 1.0$ (the completeness magnitude of the catalog). Moreover, there are numerous foreshock sequences associated with mainshocks of magnitude $Mw \geq 3.5$

for which the magnitude of the largest foreshock is at least 2 orders of moment magnitude less than that of the mainshock. If 100 % of coupling was consistently expected during nucleation, we would expect to observe very often intense foreshock activity prior to the time of the mainshock. One possibility is that the power law 4 that we find between M_a and M_p is related to the experimental conditions such as the rapid loading which likely prevents healing, the smoothness of the fault which may promote pre-slip or its simple geometry which could favor smooth acceleration of the fault plane during nucleation.
In a recent study, Acosta et al. (2019) argued that the pre-seismic moment release M_p should scale with the co-seismic moment release M_c. This scaling relationship is expected if the fracture energy G of earthquakes increases as a power law of their co-seismic displacement (Abercrombie and Rice, 2005; Ohnaka, 2013; Passelègue et al., 2016) such as:

$$G = a u_{cos}^{\alpha} \tag{3.10}$$

where a is a scaling pre-factor and α is a given power and u_{cos} is the co-seismic displacement. The following empirical scaling relation between M_p and M_c was proposed (indicated by the slope of 0.56, figure 3.14 b):

$$M_p \propto M_c^{0.56} \tag{3.11}$$

On average, M_p represents about 4 %, 6 % and 2 % of M_c at $Pc = 30\ MPa$, $Pc = 45\ MPa$ and $Pc = 60\ MPa$ respectively. This is slightly less that what was found by Passelègue et al. (2016) and Acosta et al. (2019) but is typically of the same order of magnitude. If we only look at the experimental data (Figure 3.14 b.), it is hard to distinguish if M_p scales as $M_c^{0.56}$. Experimental observations may also simply indicate a linear relation between M_p and M_c as given by the slope of 1. Although the nucleation phase can not be appropriately examined through geodetic measurements for most earthquakes (either due to the lack of instrumentation or to the small earthquakes magnitude), well instrumented large interplate earthquakes form exceptions. Excepted for the 1999 Mw 7.6 Izmith earthquakes, the examples that we show in figure 3.14 b were associated with a ratio of M_p/M_c that ranges from about 0.4 % to 3 %. All those earthquakes have in common that their precursory moment was estimated using geodetic and/or repeater measurements. The precursory moment associated with the Mw 7.6 Izmith earthquake was inferred (Bouchon et al., 2011) only from repeaters and was about 6 orders of magnitude lower than the co-seismic moment. It is likely that the occurrence of repeaters in a short amount of time requires a fast reloading of stress. This is typically what is expected during nucleation since slip is accelerating up to the dynamic rupture. However, our observations suggest that the coupling may be extremely low during nucleation. Therefore, only relying on the seismic moment released by repeaters may underestimate M_p if a significant part of the precursory slip is accommodated aseismically. If we would

try to compare our results with what is typically observed for large interplate earthquakes, it suggests a simple linear relation between M_p and M_c (Figure 3.14). This would imply that the fracture energy is proportional to the co-seismic displacement. Note that different forms of (3.11) were proposed. For instance, under the context of slip-weakening theory and based on seismological observations, Abercrombie and Rice (2005) proposed that $M_p \propto M_c^{0.78}$.

If we compare the total AE moment release M_a with the co-seismic moment release M_p this yields that there is up to 8 orders of magnitude difference between M_a and M_c which corresponds to slightly less than 5 orders of magnitude difference in terms of moment magnitude M_w. This is intriguing since one of the commonest argument to claim that earthquakes begin as small instabilities that rapidly grow into larger ruptures (i.e. the so-called cascade model, Beroza and Ellsworth, 1996) is the lack of detectable foreshock activity prior to the mainshock. Nucleation process may be so silent that most of the time the nucleation phase cannot be detected. This requires additional experiments to be further discussed. It would be interesting to make vary the experimental conditions such as the initial roughness of the fault plane, the type of lithologie, the loading rate or by adding temperature.

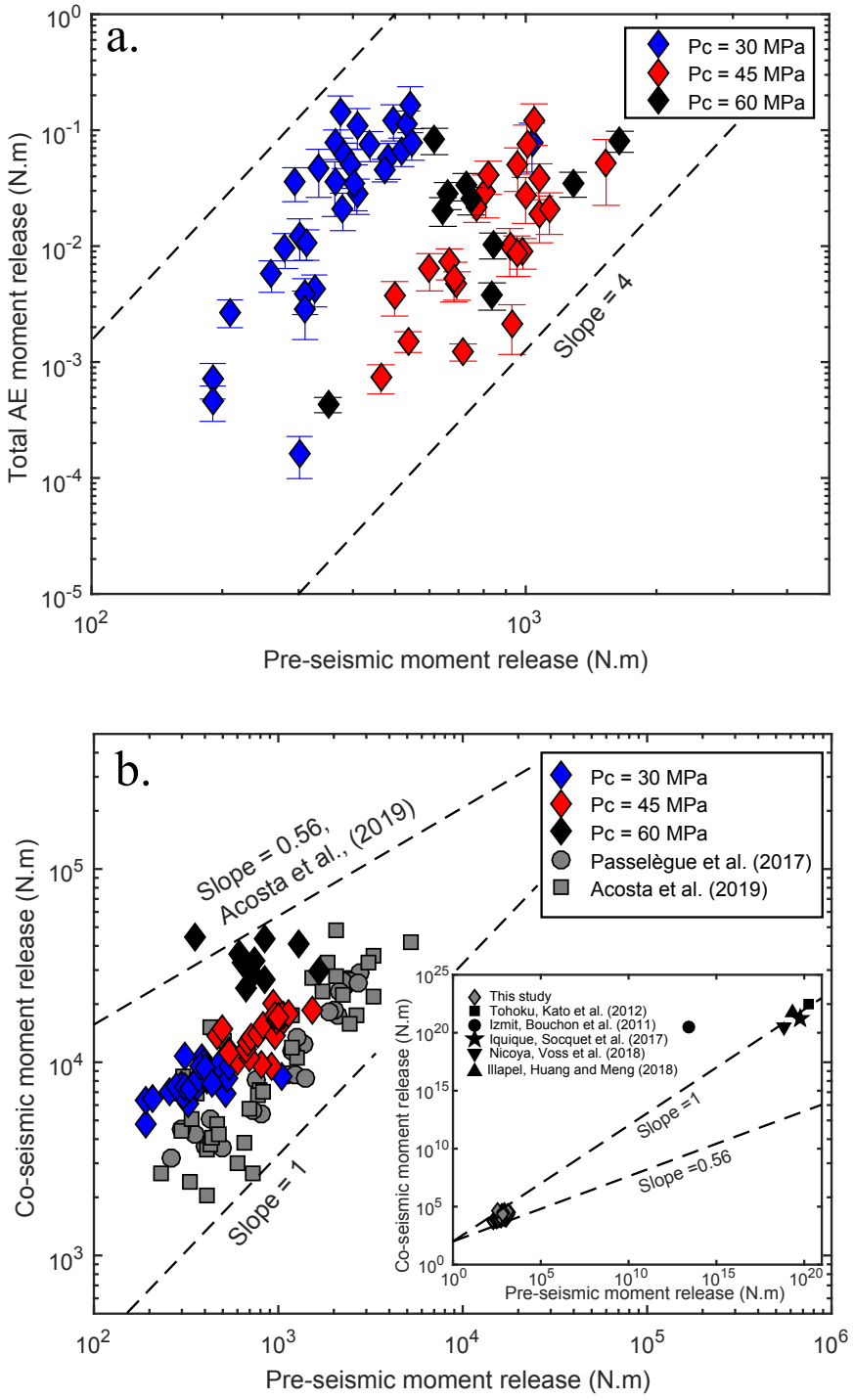

FIGURE 3.14: **a.** Relationship between the pre-seismic moment release and the total AE moment release. Each diamond represents one SSE. Only the AE sequences that do not contain saturated AEs are shown here. The black-dashed lines indicate a power-law exponent of 4. **b.** Relationship between the pre-seismic moment release and the co-seismic moment release. The grey squares and circles correspond to the observations of two other experimental studies (Passelègue et al., 2017; Acosta et al., 2019). The black dashed line which indicates a slope of 0.56 corresponds to the scaling law between the pre-seismic moment release M_p and the co-seismic moment release M_c proposed by Acosta et al. (2019). A linear relation between both is given by the black dashed line whose slope = 1. The inserted figure displays the comparison between our observations and what was found for a set of large earthquakes ($Mw \geq 7.6$).

Scaling of the AE moment release.

Here we attempt to give a quantitative explanation of the total AE moment release during the experiments. The reasoning is straightforward. During nucleation, the fault slip over a distance D and a surface S. Most of the slip is accommodated aseismically and a small fraction γ of this surface is released seismically via AEs. The total AE moment release during an individual AEs sequence which contains n AEs M_a can be expressed as:

$$M_a = \sum_n \mu.D_n.S_n \tag{3.12}$$

with μ the shear modulus of the gabbro (40 GPa), D_n the quantity of slip associated with the n'ieth AE and S_n the contact area of the source which equates to $2.\pi.a^2$ for a circular source whose radius is a. Thus (3.12) can be expressed as :

$$M_a = \mu.\gamma.D.S \tag{3.13}$$

We can assume that γ will depend on the available surface of contact A_c which will be a function of the roughness R and the applied normal stress σ_n due to elastic deformation. We will consider the simplest scenario in which fault surfaces can be approximated as a sum of non-adhesive contacts of elastic spheres with various radius r within an elastic half-space. Neglecting the depth of indentation of the elastic spheres in the elastic half-space, we find according to Hertz contact theory (Johnson, 1982) that the surface of contact S_r will scale as:

$$S_r \propto \sigma_n^{\frac{2}{5}} \tag{3.14}$$

thus

$$\gamma \propto A_c.\sigma_n^{\frac{2}{5}} \tag{3.15}$$

The available surface of contact A_c will be a function of the fault surface roughness at each wave number k in the directions orthogonal and parallel to slip such that

$$A_c \propto \sum_k (P_o(k)).^{\frac{1}{2}}.(P_p(k)).^{\frac{1}{2}} \tag{3.16}$$

with $P_o(k)$ and $P_p(k)$ the Fourier power spectrum of the fault surface elevations in the directions orthogonal and parallel to slip respectively. Therefore we can rewrite (3.15) as :

$$\gamma \propto \sigma_n^{\frac{2}{5}}.\sum_k (P_o(k)).^{\frac{1}{2}}.(P_p(k)).^{\frac{1}{2}} \tag{3.17}$$

and thus :

$$M_a \propto D.S.\sigma_n^{\frac{2}{5}}.\sum_k (P_o(k)).^{\frac{1}{2}}.(P_p(k)).^{\frac{1}{2}} \tag{3.18}$$

Thus according to (3.18) both the normal stress and the roughness will have a positive effect on A_c and thus on M_a. For of set of N AE sequences, the total AE moment release M_a^T related to all the AE sequences will simply be:

$$M_a^T \propto \sum_N D_N.S.\sigma_{n,N}^{\frac{2}{5}}.\sum_k (P_o(k))^{\frac{1}{2}}.(P_p(k))^{\frac{1}{2}} \tag{3.19}$$

with D_N the amount of pre-slip associated with N'ieth AE sequence. We will make the assumption that fault surfaces roughness do not vary much over the fault plane (comparatively to the sampled portion of the surface) and that pre-slip extends over the entire fault surface in all the experiments.
We have applied the preceding reasoning to our experimental data (Figure 3.15). On top is displayed the total AE moment release as a function of the normalized time to failure which results from the stacking of all AE sequences that do not contain saturated AEs (i.e. $Mw > 7$) and below the same but scaled according to (3.19). To be fully consistent, we integrated the Fourier power spectra $P_o(k)$ and $P_p(k)$ over the wavelengths smaller or equal to the typical size inferred for AEs with moment magnitudes Mw close to -7 which is of about 2 mm ($k = 5.10^2\ m^{-1}$). This gives that $\sum_k (P_o(k))^{\frac{1}{2}}.(P_p(k))^{\frac{1}{2}}$ for $k \geq 5.10^2$ is approximately equal at $Pc = 45\ MPa$ and $Pc = 60\ MPa$ (a factor of 1.1 between) but about three times larger at $Pc = 30\ MPa$ compared to the other two experiments.
The scaled AE moment release collapses almost perfectly at $Pc = 45\ MPa$ and $Pc = 60\ MPa$ (Figure 3.15 bottom) but is slightly overestimated at $Pc = 30\ MPa$ (about two times larger). However, this yields a satisfactory quantitative explanation of the amount of radiated energy (even if the latter is extremely low) during nucleation relying only on simple and accessible parameters that are the fault geometry, the amount of pre-slip and normal stress conditions.
Trying to do the same would probably fail in the case of natural earthquakes given the richness of the mechanical behaviors of fault systems. However, this kind of simple reasoning can be easily supplemented by implementing additional factors such as complex geometries, various rheologies, temperature or pore-fluid overpressure.

3.6 Summary

In this study, we continuously recorded the microseismicity generated during stick-slip experiments and analyzed the dynamics of precursory AEs prior to stick-slip instabilities. Using calibrated acoustic sensors we were able to analyze AE source parameters. According to the scaling laws that describe the frequency-magnitude distribution of earthquakes and that link the size of an earthquake to its magnitude,

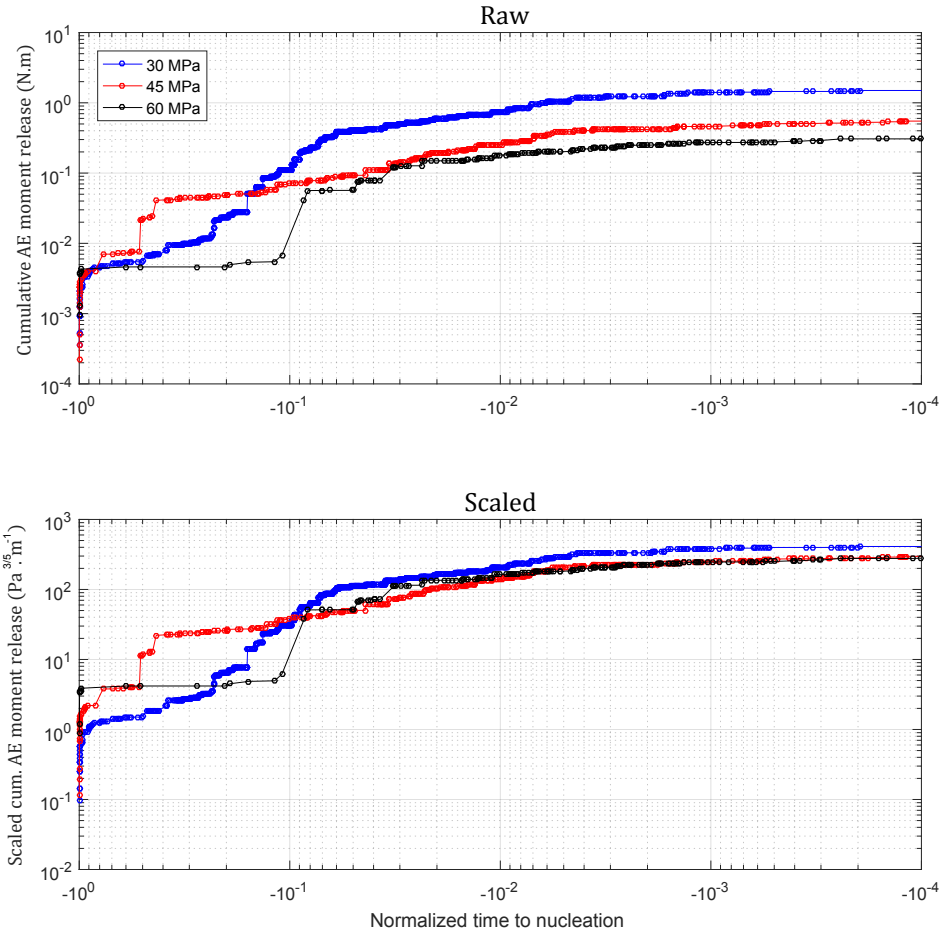

FIGURE 3.15: Scaling of the cumulative AE moment release with fault surface roughness and normal stress. On top is displayed the raw cumulative AE moment release in function of the normalized time to failure and below is displayed the same but scaled according to the fault surfaces roughness and to normal stress conditions. All curves result from the stacking of all the AE sequences excepted those which contained saturated AEs.

our results suggest that millimetric generated AEs can be fairly considered as microearthquakes. We found clear evidences that the occurrence of AEs was driven by fault slip acceleration during the nucleation phase of the stick-slip instability. The spatial and temporal behavior of precursory AEs towards failure shares similarities with the one of foreshocks towards mainshock. The AE rate rapidly accelerates as an inverse power law of the time to failure. Increasing the normal stress conditions onto the fault causes (i) an increase of AE rate prior to failure, which can be directly related to pre-slip acceleration, and (ii) promotes the migration of precursory AEs towards nucleation initiation. Relying on the fine AE and stick-slip nucleation locations together with comparing the pre-seismic moment release and the total AE moment release, we suggested that nucleation is an almost full aseismic process. This might therefore explain why most of the time, foreshocks are not detected preceding the mainshock. Finally, we argued, based on fault surface analysis, that fault strength heterogeneity controls the coupling of the fault. Higher the roughness, stronger the coupling. This was confirmed, at first order, by finding a simple scaling relation of the total AE moment release that only involves normal-stress, amount of pre-slip and roughness. As a consequence, topographical modifications of the fault during rapid slip episodes such as mechanical abrasion, plastic deformation processes or partial/complete melting of the fault may reduce or increase fault strength heterogeneity.

Chapter 4

Origin of high-frequency radiation during laboratory earthquakes

This chapter is an experimental study of the origin of high-frequency radiation during rupture propagation and of the influence of stress-state and rupture velocity on waves frequency content. The results presented here were published in the journal *Geophysical Research Letter* in February 2019. The article is inserted in the appendix.

Abstract

We monitor dynamic rupture propagation during laboratory stick-slip experiments performed on saw-cut Westerly granite under upper crustal conditions (10-90 MPa). Spectral analysis of high-frequency acoustic waveforms provided evidence that energy radiation is enhanced with stress conditions and rupture velocity. Using acoustic recordings bandpass filtered to 400-800 kHz (7-14 mm wavelength) and highpass filtered above 800 kHz, we back projected high-frequency energy generated during rupture propagation. Our results show that the high-frequency radiation originates behind the rupture front during propagation and propagates at a speed close to that obtained by our rupture velocity inversion. From scaling arguments, we suggest that the origin of high-frequency radiation lies in the fast dynamic stress-drop in the breakdown zone together with off-fault co-seismic damage propagating behind the rupture tip. The application of the back-projection method at the laboratory scale provides new ways to locally investigate physical mechanisms that control high-frequency radiation.

4.1 Introduction

Even though high-frequency waves (> 1 Hz) are likely to be the most damaging during earthquakes propagation, physical processes at the origin of high-frequency radiation are still under debate and relatively less well understood (Das, 2007). First kinematic models used to invert seismic slip distribution (Haskell, 1964; Savage, 1966) were unable to describe high-frequency radiation because they assumed flat

source models with constant slip and stress drop on the fault.
Fracture models which introduced variable slip function and rupture velocity showed that changes in rise time and rupture velocity lead to high-frequency radiation (Madariaga, 1977; Madariaga, 1983). Later, seismologists used ray-theory to calculate high-frequency radiation from earthquakes having spatial variations of rupture velocity, slip velocity and stress drop (Bernard and Madariaga, 1984; Spudich and Frazer, 1984) and predicted that the starting and stopping phases of earthquakes to be responsible of high-frequency radiation. A good illustration of this phenomena is the January 17th 1984 Northridge earthquake (Mw 6.7) for which Hartzell at al (Hartzell et al., 1996) identified the initiation of the rupture and its stopping to be concurrent with high-frequency radiation.
An interesting case of the rupture velocity effects on high-frequency radiation is that of earthquakes propagating at supershear velocities (i.e. velocities higher than the shear wave speed). Supershear earthquakes are suspected to be more devastating than sub-Rayleigh earthquakes (with rupture velocities slower than the S-wave velocity) due to the formation of Mach-wave fronts (Dunham and Archuleta, 2004; Bhat et al., 2007; Bruhat et al., 2016). Theoretical studies of supershear rupture (Hamano, 1974; Andrews, 1976; Das and Aki, 1977) followed by experimental works on plastic polymer (Wu et al., 1972; Rosakis et al., 1999) demonstrated the existence of possible supershear scenarios. Following the Mw 7.6 devastating Izmit earthquake in Turkey, Bouchon et al. (2001) successfully made the observation that certain parts of the fault ruptured at supershear speeds. Passelègue et al. (2013) were the first to experimentally illustrate the rupture transition from sub-Rayleigh regime to supershear regime on centimetric rock samples at upper crustal stress conditions. In these experiments, Passelègue et al. (2016) observed particularly energetic high-frequency radiation during stick-slip rupture propagation, the origin of which remained obscure.
Quite recently, the emergence of dense and large aperture seismic arrays has provided a new method to investigate the spatial and temporal behavior of seismic energy release during large earthquakes. This method, called back-projection, utilizes the time-reversal property of seismic waves to retrieve their sources and was introduced by Spudich and Frazer (1984). Following the successful application of the back-projection method to the 2004 Sumatra-Andaman earthquake by Ishii et al. (2005), the back-projection method has been applied to numerous earthquakes (Kiser and Ishii, 2011; Zhang and Ge, 2010; Ishii, 2011; Wang and Mori, 2011; Okuwaki et al., 2014). To the best of our knowledge, the technique has never been applied in the laboratory yet, where it might shed light on the origin of high-frequency radiation. This study presents results from stick-slip experiments conducted on saw cut Westerly granite under tri-axial conditions and is devoted to investigate the dynamics of high-frequency radiation during rupture propagation. First, the rupture velocity of dynamic stick-slip instabilities was measured using piezoelectric acoustic sensors by tracking the propagation of the rupture front. We then investigate the influence

of stress conditions and rupture velocity on high-frequency radiation. Second, we apply the back-projection method to image high-frequency sources during rupture history and discuss their link to rupture front propagation.

4.2 Experimental set-up and methodology.

Here, we summarize the experimental set-up used in the experiments and the methods yo process and analyse the data. A detailed description is given in chapter 2.
All experiments were conducted on Westerly granite under triaxial stress conditions (section 2.1.2). Stick-slip nucleation was located using first P-wave arrivals recorded by the far-field acoustic sensors (section 2.3.3). Rupture velocities were estimated according to rupture front arrivals to near-field acoustic sensors (section 2.4.1). Finally, back-projection analysis (section 2.4.2) were performed on far-field acoustic sensor recordings (Figure 2.7, section 2.1.3).

4.3 Results

4.3.1 Mechanical behavior of stick-slip instabilities

Stick-slip experiments presented in this study were performed at confining pressure Pc ranging from 10 to 90 MPa. All experiments were conducted using a similar fault geometry and imposing a constant displacement rate resolved on the fault plane of around 1 $\mu m/s$. Figure 4.1 a reports the evolution of both shear stress and fault slip with time for a stick-slip experiment at 60 MPa confining pressure. Increasing the axial stress leads first to the elastic increase of both shear stress and normal stress acting on the fault plane. Once the shear stress reaches a critical value τ_c, corresponding to the critical strength of the fault, slip initiates leading to an abrupt stress release. The stress drop is proportional to the slip and both increase with the confining pressure. Regardless of the confining pressure, the system displays the same mechanical behavior. Figure 3.4 b shows that slip increases linearly with the stress drop for all stick-slip experiments. The slope is equal to the stiffness of the whole system (machine and rock specimen). This has been observed in many other experiments on crustal rocks and can be explained by the increase of the normal stress on the fault with increasing in confining pressure, which enhances the strain energy stored in the medium during loading (Brace and Byerlee, 1966; Byerlee and Brace, 1968; Johnson et al., 1973; Johnson and Scholz, 1976; Passelègue et al., 2016).

4.3.2 Influence of rupture velocity and confining pressure on high-frequency radiation

Rupture velocities during stick-slip instabilities were estimated according to rupture front arrivals to near-field acoustic sensors. Figures 4.2 a and 4.2 b show examples of near field acoustic sensor recordings and theoretical rupture front arrivals (dashed

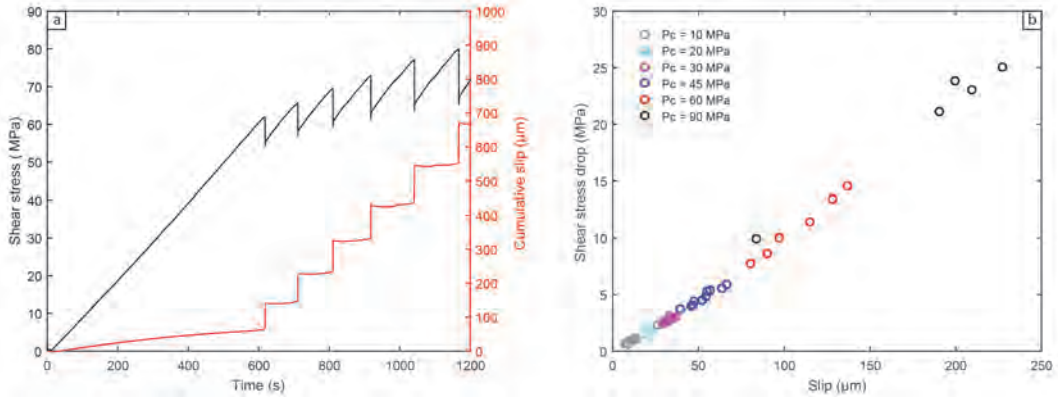

FIGURE 4.1: **a.** Evolution of shear stress and slip versus time at $Pc = 60MPa$. When the shear stress on the frictional interface exceeds the fault strength the stored elastic is suddenly released by seismic slip. The cumulative slip remains constant during loading because it is corrected from the elastic part of the deformation (sample + apparatus). **b.** Relationship between shear stress drop and slip for all experiments. The ratio between the stress drop and the slip is preserved (higher the stress drop, higher the amount of slip) and is equal to the stiffness of the whole system (sample + apparatus).

blue lines) according to the estimated rupture velocities for one stick-slip event event whose rupture propagated at supershear speed ($V_r \approx 5100m/s$) and for one stick-slip event that propagated at sub-Rayleigh speed ($V_r \approx 1800m/s$). Waveforms have been aligned with respect to their distance to the nucleation. The original time corresponds to the initiation of the dynamic instability and all traces were normalized by their maximum amplitude. Theoretical P and S wave arrival times are also indicated by the black and red dashed lines respectively. Figures 4.2 c and 4.2 d display time residual as a function of the rupture velocity for both stick-slip events. As we could have expected for acoustic sensors positioned close to the nodal plane we do not observe P-wave arrivals. Indeed, P-wave amplitude close to the nodal plane drops to zero which is convenient because it avoids ambiguity between what we could interpret as the rupture front and the first P-wave arrival.

To demonstrate the occurrence of supershear ruptures, we predicted the theoretical time arrivals of the Mach wave front which forms during the propagation of supershear ruptures. According to the referential defined in Figure 4.3 a, the theoretical arrival time of the Mach wave front is the sum of the time required for the rupture tip to reach the point E at the rupture velocity along the fault length and the time required for the Mach wave to travel the distance ES at the shear wave speed (Note that the Mach wave propagates at the shear wave velocity in the normal direction to its propagation front). The theoretical arrival time of the Mach wave t_m front at the receiver S is then a function of the rupture velocity and can be expressed as follow:

$$t_m = \frac{Z_c}{C_s.sin(\beta)} + \frac{NE}{V_r} \tag{4.1}$$

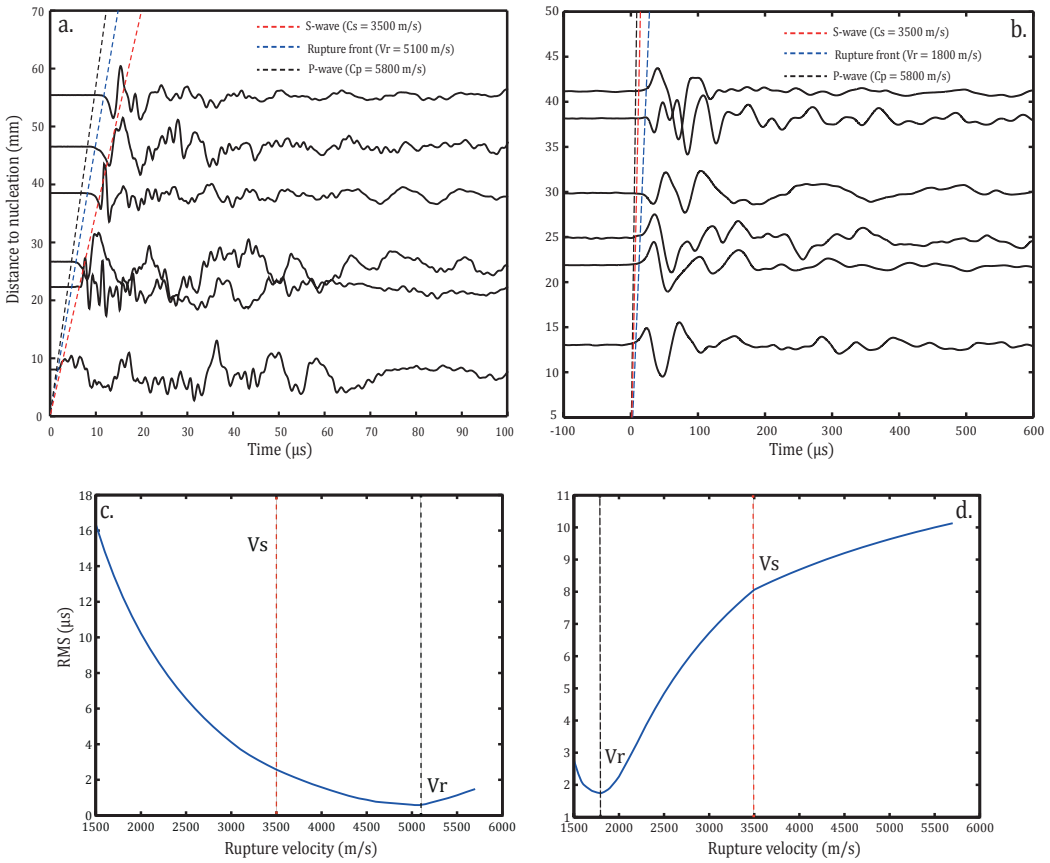

FIGURE 4.2: **a.** Travel time plot of near field acoustic recordings in function of their distance to the nucleation for one stick-slip event that ruptured at supershear speed. Blue, black and red dashed lines represent isochrones of rupture front arrivals and first P and S wave arrivals respectively. **b.** Same as (**a**) but for a sub-Rayleigh rupture. **c.** Time residual as a function of rupture velocity for the supershear event. **d.** Same as (c) but for the sub-Rayleigh event.

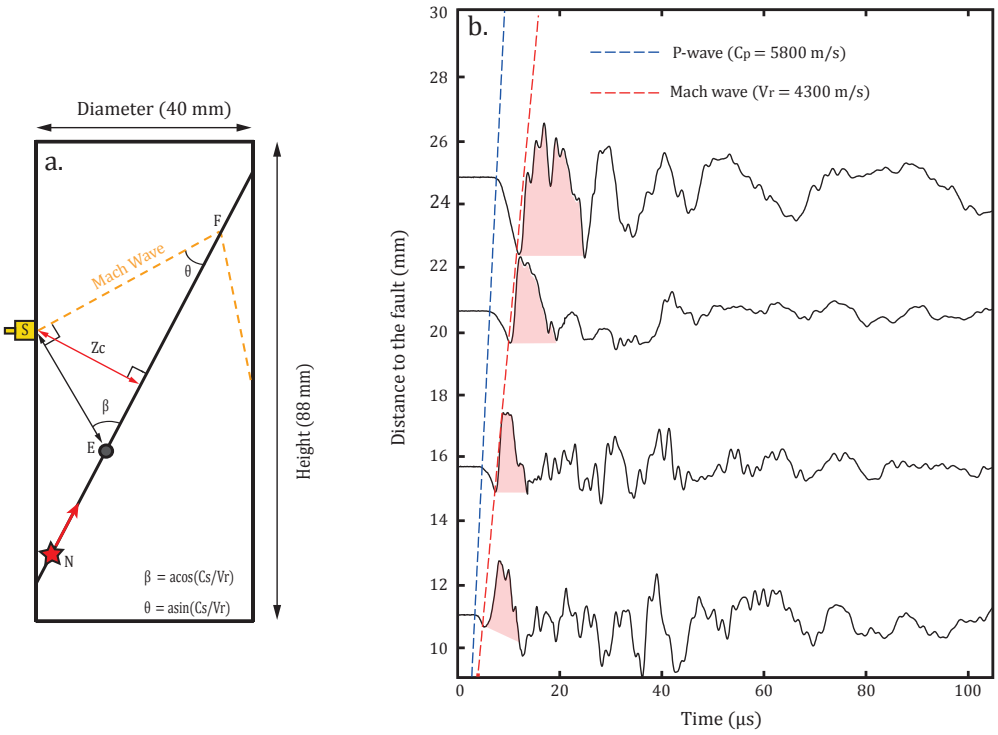

FIGURE 4.3: **a.** Schematic view of the arrival to a receiver S at distance Z_c to the fault of a Mach front emitted from a single point E. The position of the nucleation is indicated by N. **b.** Waveforms recorded by 4 far-field acoustic sensors positioned at different distances Z_s to the fault during a supershear event at $Pc = 45\ MPa$. Blued and red dashed lines represent the first P-wave and S Mach front arrivals respectively. The Mach wave corresponds to the light red area.

In particular, we are searching for Mach wave front arrivals for ruptures that nucleate at one end of the fault so the Mach wave has the time to develop and for ruptures that propagate at velocities faster than the shear-wave and different from $\sqrt{2}.C_s$ for which no Mach wave is expected. Figure 4.3 b displays the waveforms recorded by 4 far-field acoustic sensors positioned at various distances to the fault for one stick-slip event at $Pc = 45\ MPa$ whose estimated rupture velocity was equal to 4300 m/s. Acoustic sensors were first hit by the compressional-dilatational wavefield (indicated by the blue dashed line in Figure 4.3 b) which corresponds to the continuous emission of P-waves at the rupture tip during rupture propagation. As we could have expected for a rupture that nucleated at one end of the fault interface, first-motion polarities are the same. Following first P-wave arrivals, we observe the arrival of a coherent and dominant wave front. The arrival times of this wave front are fairly consistent with the predicted arrival times of the Mach wave front, represented by the red dashed line (Figure 4.3 b). It, in part, attests to the reliability of our method to invert the rupture velocity and that supershear ruptures were generated during the experiments.

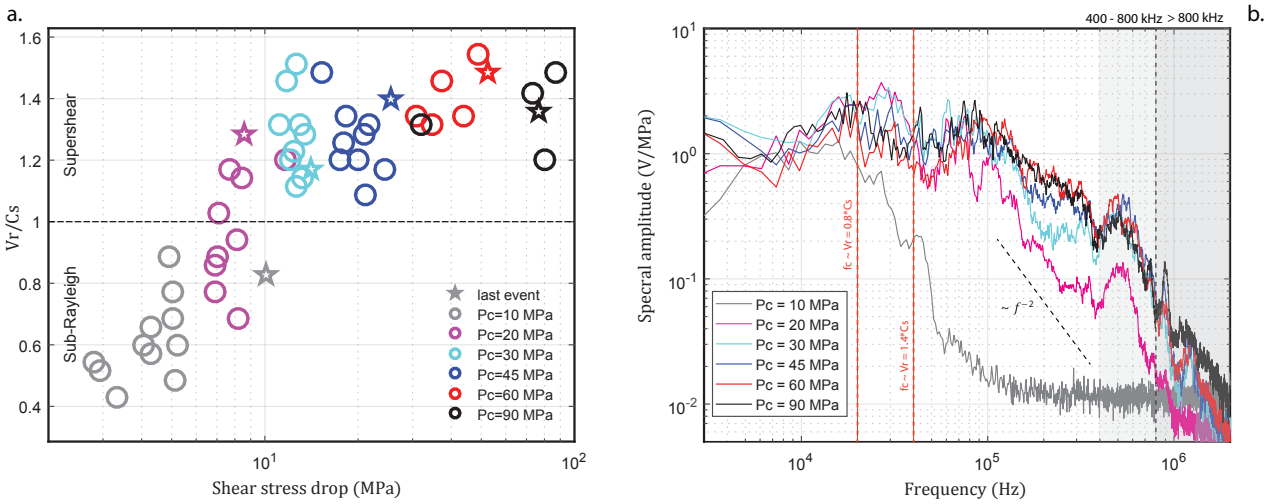

FIGURE 4.4: **a.** Rupture velocities obtained by inversion as a function of static shear stress drop. Rupture velocities are normalized by the shear wave velocity, values higher than 1 correspond to supershear velocity and lower than 0.92 to sub-Rayleigh velocities. Stars indicate stick-slip events whose Fourier spectra are displayed in Figure 4.4 b. **b.** Fourier spectra of the last stick-slip event during stick-slip experiments at varying confining pressures. Fourier spectra are averaged using both near-field and far-field acoustic sensors, and normalized by their respective stress-drop. The gray shaded areas indicate frequency bands used for the back-projection analysis.

The relation between the inverted rupture velocities, the stress drop and the confining pressure is shown in Figure 4.4 a. Rupture velocities are normalized by the S-wave velocity of the medium, values under 0.92 correspond to sub-Rayleigh ruptures and values above 1 correspond to supershear ruptures. The overall trend of the rupture velocity is to increase with confinement and stress drop. For stress drops higher than 10 MPa, only supershear ruptures are observed which is consistent with the observations made by Passelègue et al. (2013). This general trend and the prevalence of supershear ruptures at high confinement can be understood in terms of the seismic ratio S and the initial strength that precedes the rupture. S decreases with increasing the confining pressure and controls the transition from sub-Rayleigh to supershear rupture (Andrews, 1976) and can be expressed as:

$$S = \frac{\tau_p - \tau_0}{\tau_0 - \tau_r} \tag{4.2}$$

Where τ_p,τ_0 and τ_r are respectively the peak frictional strength, the initial strength and the residual frictional strength. In our study we did not use dynamic strain gages, therefore we could only have access to τ_0 through external measurements but not τ_p and τ_r. However, the seismic ratio S can be related to the static friction coefficient τ_0/σ_n with the following formula (Ben-David et al., 2010):

$$\frac{1}{1+S} = \frac{1}{f_s - f_d} \cdot \frac{\tau_0}{\sigma_n} - f_d \tag{4.3}$$

Where f_s and f_d are the static friction coefficient and the dynamic friction coefficient respectively. Assuming $f_s = 0.85$ and $f_d = 0.1$ we reported in figure 4.5 the linear relationship between $1/1 + S$ and the static friction coefficient τ_0/σ_n. Theoretically, ruptures may transition from sub-Rayleigh to supershear velocity if the two following conditions are satisfied: (i) the size of the fault is larger than the transition length from sub-Rayleigh to supershear propagation L_c and (ii) S is smaller than S_c (equal to 1.77 or 1.19 in 2D or 3D respectively). The transition length L_c is inversely proportional to the normal stress σ_n and is expressed by the following semi-empirical relation:

$$L_c = \frac{39.2}{\pi(1-\nu)} \cdot \frac{1}{(S_c - S)^3} \cdot \frac{\mu G}{[\sigma_n.(\frac{f_s - f_d}{1+S})]^2} \tag{4.4}$$

Where ν, μ and G are the Poisson ratio, the shear modulus and the fracture energy respectively. In 3D, $S_c = 1.19$ gives $1/1 + Sc \approx 0.45$, then $S < S_c$ was always satisfied in the experiments (Figure 4.5). Taking $\nu = 0.25$, $\mu = 35\ GPa$ and assuming a lower bound for G of $10 J/m^2$ ($G = 10\ J/m^2$ is the typical value found for stick-slip experiments conducted at low stress conditions, Ohnaka, 2003, we find that L_c is of the order 10 cm for $\sigma_n = 10MPa$ which is larger than the size of the fault. L_c drops rapidly to about 2 cm for $\sigma_n = 30MPa$. This might explain why ruptures at low confinement ($Pc = 10MPa$) were sub-Rayleigh while supershear ruptures became a normal phenomena for $Pc \geq 30MPa$ (Figure 4.4 a). It is likely that on a larger fault, stick-slip events at low confinement would have transition to supershear regime.

In Figure 4.4 b the Fourier spectra that correspond to the last stick-slip event at each confining pressure are displayed (star symbols, Figure 4.4a). Directivity effects cannot be fully suppressed because our acoustic sensor network is not perfectly symmetric. Hence Fourier spectra were averaged over all acoustic sensors (i.e. from both near-field and far-field acoustic sensor arrays) in order to minimize directivity bias. To compare the high-frequency content of the spectra, the latter have to scale at low frequency. As we expected the stress-drop to control the amplitude of low frequency waves, each spectrum is normalized by its corresponding stress-drop. We find a double correlation between the spectral amplitude of high-frequency radiation, the rupture velocity and the confining pressure. This is particularly well illustrated at the lowest confining pressure (Pc = 10 MPa), where stick-slip events ruptured at sub-Rayleigh velocity. The Fourier spectrum of these events is strongly depleted of high frequencies. In contrast, the effect of the confining pressure prevails over the effect of the rupture velocity, in the high-frequency radiation range,

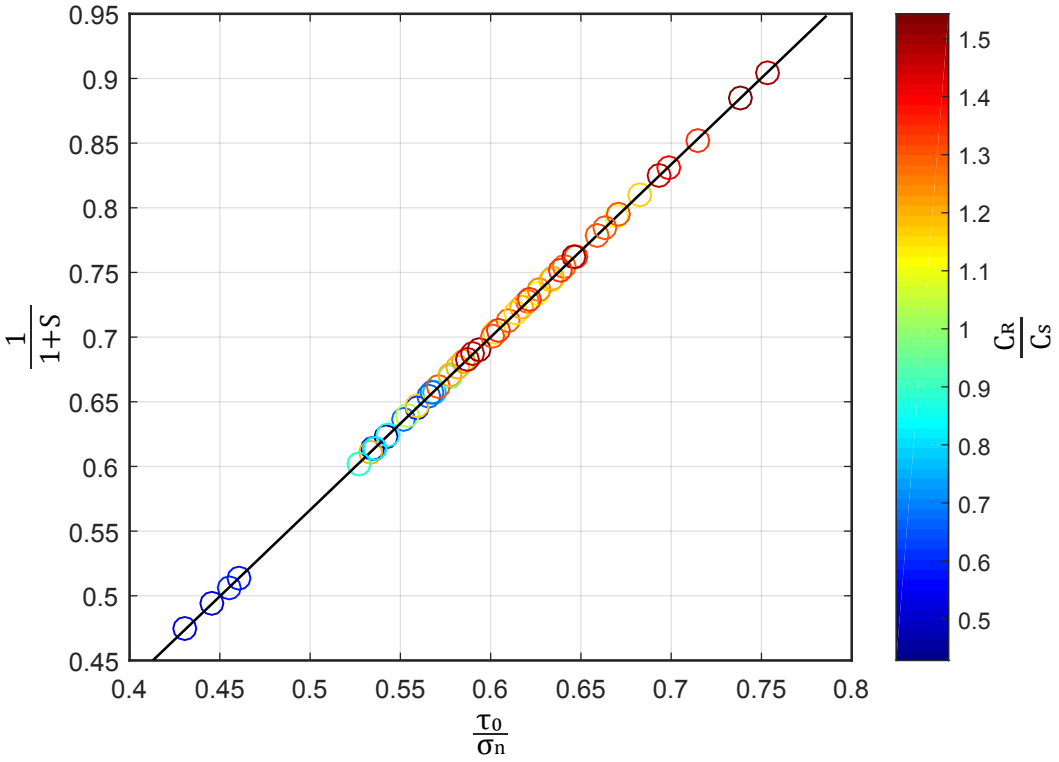

FIGURE 4.5: Relationship between the static friction coefficient and the Seismic ratio according to eq. (4.3).

when comparing the spectra at Pc = 20 and 30 MPa (Vr = 4500 and 4100 m/s respectively). Similarly, the Fourier spectra at Pc = 45, 60 and 90 MPa which correspond to the highest rupture velocities (Vr = 4900, 5200, 4700 m/s respectively) are the most enhanced in high-frequency radiation. Note that at $Pc \geq 20MPa$, we consistently observe the emergence of two frequency bands. The first one is centered at 100 kHz and the second one lies between 400 and 800 kHz. In the following section, we show results of back-projection analysis applied to acoustic waveforms (i) bandpass filtered to 400-800 kHz and (ii) highpass filtered above 800 kHz.

4.3.3 Back-projection analysis during rupture propagation.

Unfiltered and band-pass filtered between 400 and 800 kHz far-field waveforms are displayed in Figure 4.6. Waveforms are lined up with the first P-wave arrivals at each station. Only filtered waveforms were used for back-projection. We implicitly make the hypothesis that high-frequency sources are located on the fault plane. This assumption seems reasonable given that new fracture formations were never observed during any of the experiments performed for this study. Because the acoustic sensors are sensitive to only one component of surface vibration, we are not able to distinguish between P and S, surface waves and reverberations, which would make the back-projection results poorly resolved. As a consequence, the back-projection analysis are restrained to the beginning of the acoustic waveforms, i.e. before first S-wave arrivals at each station (on average, 6 μs after first P-wave arrivals). P-wave

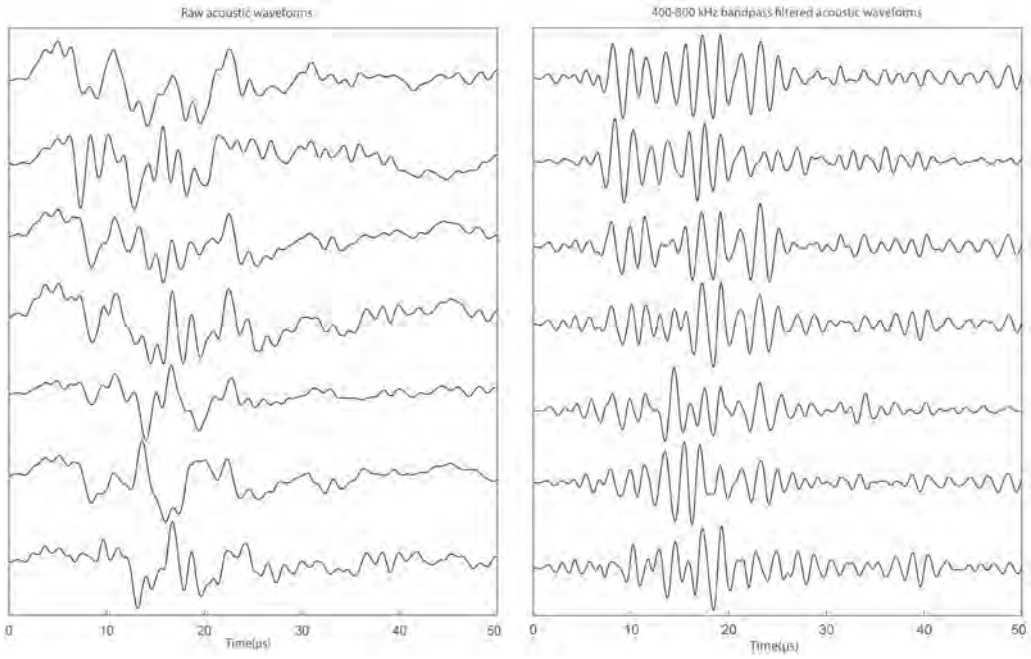

FIGURE 4.6: Acoustic waveforms used for the back-projection analysis displayed in Figure 4.7: raw acoustic waveforms (left) and band-pass (400-800 kHz) acoustic waveforms (right). Waveforms are aligned on the first P-wave arrivals and are normalized by their maximum amplitudes

signals are back-projected on the fault plane by computing the coherency function over 2 μs time windows, with respect to the nucleation time.

Figure 4.7 presents back-projection results in the 400-800 kHz frequency band (top) and above 800 kHz (bottom) for one event at Pc = 90 MPa whose average rupture velocity was 5.1 km/s and which nucleated at one end of the fault plane. The colorbar indicates the value of the coherency function normalized by its maximum value. The red star indicates the position of the nucleation and the black dashed line the theoretical position of the rupture front (at 1 μs for the 0-2 μs time window, at 2 μs for the 1-3 μs time window and so on) according to the estimated rupture velocity in section 4.2.2. In the supershear case, this theoretical rupture front is elliptical and propagates at constant velocities C_s and V_r along the ellipse's minor and major axes respectively, where C_s and V_r are the S-wave and in-plane rupture velocities.

The 400-800 kHz frequency band (Figure 4.7 top) gives the clearest results. Throughout the rupture history, high-frequency energy sources are always localized behind the theoretical rupture front position. When rupture initiates (0-2 μs) high-frequency energy localizes slightly behind the nucleation and spreads over the width of the fault plane. At t = 1-3 μs period, high-frequency energy starts to propagate consistently in the direction of the rupture front at relatively low speed and spreads over the entire width of the fault. The source of high-frequencies then accelerates (2-4 μs) along the fault plane until it roughly reaches the average rupture velocity (3-5 μs, 4-6μs) while concentrating in the middle of the fault. Compared to the 400-800

kHz frequency band, back-projection images for high-frequency sources above 800 kHz (Figure 4.7 bottom) are less clear. When rupture initiates (0-2 μs), the maximum coherence is still focused close to the nucleation zone. It was also observed that the maximum coherence propagating consistently matched the theoretical rupture front (1-3 μs, 2-4 μs, 3-5 μs), although high-frequency energy was more diffuse and patchy. In contrast, between 4-6 μs, high-frequency energy starts to diffuse over the entire fault. Also, relative to high-frequency energy between 400-800 kHz, high-frequency energy above 800 kHz is always focused closer to the theoretical rupture front.

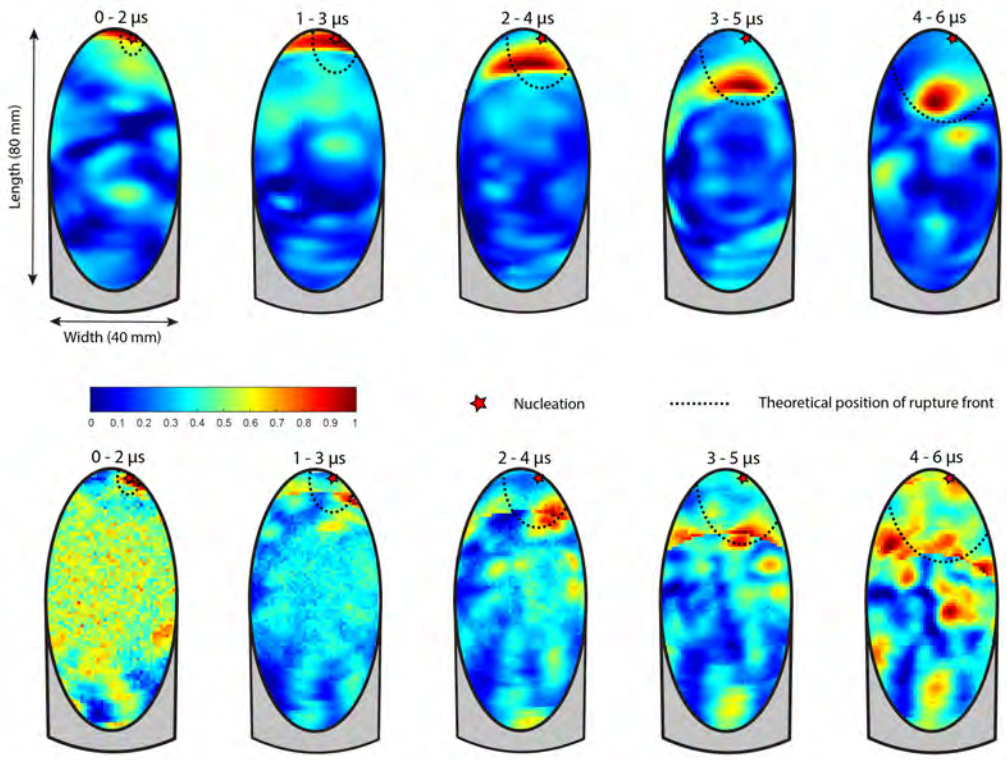

FIGURE 4.7: Snapshots of back-projection results for one stick-slip event at Pc = 90 MPa from far-field waveforms bandpass filtered to 400-800 kHz (**top**) and highpass filtered above 800 kHz (**bottom**). The colorbar represents the value of the normalized coherency function on the fault plane. The time is relative to the onset of the nucleation. The red star indicates the nucleation location and the black dashed line indicates the rupture front theoretical position estimated from the average rupture velocity V_r obtained by inversion, here equal to 5.1 km/s.

4.4 Discussion and conclusions

We summarize below the four key conclusions of this body of work:

High frequency radiation is related to stress and rupture velocity conditions: Observations of Fourier analysis (Figures 4.4 a and 4.4 b) have shown that high-frequency radiation is enhanced with both the stress conditions (i.e. normal stress acting on

the fault) and the rupture velocity. This is consistent with seismological observations of mega-thrust subduction earthquakes where zones of high-frequency energy release correspond to deeper portions of the fault (Ishii, 2011). There are different ways to interpret these results. First, the increase of stress concentrations in the process zone with stress conditions and rupture velocity would likely enhance physical processes as off-fault damage (Thomas et al., 2017; Thomas and Bhat, 2018; Okubo et al., 2019) taking place in the vicinity of the rupture front leading to more radiated high-frequency energy. Also, as the rupture velocity increases, more abrupt acceleration/deceleration phases of the rupture front develop, leading to local slip accelerations which would enhance high-frequency radiation (Olson and Apsel, 1982; Hartzell and Heaton, 1983). Our laboratory observations may further our understanding of high-frequency radiation under controlled conditions.

High frequency radiation content depends on the speed regime: Here we observed a net enhancement of high-frequency radiation when the rupture transition from sub-Rayleigh regime to supershear regime (Figures 4.4 a and 4.4 b), in agreement with what has been observed by previous studies (Bizzarri and Spudich, 2008; Vallée et al., 2008). In order to investigate the consequences of supershear rupture velocities to high-frequency, we give an order magnitude estimate (Figure 4.4 b) of the theoretical corner frequencies ω_c of far-field displacement spectrum for rupture velocities equal to $0.8.C_s$ ($\approx 2800\ m/s$) and to $1.4.C_s$ ($\approx 5000\ m/s$) based on the kinematic model for a circular crack of Sato and Hirasawa (1973). The corner frequencies correspond to the average of the expected P and S-wave corner frequencies which are given by the following expressions:

$$\omega_c^p = \frac{A_p.C_p}{2\pi.R} \tag{4.5}$$

and

$$\omega_c^s = \frac{A_s.C_s}{2\pi.R} \tag{4.6}$$

where R is the radius of the crack (we use $R = \sqrt{S/\pi}$, with S the area of the fault), C_p is the P-wave velocity, C_s is the S-wave velocity and A_p and A_s are functions of the rupture velocity V_r. Note that the model of Sato and Hirasawa (1973) was developed for rupture velocities ranging from $V_r = 0.5.C_s$ to $V_r = 0.9.C_s$. Therefore, the theoretical corner frequency for $V_r = 1.4.C_s$ was computed by extrapolating A_p and A_s to $1.4.C_s$. For the sub-Rayleigh rupture at $Pc = 10\ MPa$, the corner frequency beyond which we expect a high-frequency asymptote going as ω^{-2} is compatible with $V_r = 0.8.C_s$. However, for supershear ruptures ($Pc \geq 20\ MPa$) the expected corner frequency for $V_r = 1.4.C_s$ (the average rupture velocity of those stick-slip events) is clearly lower than the one observed which is close to 100 kHz. The peak of energy at 100 kHz may be interpreted as the spectral signature of the conical Mach wave which is less attenuated with distance than spherical waves. It should be noted that

because acoustic sensors are at distances to the fault comparable to its size, there might be a significant contribution to the spectra from the near-field, in which case the use of the far-field approximation would not be appropriate to compare the frequency content of the spectra. Andrews (1981) has shown that, for a coherent crack model, near-field motion is enhanced in high-frequencies relative to far-field motion. It is, in part, explained by inhomogeneous waves which do not leave the vicinity of the rupture front. In the far-field the corner frequency is related to source size, while in the near-field the corner frequency is related to propagation and attenuation effects and, thus, should not be interpreted in the same way. If the contribution of the near-field to the spectra was significant, we would expect the spectra to be quite similar for relatively same confining pressure as well as significant differences with increasing the confining pressure which is not what we observe. We therefore believe that the contribution of the near-field to the spectra is a second order effect and a far-field approximation is still acceptable.

Back-projection into the lab provides new inshights into earthquake processes: The fact that (i) we have been able to coherently back-propagate high-frequency energy at 400-800 kHz (ii) Fourier spectra show high-frequency asymptotes like ω^{-2} independent of the confining pressure and (iii) the peak of energy at 100 kHz is absent at low confinement ($Pc = 10\ MPa$) strongly suggest that the information contained in the spectra is linked to the source. Thus, back-projection analysis (Figure 4.7) can provide new insights on the radiation of high-frequency waves and rupture processes. In order to ensure that the back-projection results are reliable and are not manifestations of system noise, we performed back-projection analysis on a selected noise noise window in the 400-800 kHz frequency band and above 800 kHz (Figures 4.8 a and 4.8 b). In comparison with what is observed during the rupture propagation (Figure 4.7), the back-projection analysis produces images with very few variations. The high-frequency energy is almost stationary, either in the 400-800 kHz frequency band or above 800 kHz. This is consistent with the noise spectrum (Figure 4.8 c) which is almost flat any frequency. Such spectrum is typical of a white noise having zero mean and that underlies stochastic and uncorrelated physical processes.
The most robust and interpretable back-projection result obtained was in the 400–800 kHz frequency band (Figure 4.7 top). The correlation between the spatial and temporal evolution of high-frequency sources and the propagation of the rupture front provides concrete experimental evidence that high-frequency waves are concurrent with the propagation phase of the rupture front and that high-frequency radiation is emitted close to or behind the rupture tip. Figures 4.9 displays back-projection results in the 400-800 kHz frequency band for the last stick-slip event at Pc = 90 MPa. This stick-slip event was a « twin event » of the one whose back-projection analysis is shown in Figure 4.7. Both nucleated almost at the same location and

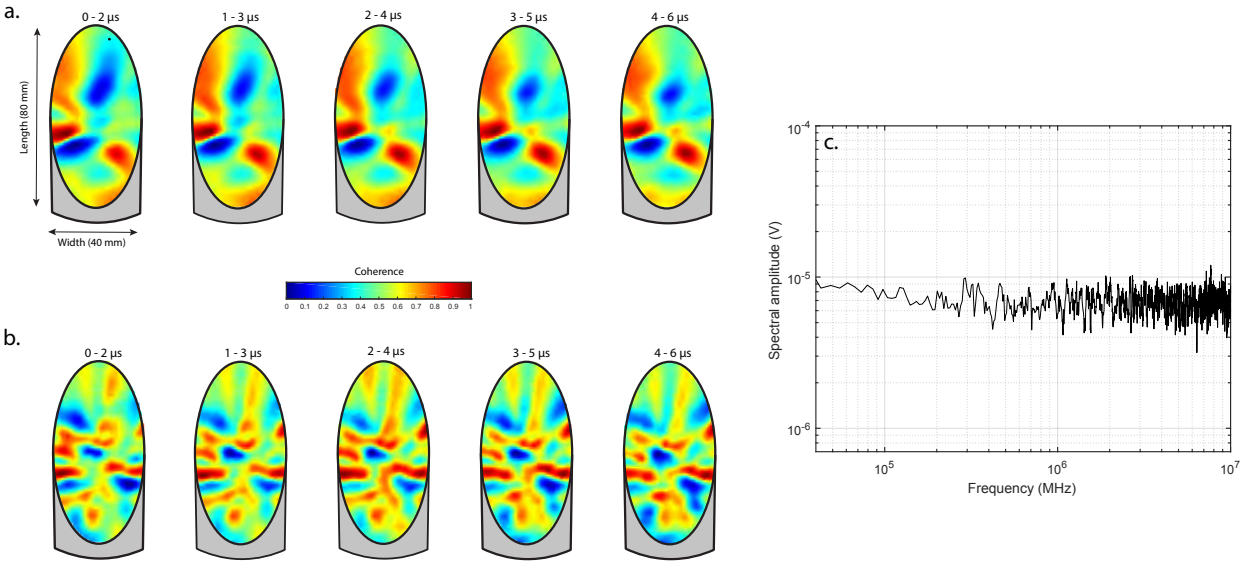

FIGURE 4.8: Back-projection analysis applied on a noise window. **a.** Back-projection results in the 400-800 kHz frequency band. **b.** Same as (a) but above 800 kHz. **c.** Noise spectrum

propagated at the almost same averaged rupture velocity ($V_r \approx 4700\ m/s$). Although high-frequency energy is more diffuse (especially in the two last time windows, $3-5\mu s$ and $4-6\mu s$), we also observed a net correlation between the estimated position of the rupture front and high-frequency radiation. This result is in agreement with most of the studies that addressed the issue of high-frequency radiation which proposed that high-frequency radiation is related to changes in rupture velocity due to fault stress or frictional heterogeneity, and predict high-frequency waves to be mainly generated in the vicinity of the rupture front (Haskell, 1964; Aki, 1967; Madariaga, 1977; Madariaga, 1983; Spudich and Frazer, 1984). Recent numerical studies (Thomas et al., 2017; Thomas and Bhat, 2018; Okubo et al., 2019) also demonstrated that high-frequency radiation was highly enhanced when co-seismic damage was implemented in their rupture propagation models. This is supported by post-experiment microscopic analysis of the fault surface at $Pc = 90\ MPa$ under Scanning Electron Microscopy (Figure 3.10). Figure 3.10 b reveals a connected network of cracks with typical sizes of 10 μm. Those cracks intersect highly deformed zones that might be partially melted and stretched asperities and, thus, have been produced during stick-slip instabilities. The fault surface (Figure 3.10 a) also presents elongated amorphous residual material with gas bubbles trapped in, which suggests that the asperities of the fault interface were, at least, partially melted due to heat generation during stick-slip instabilities. We can also observe gouge particles (white particles) with various sizes, ranging from less than one μs to several μs. Gouge particles overlap zones with melted material or are even trapped into the melt. Therefore it is likely than they have been produced during frictional sliding phases.

Above 800 kHz (Figure 4.7, bottom), the back-projection results are less clear. It is

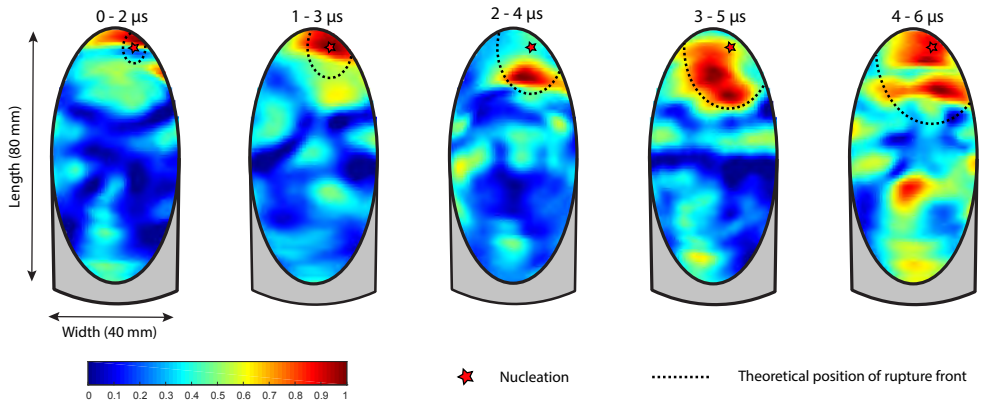

FIGURE 4.9: Snapshots of back-projection results for the last stick-slip event at $Pc = 90\ MPa$ in the 400-800 kHz frequency band. The color scale represents the normalized coherency function and the time is relative to the onset of the nucleation.

not surprising given the fact that the signal to noise ratio is significantly lower relative to the 400-800 kHz frequency band and also that acoustic waves above 800 kHz are more sensitive to scattering effects due to small-scale heterogeneities. It might explain why, between 4-6 μs, high frequency energy diffuses over the entire fault. However, an observable feature is that high-frequency sources above 800 kHz (Figure 4.7, bottom) seem to localize slightly forward ahead of the one at 400-800 kHz. One hypothesis is that high-frequency radiation above 800 kHz highlights other physical processes. Doan and Gary (2009) suggested that grain pulverization and comminution and small-scale gouge particles production could produce high-frequency radiation. Such processes should indeed happen within the breakdown zone, very near the rupture front and should be followed by asperity melting (Passelègue et al., 2016; Aubry et al., 2018).

Back-projection method can approximate the geometry of high frequency sources:

Synthetic tests (Figure 4.11) were performed to explore the reliability of the back-projection method to successfully image high-frequency sources and the influence of the acoustic waveforms characteristic frequency on the spatial resolution. Synthetic acoustic waveforms are generated using sinusoidal wavelets with central frequencies of either f = 400 kHz (14.250 mm wavelength) or f = 800 MHz (7.125 mm wavelength). To take into account spatial attenuation, we associated to the sinusoidal wavelets an exponential decay with time. Arrival times of the wavelets are computed using a 1-D velocity model only considering P-waves for which $C_p = 5800\ m/s$. The input point sources locations and the acoustic sensors array are displayed in Figure 4.11. The back-projection results from both models show an elliptical patch of energy that passes through and is maximum at the input point source in the middle (Figure 4.11, bottom). The overall shape of the patches of energy reflects the geometry of the acoustic sensors array and is slightly smearing along the fault's long axis. The resolution of the back-projection method depends on the characteristic

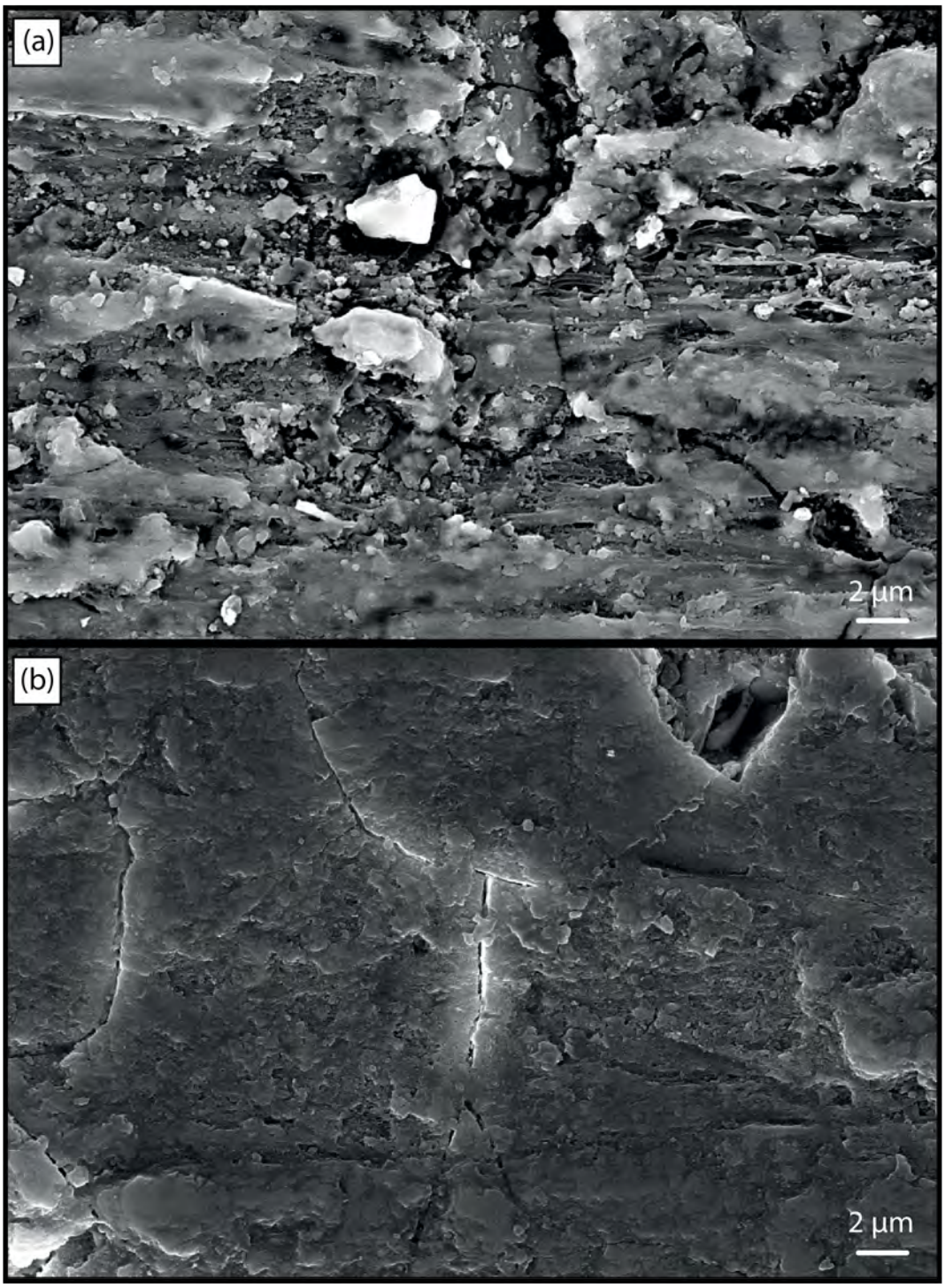

FIGURE 4.10: Microtextures of the fault surface under Scanning Electron Microscope. **a.** Gouge particles and elongated residual material which supports that part of the surface melted due to frictional heating. **b.** Micro-cracks at the micrometer scale.

frequencies of the input acoustic signals and is approximately equal to their characteristic wavelength. In both scenarios, it is not possible to distinguish the different input point sources but the geometry of the latter can be roughly determined.
Back-projection results at 400-800 kHz have shown that at the beginning of the rupture and during rupture propagation, high-frequency radiation is drawing a pattern that is spread over almost the entire width of the fault and that is linear along the width of the fault, although it is less noticeable between 4 μs and 6 μs. However, because acoustic recordings have been aligned to the nucleation zone, the cross-correlation procedure is expected to be less efficient as the source is moving away from the nucleation. This could explain why the initial pattern is not preserved and is concentrated in the middle of the fault with time. Under the assumption that high-frequency sources are representative of the shape of the rupture front, the observations do not match with what would be expected for an elliptical crack in an infinite medium but that of a rupture front strongly interacting with a free surface (Passelègue et al., 2016; Fukuyama et al., 2018).
This study has shown that back-projection analysis at the laboratory scale could be of relevance to understand the nucleation and propagation dynamics of earthquakes. In the future, the combined use of additional phases (S-waves, surface waves, reflected waves) and the deconvolution of acoustic recordings from Green's function describing the medium should help to get a more detailed and complete description of the source.

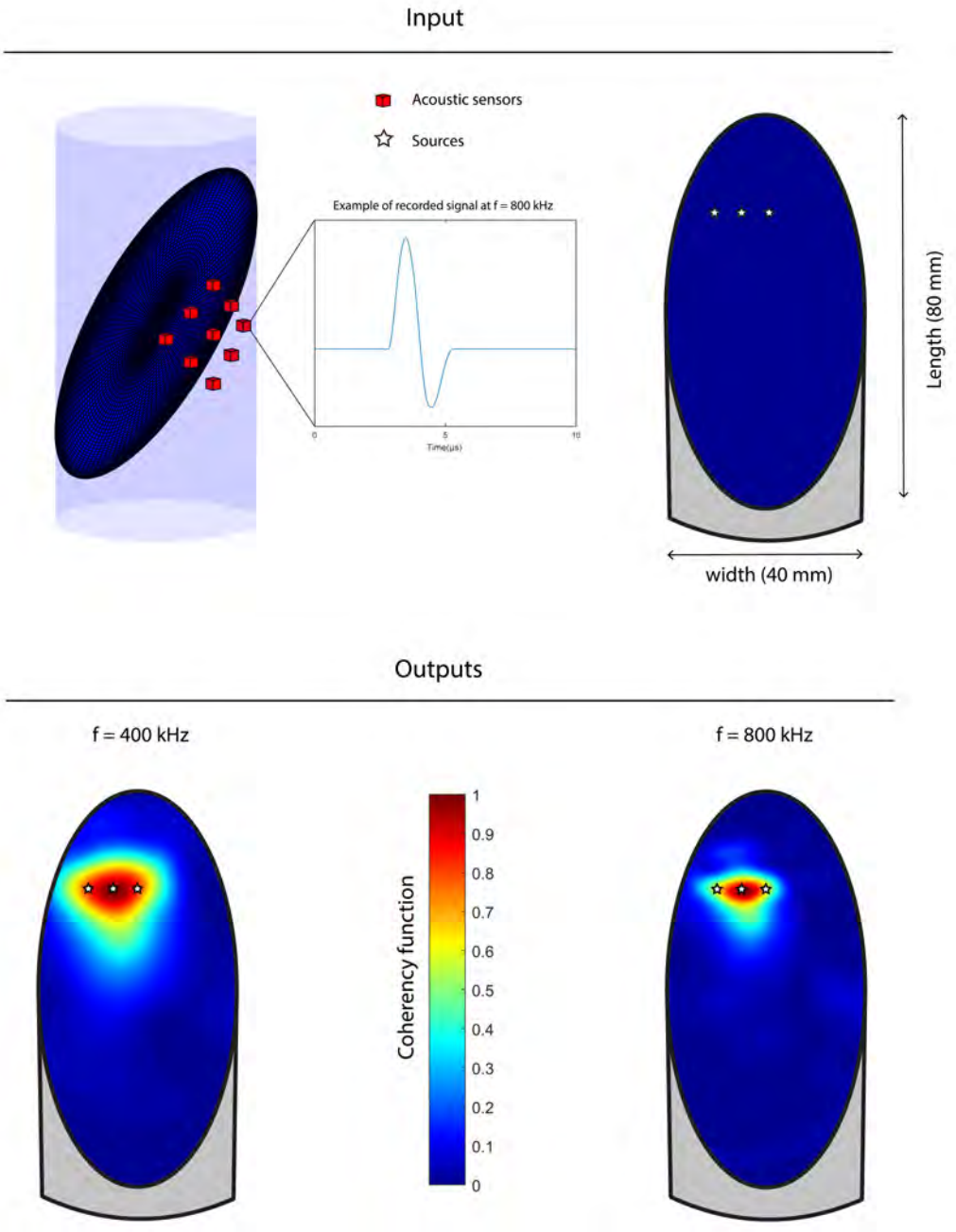

FIGURE 4.11: Synthetic tests. On the top is displayed the geometry of the far-field acoustic sensor array with respect to the fault (dark blue ellipse) used in the model. The sensor array geometry is similar than the one used for the back-projection analysis. On the top right is displayed the locations of the input point sources on the fault interface. An example of synthetic acoustic sensor recording is displayed in the middle. On the bottom are displayed synthetic tests for two scenarios, either for sources with a characteristic frequency equal to 400 kHz (left) or with a characteristic frequency equal to 800 kHz (right). The color-bar indicates the value of the normalized coherency function. The red color represents the maximum of energy and the blue color the minimum of energy.

Chapter 5

Conclusions and perspectives

Undoubtedly, friction experiments conducted on saw-cut samples represent a good proxy to reproduce experimentally the frictional behavior of natural faults under controlled conditions and consequently to address issues related to the physics of earthquakes. Most of the experimental works usually focus on the mechanical data (global/local strain and stress measurements) to constrain the mechanical behavior of natural fault systems. Most of the work done during this thesis was devoted to the introduction of a bit of seismology into the laboratory. In the following, we will first summarize the principal results obtained during this thesis. Then we will move on to the perspectives which will allow us for presenting ongoing and future works.

5.1 Summary of the results obtained during this thesis

First we studied the influence of the rupture velocity and the state of stress on high-frequency radiation and how the latter correlates with the propagation of the rupture front. Our results have shown that high-frequency radiation is enhanced by both increasing the normal stress onto the fault and the rupture velocity. We have interpreted this to be related to (i) the increase of stress concentrations in the breakdown zone zone with stress conditions which in turns promotes the production of off-fault damage. The latter is expected to generate high-frequency waves as demonstrated by numerical simulations (Thomas et al., 2017; Thomas and Bhat, 2018; Okubo et al., 2019) (ii) small scale local slip accelerations caused by more abrupt deceleration/acceleration of the rupture front as the rupture velocity is increasing. Local slip acceleration is expected to enhance high-frequency radiation based on seismological observations (Olson and Apsel, 1982) and theoretical models (Madariaga, 1983). During this experiments we also observed that ruptures can easily propagate at supershear velocities and that ruptures which transition to this speed regime generate significantly more high-frequency waves. We suggested that this is caused by the conical Mach wave formed during supershear ruptures which (i) is less attenuated with distance than spherical waves and (ii) leads to positive interference of high-frequency waves close to its propagation front. Applying the back-projection method at the laboratory scale, we were able to back-project high-frequency waves

onto the simulated fault plane during rupture propagation. Our results have provided a concrete experimental evidence that high-frequency waves are emitted close to or behind the rupture front. In the latter case, we argued, based on microstructural analysis, that high-frequency waves are indeed related to physical processes such as, co-seismic damage or gouge particles production caused by the fast dynamic stress drop in the breakdown zone.

Then we developed an experimental methodology to calibrate the acoustic sensors used to record sample surface vibration during the experiments. Uncalibrated acoustic sensors give only few information since the waveforms they record has a unit of voltage and part of the information is related to the instrumental response. We used a calibrated laser Doppler vibrometer to obtain the transfer function specific to the acoustic sensors, which allowed us to (i) convert an input voltage into an absolute velocity measurement and (ii) to get rid of the instrumental response. The principle was straightforward, we used a broadband transducer as a source to generate sample surface vibrations. Surface vibrations were recorded by both the acoustic sensor and the laser Doppler vibrometer. From the spectral ratio of the Fourier transforms of the acoustic sensor and the laser Doppler vibrometer measurements we obtained the transfer function. To obtain smooth and usable calibration curves, Fourier spectra were estimated using the multitaper spectral analysis method (Thomson, 1982). Calibrations were performed using two different types of source and by changing the frequency at which the source was excited. We found that the excitation frequency of the source had little effect on the transfer function but rather the size of the source mattered. Based on scaling arguments we made the choice to use the calibration curve that corresponded to the smallest source.

Finally, we addressed the issue of foreshocks occurrence and their link to nucleation. During experiments conducted under upper crustal conditions, we continuously recorded the precursory AE activity prior to stick-slip instabilities. Using the calibration curves, we were able to estimate the following seismological parameters of the AEs : seismic moment, corner frequency, source size and stress-drop. First, our results demonstrated that millimetric generated AEs satisfied the scaling laws that characterized natural earthquakes at the kilometric scale : the G-R frequency magnitude distribution of earthquakes magnitudes and the power law between the size of an earthquake and its magnitude. This has provided experimental evidence that generated AEs can be considered as microearthquakes and, consequently, that the physical processes at their origin may be similar at the scale of natural earthquakes. We found that precursory AEs were a by-product of the large stick-slip instability nucleation and were driven by local slip acceleration. In our experimental conditions, the comparison between the pre-seismic moment release and the total AE moment release suggested that nucleation is an almost full aseismic process. Similarly

to the power law acceleration of foreshock rate as a function of time to the mainshock, precursory AE activity increases on average as an inverse power law of the time to failure. Increasing the normal stress conditions leads to (i) an increase of AE rate prior to failure, which can be directly related to the pre-slip acceleration, and (ii) homogenizes stresses which promotes the migration of precursory AEs towards the nucleation. Relying on fault surface analysis, we suggested that fault strength is primarily controlled by the topography of the interacting rock surfaces. This was confirmed, at first order, by finding a simple scaling relation of the total AE moment release that only involves normal-stress, amount of pre-slip and roughness.

5.2 Perspectives: ongoing and future works

5.2.1 Similar events, relative localization and completeness magnitude

Throughout this manuscript we have mostly paid attention to the general behavior of the acoustic precursors prior to failure. From what we observed, precursory AE sequences behave in different ways from one to another, either in terms of temporal, spatial evolution towards failure or in term of moment release. These fluctuations highlight a richness of behaviors and require a detailed analysis of the AEs catalogs to be well characterized. For that purpose, we, in collaboration with Blandine Gardonio (https://www.researchgate.net/profile/Blandine_Gardonio), plan to and recently started to work on (i) quantifying the similarity of the AEs, (ii) refining the AEs localizations and (iii) decreasing the completeness magnitude of the catalogs. To examine the similarity of the AEs, we have computed for each experiment (i.e., $Pc = 30, 45$ and $60\ MPa$) the average spectral coherence $C(\Delta\omega)$ between pairs of AEs which for two events A and B takes the form:

$$C(\Delta\omega) = \frac{\overline{A(\Delta\omega).B^*(\Delta\omega)}}{\sqrt{\overline{A(\Delta\omega).A^*(\Delta\omega)}}\sqrt{\overline{B(\Delta\omega).B^*(\Delta\omega)}}} \tag{5.1}$$

where $A(\Delta\omega)$ is the Fourier transform of the event A in the frequency band $\Delta\omega$ (same for B). The star symbol indicates the conjugate of the Fourier transform. The spectral coherence is computed for each pair of AEs (only the ones that we could localized) and for each acoustic sensor. Computing the spectral coherence yields an additional information which is the phase delay between two events. This phase delay in spectral domain corresponds to a time delay in time domain and can be used to perform relative localization between pairs of events. Relative localization can significantly improve the accuracy of the AEs locations since the resolution of the time delays obtained by cross-spectral correlation can be as low as $10^{-10}\ s$. This is three orders of magnitude less than the maximal resolution of the manual picking procedure which is $10^{-7}\ s$ and should make it possible to obtain a location accuracy of the order of the micrometer. The figure 5.1 a shows, for the experiment conducted

at $Pc = 45\ MPa$, the coherence matrix for the pairs of localized AEs whose coherence is higher than 0.95 for at least 3 acoustic sensors. The coherence was computed in the frequency band [100 kHz - 1 MHz] over a 100 μs long time window starting 10 μs before the first P-wave arrival. The average coherence (i.e. over all the acoustic sensors) in function of the average time delay is displayed in figure 5.1 b. The relationship between the coherence and the time delay gives useful information regarding the coherence threshold that can be used for relative localization. For an average coherence greater than about 0.95 we found that the average time delay was less than 0.2 μs (which equates to about 1.5 mm in term of distance) which is less than most of the absolute time residuals of location. Therefore, we used this coherence threshold to link pairs of similar AEs. The figure 5.1 c shows an example of the acoustic waveforms (i.e. for the same acoustic sensor) for a family of 10 similar AEs with $C(\Delta\omega) > 0.95$. Based on visual inspection, those events exhibit significant differences which implies that they may be not collocated. However, we have to remind that the acoustic sensors array is affixed to one edge of the sample. One side of the fault is fixed while the other side moves relatively to the acoustic sensors array. Similar events may highlight the rupture of a single asperity but if it moves relative to the acoustic sensors array, the acoustic waveforms will be modified. This raises an interesting question, how long can an asperity survive during the experiments and how long (if it is the case) does it take to reform it, in other terms how the surface roughness evolves? We suspect that the evolution of the fault roughness may also impact the nucleation processes, for instance where the nucleation starts or how the nucleation zone expands. Fine relocation can also give some insights on the plausible interactions between AEs. In our experiments we found that the occurrence of the precursory AEs was mostly driven by the nucleation of the main instability (i.e. the SSE), however it is plausible that the AEs also trigger each other. So far we only built the families of similar events for the three experiments, we are working on adapting a code that was developed for relative relocation of natural earthquakes. The final stage will be to use the families of similar AEs as reference templates to perform template matching analysis (Gardonio et al., 2019) within the continuous waveforms. It is likely that a significant number of AEs could not be detected due their low signal to noise ratio. Under the assumption that the G-R frequency magnitude distribution of the AEs can be extrapolated to lower magnitudes, decreasing the magnitude of completeness of 0.5 would make the number of detected AEs three times higher. This may help to better constrain the dynamics of the nucleation, relying on detailed description of the spatial and temporal evolution of the precursory AEs towards failure.

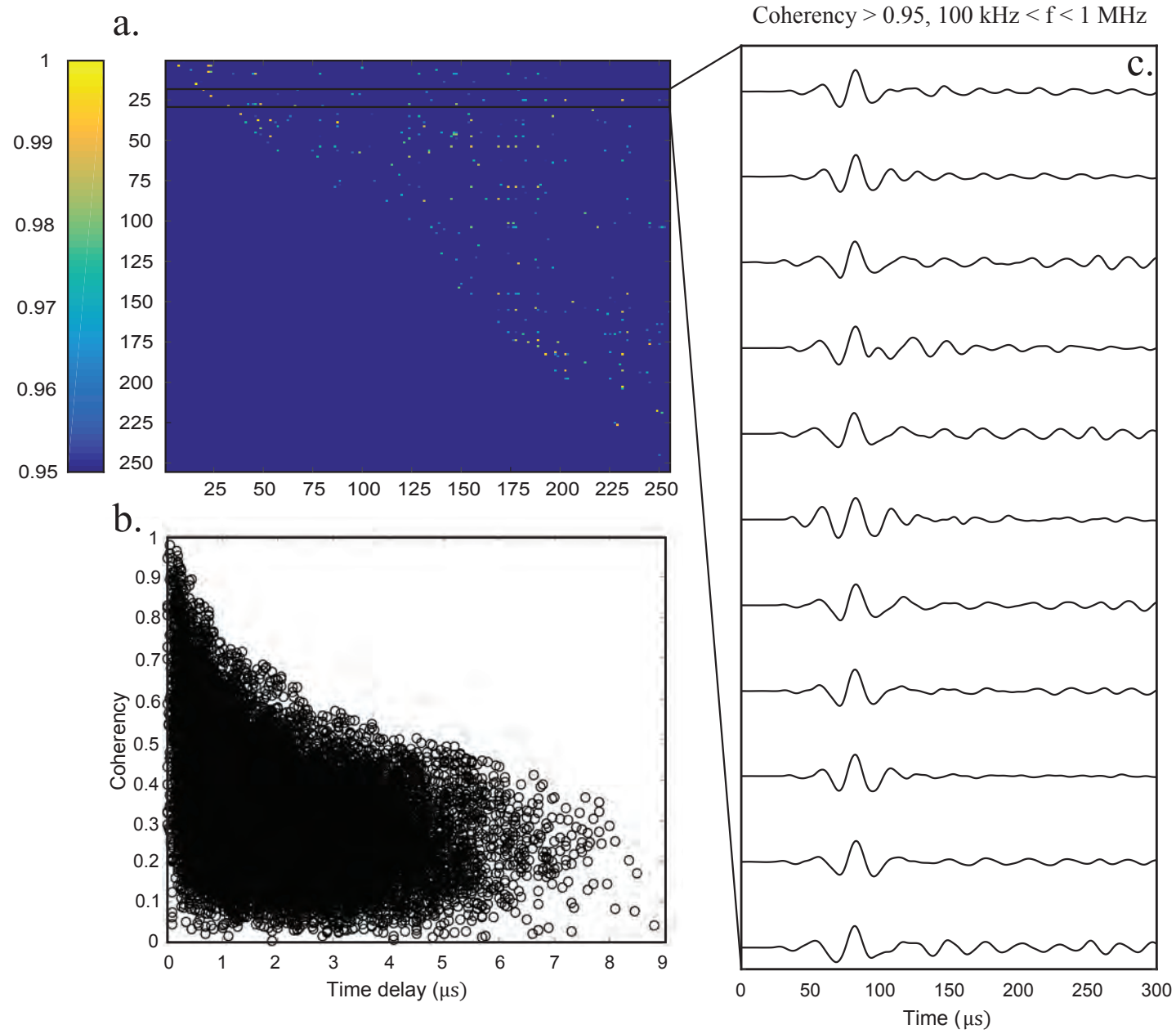

FIGURE 5.1: **a.** Example of the coherency matrix for the experiment conducted at $Pc = 45\ MPa$. Here, only pairs of events whose coherence $C(\Delta\omega)$ was higher than 0.95 for at least 3 acoustic sensors are shown. **b.** Relationship between the average time delay and the average coherence. The time delay is the reciprocal in time domain of the phase delay in frequency domain. **c.** Extracted family of 10 similar AEs. Waveforms have been aligned to their first P-wave arrival but have been slightly shifted for visualization.

5.2.2 Damage production during stick-slip instability

• End of March 2018, Yehuda Ben-Zion (https://earth.usc.edu/~ybz/) came to visit the ENS-Paris Laboratory of Geology. In a recent paper (Ben-Zion and Lyakhovsky,

2019), Yehuda Ben-Zion and Vladimir Lyakhovsky addressed the issue of the contribution of co-seismic damage to spatial and temporal variation of elastic moduli in the source volumes and the implications this may have in estimating the seismic moment M_0. The seismic moment M_0 can be expressed by the product of the rigidity μ_0 in the source region and the potency P_0 such as:

$$M_0 = \mu_0.P_0 \tag{5.2}$$

where μ_0 is the rigidity and P_0 is the amplitude of the potency which contains the information of the permanent inelastic deformation such as:

$$P_{ij} = \int_{V,t} \dot{\epsilon}^T_{ij}(x,t)dVdt \tag{5.3}$$

where P_{ij} is the total potency tensor which is defined as the integral of the transformational strain rate $\dot{\epsilon}^T_{ij}$ over the total duration and volume of the source and x is the position vector. While a particular attention is given to spatial variations of μ_0, its temporal variations are usually ignored. Ben-Zion and Lyakhovsky (2019) then proposed to reconsider eq (5.2) and to include temporal variations of μ_0 such as:

$$M_0 = (1-\alpha)\mu_0.P_0 \tag{5.4}$$

where α accounts for the temporal variation of μ_0 due to the production of damage during failure. Numerical simulations (Lyakhovsky and Ben-Zion, 2009) and laboratory experiments (Gupta, 1973; Hamiel et al., 2004) suggest that α can exceed 0.5 which could imply that seismic moment estimations may be overestimated by a factor of two or more. One possibility to quantify the amount of generated damage during the dynamic rupture is to rely on variations of seismic-waves velocity since the latter are a function of the elastic moduli. To do so, a series of experiments were conducted on saw-cut samples of Indian gabbro at three different confining pressures, $Pc = 10\ MPa$, $Pc = 45\ MPa$ and $Pc = 90\ MPa$. The idea was simple, one acoustic sensor was used as a source and was facing the fault on one edge of the sample (Figure 5.2 c.). On the other edge were positioned seven other acoustic sensors equally spaced along the vertical axis of the rock sample. These one were used as receivers. At the beginning of the experiments, we applied to the source a step voltage of 200 V to generate a P-wave. The signal was recorded by the receivers on the other side of the sample which allowed us to obtain a set of reference signals (i.e. for each source-receiver pair). The same procedure was reproduced following each stick-slip instability and time delays were obtained by cross-correlating the recorded signals with the reference signals. The figure 5.2 b shows the shear-stress and along fault displacement during the experiment conducted at $Pc = 45\ MPa$ which corresponds to a sequence of 22 SSEs. The figure 5.2 a displays the evolution of the accumulated

time delays during the experiment. Time delays are plotted in function of the angle between the direction of the ray source-receiver and the perpendicular direction to the fault plane (Figure 5.2 c) and the colorscale indicates the SSE index. We obtain that the time delays increase significantly with the successive ruptures which therefore implies a reduction of elastic moduli. The largest time delays correspond to the ray with a maximum obliquity with respect to the perpendicular direction to the fault. If we assume that damage localizes within a small region close to the fault plane this is what we could have expected at first order since the larger the obliquity the larger the sampled damaged region along the ray path. However, by considering damage as microcracks, time delays will also be function of the spatial distribution and orientation of the micro-cracks which may explain why time delays do not necessarily increase with the obliquity of the ray with respect to the normal direction of the fault. Taking the largest time delay as an example, the latter is about $3.5.10^{(7} \mu s$ which equates to an increase of the P-wave travel time of about 5%. Although the time delay is integrated throughout the ray path, we can assume that it is mainly caused by the thin, localized damaged region close to the fault plane, the question being how much damage is required to explain this decrease of P-wave velocity. This will require to estimate the microcracks density, their geometry and the spatial extent of the damaged region. We can intuit that if the damaged region is small, 5% of P-wave velocity implies a significant amount of accumulated/generated damage and thus a significant drop of elastic moduli during rupture propagation. This may have some important implications. Since generated damage is mostly related to the production of mode I cracks, it may cause substantial dynamic changes of normal stress close to the rupture front which, for instance, may facilitate rupture propagation (only in the tensional quadrant that being said). In the present case, this study is embryonic but we will get back to it in the near future.

5.2.3 Future works

In what follows, we list some ideas for future experiments and related issues. This will allow us to discuss the improvement of the methods and techniques of analysis that we developed during this thesis.

– In chapter 4, we have addressed the issue of high-frequency radiation during rupture propagation. This has been the occasion to introduce the back-projection method at the laboratory scale. We have obtained interesting insights on the physical parameters controlling the production of high-frequency waves. However, in the current state of things, without additional procedures the use of the back-projection method will rapidly reach its limits. The best we can hope for is the full picture of the high-frequency radiation released during rupture propagation. There is only one possibility to achieve this goal,

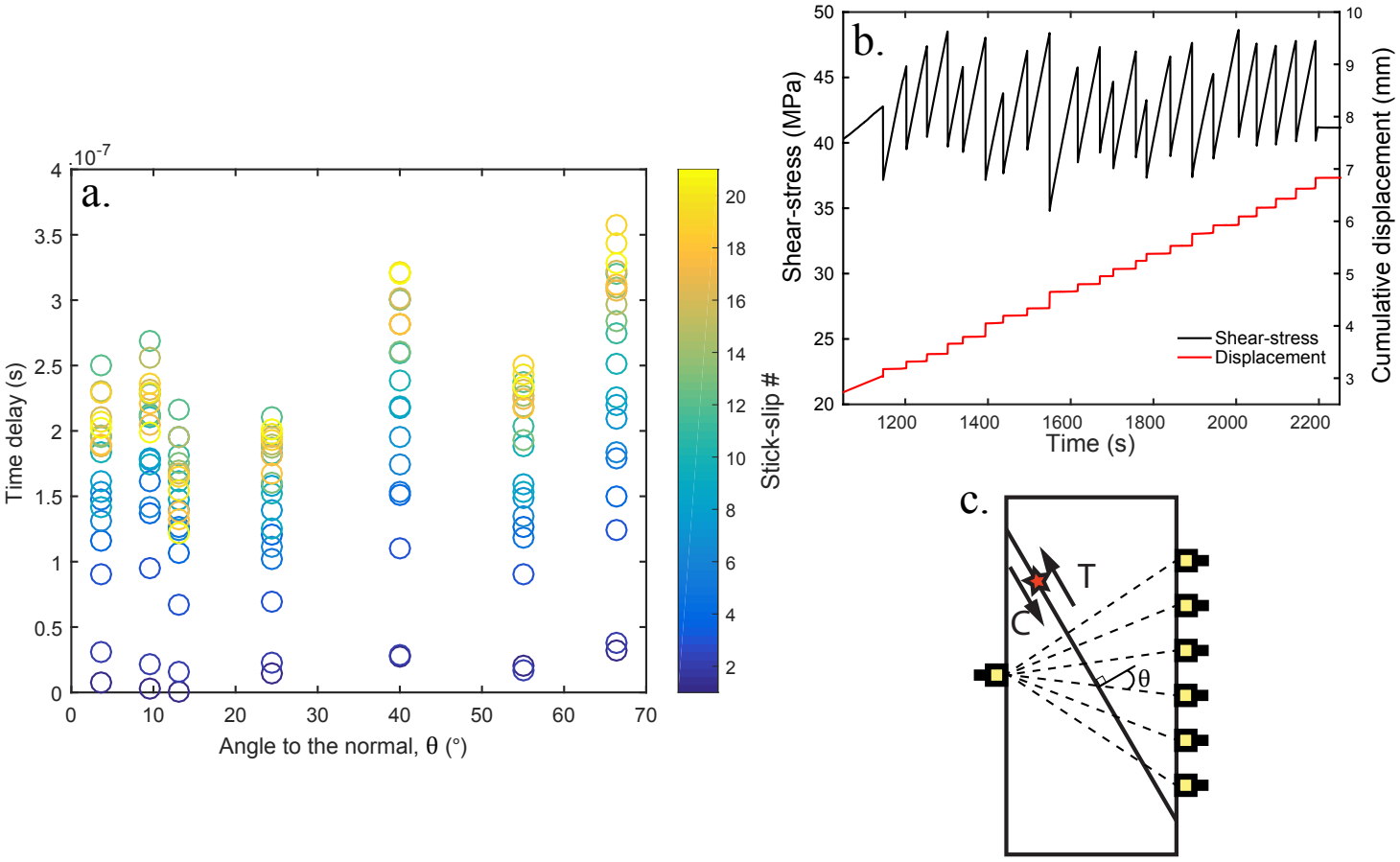

FIGURE 5.2: **a.**Example of the evolution of the time delays during one stick-slip experiment conducted at $Pc = 45\ MPa$. Time delays were measured following each stick-slip instability. Each vertical alignment of colored circles represents a source-receiver pair and is defined by the angle θ. The colorscale refers to the SSE index. **b.** Shear-stress and along fault displacement versus time. A sequence of 22 SSEs were reproduced. **c.** Schematic view of the acoustic sensors array geometry. One acoustic sensor is used as a source and is affixed on one edge of the sample. Seven acoustic sensors are used as receivers and are positioned on the other edge of the sample. Pairs of source-receiver are defined according to the angle θ between the ray source-receiver and the direction perpendicular to the fault plane. Damage will be concentrated in the tensional quadrant (T).

which is to deconvolve the acoustic waveforms from the acoustic sensors response and from the Green function that describes the medium. Now that we have an experimental acoustic sensor calibration set-up, getting the instrumental response will be easy. To obtain the Green function of the medium there are probably two possibilities: (i) to compute empirical Green functions based on the point source approximation, this would require to regularly sample the fault surface using small AEs or (ii) to run numerical simulations of the Green function using different types of source. We are actually working on the latter scenario with a Phd student (Ssu-Ting Lai, who is working at IPGP, http://www.ipgp.fr/fr). Obtaining a complete and quantitative description of the high-frequency radiation during rupture propagation may bring out precious insights. For instance, it would allow to interpret high-frequency radiation in light of local kinematic parameters such as rupture/slip velocity or rise time. It would also be possible to examine in detail the coupling between topographic heterogeneities and high frequency radiation. Using thermally cracked saw-cut samples, it would be interesting to estimate the contribution of generated damage to high frequency radiation.

– In chapter 3, we examined the dynamics of precursory AEs during nucleation phase. Although rock friction experiments present the disadvantage of being a simplified version of natural earthquakes, we are able to couple seismology, local and global geodesy during experiments conducted under controlled conditions. Moreover, since everything is happening onto the fault, problems are well-posed. Based on strain gauge recordings, we plan to perform simple simulations to obtain the strain field evolution during nucleation. This might help in better understanding the variability of the precursory AE sequences in terms of timing, migration and moment release. In addition, many other parameters should affect the precursory AE activity during nucleation. Temperature is probably one important parameter that needs to be examined. We may expect that mechanisms such as dislocation motion or slow crack growth, favored by temperature increase, will allow potential sites of AEs to slip slowly and aseismically. Also, loading rate is a parameter that should get all our attention. We may expect that decreasing the loading rate will promote fault healing since inter SSE time will increase. As a consequence, fault strength could be sufficiently homogeneous to lead to a completely aseismic nucleation process. It will be interesting to decrease the loading rate by a factor of 10 in future experiments. However, this will also require a decrease by a factor of 10 of the sampling frequency of the continuous recording. In that case, only the magnitudes of AEs can be estimated.

– The ability for the rupture to propagate further or to arrest will depend on the local energy budget at the rupture tip. Jérôme Aubry (https://www.researchgate.

net/profile/Aubry_Jerome) started his Phd at the same time as me with Alexandre as supervisor. Aubry et al. (2018) developed a carbonization related in-situ thermometer to measure heat production during cosesimic slip. We may be able to measure independently the fracture energy (including on and off-fault damage terms), the heat produced (carbonization related in-situ thermometer) and the radiated energy (calibrated acoustic sensors). Although seismological and geodetic observations techniques have been considerably improved in recent decades, crustal faults are inaccessible so that the earthquake energy budget cannot be fully constrained. Therefore, it may be of great interest to examine energy partitioning during stick-slip instabilities in light of of stress/temperature conditions, rupture/slip velocity, loading rate, surface roughness, fluid pressure or lithology contrast (i.e., bi-material interface). We have not collaborated yet, but it is a project in progress.

5.2.4 QTM catalog analysis

• We begin here the last paragraph of this manuscript. At the beginning of this summer, Emily Brodsky (https://websites.pmc.ucsc.edu/~seisweb/emily_brodsky/) came to visit the ENS Paris Laboratory of Geology. We were discussing the results that we obtained on precursory AE activity prior to stick-slip instabilities (Chapter 3). She suggested that we should now examine the real seismicity to connect the laboratory observations to the natural field. In what follows, we present a recently started work that consists in the analysis of the seismicity catalog QTM (Quake Template Matching) produced by Ross et al. (2019). The QTM catalog contains more than 1.81 millions of earthquakes in southern California for the period 2008-2017 which is about 10 times more than the regional SCSN catalog (Southern California Seismic Network, https://service.scedc.caltech.edu/eq-catalogs/date_mag_loc.php) for the same period. This was made possible by performing template matching analysis on the continuous waveform of the regional SCSN. The figure 5.3 displays the summary of the QTM catalog. The completeness magnitude of the QTM catalog is close to 0.3 (Figures 5.3 a and b). In comparison, the completeness magnitude of the SCNS catalog is about 1.7. The earthquakes density computed over 2 km by 2 km bins is displayed in figure 5.3 c.

As we are seeking for investigating the foreshock activity characteristics, we classified the earthquakes into clustered and background seismicity using the nearest-neighbor distance approach (Baiesi and Paczuski, 2004; Zaliapin and Ben-Zion, 2013) which has the the advantage of not requiring a priori information and can objectively separate clustered earthquakes from background earthquakes. The nearest-neighbor distance clustering method is a statistical approach which search for earthquakes that happen sufficiently close in time and space to deviate from what would be expected in the case of a SIP (Stationary space-Inhomogeneous marked Poisson) process. Families of foreshocks-mainshock-aftershocks are built by linking event pairs (child event and parent event) using the metric η called "distance" which only relies

on the distance between event pairs, the time difference between event pairs and the magnitude of the parent event such as:

$$\begin{cases} \eta_{ij} = t_{ij}(r_{ij})^{df}.10^{-bm_i}, & t_{ij} > 0 \\ \eta_{ij} = \infty, & t_{ij} \leq 0 \end{cases} \tag{5.5}$$

where η_{ij} is the distance between the events, r_{ij} is the distance between the parent event i and the child event j (km), t_{ij} is the difference in the origin time (year), m_i is the magnitude of the parent event and df and b are the fractal dimensions of the epicentral distributions of earthquakes and the b-value that characterizes the frequency-magnitude distribution of the seismicity respectively. The rescaled spatial and temporal components of the distance η_{ij} can be separated from each other such as $\eta_{ij} = T_{ij}R_{ij}$ with:

$$\begin{cases} T_{ij} = t_{ij}.10^{-qbm_i} \\ R_{ij} = (r_{ij})^{df}.10^{-(1-q)bmi} \end{cases} \tag{5.6}$$

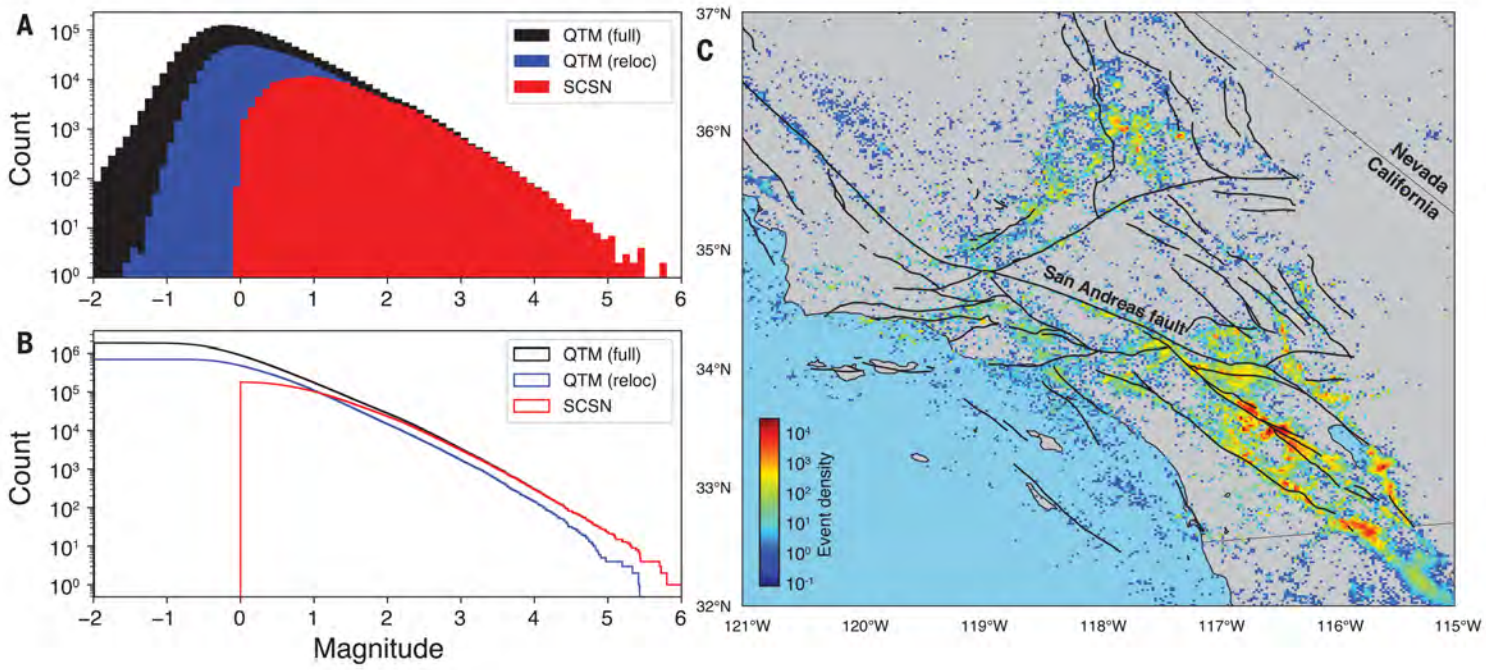

FIGURE 5.3: Summary of the QTM catalog. **a** Non cumulative frequency-magnitude distribution of earthquakes contained in the SCSN catalog, the full QTM catalog and the relocated QTM catalog. **b** Same as A but for the cumulative frequency-magnitude distribution of earthquakes. **c** Earthquake density in the QTM catalog computed into 2 km x 2 km bins. (Taken from Ross et al., 2019)

where q is a free parameter. For each hypothetical child event j the distance η_{ij}

was computed and event pairs were given by the shortest distance η_{ij}. To compute η_{ij} we used the following parameters (the same than Zaliapin and Ben-Zion, 2013), $q = 0.5$, $b = 1.0$ and $df = 1.6$. In principle, the distribution of $log(\eta_{ij})$ will follow a bimodal distribution (Figure 5.4 a). A first subpopulation corresponds to the weakly related event pairs. This subpopulation contain events which happen at large distances η_{ij} to their nearest neighbor and corresponds to the background seismicity. The second subpopulation contains the clustered events that occur at close distances η_{ij} to their nearest neighbor. Assuming a two mixed Weitbull distributions (Zaliapin and Ben-Zion, 2013) for both the weakly and strongly related seismicity, we can define a threshold η_0 that can be used to separate the clustered from the background events. The threshold η_0 is given by the intersection of the two distributions. When plotting the joint distribution (T, R) in logarithmic scale, two modes appear (Figure 5.4 b). The weakly related background seismicity forms a first mode which is elongated in the diagonal and is characteristic of a random Poisson process. The second mode which has this characteristic flat shape concentrates closer to the origin and corresponds to the clustered events. The diagonal line that separates the two modes indicates $log10(\eta_0) = log10(T_{ij}) + log10(R_{ij})$. The figure 5.4 c displays the distribution of the nearest neighbor distance between events for events of $M_w > 0$. Note that we limited the analysis to the relocated QTM (`https://scedc.caltech.edu/research-tools/QTMcatalog.html`), catalog which contains less events (about 900000). However, this ensures to not bias the results due to poorly resolved epicenter locations. We are able to retrieve the expected bimodal distribution. When plotting the rescaled distance R in function of the rescaled time T, the two modes can be clearly identified (Figure 5.4 d). Although both seems to be separated by a constant threshold $log10(\eta_0) \approx -4.2$, we made the choice to use $log10(\eta_0) \approx -5$ (as suggested by Zaliapin and Ben-Zion, 2013) to separate the clustered seismicity from the background seismicity. The families of foreshock(s), mainshock and aftershock(s) were built by sequentially linking the strongly related event pairs. In each cluster, the mainshock is defined as the largest magnitude. Out of 506794 events, we extracted 19653 families that all together contain 249576 events. The clustered events form the data base that we will use to investigate foreshock activity characteristics and, more precisely, in order to search for similar patterns than those observed at the laboratory scale.

The figure 5.5 displays an intriguing observation that we have made on the temporal evolution of foreshocks towards the time of the mainshock. The figure 5.5 c shows, for the whole region (Figure 5.5 a), the normalized cumulative number of foreshocks in the last 5 days prior to the time of the mainshocks. Curves were obtained for various depth layers (0-5 km, 5-10 km and 10-15 km, blue, red and black lines respectively) using clusters whose mainshock magnitude is comprised between 2.0 and 2.5. Similarly to what was done in the laboratory, curves result from the stacking of all foreshock sequences. The figure 5.5 d shows the same but for a smaller

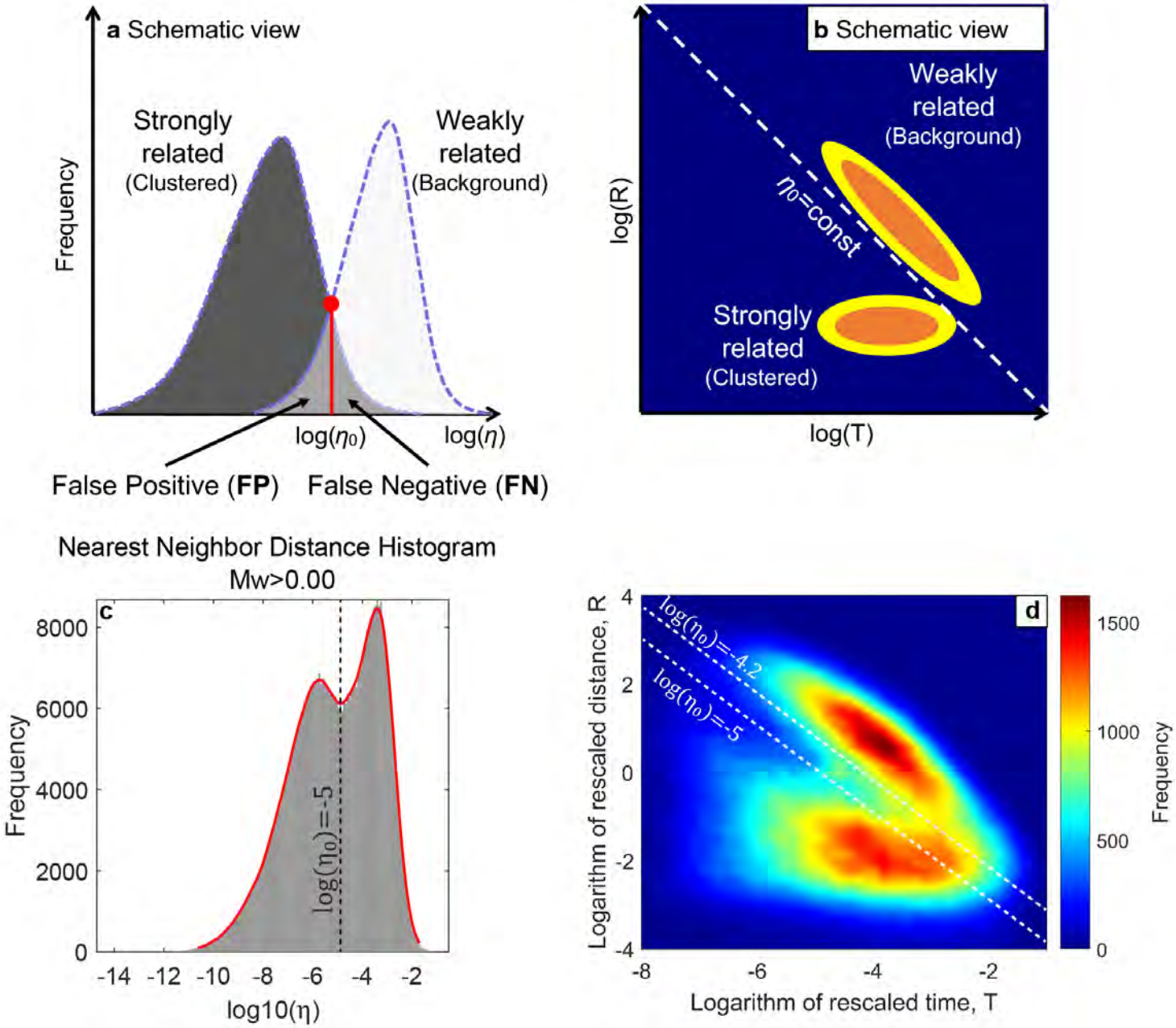

FIGURE 5.4: Nearest neighbor distance analysis. **a** Schematic view of the bimodal distribution of $log(\eta)$ in the case of the coexistence of weakly related and strongly related events. The threshold $log(\eta_0)$ is used to distinguish the clustered events from the background events and is given by the intersection of the two distributions. **b** Schematic view of the joint distribution of the rescaled time and space components T, R. The dashed line shows η_0. **c** Distribution of the nearest-neighbor distance η using the relocated QTM catalog. The blacked dashed line indicates the threshold η_0 used to cluster the event pairs. **d** Joint distribution of the rescaled time and space components T, R. The dashed lines show $log(\eta_0) = -4.2$ and $log(\eta_0) = -5$. Following Zaliapin and Ben-Zion, 2013, we used $log(\eta_0) = -5$. The figures **a** and **b** were extracted from Tamaribuchi et al., 2018

region ($117^\circ \leq$ longitudes $\leq 116^\circ$ and $33^\circ \leq$ latitudes $\leq 34^\circ$, figure 5.5 a.), for different depth (6-9 *km*, 7-10 *km* and 11-14 *km*, blue, red and black lines respectively) and by using all clusters whose mainshock magnitude was less than $Mw = 3$. Note that in both cases we only used the clusters for the period 2008-2010, period which precedes the occurrence of the 2010 Mw 7.2 El Mayor–Cucapah earthquake which has considerably changed the rate of seismicity. Similarly to what we have observed in laboratory (figure 5.5 b), the rate of foreshocks towards mainshock seems to increase with depth and thus with stress conditions. However, we will not pretend that this positive correlation between foreshocks rate and stress conditions can be directly compared to what we observe in the laboratory. We inferred that the occurrence of precursory AEs was mostly driven by the slow but accelerating nucleation of the main stick-slip instability. This is partly caused by the fact that we impose on the system its own temporal and spatial limits. Earthquakes can interact with each other over various time and space scales which is the richness of the complex interactions between them. It is likely that foreshocks occur due to the superposition of different processes such as slow slip transients, partial stress release, Coulomb stress transfer or the slow nucleation of a larger upcoming earthquake. Thus, this depth dependence of the rate of foreshocks is intriguing but requires to be carefully examined. Considering that the typical source size for a magnitude $Mw = 3$ earthquake is typically of the order of few hundred meters, 5 days for the nucleation to develop and expand may be too long or too short. We have at our disposal a catalog which contains numerous foreshock sequences. Combine them at different space and time scales may give some insights on the physical parameters which, at first order, control the characteristics of foreshock activity (occurrence rate, spatial migration, b-value changes, moment release...).

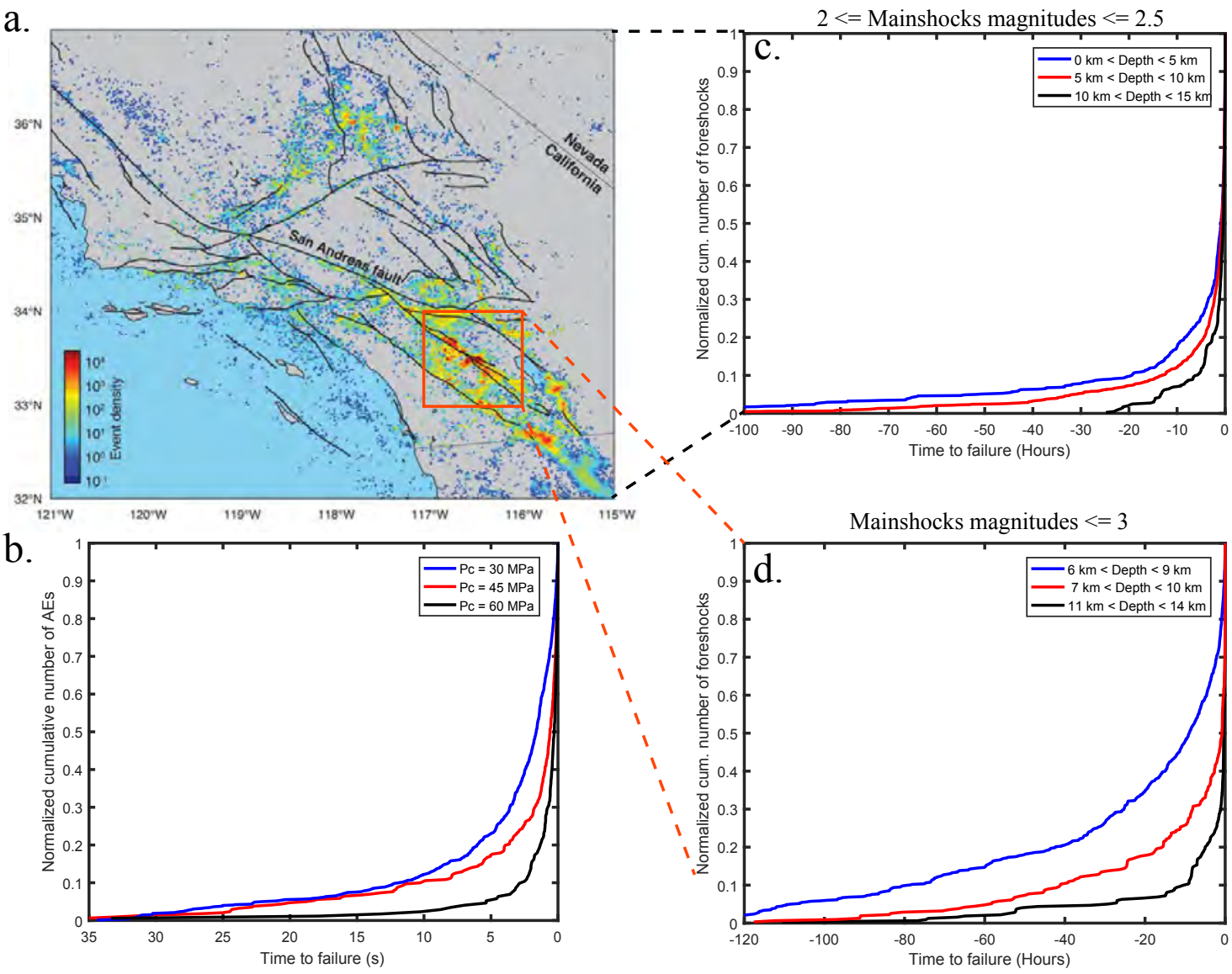

FIGURE 5.5: Cumulative number of foreshocks towards failure. **a.** Map of earthquake density in the QTM catalog (taken from Ross et al., 2019). The black dashed lines and the red dashed lines indicate the corresponding regions to figures **c.** and **d**. **b.** Normalized cumulative number of precursory AEs towards failure during the experiments conducted at $Pc = 30, 45$ and 60 MPa. **c.** Normalized cumulative number of foreshocks towards failure for various depth layers for the period 2008-2010. Only clusters whose mainshock magnitude Mw is comprised between 2 and 2.5 were used. All foreshocks were synchronized to the time of their respective mainshock and stacked. **d.** Same as **c.** but for the reduced region (red rectangle). In the former, all clusters whose mainshock magnitude was less or equal to 3 were used.

References

Abercrombie, Rachel E (1995). "Earthquake source scaling relationships from- 1 to 5 ML using seismograms recorded at 2.5-km depth". In: *Journal of Geophysical Research: Solid Earth* 100.B12, pp. 24015–24036.

Abercrombie, Rachel E and Jim Mori (1996). "Occurrence patterns of foreshocks to large earthquakes in the western United States". In: *Nature* 381.6580, p. 303.

Abercrombie, Rachel E and James R Rice (2005). "Can observations of earthquake scaling constrain slip weakening?" In: *Geophysical Journal International* 162.2, pp. 406–424.

Abercrombie, Richael and Jim Mori (1994). "Local observations of the onset of a large earthquake: 28 June 1992 Landers, California". In: *Bulletin of the Seismological Society of America* 84.3, pp. 725–734.

Achenbach, Elmar (1975). "Total and local heat transfer from a smooth circular cylinder in cross-flow at high Reynolds number". In: *International Journal of Heat and Mass Transfer* 18.12, pp. 1387–1396.

Acosta, Mateo et al. (2019). "Precursory moment release scales with earthquake magnitude". In: *arXiv preprint arXiv:1901.06908*.

Aki, Keiiti (1967). "Scaling law of seismic spectrum". In: *Journal of geophysical research* 72.4, pp. 1217–1231.

Aki, Keiiti and Paul G Richards (2002). *Quantitative seismology*.

Allmann, Bettina P and Peter M Shearer (2009). "Global variations of stress drop for moderate to large earthquakes". In: *Journal of Geophysical Research: Solid Earth* 114.B1.

Ampuero, Jean-Paul and Allan M Rubin (2008). "Earthquake nucleation on rate and state faults–Aging and slip laws". In: *Journal of Geophysical Research: Solid Earth* 113.B1.

Andrews, DJ (1976). "Rupture velocity of plane strain shear cracks". In: *Journal of Geophysical Research* 81.32, pp. 5679–5687.

Andrews, DJ (1981). "A stochastic fault model: 2. Time-dependent case". In: *Journal of Geophysical Research: Solid Earth* 86.B11, pp. 10821–10834.

Archuleta, Ralph J (1984). "A faulting model for the 1979 Imperial Valley earthquake". In: *Journal of Geophysical Research: Solid Earth* 89.B6, pp. 4559–4585.

Aubry, Jeremy et al. (2018). "Frictional heating processes and energy budget during laboratory earthquakes". In: *Geophysical Research Letters* 45.22, pp. 12–274.

Baiesi, Marco and Maya Paczuski (2004). "Scale-free networks of earthquakes and aftershocks". In: *Physical review E* 69.6, p. 066106.

Baumberger, T, P Berthoud, and C Caroli (1999). "Physical analysis of the state- and rate-dependent friction law. II. Dynamic friction". In: *Physical Review B* 60.6, p. 3928.

Ben-David, Oded, Gil Cohen, and Jay Fineberg (2010). "The dynamics of the onset of frictional slip". In: *Science* 330.6001, pp. 211–214.

Ben-Zion, Yehuda and Vladimir Lyakhovsky (2019). "Representation of seismic sources sustaining changes of elastic moduli". In: *Geophysical Journal International* 217.1, pp. 135–139.

Bernard, P and R Madariaga (1984). "A new asymptotic method for the modeling of near-field accelerograms". In: *Bulletin of the Seismological Society of America* 74.2, pp. 539–557.

Beroza, Gregory C and William L Ellsworth (1996). "Properties of the seismic nucleation phase". In: *Tectonophysics* 261.1-3, pp. 209–227.

Bhat, Harsha S et al. (2007). "Off-fault damage patterns due to supershear ruptures with application to the 2001 Mw 8.1 Kokoxili (Kunlun) Tibet earthquake". In: *Journal of Geophysical Research: Solid Earth* 112.B6.

Bizzarri, A and P Spudich (2008). "Effects of supershear rupture speed on the high-frequency content of S waves investigated using spontaneous dynamic rupture models and isochrone theory". In: *Journal of Geophysical Research: Solid Earth* 113.B5.

Blanpied, Michael L and Terry E Tullis (1986). "The stability and behavior of a frictional system with a two state variable constitutive law". In: *Friction and Faulting*. Springer, pp. 415–444.

Bouchon, Michel and Martin Vallée (2003). "Observation of long supershear rupture during the magnitude 8.1 Kunlunshan earthquake". In: *Science* 301.5634, pp. 824–826.

Bouchon, Michel et al. (2001). "How fast is rupture during an earthquake? New insights from the 1999 Turkey earthquakes". In: *Geophysical Research Letters* 28.14, pp. 2723–2726.

Bouchon, Michel et al. (2002). "Space and time evolution of rupture and faulting during the 1999 Izmit (Turkey) earthquake". In: *Bulletin of the Seismological Society of America* 92.1, pp. 256–266.

Bouchon, Michel et al. (2011). "Extended nucleation of the 1999 Mw 7.6 Izmit earthquake". In: *science* 331.6019, pp. 877–880.

Bouchon, Michel et al. (2013). "The long precursory phase of most large interplate earthquakes". In: *Nature geoscience* 6.4, p. 299.

Brace, WF and JD Byerlee (1966). "Stick-slip as a mechanism for earthquakes". In: *Science* 153.3739, pp. 990–992.

Brace, W.F. and D.L. Kohlstedt (1980). "Limits on lithospheric stress imposed by laboratory experiments". In: *Journal of Geophysical Research: Solid Earth* 85.B11, pp. 6248–6252.

Bruhat, Lucile, Zijun Fang, and Eric M Dunham (2016). "Rupture complexity and the supershear transition on rough faults". In: *Journal of Geophysical Research: Solid Earth* 121.1, pp. 210–224.

Brune, James N (1970). "Tectonic stress and the spectra of seismic shear waves from earthquakes". In: *Journal of geophysical research* 75.26, pp. 4997–5009.

Burridge, R and L Knopoff (1964). "Body force equivalents for seismic dislocations". In: *Bulletin of the Seismological Society of America* 54.6A, pp. 1875–1888.

Burridge, R, ER Lapwood, and L Knopoff (1964). "First motions from seismic sources near a free surface". In: *Bulletin of the Seismological Society of America* 54.6A, pp. 1889–1913.

Byerlee, James (1978). "Friction of rocks". In: *Rock friction and earthquake prediction*. Springer, pp. 615–626.

Byerlee, James D and WF Brace (1968). "Stick slip, stable sliding, and earthquakes—effect of rock type, pressure, strain rate, and stiffness". In: *Journal of Geophysical Research* 73.18, pp. 6031–6037.

Cai, Dai-en et al. (1988). "The b-value of acoustic emission during the complete process of rock fracture". In: *Acta Seismol. Sinica* 2, pp. 129–134.

Campillo, Michel and Ioan R Ionescu (1997). "Initiation of antiplane shear instability under slip dependent friction". In: *Journal of Geophysical Research: Solid Earth* 102.B9, pp. 20363–20371.

Candela, Thibault et al. (2009). "Characterization of fault roughness at various scales: Implications of three-dimensional high resolution topography measurements". In: *Mechanics, structure and evolution of fault zones*. Springer, pp. 1817–1851.

Cocco, Massimo et al. (2009). "Scaling of slip weakening distance with final slip during dynamic earthquake rupture". In: *International Geophysics* 94, pp. 163–186.

Das, Shamita (2007). "The need to study speed". In: *Science* 317.5840, pp. 905–906.

Das, Shamita (2010). "Earthquake supershear rupture speeds Preface". In: *Tectonophysics* 493.3-4.

Das, Shamita and Keiiti Aki (1977). "A numerical study of two-dimensional spontaneous rupture propagation". In: *Geophysical journal international* 50.3, pp. 643–668.

Das, Shamita and CH Scholz (1983). "Why large earthquakes do not nucleate at shallow depths". In: *Nature* 305.5935, p. 621.

Davis, S. D. and C. Frohlich (1991). "Single-link cluster analysis, synthetic earthquake catalogues, and aftershock identification". In: *Geophysical Journal International* 104.2, pp. 289–306.

Dieterich, James (1994). "A constitutive law for rate of earthquake production and its application to earthquake clustering". In: *Journal of Geophysical Research: Solid Earth* 99.B2, pp. 2601–2618.

Dieterich, James H (1978). "Time-dependent friction and the mechanics of stick-slip". In: *Rock Friction and Earthquake Prediction*. Springer, pp. 790–806.

Dieterich, James H (1979). "Modeling of rock friction: 1. Experimental results and constitutive equations". In: *Journal of Geophysical Research: Solid Earth* 84.B5, pp. 2161–2168.

Dieterich, James H (1992). "Earthquake nucleation on faults with rate-and state-dependent strength". In: *Tectonophysics* 211.1-4, pp. 115–134.

Doan, Mai-Linh and Gérard Gary (2009). "Rock pulverization at high strain rate near the San Andreas fault". In: *Nature Geoscience* 2.10, p. 709.

Dodge, Douglas A, Gregory C Beroza, and WL Ellsworth (1995). "Foreshock sequence of the 1992 Landers, California, earthquake and its implications for earthquake nucleation". In: *Journal of Geophysical Research: Solid Earth* 100.B6, pp. 9865–9880.

Dodge, Douglas A, Gregory C Beroza, and WL Ellsworth (1996). "Detailed observations of California foreshock sequences: Implications for the earthquake initiation process". In: *Journal of Geophysical Research: Solid Earth* 101.B10, pp. 22371–22392.

Dunham, Eric M and Ralph J Archuleta (2004). "Evidence for a supershear transient during the 2002 Denali fault earthquake". In: *Bulletin of the Seismological Society of America* 94.6B, S256–S268.

Ellsworth, William L and Fatih Bulut (2018). "Nucleation of the 1999 Izmit earthquake by a triggered cascade of foreshocks". In: *Nature Geoscience* 11.7, p. 531.

Ellsworth, WL and GC Beroza (1995). "Seismic evidence for an earthquake nucleation phase". In: *Science* 268.5212, pp. 851–855.

Enescu, Bogdan and Kiyoshi Ito (2001). "Some premonitory phenomena of the 1995 Hyogo-Ken Nanbu (Kobe) earthquake: seismicity, b-value and fractal dimension". In: *Tectonophysics* 338.3-4, pp. 297–314.

Eshelby, JD (1969). "The elastic field of a crack extending non-uniformly under general anti-plane loading". In: *Journal of the Mechanics and Physics of Solids* 17.3, pp. 177–199.

Eshelby, John Douglas (1957). "The determination of the elastic field of an ellipsoidal inclusion, and related problems". In: *Proceedings of the Royal Society of London. Series A. Mathematical and Physical Sciences* 241.1226, pp. 376–396.

Fang, Zijun, James H Dieterich, and Guanshui Xu (2010). "Effect of initial conditions and loading path on earthquake nucleation". In: *Journal of Geophysical Research: Solid Earth* 115.B6.

Freund, LB (1972). "Crack propagation in an elastic solid subjected to general loading—II. Non-uniform rate of extension". In: *Journal of the Mechanics and Physics of Solids* 20.3, pp. 141–152.

Fukuyama, Eiichi, Takeshi Mikumo, and Kim B Olsen (2003). "Estimation of the critical slip-weakening distance: Theoretical background". In: *Bulletin of the Seismological Society of America* 93.4, pp. 1835–1840.

Fukuyama, Eiichi et al. (2018). "Spatiotemporal complexity of 2-D rupture nucleation process observed by direct monitoring during large-scale biaxial rock friction experiments". In: *Tectonophysics* 733, pp. 182–192.

Gardonio, B et al. (2019). "Seismic Activity Preceding the 2011 M w 9.0 Tohoku Earthquake, Japan, Analyzed With Multidimensional Template Matching". In: *Journal of Geophysical Research: Solid Earth* 124.7, pp. 6815–6831.

Goebel, THW et al. (2012). "Identifying fault heterogeneity through mapping spatial anomalies in acoustic emission statistics". In: *Journal of Geophysical Research: Solid Earth* 117.B3.

Goldberg, David, Mohammed Badri, and William Wepfer (1992). "Acoustic attenuation in oceanic gabbro". In: *Geophysical Journal International* 111.2, pp. 193–202.

Griffith, AA (1920). "The phenomena of flow and rupture in solids: Phil". In: *Trans. Roy. Soc. Lond. Ser. A* 221, pp. 163–98.

Griggs, 2DT (1960). "Deformation of rocks at 500 to 800". In: *Geol. Soc. America. Mem.* 79, pp. 39–104.

Gupta, Indra N (1973). "Seismic velocities in rock subjected to axial loading up to shear fracture". In: *Journal of Geophysical Research* 78.29, pp. 6936–6942.

Gutenberg, B. and C. F. Richter (1956). "Earthquake magnitude, intensity, energy, and acceleration: (Second paper)". In: *Bulletin of the seismological society of America* 46.2, pp. 105–145.

Hamano, Y (1974). "Dependence of rupture-time history on heterogeneous distribution of stress and strength on fault plane". In: *TRANSACTIONS-AMERICAN GEOPHYSICAL UNION*. Vol. 55. 4. AMER GEOPHYSICAL UNION 2000 FLORIDA AVE NW, WASHINGTON, DC 20009, pp. 352–352.

Hamiel, Yariv et al. (2004). "A viscoelastic damage model with applications to stable and unstable fracturing". In: *Geophysical Journal International* 159.3, pp. 1155–1165.

Hartley, RR and RP Behringer (2003). "Logarithmic rate dependence of force networks in sheared granular materials". In: *Nature* 421.6926, p. 928.

Hartzell, Stephen, Pengcheng Liu, and Carlos Mendoza (1996). "The 1994 Northridge, California, earthquake: Investigation of rupture velocity, risetime, and high-frequency radiation". In: *Journal of Geophysical Research: Solid Earth* 101.B9, pp. 20091–20108.

Hartzell, Stephen H and Thomas H Heaton (1983). "Inversion of strong ground motion and teleseismic waveform data for the fault rupture history of the 1979 Imperial Valley, California, earthquake". In: *Bulletin of the Seismological Society of America* 73.6A, pp. 1553–1583.

Haskell, NA (1964). "Total energy and energy spectral density of elastic wave radiation from propagating faults". In: *Bulletin of the Seismological Society of America* 54.6A, pp. 1811–1841.

Haskell, N.A. (1966). "Total energy and energy spectral density of elastic wave radiation from propagating faults. Part II. A statistical source model". In: *Bulletin of the Seismological Society of America* 56.1, pp. 125–140.

Helmstetter, A. and D. Sornette (2002a). "Sub-critical and Super-critical Regimes in Epidemic Models of Earthquake Aftershocks, in press in J". In: *Geophys. Res.(e-print at http://arXiv. org/abs/condmat/0109318)*.

Helmstetter, A and D Sornette (2002b). "Diffusion of Earthquake Aftershock Epicenters and Omori's Law: Exact Mapping to Generalized Continuous-Time Random Walk Models". In: *Phys. Rev. E* 6606.cond-mat/0203505, pp. 1–1104.

Helmstetter, A. and D. Sornette (2003b). "Foreshocks explained by cascades of triggered seismicity". In: *Journal of Geophysical Research: Solid Earth* 108.B10.

Helmstetter, A., D. Sornette, and J.-R. Grasso (2003a). "Mainshocks are aftershocks of conditional foreshocks: How do foreshock statistical properties emerge from aftershock laws". In: *Journal of Geophysical Research: Solid Earth* 108.B1.

Helmstetter, A., S. Hergarten, and D. Sornette (2004). "Properties of foreshocks and aftershocks of the nonconservative self-organized critical Olami-Feder-Christensen model". In: *Physical Review E* 70.4, p. 046120.

Hiramatsu, Yoshihiro et al. (2002). "Scaling law between corner frequency and seismic moment of microearthquakes: Is the breakdown of the cube law a nature of earthquakes?" In: *Geophysical research letters* 29.8, pp. 52–1.

Hirata, Takayuki (1987). "Omori's power law aftershock sequences of microfracturing in rock fracture experiment". In: *Journal of Geophysical Research: Solid Earth* 92.B7, pp. 6215–6221.

Honda, H (1962). "Earthquake mechanism and seismic waves". In: *Journal of Physics of the Earth* 10.2, pp. 1–97.

Huang, Hui and Lingsen Meng (2018). "Slow unlocking processes preceding the 2015 Mw 8.4 Illapel, Chile, earthquake". In: *Geophysical Research Letters* 45.9, pp. 3914–3922.

Ida, Yoshiaki (1972). "Cohesive force across the tip of a longitudinal-shear crack and Griffith's specific surface energy". In: *Journal of Geophysical Research* 77.20, pp. 3796–3805.

Ide, Satoshi and Minoru Takeo (1997). "Determination of constitutive relations of fault slip based on seismic wave analysis". In: *Journal of Geophysical Research: Solid Earth* 102.B12, pp. 27379–27391.

Ide, Satoshi et al. (2007). "A scaling law for slow earthquakes". In: *Nature* 447.7140, p. 76.

Ishii, Miaki (2011). "High-frequency rupture properties of the M w 9.0 off the Pacific coast of Tohoku Earthquake". In: *Earth, planets and space* 63.7, p. 18.

Ishii, Miaki et al. (2005). "Extent, duration and speed of the 2004 Sumatra–Andaman earthquake imaged by the Hi-Net array". In: *Nature* 435.7044, p. 933.

Jin-Biao, L. Q.-L. C. and Y. Bai-Lin (1978). "Time and space scanning of the b-value - A method for monitoring the development of catastrophic earthquakes". In: *Chinese Journal of Sinica* 2, p. 1.

Johnson, KL (1982). "One hundred years of Hertz contact". In: *Proceedings of the Institution of Mechanical Engineers* 196.1, pp. 363–378.

Johnson, TL and CH Scholz (1976). "Dynamic properties of stick-slip friction of rock". In: *Journal of Geophysical Research* 81.5, pp. 881–888.

Johnson, Tracy, Francis T Wu, and Christopher H Scholz (1973). "Source parameters for stick-slip and for earthquakes". In: *Science* 179.4070, pp. 278–280.

Jones, L. M. and P. Molnar (1979). "Some characteristics of foreshocks and their possible relationship to earthquake prediction and premonitory slip on faults". In: *Journal of Geophysical Research: Solid Earth* 84.B7, pp. 3596–3608.

Jones, Lucile and Peter Molnar (1976). "Frequency of foreshocks". In: *Nature* 262.5570, p. 677.

Kagan, Y. and L. Knopoff (1978). "Statistical study of the occurrence of shallow earthquakes". In: *Geophysical Journal International* 55.1, pp. 67–86.

Kammer, David S et al. (2018). "The equation of motion for supershear frictional rupture fronts". In: *Science advances* 4.7, eaat5622.

Kanamori, H. (1977). "The energy release in great earthquakes". In: *Journal of geophysical research* 82.20, pp. 2981–2987.

Kanamori, Hiroo and Emily E Brodsky (2004). "The physics of earthquakes". In: *Reports on Progress in Physics* 67.8, p. 1429.

Kaneko, Y and N Lapusta (2008). "Variability of earthquake nucleation in continuum models of rate-and-state faults and implications for aftershock rates". In: *Journal of Geophysical Research: Solid Earth* 113.B12.

Kato, Aitaro and Shigeki Nakagawa (2014). "Multiple slow-slip events during a foreshock sequence of the 2014 Iquique, Chile Mw 8.1 earthquake". In: *Geophysical Research Letters* 41.15, pp. 5420–5427.

Kato, Aitaro et al. (2012). "Propagation of slow slip leading up to the 2011 Mw 9.0 Tohoku-Oki earthquake". In: *Science* 335.6069, pp. 705–708.

Kato, Aitaro et al. (2016). "Accelerated nucleation of the 2014 Iquique, Chile Mw 8.2 earthquake". In: *Scientific reports* 6, p. 24792.

Kilb, Debi and Joan Gomberg (1999). "The initial subevent of the 1994 Northridge, California, earthquake: Is earthquake size predictable?" In: *Journal of Seismology* 3.4, pp. 409–420.

King, Geoffrey CP, Ross S Stein, and Jian Lin (1994). "Static stress changes and the triggering of earthquakes". In: *Bulletin of the Seismological Society of America* 84.3, pp. 935–953.

Kiser, Eric and Miaki Ishii (2011). "The 2010 Mw 8.8 Chile earthquake: Triggering on multiple segments and frequency-dependent rupture behavior". In: *Geophysical Research Letters* 38.7.

Knopoff, L. and Y. Kagan (1982). "b Values for foreshocks and aftershocks in real and simulated earthquake sequences". In: *Bulletin of the Seismological Society of America* 72.5, pp. 1663–1676.

Kostrov, BV (1964). "Selfsimilar problems of propagation of shear cracks". In: *Journal of Applied Mathematics and Mechanics* 28.5, pp. 1077–1087.

Kostrov, BV (1966). "Unsteady propagation of longitudinal shear cracks". In: *Journal of applied Mathematics and Mechanics* 30.6, pp. 1241–1248.

Kwiatek, Grzegorz et al. (2011). "Source parameters of picoseismicity recorded at Mponeng deep gold mine, South Africa: Implications for scaling relations". In: *Bulletin of the Seismological Society of America* 101.6, pp. 2592–2608.

Kwiatek, Grzegorz, THW Goebel, and Georg Dresen (2014). "Seismic moment tensor and b value variations over successive seismic cycles in laboratory stick-slip experiments". In: *Geophysical Research Letters* 41.16, pp. 5838–5846.

LaBonte, Alison L, Kevin M Brown, and Yuri Fialko (2009). "Hydrologic detection and finite element modeling of a slow slip event in the Costa Rica prism toe". In: *Journal of Geophysical Research: Solid Earth* 114.B4.

Lange, D. et al. (2017). "The Chiloé M w 7.6 earthquake of 2016 December 25 in Southern Chile and its relation to the M w 9.5 1960 Valdivia earthquake". In: *Geophysical Journal International* 213.1, pp. 210–221.

Lapusta, Nadia and James R Rice (2003). "Nucleation and early seismic propagation of small and large events in a crustal earthquake model". In: *Journal of Geophysical Research: Solid Earth* 108.B4.

Latour, S et al. (2013). "Characterization of nucleation during laboratory earthquakes". In: *Geophysical Research Letters* 40.19, pp. 5064–5069.

Lei, Xinglin et al. (2000). "Quasi-static fault growth and cracking in homogeneous brittle rock under triaxial compression using acoustic emission monitoring". In: *Journal of Geophysical Research: Solid Earth* 105.B3, pp. 6127–6139.

Lei, Xinglin, Shinian Li, and Liqiang Liu (2018). "Seismic b-Value for Foreshock AE Events Preceding Repeated Stick-Slips of Pre-Cut Faults in Granite". In: *Applied Sciences* 8.12, p. 2361.

Liu, Cangli and Thomas J Ahrens (1997). "Stress wave attenuation in shock-damaged rock". In: *Journal of Geophysical Research: Solid Earth* 102.B3, pp. 5243–5250.

Lockner, D (1993). "The role of acoustic emission in the study of rock fracture". In: *International Journal of Rock Mechanics and Mining Sciences & Geomechanics Abstracts*. Vol. 30. 7. Elsevier, pp. 883–899.

Lockner, D and J Byerlee (1977). "Acoustic emission and creep in rock at high confining pressure and differential stress". In: *Bulletin of the Seismological Society of America* 67.2, pp. 247–258.

Lockner, DA (1980). "Development of fracture planes during creep in granite". In: *Proc. 2nd Conf. on Acoustic Emission/Microseismic Activity in Geological Structures and Materials, 1980*. Trans Tech Publications, pp. 11–25.

Lockner, David A and Paul G Okubo (1983). "Measurements of frictional heating in granite". In: *Journal of Geophysical Research: Solid Earth* 88.B5, pp. 4313–4320.

Lord Jr, Arthur E and Robert M Koerner (1983). "Acoustic emission in geological materials". In: *Journal of Acoustic Emission* 2.3, pp. 195–219.

Lyakhovsky, Vladimir and Yehuda Ben-Zion (2009). "Evolving geometrical and material properties of fault zones in a damage rheology model". In: *Geochemistry, Geophysics, Geosystems* 10.11.

Madariaga, Raul (1976). "Dynamics of an expanding circular fault". In: *Bulletin of the Seismological Society of America* 66.3, pp. 639–666.

Madariaga, Raul (1977). "High-frequency radiation from crack (stress drop) models of earthquake faulting". In: *Geophysical Journal International* 51.3, pp. 625–651.

Madariaga, Raúl (1978). "The dynamic field of Haskell's rectangular dislocation fault model". In: *Bulletin of the Seismological Society of America* 68.4, pp. 869–887.

Madariaga, Raul (1983). "High frequency radiation from dynamic earthquake fault models". In: *Ann. Geophys.* 1, p. 17.

Main, Ian G, Philip G Meredith, and Colin Jones (1989). "A reinterpretation of the precursory seismic b-value anomaly from fracture mechanics". In: *Geophysical Journal International* 96.1, pp. 131–138.

Mair, Karen, Kevin M Frye, and Chris Marone (2002). "Influence of grain characteristics on the friction of granular shear zones". In: *Journal of Geophysical Research: Solid Earth* 107.B10, ECV–4.

Marone, Chris (1998). "Laboratory-derived friction laws and their application to seismic faulting". In: *Annual Review of Earth and Planetary Sciences* 26.1, pp. 643–696.

Marsan, D et al. (2014). "Foreshock activity related to enhanced aftershock production". In: *Geophysical Research Letters* 41.19, pp. 6652–6658.

Maruyama, T (1963). "On the Force Equivalent of Dynamic Elastic Elastic Dislocation with Reference to the Earthquake Mechanism". In: *Bull. Earthq. Res. Inst.* 41, pp. 467–488.

McGuire, Jeffrey J, Margaret S Boettcher, and Thomas H Jordan (2005). "Foreshock sequences and short-term earthquake predictability on East Pacific Rise transform faults". In: *Nature* 434.7032, p. 457.

McLaskey, Gregory C and Brian D Kilgore (2013). "Foreshocks during the nucleation of stick-slip instability". In: *Journal of Geophysical Research: Solid Earth* 118.6, pp. 2982–2997.

McLaskey, Gregory C and David A Lockner (2014). "Preslip and cascade processes initiating laboratory stick slip". In: *Journal of Geophysical Research: Solid Earth* 119.8, pp. 6323–6336.

McLaskey, Gregory C et al. (2015). "A robust calibration technique for acoustic emission systems based on momentum transfer from a ball drop". In: *Bulletin of the Seismological Society of America* 105.1, pp. 257–271.

Mitchell, EK, Y Fialko, and KM Brown (2015). "Frictional properties of gabbro at conditions corresponding to slow slip events in subduction zones". In: *Geochemistry, Geophysics, Geosystems* 16.11, pp. 4006–4020.

Mogi, K (1968). "Source locations of elastic shocks in fracturing process in rocks (1)". In: *Bull. Earthq. Res. Inst.* 46, pp. 1103–1125.

Mogi, Kiyoo (1962). "Study of elastic shocks caused by the fracture of heterogeneous materials and its relation to earthquake phenomena". In: *Bull. Earthq. Res. Inst., Univ. Tokyo* 40, pp. 125–173.

Moreno, M et al. (2015). "The 2014 Iquique Chile earthquake: Preparatory breaking processes of a locked asperity and natural constraints for fluid migration along the plate interface". In: *AGU Fall Meeting Abstracts*.

Mori, Jim (1996). "Rupture directivity and slip distribution of the M 4.3 foreshock to the 1992 Joshua Tree earthquake, Southern California". In: *Bulletin of the Seismological Society of America* 86.3, pp. 805–810.

Nadeau, Robert M and David Dolenc (2005). "Nonvolcanic tremors deep beneath the San Andreas Fault". In: *Science* 307.5708, pp. 389–389.

Nakatani, Masao (2001). "Conceptual and physical clarification of rate and state friction: Frictional sliding as a thermally activated rheology". In: *Journal of Geophysical Research: Solid Earth* 106.B7, pp. 13347–13380.

Nanjo, KZ et al. (2012). "Decade-scale decrease inb value prior to the M9-class 2011 Tohoku and 2004 Sumatra quakes". In: *Geophysical Research Letters* 39.20.

Nielsen, S, J Taddeucci, and S Vinciguerra (2010). "Experimental observation of stick-slip instability fronts". In: *Geophysical Journal International* 180.2, pp. 697–702.

Nuannin, Paiboon, Ota Kulhanek, and Leif Persson (2005). "Spatial and temporal b value anomalies preceding the devastating off coast of NW Sumatra earthquake of December 26, 2004". In: *Geophysical research letters* 32.11.

Obara, Kazushige and Yoshihiro Ito (2005). "Very low frequency earthquakes excited by the 2004 off the Kii peninsula earthquakes: A dynamic deformation process in the large accretionary prism". In: *Earth, Planets and Space* 57.4, pp. 321–326.

Obara, Kazushige et al. (2004). "Episodic slow slip events accompanied by non-volcanic tremors in southwest Japan subduction zone". In: *Geophysical Research Letters* 31.23.

Ogata, Y. (1988). "Statistical models for earthquake occurrences and residual analysis for point processes". In: *Journal of the American Statistical association* 83.401, pp. 9–27.

Ogata, Y., T. Utsu, and K. Katsura (1996). "Statistical discrimination of foreshocks from other earthquake clusters". In: *Geophysical journal international* 127.1, pp. 17–30.

Ogata, Yosihiko (1983). "Estimation of the parameters in the modified Omori formula for aftershock frequencies by the maximum likelihood procedure". In: *Journal of Physics of the Earth* 31.2, pp. 115–124.

Ohnaka, M, Y Kuwahara, and Kiyohiko Y (1987). "Nucleation and propagation processes of stick-slip failure and normal stress dependence of the physical parameters of dynamic slip failure". In: *Natural disaster science* 9.1, pp. 1–21.

Ohnaka, Mitiyasu (2000). "A physical scaling relation between the size of an earthquake and its nucleation zone size". In: *pure and applied geophysics* 157.11-12, pp. 2259–2282.

Ohnaka, Mitiyasu (2003). "A constitutive scaling law and a unified comprehension for frictional slip failure, shear fracture of intact rock, and earthquake rupture". In: *Journal of Geophysical Research: Solid Earth* 108.B2.

Ohnaka, Mitiyasu (2013). *The physics of rock failure and earthquakes*. Cambridge University Press.

Ohnaka, Mitiyasu and Yasuto Kuwahara (1990). "Characteristic features of local breakdown near a crack-tip in the transition zone from nucleation to unstable rupture during stick-slip shear failure". In: *Tectonophysics* 175.1-3, pp. 197–220.

Ohnaka, Mitiyasu and Kiyoo Mogi (1982). "Frequency characteristics of acoustic emission in rocks under uniaxial compression and its relation to the fracturing process to failure". In: *Journal of geophysical research: Solid Earth* 87.B5, pp. 3873–3884.

Ohnaka, Mitiyasu and Lin-feng Shen (1999). "Scaling of the shear rupture process from nucleation to dynamic propagation: Implications of geometric irregularity of the rupturing surfaces". In: *Journal of Geophysical Research: Solid Earth* 104.B1, pp. 817–844.

Ojala, Ira O, Ian G Main, and Bryne T Ngwenya (2004). "Strain rate and temperature dependence of Omori law scaling constants of AE data: Implications for earthquake foreshock-aftershock sequences". In: *Geophysical Research Letters* 31.24.

Okubo, Kurama et al. (2019). "Dynamics, radiation and overall energy budget of earthquake rupture with coseismic off-fault damage". In: *arXiv preprint arXiv:1901.01771*.

Okubo, Paul G and James H Dieterich (1984). "Effects of physical fault properties on frictional instabilities produced on simulated faults". In: *Journal of Geophysical Research: Solid Earth* 89.B7, pp. 5817–5827.

Okuwaki, Ryo, Yuji Yagi, and Shiro Hirano (2014). "Relationship between high-frequency radiation and asperity ruptures, revealed by hybrid back-projection with a non-planar fault model". In: *Scientific reports* 4, p. 7120.

Olsen, KB, R Madariaga, and Ralph J Archuleta (1997). "Three-dimensional dynamic simulation of the 1992 Landers earthquake". In: *Science* 278.5339, pp. 834–838.

Olson, Allen H and Randy J Apsel (1982). "Finite faults and inverse theory with applications to the 1979 Imperial Valley earthquake". In: *Bulletin of the Seismological Society of America* 72.6A, pp. 1969–2001.

Omori, F. (1894). "On after-shocks". In: *Seismological journal of Japan* 19, pp. 71–80.

Palmer, Andrew Clennel and James Robert Rice (1973). "The growth of slip surfaces in the progressive failure of over-consolidated clay". In: *Proceedings of the Royal Society of London. A. Mathematical and Physical Sciences* 332.1591, pp. 527–548.

Papazachos, B et al. (1967). "Aftershock sequences of some large earthquakes in the region of Greece". In: *Annals of Geophysics* 20.1, pp. 1–93.

Papazachos, BC (1973). "The time distribution of the reservoir-associated foreshocks and its importance to the prediction of the principal shock". In: *Bulletin of the Seismological Society of America* 63.6-1, pp. 1973–1978.

Park, Jeffrey, Craig R Lindberg, and Frank L Vernon III (1987). "Multitaper spectral analysis of high-frequency seismograms". In: *Journal of Geophysical Research: Solid Earth* 92.B12, pp. 12675–12684.

Passelègue, François X et al. (2013). "From sub-Rayleigh to supershear ruptures during stick-slip experiments on crustal rocks". In: *Science* 340.6137, pp. 1208–1211.

Passelègue, François X et al. (2016). "Dynamic rupture processes inferred from laboratory microearthquakes". In: *Journal of Geophysical Research: Solid Earth* 121.6, pp. 4343–4365.

Passelègue, François X et al. (2017). "Influence of fault strength on precursory processes during laboratory earthquakes". In: *Fault Zone Dynamic Processes: Evolution of Fault Properties During Seismic Rupture* 227, p. 229.

Payero, Juan S et al. (2008). "Nonvolcanic tremor observed in the Mexican subduction zone". In: *Geophysical Research Letters* 35.7.

Peng, Zhigang and Joan Gomberg (2010). "An integrated perspective of the continuum between earthquakes and slow-slip phenomena". In: *Nature geoscience* 3.9, p. 599.

Perfettini, H, Michel Campillo, and I Ionescu (2003). "On the scaling of the slip weakening rate of heterogeneous faults". In: *Journal of Geophysical Research: Solid Earth* 108.B9.

Prieto, GA et al. (2007). "Reducing the bias of multitaper spectrum estimates". In: *Geophysical Journal International* 171.3, pp. 1269–1281.

Prieto, Germán A et al. (2004). "Earthquake source scaling and self-similarity estimation from stacking P and S spectra". In: *Journal of Geophysical Research: Solid Earth* 109.B8.

Rabinowicz, E (1958). "The intrinsic variables affecting the stick-slip process". In: *Proceedings of the Physical Society* 71.4, p. 668.

Rice, James R and Andy L Ruina (1983). "Stability of steady frictional slipping". In:

Rice, James R, Nadia Lapusta, and K Ranjith (2001). "Rate and state dependent friction and the stability of sliding between elastically deformable solids". In: *Journal of the Mechanics and Physics of Solids* 49.9, pp. 1865–1898.

Rice, JR (1979). *The mechanics of earthquake rupture*. Division of Engineering, Brown University Providence.

Richards, Paul G and Keiiti Aki (1980). *Quantitative seismology: theory and methods*. Freeman.

Rivière, Jacques et al. (2018). "Evolution of b-value during the seismic cycle: Insights from laboratory experiments on simulated faults". In: *Earth and Planetary Science Letters* 482, pp. 407–413.

Rogers, Garry and Herb Dragert (2003). "Episodic tremor and slip on the Cascadia subduction zone: The chatter of silent slip". In: *Science* 300.5627, pp. 1942–1943.

Rosakis, AJ, O Samudrala, and D Coker (1999). "Cracks faster than the shear wave speed". In: *Science* 284.5418, pp. 1337–1340.

Ross, Zachary E et al. (2019). "Searching for hidden earthquakes in Southern California". In: *Science* 364.6442, pp. 767–771.

Roth, Frank (1988). "Modelling of stress patterns along the western part of the North Anatolian fault zone". In: *Tectonophysics* 152.3-4, pp. 215–226.

Rubin, Allan Mattathias and J-P Ampuero (2005). "Earthquake nucleation on (aging) rate and state faults". In: *Journal of Geophysical Research: Solid Earth* 110.B11.

Ruina, Andy (1983). "Slip instability and state variable friction laws". In: *Journal of Geophysical Research: Solid Earth* 88.B12, pp. 10359–10370.

Ruiz, S et al. (2014). "Intense foreshocks and a slow slip event preceded the 2014 Iquique Mw 8.1 earthquake". In: *Science* 345.6201, pp. 1165–1169.

Sato, Tamao and Tomowo Hirasawa (1973). "Body wave spectra from propagating shear cracks". In: *Journal of Physics of the Earth* 21.4, pp. 415–431.

Savage, JC (1966). "Radiation from a realistic model of faulting". In: *Bulletin of the Seismological Society of America* 56.2, pp. 577–592.

Savage, JC (1972). "Relation of corner frequency to fault dimensions". In: *Journal of geophysical research* 77.20, pp. 3788–3795.

Schaff, David P et al. (2002). "High-resolution image of Calaveras fault seismicity". In: *Journal of Geophysical Research: Solid Earth* 107.B9, ESE–5.

Scholz, CH (1968a). "Experimental study of the fracturing process in brittle rock". In: *Journal of Geophysical Research* 73.4, pp. 1447–1454.

Scholz, CH (1968b). "The frequency-magnitude relation of microfracturing in rock and its relation to earthquakes". In: *Bulletin of the seismological society of America* 58.1, pp. 399–415.

Scholz, CH (1986). "Preface: A short geophysical history of Westerly granite". In: *Washington DC American Geophysical Union Geophysical Monograph Series* 37.

Scholz, CH (1988). "The critical slip distance for seismic faulting". In: *Nature* 336.6201, p. 761.

Scholz, Christopher H (2019). *The mechanics of earthquakes and faulting*. Cambridge university press.

Schubnel, A et al. (2006). "Transient creep, aseismic damage and slow failure in Carrara marble deformed across the brittle-ductile transition". In: *Geophysical Research Letters* 33.17.

Schubnel, A et al. (2007). "Fluid-induced rupture experiment on Fontainebleau sandstone: Premonitory activity, rupture propagation, and aftershocks". In: *Geophysical research letters* 34.19.

Schubnel, Alexandre et al. (2011). "Photo-acoustic study of subshear and supershear ruptures in the laboratory". In: *Earth and Planetary Science Letters* 308.3-4, pp. 424–432.

Sellers, Ewan J, Milton O Kataka, and Lindsay M Linzer (2003). "Source parameters of acoustic emission events and scaling with mining-induced seismicity". In: *Journal of Geophysical Research: Solid Earth* 108.B9.

Shelly, David R et al. (2006). "Low-frequency earthquakes in Shikoku, Japan, and their relationship to episodic tremor and slip". In: *Nature* 442.7099, p. 188.

Shimamoto, T. (1989). "The origin of SC mylonites and a new fault-zone model". In: *Journal of Structural Geology* 11.1-2, pp. 51–64.

Slepian, David (1978). "Prolate spheroidal wave functions, Fourier analysis, and uncertainty—V: The discrete case". In: *Bell System Technical Journal* 57.5, pp. 1371–1430.

Socquet, Anne et al. (2017). "An 8 month slow slip event triggers progressive nucleation of the 2014 Chile megathrust". In: *Geophysical Research Letters* 44.9, pp. 4046–4053.

Sondergeld, Carl H and Louis H Estey (1981). "Acoustic emission study of microfracturing during the cyclic loading of Westerly granite". In: *Journal of Geophysical Research: Solid Earth* 86.B4, pp. 2915–2924.

Sondergeld, CH and LH Estey (1982). "Source mechanisms and microfracturing during uniaxial cycling of rock". In: *pure and applied geophysics* 120.1, pp. 151–166.

Sornette, Didier, Christian Vanneste, and Leon Knopoff (1992). "Statistical model of earthquake foreshocks". In: *Physical Review A* 45.12, p. 8351.

Spudich, Paul and L Neil Frazer (1984). "Use of ray theory to calculate high-frequency radiation from earthquake sources having spatially variable rupture velocity and stress drop". In: *Bulletin of the Seismological Society of America* 74.6, pp. 2061–2082.

Stein, Ross S, Aykut A Barka, and James H Dieterich (1997). "Progressive failure on the North Anatolian fault since 1939 by earthquake stress triggering". In: *Geophysical Journal International* 128.3, pp. 594–604.

Steinbrugge, Karl V et al. (1960). "Creep on the San Andreas fault". In: *Bulletin of the Seismological Society of America* 50.3, pp. 389–415.

Suyehiro, Shigeji (1966). "Difference between aftershocks and foreshocks in the relationship of magnitude to frequency of occurrence for the great Chilean earthquake of 1960". In: *Bulletin of the Seismological Society of America* 56.1, pp. 185–200.

Tamaribuchi, Koji et al. (2018). "Characteristics of foreshock activity inferred from the JMA earthquake catalog". In: *Earth, Planets and Space* 70.1, p. 90.

Tapponnier, Paul and WF Brace (1976). "Development of stress-induced microcracks in Westerly granite". In: *International Journal of Rock Mechanics and Mining Sciences & Geomechanics Abstracts*. Vol. 13. 4. Elsevier, pp. 103–112.

Thomas, Marion Y and Harsha S Bhat (2018). "Dynamic evolution of off-fault medium during an earthquake: a micromechanics based model". In: *Geophysical Journal International* 214.2, pp. 1267–1280.

Thomas, Marion Y, Thomas M Mitchell, and Harsha S Bhat (2017). *Fault zone dynamic processes: Evolution of fault properties during seismic rupture*. Vol. 227. John Wiley & Sons.

Thompson, BD, RP Young, and David A Lockner (2009). "Premonitory acoustic emissions and stick-slip in natural and smooth-faulted Westerly granite". In: *Journal of Geophysical Research: Solid Earth* 114.B2.

Thomson, David J (1982). "Spectrum estimation and harmonic analysis". In: *Proceedings of the IEEE* 70.9, pp. 1055–1096.

Tinti, E, P Spudich, and M Cocco (2005). "Earthquake fracture energy inferred from kinematic rupture models on extended faults". In: *Journal of Geophysical Research: Solid Earth* 110.B12.

Togo, Tetsuhiro et al. (2015). "Stick–slip behavior of Indian gabbro as studied using a NIED large-scale biaxial friction apparatus". In: *Earthquake Science* 28.2, pp. 97–118.

Tormann, Thessa et al. (2015). "Randomness of megathrust earthquakes implied by rapid stress recovery after the Japan earthquake". In: *Nature Geoscience* 8.2, p. 152.

Tullis, J and R Yund (1992). "The brittle-ductile transition in feldspar aggregates: An experimental study". In: *International Geophysics*. Vol. 51. Elsevier, pp. 89–117.

Uenishi, Koji and James R Rice (2003). "Universal nucleation length for slip-weakening rupture instability under nonuniform fault loading". In: *Journal of Geophysical Research: Solid Earth* 108.B1.

Urata, Yumi et al. (2018). "Apparent dependence of rate-and state-dependent friction parameters on loading velocity and cumulative displacement inferred from large-scale biaxial friction experiments". In: *Earthquakes and Multi-hazards Around the Pacific Rim, Vol. I*. Springer, pp. 23–43.

Utsu, T., Y. Ogata, et al. (1995). "The centenary of the Omori formula for a decay law of aftershock activity". In: *Journal of Physics of the Earth* 43.1, pp. 1–33.

Utsu, Tokuji (1961). "A statistical study on the occurrence of aftershocks". In: *Geophys. Mag.* 30, pp. 521–605.

Vallée, Maxime et al. (2008). "The 14 November 2001 Kokoxili (Tibet) earthquake: High-frequency seismic radiation originating from the transitions between sub-Rayleigh and supershear rupture velocity regimes". In: *Journal of Geophysical Research: Solid Earth* 113.B7.

Voss, N et al. (2018). "Do slow slip events trigger large and great megathrust earthquakes?" In: *Science advances* 4.10, eaat8472.

W. Goebel, TH et al. (2013). "Acoustic emissions document stress changes over many seismic cycles in stick-slip experiments". In: *Geophysical Research Letters* 40.10, pp. 2049–2054.

Wang, Dun and Jim Mori (2011). "Rupture process of the 2011 off the Pacific coast of Tohoku Earthquake (M w 9.0) as imaged with back-projection of teleseismic P-waves". In: *Earth, planets and space* 63.7, p. 17.

Weeks, J, D Lockner, and J Byerlee (1978). "Change in b-values during movement on cut surfaces in granite". In: *Bulletin of the Seismological Society of America* 68.2, pp. 333–341.

Wicks, Charles et al. (2011). "InSAR observations of aseismic slip associated with an earthquake swarm in the Columbia River flood basalts". In: *Journal of Geophysical Research: Solid Earth* 116.B12.

Wong, T.-F., S.-C. Ko, and D. L. Olgaard (1997). "Generation and maintenance of pore pressure excess in a dehydrating system 2. Theoretical analysis". In: *Journal of Geophysical Research: Solid Earth* 102.B1, pp. 841–852.

Wong, Teng-fong (1982). "Shear fracture energy of Westerly granite from post-failure behavior". In: *Journal of Geophysical Research: Solid Earth* 87.B2, pp. 990–1000.

Wu, Francis T, KC Thomson, and H Kuenzler (1972). "Stick-slip propagation velocity and seismic source mechanism". In: *Bulletin of the Seismological Society of America* 62.6, pp. 1621–1628.

Xia, Kaiwen, Ares J Rosakis, and Hiroo Kanamori (2004). "Laboratory earthquakes: The sub-Rayleigh-to-supershear rupture transition". In: *Science* 303.5665, pp. 1859–1861.

Xu, Shiqing et al. (2018). "Strain rate effect on fault slip and rupture evolution: Insight from meter-scale rock friction experiments". In: *Tectonophysics* 733, pp. 209–231.

Yamada, Takuji et al. (2007). "Stress drops and radiated seismic energies of microearthquakes in a South African gold mine". In: *Journal of Geophysical Research: Solid Earth* 112.B3.

Yamashita, Futoshi, Eiichi Fukuyama, and Kazuo Mizoguchi (2014). "Probing the slip-weakening mechanism of earthquakes with electrical conductivity: Rapid transition from asperity contact to gouge comminution". In: *Geophysical Research Letters* 41.2, pp. 341–347.

Yamashita, Futoshi et al. (2018). "Rupture preparation process controlled by surface roughness on meter-scale laboratory fault". In: *Tectonophysics* 733, pp. 193–208.

Yamashita, T and L Knopoff (1989). "A model of foreshock occurrence". In: *Geophysical Journal International* 96.3, pp. 389–399.

Yoshimitsu, Nana, Hironori Kawakata, and Naoki Takahashi (2014). "Magnitude- 7 level earthquakes: A new lower limit of self-similarity in seismic scaling relationships". In: *Geophysical Research Letters* 41.13, pp. 4495–4502.

Zaliapin, Ilya and Yehuda Ben-Zion (2013). "Earthquake clusters in southern California I: Identification and stability". In: *Journal of Geophysical Research: Solid Earth* 118.6, pp. 2847–2864.

Zhang, Hao and Zengxi Ge (2010). "Tracking the rupture of the 2008 Wenchuan earthquake by using the relative back-projection method". In: *Bulletin of the Seismological Society of America* 100.5B, pp. 2551–2560.

Appendix

Geophysical Research Letters

RESEARCH LETTER
10.1029/2018GL080519

Key Points:
- High-frequency radiation is enhanced with both confining pressure and rupture velocity
- Acoustic sensors can be used as an array to track high-frequency sources during rupture propagation
- High-frequency radiation sources propagate consistently with the rupture front and are located behind it

Supporting Information:
- Supporting Information S1

Correspondence to:
S. Marty,
marty@geologie.ens.fr

Citation:
Marty, S., Passelègue, F. X., Aubry, J., Bhat, H. S., Schubnel, A., & Madariaga, R. (2019). Origin of high-frequency radiation during laboratory earthquakes. *Geophysical Research Letters*, *46*, 3755–3763. https://doi.org/10.1029/2018GL080519

Received 17 SEP 2018
Accepted 1 MAR 2019
Accepted article online 13 MAR 2019
Published online 15 APR 2019

Origin of High-Frequency Radiation During Laboratory Earthquakes

S. Marty[1], F. X. Passelègue[2], J. Aubry[1], H. S. Bhat[1], A. Schubnel[1], and R. Madariaga[1]

[1]Laboratoire de Géologie, École Normale Supérieure/CNRS UMR 8538, PSL Research University, Paris, France, [2]École Polytechnique Fédérale de Lausanne, Lausanne, Switzerland

Abstract We monitor dynamic rupture propagation during laboratory stick-slip experiments performed on saw-cut Westerly granite under upper crustal conditions (10–90 MPa). Spectral analysis of high-frequency acoustic waveforms provided evidence that energy radiation is enhanced with stress conditions and rupture velocity. Using acoustic recordings band-pass filtered to 400–800 kHz (7–14 mm wavelength) and high-pass filtered above 800 kHz, we back projected high-frequency energy generated during rupture propagation. Our results show that the high-frequency radiation originates behind the rupture front during propagation and propagates at a speed close to that obtained by our rupture velocity inversion. From scaling arguments, we suggest that the origin of high-frequency radiation lies in the fast dynamic stress-drop in the breakdown zone together with off-fault coseismic damage propagating behind the rupture tip. The application of the back-projection method at the laboratory scale provides new ways to locally investigate physical mechanisms that control high-frequency radiation.

Plain Language Summary Over geological time scales, partially or fully locked tectonic plates accumulate stress and strain. The stress and the strain build up on discontinuities that we call "faults." Natural faults exist either inside a tectonic plate or at the boundary between two distinct tectonic plates. When the stress accumulated on a fault exceeds the strength of the fault, the accumulated stress and strain, which can be interpreted in term of accumulated energy, are suddenly released. This natural phenomenon is called an "earthquake." During an earthquake, part of the energy is released in the form of seismic waves. Those seismic waves are responsible for the ground shaking. High-frequency waves usually cause most of the damage. To better understand the physical parameters that influence the generation of high-frequency waves, we experimentally reproduced microearthquakes and used them as a proxy to study real earthquakes. Our results showed that the higher the pressure acting on the fault when an earthquake is generated, the higher the amount of high-frequency radiations. Moreover, our observations underlined that, during an earthquake, high-frequency waves are released in specific areas on the fault. Thus, these results might be of relevance to improve seismic hazard assessment.

1. Introduction

Even though high-frequency waves (>1 Hz) are likely to be the most damaging during earthquakes propagation, physical processes at the origin of high-frequency radiation are still under debate and relatively less well understood (Das, 2007). First kinematic models used to invert seismic slip distribution (Haskell, 1964; Savage, 1966) were unable to describe high-frequency radiation because they assumed flat source models with constant slip and stress drop on the fault.

Fracture models which introduced variable slip function and rupture velocity showed that changes in rise time and rupture velocity lead to high-frequency radiation (Madariaga, 1977, 1983). Later, seismologists used ray-theory to calculate high-frequency radiation from earthquakes having spatial variations of rupture velocity, slip velocity, and stress drop (Bernard & Madariaga, 1984; Spudich & Frazer, 1984) and predicted that the starting and stopping phases of earthquakes to be responsible of high-frequency radiation. A good illustration of this phenomena is the 17th of January 1984 Northridge earthquake (Mw 6.7) for which Hartzell et al. (1996) identified the initiation of the rupture and its stopping to be concurrent with high-frequency radiation.

An interesting case of the rupture velocity effects on high-frequency radiation is that of earthquakes propagating at supershear velocities (i.e., velocities higher than the shear wave speed). Supershear earthquakes are suspected to be more devastating than sub-Rayleigh earthquakes (with rupture velocities slower than the *S*

wave velocity) due to the formation of Mach-wave fronts (Bhat et al., 2007; Bruhat et al., 2016; Dunham & Archuleta, 2004). Theoretical studies of supershear rupture (Andrews, 1976; Das & Aki, 1977; Hamano, 1974) followed by experimental works on plastic polymer (Rosakis et al., 1999; Wu et al., 1972) demonstrated the existence of possible supershear scenarios. Following the Mw 7.6 devastating Izmit earthquake in Turkey, Bouchon et al. (2001) successfully made the observation that certain parts of the fault ruptured at supershear speeds. Passelègue et al. (2013) were the first to experimentally illustrate the rupture transition from sub-Rayleigh regime to supershear regime on centimetric rock samples at upper crustal stress conditions. In these experiments, Passelègue et al. (2016) observed particularly energetic high-frequency radiation during stick-slip rupture propagation, the origin of which remained obscure.

Quite recently, the emergence of dense and large aperture seismic arrays has provided a new method to investigate the spatial and temporal behavior of seismic energy release during large earthquakes. This method, called back-projection, utilizes the time-reversal property of seismic waves to retrieve their sources and was introduced by Spudich and Frazer (1984). Following the successful application of the back-projection method to the 2004 Sumatra-Andaman earthquake by Ishii et al. (2005), the back-projection method has been applied to numerous earthquakes (Kiser & Ishii, 2011, Okuwaki et al., 2014, Zhang & Ge, 2010, Ishii, 2011, Wang & Mori, 2011). To the best of our knowledge, the technique has never been applied in the laboratory yet, where it might shed light on the origin of high-frequency radiation.

This study presents results from stick-slip experiments conducted on saw cut Westerly granite under triaxial conditions and is devoted to investigate the dynamics of high-frequency radiation during rupture propagation. First, the rupture velocity of dynamic stick-slip instabilities was measured using piezoelectric acoustic sensors by tracking the propagation of the rupture front. We then investigate the influence of stress conditions and rupture velocity on high-frequency radiation. Second, we apply the back-projection method to image high-frequency sources during rupture history and discuss their link to rupture front propagation.

2. Experimental Setup

Stick-slip experiments were performed on Westerly granite using a triaxial oil-medium loading cell ($\sigma_1 > \sigma_2 = \sigma_3$). The confining pressure and the differential stress (i.e., the axial stress) can go up to 100 (about 3 km depth) and 700 MPa, respectively. Experiments were conducted on Westerly granite which is a rock-mechanics standard with millimetric grain sizes and *P*, *S*, and Rayleigh wave velocities that are, respectively, 5,700, 3,500, and 3,200 m/s (Scholz, 1986). Cylindrical samples were 40 mm wide and 88 mm long and were cut at an angle of 60° from the horizontal plane in order to create a weak fault interface. Fault interface was roughened with a #160 grit paper to create homogeneous roughness and to minimize cohesion. The axial displacement of the piston, the confining pressure, and the axial stress were measured by external sensors.

Acoustic emissions were recorded during the experiments using a high-frequency acoustic monitoring system at a sampling rate of 10 MHz. There were 16 piezo-ceramics acoustic sensors that were used in this study. All the acoustic sensors were polarized in the same way and were mostly sensitive to *P* waves (i.e., motion perpendicular to the sample surface). A complete description of the triaxial apparatus and of the high-frequency acoustic monitoring system is given in the supporting information and in Passelègue et al. (2016).

3. Methodology

In our study we subdivide the 16 acoustic sensors into two arrays. The first array consists of seven acoustic sensors evenly distributed along the fault plane which were used to monitor the rupture front propagation. The nine remaining acoustic sensors form the second array, which is used to both locate the nucleation zone of the stick-slip instability and for the back-projection analysis. The nine sensors were arranged as close as possible to each other and face the fault. Hereafter, we refer to the first array as AFAS (along fault acoustic sensors) and to the second array as OFAS (off-fault acoustic sensors). The geometry of both arrays is shown in the supporting information (Figures S1b and S1c).

3.1. Rupture Velocity Inversion

Previous studies have already used acoustic sensors to monitor rupture front propagation during stick-slip instability either on plastic polymers (Schubnel et al., 2011) or crustal rocks (Passelègue et al., 2013).

Linear elasticity predicts the existence of an elastic strain singularity at the head of the rupture tip which is proportional to r^{-n} where r is the distance to the rupture tip and n an exponent which depends on the rupture velocity ($0 \leq n \leq 0.5$). Acoustic sensors located along the fault will record the passage of the rupture front and can be used to estimate the rupture velocity.

In our rupture velocity inversion we apply the following methodology: (i) P wave arrival times are manually picked on OFAS recordings and are used to determine the initiation time as well as the location of the nucleation zone on the fault (ii) using the least square method, we search for the average rupture velocity that best matches the observed rupture front arrival times on the AFAS recordings. The method is exhaustively described in the supporting information and in Passelègue et al. (2013, 2016).

3.2. The Back-Projection Method

The back-projection technique propagates seismogram waveforms backward in time to a grid of potential sources, in order to determine the spatial and temporal evolution of seismic sources during an earthquake. The strength of the technique lies in its simplicity since it only requires a velocity structure model and a grid of potential sources.

In the present study, we use the coherency function $x(t)$ first introduced by Ishii (2011) to track high-frequency sources during rupture propagation. The coherency function quantifies the average cross-correlation over a time window T of the stacked waveform and each individual acoustic waveform. For a set of k acoustic sensors, at a time t and from a source i, the coherency function $x_i(t)$ takes the form

$$x_i(t) = \frac{1}{k}\sum_{n=1}^{k} \frac{p_n \sum_{\tau=t}^{t+T} u_n(\tau + t_{i,n} + \Delta t_n) * s_i(\tau)}{\sqrt{\sum_{\tau=t}^{t+T} u_n^2(\tau + t_{i,n} + \Delta t_n)}\sqrt{\sum_{\tau=t}^{t+T} s_i^2(\tau)}},$$

where s is the stacked waveform which for a source i and at time t takes the form

$$s_i(t) = \frac{1}{k}\sum_{n=1}^{k} w_n u_n(t + t_{i,n} + \Delta t_n),$$

with k the total number of acoustic sensors, $u_n(t)$ the recorded acoustic waveform of the nth acoustic sensor, $t_{i,n}$ the predicted P wave travel time between ith grid location and the acoustic sensor k, Δt_n the time correction of the nth acoustic sensor that we obtain by cross-correlating the initial few microseconds of each acoustic waveform with a reference waveform. Δt_n ensures that all waveforms align well at the nucleation location. The cross-correlation also yields the weighting factor $w_n = p_n/A_n$ with p_n that corrects for first P wave polarity (either equals to -1 or 1) and A_n a normalization factor equal to the ratio of the maximum absolute amplitude of the reference acoustic sensor waveform over the maximum absolute amplitude of the nth acoustic sensor waveform. Synthetic tests (Figure S8) were performed to assess the resolution of the method using the OFAS array geometry presented above. A detailed description of the method is given in the supporting information.

4. Results

4.1. Mechanical Behavior of Stick-Slip Instabilities

Stick-slip experiments presented in this study were performed at confining pressure Pc ranging from 10 to 90 MPa. All experiments were conducted using a similar fault geometry and imposing a constant displacement rate resolved on the fault plane of around 1 μm/s. Figure 1a reports the evolution of both shear stress and fault slip with time for a stick-slip experiment at 60 MPa confining pressure. Increasing the axial stress leads first to the elastic increase of both shear stress and normal stress acting on the fault plane. Once the shear stress reaches a critical value τ_c, corresponding to the critical strength of the fault, slip initiates leading to an abrupt stress release. The stress drop is proportional to the slip and both increase with the confining pressure. Regardless of the confining pressure, the system displays the same mechanical behavior. Figure 1b shows that slip increases linearly with the stress drop for all stick-slip experiments. The slope is equal to the stiffness of the whole system (machine and rock specimen). This has been observed in many other experiments on crustal rocks and can be explained by the increase of the normal stress on the fault

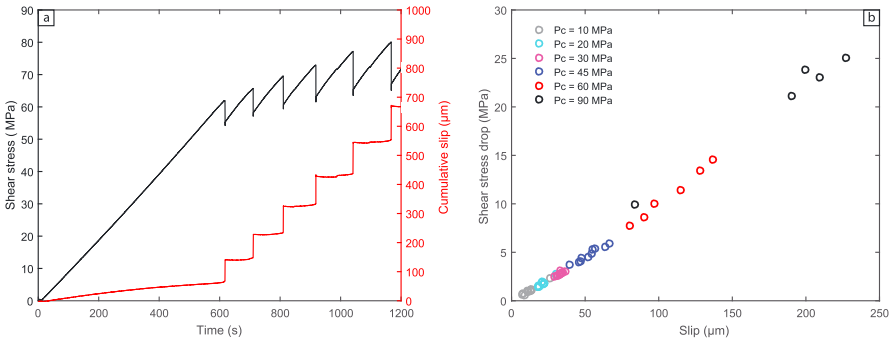

Figure 1. (a) Evolution of shear stress and slip versus time at $Pc = 60$ MPa. When the shear stress on the frictional interface exceeds the fault strength the stored elastic energy is suddenly released by seismic slip. The cumulative slip remains constant during loading because it is corrected from the elastic part of the deformation (sample and apparatus). (b) Relationship between shear stress drop and slip for all experiments. The ratio between the stress drop and the slip is preserved (higher the stress drop, higher the amount of slip) and is equal to the stiffness of the whole system (sample and apparatus).

with increasing in confining pressure, which enhances the strain energy stored in the medium during loading (Brace & Byerlee, 1966; Byerlee & Brace, 1968; Johnson et al., 1973; Johnson & Scholz, 1976; Passelègue et al., 2016).

4.2. Influence of Rupture Velocity and Confining Pressure on High-Frequency Radiation

The relation between the inverted rupture velocities, the stress drop, and the confining pressure is shown in Figure 2a. Rupture velocities are normalized by the S wave velocity of the medium, values under 0.92 correspond to sub-Rayleigh ruptures and values above 1 correspond to supershear ruptures. The overall trend of the rupture velocity is to increase with confinement and stress drop. For stress drops higher than 10 MPa, only supershear ruptures are observed. This was already well described by Passelègue et al. (2013) and can be understood in terms of the seismic ratio S and the initial strength that precedes the rupture. S controls the transition from sub-Rayleigh to supershear rupture (Andrews, 1976) and can be expressed as

$$S = \frac{\tau_p - \tau_0}{\tau_0 - \tau_r},$$

where τ_p, τ_0, and τ_r are, respectively, the peak frictional stress, the initial stress, and the residual frictional stress. Ruptures may transition from sub-Rayleigh to supershear velocity if the two conditions are satisfied:

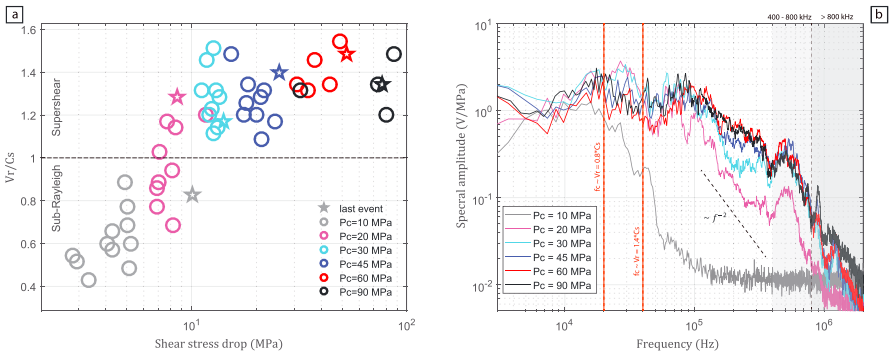

Figure 2. (a) Rupture velocity obtained by inversion as a function of static shear stress drop. Rupture velocities are normalized by the shear wave velocity, values higher than 1 correspond to supershear velocities and lower than 0.92 to sub-Rayleigh velocities. Stars indicate stick-slip events whose Fourier spectra are displayed in Figure 2b. (b) Fourier spectra of the last stick-slip event during stick-slip experiments at varying confining pressures. Fourier spectra are averaged using both AFAS and OFAS arrays, and normalized by their respective stress-drop. The gray shaded areas indicate frequency bands used for the back-projection analysis.

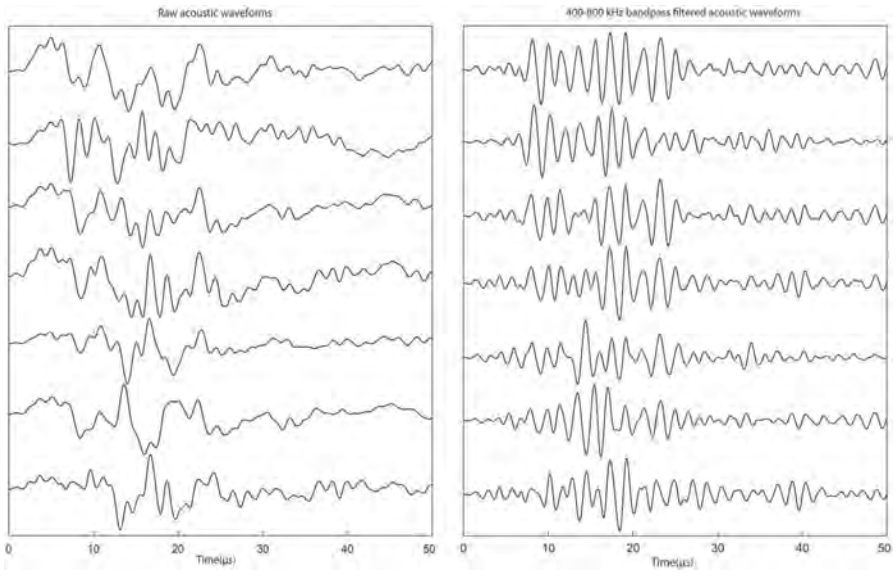

Figure 3. Example of acoustic waveforms used for the back-projection analysis: raw acoustic waveforms (left) and band-pass (400–800 KHz) acoustic waveforms (right). In both cases waveforms are aligned on the first *P* wave arrivals and are normalized by their maximum amplitudes.

(i) the size of the fault is larger than the transition length from sub-Rayleigh to supershear rupture propagation L_c which decreases with normal stress (ii) S is smaller than S_c (equal to 1.77 or 1.19 in 2-D or 3-D, respectively).

In our experiments, the initial stress was always very close to peak frictional stress so that $S < S_c$ was always satisfied. However, estimates of L_c at low confinement ($Pc \leq 20$ MPa) give values that are larger or of the same order of the size of our experimental fault, which explains why most of the ruptures were sub-Rayleigh at $Pc \leq 20$ MPa. Additional details are given in the supporting information.

In Figure 2b the Fourier spectra that correspond to the last stick-slip event at each confining pressure are displayed (star symbols, Figure 2a). Directivity effects cannot be fully suppressed because our acoustic sensor network is not perfectly symmetric. Hence, Fourier spectra were averaged over all acoustic sensors (i.e., from both AFAS and OFAS arrays) in order to minimize directivity bias. To compare the high-frequency content of the spectra, the latter have to scale at low frequency. As we expected the stress-drop to control the amplitude of low frequency waves, each spectrum is normalized by its corresponding stress-drop. We find a double correlation between the spectral amplitude of high-frequency radiation, the rupture velocity, and the confining pressure. This is particularly well illustrated at the lowest confining pressure ($Pc = 10$ MPa), where stick-slip events ruptured at sub-Rayleigh velocity. The Fourier spectrum of these events is strongly depleted of high frequencies. In contrast, the effect of the confining pressure prevails over the effect of the rupture velocity, in the high-frequency radiation range, when comparing the spectra at $Pc = 20$ and 30 MPa ($Vr = 4{,}500$ and 4,100 m/s, respectively). Similarly, the Fourier spectra at $Pc = 45$, 60, and 90 MPa which correspond to the highest rupture velocities ($Vr = 4{,}900$, 5,200, 4,700 m/s, respectively) are the most enhanced in high-frequency radiation. Note that at $Pc \geq 20$ MPa, we consistently observe the emergence of two frequency bands. The first one is centered at 100 kHz and the second one lies between 400 and 800 kHz. In the following section, we show results of back-projection analysis applied to acoustic waveforms (i) band-pass filtered to 400–800 kHz and (ii) high-pass filtered above 800 kHz.

4.3. Back-Projection Analysis During Rupture Propagation

Unfiltered and band-pass filtered between 400 and 800 kHz OFAS waveforms are displayed in Figure 3. Waveforms are lined up with the first *P* wave arrivals at each station. Only filtered waveforms were used for back-projection. We implicitly make the hypothesis that high-frequency sources are located on the fault plane. This assumption seems reasonable given that new fracture formations were never observed during any of the experiments performed for this study. Because our sensors are single components, we are not

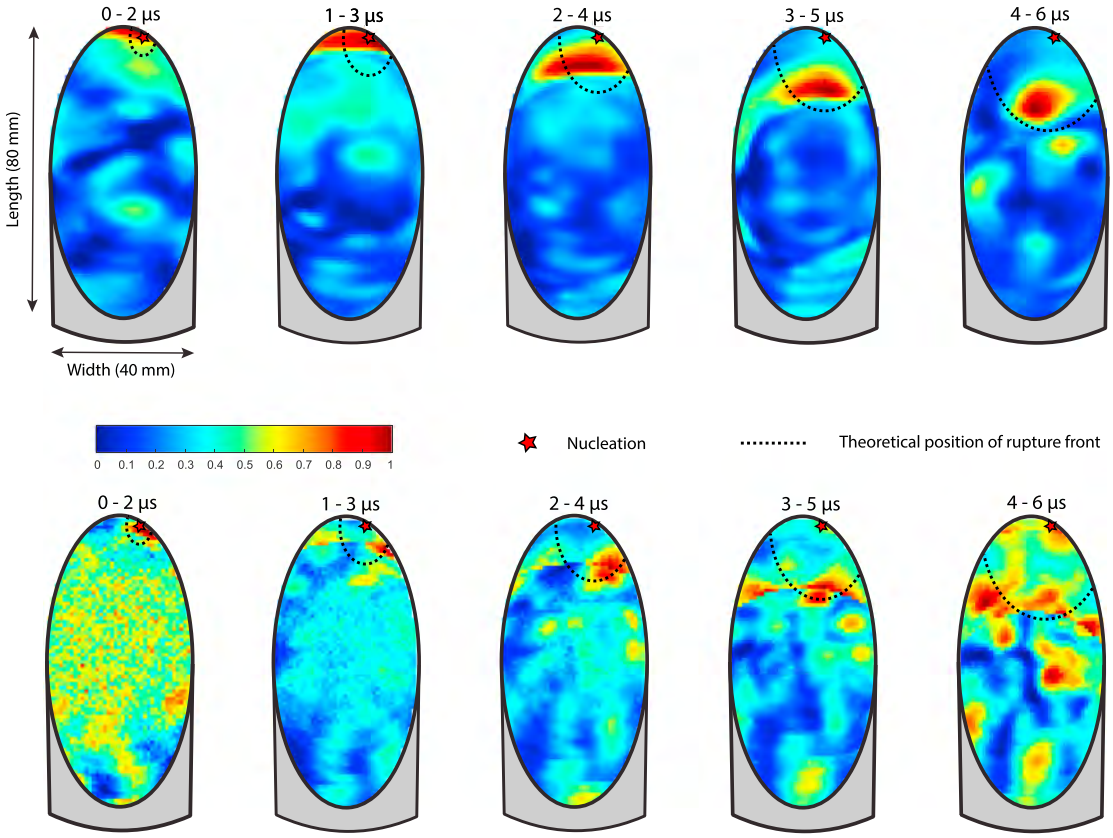

Figure 4. Snapshots of back-projection results for one stick-slip event at $Pc = 90$ MPa from off-fault acoustic sensors waveforms band-pass filtered to 400–800 kHz (top) and high-pass filtered above 800 kHz (bottom). The colorbar represents the value of the coherency function on the fault plane. The time is relative to the onset of the nucleation. The red star indicates the nucleation location and the black dashed line indicates the rupture front theoretical position estimated from the average rupture velocity Vr obtained by inversion, here equal to 5.1 km/s.

able to distinguish between *P* and *S* waves (and also surface waves and reverberations), which would make the back-projection results poorly resolved. As a consequence, the back-projection analysis are restrained to the beginning of the acoustic waveforms, that is, before first *S* wave arrivals at each stations (on average, 6 µs after first *P* wave on the OFAS array). *P* wave signals are back projected on the fault plane by computing the coherency function over 2 µs time windows, with respect to the nucleation time. Figure 4 presents back-projection results in the 400–800 kHz frequency band (top) and above 800 kHz (bottom) for one event at $Pc = 90$ MPa whose average rupture velocity was 5.1 km/s. The colorbar indicates the value of the coherency function normalized by its maximum value. The red star indicates the position of the nucleation and the black dashed line the theoretical position of the rupture front (at 1 µs for the 0–2 µs time window, at 2 µs for the 1–3 µs time window and so on) according to the estimated rupture velocity in section 4.2. In the supershear case, this theoretical rupture front is elliptical and propagates at constant velocities C_s and V_r along the ellipse's minor and major axes, respectively, where C_s and V_r are the *S* wave and in-plane rupture velocities (see supporting information).

The 400–800 kHz frequency band (Figure 4 top) gives the clearest results. Throughout the rupture history, high-frequency energy sources are always localized behind the theoretical rupture front position. When rupture initiates (0–2 µs) high-frequency energy localizes slightly behind the nucleation and spreads over the width of the fault plane. At $t = 1$–3 µs period, high-frequency energy starts to propagate consistently in the direction of the rupture front at relatively low speed and spreads over the entire width of the fault. The source of high-frequencies then accelerates (2–4 µs) along the fault plane until it roughly reaches the average rupture velocity (3–5, 4–6 µs) while concentrating in the middle of the fault. Compared to the 400–800 kHz frequency band, back-projection images for high-frequency sources above 800 kHz (Figure 4 bottom) are less clear. When rupture initiates (0–2 µs), the maximum coherence is still focused close to

the nucleation zone. It was also observed that the maximum coherence propagating consistently matched the theoretical rupture front (1–3, 2–4, 3–5 μs), although high-frequency energy was more diffuse and patchy. In contrast, between 4 and 6 μs, high-frequency energy starts to diffuse over the entire fault. Also, relative to high-frequency energy between 400 and 800 kHz, high-frequency energy above 800 kHz is always focused closer to the theoretical rupture front.

5. Discussion and Conclusions

We summarize below the four key conclusions of this body of work.

5.1. High-Frequency Radiation is Related to Stress and Rupture Velocity Conditions

Observations of Fourier analysis (Figures 2a and 2b) have shown that high-frequency radiation is enhanced with both the stress conditions (i.e., normal stress acting on the fault) and the rupture velocity. This is consistent with seismological observations of mega-thrust subduction earthquakes where zones of high-frequency energy release correspond to deeper portions of the fault (Ishii, 2011). There are different ways to interpret these results. First, the increase of stress concentrations in the process zone with stress conditions and rupture velocity would likely enhance physical processes as off-fault damage (Okubo et al., 2018; Thomas et al., 2017; Thomas & Bhat, 2018) taking place in the vicinity of the rupture front leading to more radiated high-frequency energy. Also, as the rupture velocity increases, more abrupt acceleration/deceleration phases of the rupture front develop, leading to local slip accelerations which would enhance high-frequency radiation (Hartzell & Heaton, 1983; Olson & Apsel, 1982). Our laboratory observations may further our understanding of high-frequency radiation under controlled conditions.

5.2. High-Frequency Radiation Content Depends on the Speed Regime

Here, we observed a net enhancement of high-frequency radiation when the rupture transitions from sub-Rayleigh regime to supershear regime (Figures 2a and 2b), in agreement with what has been proposed by previous studies (Bizzarri & Spudich, 2008; Vallée et al., 2008). In order to investigate the consequences of supershear rupture velocities to high frequency, we give an order magnitude estimate (Figure 2b) of the theoretical corner frequencies f_c of far-field displacement spectrum for rupture velocities equal to $0.8*C_s$ (~2,800 m/s) and to $1.4*C_s$ (~5,000 m/s) based on the kinematic model for a circular crack of Sato and Hirasawa (1973; see supporting information for details). This agrees well with the observations for a sub-Rayleigh rupture but the model underestimates the corner frequency for the supershear case. This could be either because of model limitations or the fact that the geometric attenuation for supershear ruptures is significantly different (Dunham & Bhat, 2008).

5.3. Back-Projection at Laboratory Scale Provides New Insights Into Earthquake Processes

The fact that (i) we have been able to coherently back-propagate high-frequency energy at 400–800 kHz (ii) Fourier spectra show high-frequency asymptotes like f^{-2} independent of the confining pressure, (iii) the peak of energy at 100 kHz is absent at low confinement ($Pc = 10$ MPa) strongly suggest that the information contained in the spectra is linked to the source. Thus, back-projection analysis (Figure 4) can provide new insights on the radiation of high-frequency waves and rupture processes. We carefully ensured that the back-projection results are reliable and are not manifestations of system noise (see supporting information for details). The most robust and interpretable back-projection result obtained was in the 400–800 kHz frequency band (Figure 4 top). The correlation between the spatial and temporal evolution of high-frequency sources and the propagation of the rupture front provides concrete experimental evidence that high-frequency waves are concurrent with the propagation phase of the rupture front and that high-frequency radiation is emitted close to or behind the rupture tip. This result is in agreement with most of the studies that addressed the issue of high-frequency radiation which proposed that high-frequency radiation is related to changes in rupture velocity due to fault stress or frictional heterogeneity, and predict high-frequency waves to be mainly generated in the vicinity of the rupture front (Aki, 1967; Haskell, 1964; Madariaga, 1977, 1983; Spudich & Frazer, 1984). Recent numerical studies (Okubo et al., 2018; Thomas et al., 2017; Thomas & Bhat, 2018) also demonstrated that high-frequency radiation was highly enhanced when coseismic damage was implemented in their rupture propagation models. This is supported by microscopic analysis of the fault surface after stick-slip experiments under Scanning Electron Microscopy (see supporting information), which revealed the presence of microcracks at the grain scale. Above 800 kHz (Figure 4,

bottom), the back-projection results are less clear. It is not surprising given the fact that the signal to noise ratio is significantly lower relative to the 400–800 kHz frequency band and also that acoustic waves above 800 kHz are more sensitive to scattering effects due to small-scale heterogeneities. It might explain why, between 4 and 6 μs, high frequency energy diffuses over the entire fault. However, an observable feature is that high-frequency sources above 800 kHz (Figure 4 bottom) seem to localize slightly forward ahead of the one at 400–800 kHz. One hypothesis is that high-frequency radiation above 800 kHz highlights other physical processes. For instance, Doan and Gary (2009) suggested that grain pulverization and comminution and small-scale gouge particles production could produce high-frequency radiation. Such processes should indeed happen within the breakdown zone, very near the rupture front and should be followed by asperity melting (Aubry et al., 2018; Passelègue et al., 2016).

5.4. Back-Projection Method can Approximate the Geometry of High Frequency Sources

Finally, synthetic tests (Figure S8) demonstrated that the back-projection method can approximately image the high-frequency source geometry. Back-projection results at 400–800 kHz have shown that at the beginning of the rupture and during rupture propagation, high-frequency radiation is drawing a pattern that is spread over almost the entire width of the fault and that is linear along the width of the fault, although it is less noticeable between 4 and 6 μs. However, because acoustic recordings have been aligned to the nucleation zone, the cross-correlation procedure is expected to be less efficient as the source is moving away from the nucleation. This could explain why the initial pattern is not preserved and is concentrated in the middle of the fault with time. Under the assumption that high-frequency sources are representative of the shape of the rupture front, the observations do not match with what would be expected for an elliptical crack in an infinite medium but that of a rupture front strongly interacting with a free surface (Fukuyama et al., 2018; Passelègue et al., 2016).

This study has shown that back-projection analysis at the laboratory scale could be of relevance to understand the nucleation and propagation dynamics of earthquakes. In the future, the combined use of additional phases (*S* waves, surface waves, reflected waves) and the deconvolution of acoustic recordings from Green's function describing the medium should help to get a more detailed and complete description of the source.

Acknowledgments
We thank Miaki Ishii (Harvard University, USA) for her introduction to the use of the back-projection technique. Authors would also like to thank Damien Deldicque (ENS Paris, France) for his help in producing fault surface images under Scanning Electron Microscopy. Authors would also like to thank the anonymous reviewers who significantly participated in improving the quality of our study. This work was funded by the European Research Council grant REALISM (2016-grant 681346). The authors declare that they have no competing financial interests. All data are available online (https://github.com/samsonmarty/high-frequency-radiation-during-laboratory-earthquakes).

References

Aki, K. (1967). Scaling law of seismic spectrum. *Journal of Geophysical Research*, *72*(4), 1217–1231. https://doi.org/10.1029/JZ072i004p01217

Andrews, D. J. (1976). Rupture velocity of plane strain shear cracks. *Journal of Geophysical Research*, *81*(32), 5679–5687. https://doi.org/10.1029/JB081i032p05679

Aubry, J., Passelègue, F. X., Deldicque, D., Girault, F., Marty, S., Lahfid, A., et al. (2018). Frictionnal heating processes and energy budget during laboratory earthquakes. *Geophysical Research Letter*, *45*, 12,274–12,282. https://doi.org/10.1029/2018GL079263

Bernard, P., & Madariaga, R. (1984). High-frequency seismic radiation from a buried circular fault. *Geophysical Journal of the Royal Astronomical Society*, *78*(1), 1–17. https://doi.org/10.1111/j.1365-246X.1984.tb06468.x

Bhat, H. S., Dmowska, R., King, G. C. P., Klinger, Y., & Rice, J. R. (2007). Off-fault damage patterns due to supershear ruptures with application to the 2001 Mw 8.1 Kokoxili (Kunlun) Tibet earthquake. *Journal of Geophysical Research*, 112, B06301. https://doi.org/10.1029/2006JB004425

Bizzarri, A., & Spudich, P. (2008). Effects of supershear rupture speed on the high-frequency content of *S* waves investigated using spontaneous dynamic rupture models and isochrone theory. *Journal of Geophysical Research*, *113*, B05304. https://doi.org/10.1029/2007JB005146

Bouchon, M., Bouin, M. P., Karabulut, H., Toksoz, M. N., Dietrich, M., & Rosakis, A. J. (2001). How fast is rupture during an earthquake? New insights from the 1999 Turkey earthquakes. *Geophysical Research Letters*, *28*, 2723–2726. https://doi.org/10.1029/2001GL013112

Brace, W. F., & Byerlee, J. D. (1966). Stick-slip as a mechanism for earthquakes. *Science*, *153*(3739), 990–992. https://doi.org/10.1126/science.153.3739.990

Bruhat, L., Fang, Z., & Dunham, E. M. (2016). Rupture complexity and the supershear transition on rough faults. *Journal of Geophysical Research: Solid Earth*, *121*, 210–224. https://doi.org/10.1002/2015JB012512

Byerlee, J. D., & Brace, W. F. (1968). Stick slip, stable sliding, and earthquakes effect of rock type, pressure, strain rate, and stiffness. *Journal of Geophysical Research*, *73*(18), 6031–6037. https://doi.org/10.1029/JB073i018p06031

Das, S. (2007). The need to study speed. *Science*, *317*(5840), 905–906. https://doi.org/10.1126/science.1142143

Das, S., & Aki, K. (1977). A numerical study of two-dimensional spontaneous rupture propagation. *Geophysical Journal of the Royal Astronomical Society*, *50*(3), 643–668. https://doi.org/10.1111/j.1365-246X.1977.tb01339.x

Doan, M.-L., & Gary, G. (2009). Rock pulverization at high strain rate near the San Andreas fault. *Nature Geoscience*, *2*(10), 709–712. https://doi.org/10.1038/ngeo640

Dunham, E. M., & Archuleta, R. J. (2004). Evidence for a supershear transient during the 2002 Denali fault earthquake. *Bulletin of the Seismological Society of America*, *94*(6B), s256–s268. https://doi.org/10.1785/0120040616

Dunham, E. M., & Bhat, H. S. (2008). Attenuation of ground motion and stresses from three-dimensional supershear ruptures. *Journal of Geophysical Research*, *113*, B08319. https://doi.org/10.1029/2007JB005182

Fukuyama, E., Tsuchida, K., Kawakata, H., Yamashita, F., Mizoguchi, K., & Xu, S. (2018). Spatiotemporal complexity of 2-D rupture nucleation process observed by direct monitoring during large-scale biaxial rock friction experiments. *Tectono physics*, *733*, 182–192. https://doi.org/10.1016/j.tecto.2017.12.023

Hamano, Y. (1974). Dependence of rupture-time history on heterogeneous distribution of stress and strength on fault plane. *Transactions-American Geophysical Union*, *55*(4), 352–352.

Hartzell, S., Liu, P., & Mendoza, C. (1996). The 1994 Northridge, California, earthquake: Investigation of rupture velocity, risetime, and high-frequency radiation. *Journal of Geophysical Research*, *101*(B9), 20,091–20,108. https://doi.org/10.1029/96JB01883

Hartzell, S. H., & Heaton, T. H. (1983). Inversion of strong ground motion and teleseismic waveform data for the fault rupture history of the 1979 Imperial Valley, California. *Earthquake, Bulletin of the Seismological Society of America*, *73*(6A), 1553–1583.

Haskell, N. A. (1964). Total energy and energy spectral density of elastic wave radiation from propagating faults. *Bulletin of the Seismological Society of America*, *54*(6A), 1811–1841.

Ishii, M. (2011). High-frequency rupture properties of the M w 9.0 off the Pacific coast of Tohoku earthquake. *Earth, Planets and Space*, *63*(7), 18.

Ishii, M., Shearer, P. M., Houston, H., & Vidale, J. E. (2005). Extent, duration and speed of the 2004 Sumatra-Andaman earthquake imaged by the Hi-Net array. *Nature*, *435*(7044), 933–936. https://doi.org/10.1038/nature03675

Johnson, T., Wu, F. T., & Scholz, C. H. (1973). Source parameters for stick-slip and for earthquakes. *Science*, *179*(4070), 278–280. https://doi.org/10.1126/science.179.4070.278

Johnson, T. L., & Scholz, C. H. (1976). Dynamic properties of stick-slip friction of rock. *Journal of Geophysical Research*, *81*(5), 881–888. https://doi.org/10.1029/JB081i005p00881

Kiser, E., & Ishii, M. (2011). The 2010 Mw 8.8 Chile earthquake: Triggering on multiple segments and frequency-dependent rupture behavior. *Geophysical Research Letters*, *38*, L07301. https://doi.org/10.1029/2011GL047140

Madariaga, R. (1977). High-frequency radiation from crack (stress drop) models of earthquake faulting. *Geophysical Journal of the Royal Astronomical Society*, *51*(3), 625–651. https://doi.org/10.1111/j.1365-246X.1977.tb04211.x

Madariaga, R. (1983). High frequency radiation from dynamic earthquake. *Annales de Geophysique*, *1*, 17.

Okubo, K., Bhat, H. S., Rougier, E., Marty, S., Schubnel, A., Lei, Z., et al. (2018) Dynamics, radiation and overall energy budget of earthquake rupture with coseismic off-fault damage, JGR-Solid-Earth. arXiv:1901.01771v1 [physics.geo-ph].

Okuwaki, R., Yagi, Y., & Hirano, S. (2014). Relationship between high-frequency radiation and asperity ruptures, revealed by hybrid back-projection with a non-planar fault model. *Scientific Reports*, *7120*, 4.

Olson, A. H., & Apsel, R. J. (1982). Finite faults and inverse theory with applications to the 1979 Imperial Valley earthquake. *Bulletin of the Seismological Society of America*, *72*(6A), 1969–2001.

Passelègue, F. X., Schubnel, A., Nielsen, S., Bhat, H. S., Deldicque, D., & Madariaga, R. (2016). Dynamic rupture processes inferred from laboratory microearthquakes. *Journal of Geophysical Research: Solid Earth*, *121*, 4343–4365. https://doi.org/10.1002/2015JB012694

Passelègue, F. X., Schubnel, A., Nielsen, S., Bhat, H. S., & Madariaga, R. (2013). From sub-Rayleigh to supershear ruptures during stick-slip experiments on crustal rocks. *Science*, *340*(6137), 1208–1211. https://doi.org/10.1126/science.1235637

Rosakis, A. J., Samudrala, O., & Coker, D. (1999). Cracks faster than the shear wave speed. *Science*, *284*(5418), 1337–1340. https://doi.org/10.1126/science.284.5418.1337

Sato, T., & Hirasawa, T. (1973). Body waves spectra from propagating shear cracks. *Journal of Physics of the Earth*, *21*(4), 415–431. https://doi.org/10.4294/jpe1952.21.415

Savage, J. C. (1966). Radiation from a realistic model of faulting. *Bulletin of the Seismological Society of America*, *56*(2), 577–592.

Scholz, C. H. (1986). *Preface: A short geophysical history of Westerly granite, Geophysical Monograph Series* (Vol. 37) Washington, DC: American Geophysical Union.

Schubnel, A., Nielsen, S., Taddeucci, J., Vinciguerra, S., & Rao, S. (2011). The need to study speed. *Earth and Planetary Science Letters*, *308*(3–4), 424–432. https://doi.org/10.1016/j.epsl.2011.06.013

Spudich, P., & Frazer, L. N. (1984). Use of ray theory to calculate high-frequency radiation from earthquake sources having spatially variable rupture velocity and stress drop. *Bulletin of the Seismological Society of America*, *74*(6), 2061–2082.

Thomas, M. Y., & Bhat, H. S. (2018). Dynamic evolution of off-fault medium during an earthquake: A micromechanics based model. *Geophysical Journal International*, *214*(2), 1267–1280. https://doi.org/10.1093/gji/ggy129

Thomas, M. Y., Mitchell, T. M., & Bhat, H. S. (2017). Fault zone dynamic processes: Evolution of fault properties during seismic rupture. *Science*, *317*(5840), 905–906.

Vallée, M., Landès, M., Shapiro, N. M., & Klinger, Y. (2008). The 14 November 2001 Kokoxili (Tibet) earthquake: High-frequency seismic radiation originating from the transitions between sub-Rayleigh and supershear rupture velocity regimes. *Journal of Geophysical Research*, *113*, B07305. https://doi.org/10.1029/2007JB005520

Wang, D., & Mori, J. (2011). Rupture process of the 2011 on the Pacific coast of Tohoku earthquake (M w 9.0) as imaged with back-projection of teleseismic *P*-waves. *Earth, Planets and Space*, *63*(7), 17.

Wu, F. T., Thomson, K. C., & Kuenzler, H. (1972). Stick-slip propagation velocity and seismic source mechanism. *Bulletin of the Seismological Society of America*, *62*(6), 1621–1628.

Zhang, H., & Ge, Z. (2010). Tracking the rupture of the 2008 Wenchuan earthquake by using the relative back-projection method. *Bulletin of the Seismological Society of America*, *100*(5B), 2551–2560. https://doi.org/10.1785/0120090243

RÉSUMÉ

Au cours de cette thèse, nous avons reproduit expérimentalement des séismes à l'échelle centimétrique dans des conditions de pression proches de la réalité. Les expériences réalisées nous ont permis d'explorer deux grandes thématiques: (i) l'origine du rayonnement haute-fréquence pendant la rupture dynamique et (ii) les signaux précurseurs pendant la phase de nucléation de la rupture dynamique.
Nos résultats montrent que le rayonnement haute-fréquence est concomitant à la propagation du front de rupture et que deux paramètres induisent une augmentation du rayonnement haute-fréquence : l'état de contrainte initial et la vitesse de rupture. Les analyses microstructurales des échantillons de roches suggèrent que la production d'endommagement cosismique ou de particules de gouge contribue au rayonnement haute fréquence.
L'étude des signaux précurseurs (i.e., précurseurs acoustiques) montre que la nucléation est un processus en très large majorité asismique. Ce très faible couplage pourrait expliquer le peu d'observations de séismes précurseurs à l'échelle des failles crustales. L'analyse temporelle des émissions acoustiques suggère que leur dynamique est principalement contrôlée par l'accélération du glissement pendant la phase de nucléation.
La microtopographie et la microstructure des échantillons de roches montrent que le couplage est directement relié à la rugosité du plan de faille. Une augmentation des conditions de pression favorise l'occurrence de processus de déformation plastique ou de fusion partielle au cours de la rupture sismique, ce qui diminue la rugosité et donc le couplage.

MOTS CLÉS

Séisme, rayonnement haute-fréquence, nucléation, signaux précurseurs, acoustique

ABSTRACT

During this thesis, we experimentally reproduced centimeter-scale earthquakes under stress conditions close to reality. The experiments allowed us to explore two main themes: (i) the origin of high-frequency radiation during the dynamic rupture and (ii) foreshocks during the nucleation of dynamic rupture.
Our results show that the high-frequency radiation is concomitant with the propagation of the rupture front and that two parameters induce an increase of the high-frequency radiation: normal stress and rupture velocity. Microstructural analyzes of rock samples suggest that coseismic damage or gouge particles production also contribute to high-frequency radiation.
The study of foreshocks (i.e., acoustic precursors) shows that nucleation process is almost fully aseismic. This very low coupling could explain the few observations of foreshocks at the scale of crustal faults. The temporal analysis of acoustic emissions suggests that their dynamics is mainly controlled by slip acceleration during nucleation phase.
Microtopographic and microstructural analyses of the rock samples show that the coupling is directly related to the roughness of the fault plane. An increase in normal stress conditions favors the occurrence of plastic deformation processes or partial melting during the seismic rupture, which reduces the roughness and therefore the coupling.

KEYWORDS

Earthquake, high-frequency radiation, nucleation, foreshocks, acoustic